2019

Distinct Populations of Layer 5B Pyramidal Neurons in the Primary Motor Cortex

Maria V. Moya

DISTINCT POPULATIONS OF LAYER 5B PYRAMIDAL NEURONS IN THE PRIMARY MOTOR CORTEX

A Thesis Presented to the Faculty of

The Rockefeller University

in Partial Fulfillment of the Requirements for

the degree of Doctor of Philosophy

by

Maria V. Moya

June 2019

DISTINCT POPULATIONS OF LAYER 5B PYRAMIDAL NEURONS IN THE PRIMARY MOTOR CORTEX

Maria V. Moya, Ph.D.

The Rockefeller University 2019

The ability of motor cortex to plan, execute, and refine different movements depends on the coordinated activity of many neurons found across its laminar structure. Layer 5b (L5b), a deep cortical layer that drives output signals from the cortex, contains excitatory pyramidal neurons that innervate many subcortical areas of the brain. In the motor cortex, L5b is thicker and contains more pyramidal neurons than L5b of other cortical areas. Electrophysiological, anatomical, and RNA-Seq profiling of neurons in the motor cortex suggests there are diverse pyramidal neuron types within L5b. However, the precise identities of these distinct populations and their defining traits have been difficult to assess. Determining the cell type-specific properties of distinct L5b pyramidal neurons will not only help in understanding how the motor cortex is able to execute its varied functions, but may also reveal how selective vulnerability is established in neurodegenerative diseases that affect the motor cortex, such as Amyotrophic Lateral Sclerosis (ALS). Despite being expressed in all cells of the body, mutations associated with ALS lead to specific loss of LMNs in the brainstem and the ventral horn of the spinal cord, and UMNs in L5b of the motor cortex. For this reason, it is important to characterize the unique molecular profiles that may underlie an increased vulnerability of these cell

types to the ubiquitously expressed mutations. In the motor cortex, this requires us to determine the characteristics that differentiate vulnerable L5b cells from other resistant cell types in the same area, and understand how these features may contribute to their death in ALS. This study aims to understand how anatomical traits and molecular properties, defined at the level of gene expression, vary across subpopulations of L5b pyramidal neurons in the motor cortex. We show that there are two distinct, but closely related, pyramidal neuron subtypes in mouse primary motor cortex which occupy discrete sublayers of L5b. In the SOD1-G93A mouse model of ALS, we observe loss of only one of these cell types, establishing the other as an analogous resistant L5b population. Using TRAP (Translating Ribosome Affinity Purification) with RNA-Seq, we show that these cells have important baseline differences in gene expression in healthy tissues, and that they display differential molecular responses to SOD1-G93A expression. Together, these findings reveal that the gene expression differences between the distinct L5b populations not only reflect their diverse cortical and subcortical anatomy, but may also establish selective vulnerability in ALS.

“ Be sure your self and your own Reach to know,
How far your Genius, Taste, and Learning go;
Launch not beyond your Depth, but be discreet,
And mark the Point where Sense and Dulness meet;
Nature to all things fix’d the Limits fit,
And wisely curb’d proud Man’s pretending wit. ”

- Alexander Pope

Dedicated to my family.
I couldn’t have done this without you.

ACKNOWLEDGEMENTS

Conceiving, designing, and carrying out a thesis project is an exciting but occasionally painful personal growth experience. Having the guidance of E. Schmidt and N. Heintz in each of these stages was completely invaluable to easing and facilitating this, so I want to thank them first and foremost. Additionally, many experiments were devised based on the suggestions of my past and present committee members, so I'd like to thank P. Cohen, S. Shaham, M. Tessier-Lavigne, and A. Hantman for their feedback. In collaboration with H. Phatnani at NYGC, we were able push the project forward in an efficacious and productive direction, so I'd like to thank her for her help with sample sequencing and feedback on the project. So many other sources of support provided key help to me during this experience, among them I want to thank the entire Dean's office and K. Uryu in the EMRC. Thank you to L. Pomeranz for generously sharing PRV 293 for retrograde tracing experiments. Thank you to A. Hantman for helping us in generating the retrograde rAAV2 vectors used in this study. And thank you to the WCM Imaging core for producing slides of human brain tissue.

On a personal level, managing the occasional pain of PhD was carried out by a huge number of people. Principally, I would like to thank R. Kim, M. Rao, and C. Sferrazza for their help in performing a great number of the experiments discussed here. Watching you develop as scientists was an enormous honor that I'll always carry with me. Friendships in the lab kept me going through the good times and the bad, so I would like to thank my bay-mate X. Xu, as well as E. Holzner, M. Rao, and E. Stoyanova for their often-underserved support. During the particularly difficult times, J. Alvarez, R. Kim, K.

McGuire, C. Sferrazza, and F. Weiss rallied around me in the most incredible way. I have no idea how to thank you guys for it, and I can only say that I owe you the world because of it. I would also like to thank F. Piccolo, who taught me so much about both science and life. I feel incredibly privileged to not only know you as an exemplary scientist, but also as a close and treasured friend. Outside of the lab, I would like to thank P. Kidd for his enormous contribution to editing this thesis, as well as his true friendship. I'm happy we got to know each other, even if it was so late. To B. Ferris: we've got this, my man! I would like to thank R. Pisa, whom I was superbly fortunate to fall in love with. Through our mutual struggles in this stage of our lives, you have kept me grounded and unburdened in ways I could not have imagined possible. For that, I cannot find the words to thank you. I want to thank A. Gilbert for choosing me and for going on so many NYC adventures with me. Even apart, we are together. Thank you to T. Chowdhury for proving to me that this could be done. I hope your undergrad whines less now and has made you proud. I would like to thank J. Mangalindan and T. Smith for being part of my extended family. You guys have been with me for over a decade and have lifted me up off the ground countless times. Also, without your elbow macaroni and scratch-n-sniff stickers, I wouldn't have been able to design the cover of this thesis. Most importantly, I would like to thank my family, M. Martinez, J. Moya, and S. Moya, who instilled in me a drive to always be better and to keep pushing ahead. Ustedes creyeron en mi desde el principio, y les debo todo lo que resultó. Finally, I would like to thank the various donors of human brain tissue and their families. Your contributions will allow us to one day fully conquer ALS.

TABLE OF CONTENTS

DEDICATION iii
ACKNOWLEDGEMENTS iv
TABLE OF CONTENTS vi
INDEX OF FIGURES ix
INDEX OF TABLES xiii
ABBREVIATIONS USED xiv

CHAPTER 1: Study Introduction and Objectives 1

CHAPTER 2: Anatomical and molecular characterization of Colgalt2 and Gprin3 bacTRAP cell populations 16

2.1 Anatomical and distribution of EGFP-labeled cells in the Colgalt2-TRAP DU9 mouse line 18
2.2 Anatomical and distribution of EGFP-labeled cells in the Gprin3-TRAP ES152 mouse line 22
2.3 Colgalt2 and Gprin3 neurons represent two distinct populations of layer 5b pyramidal neurons in primary motor cortex of mouse 26
2.4 Colgalt2 and Gprin3 neurons share long-range projection neuron identity, but project to distinct targets 28
2.5 Gprin3 cells project to spinal motor neurons through an intermediate population of neurons in the central spinal cord 35
2.6 Colgalt2 and Gprin3 neurons represent two molecularly related, but nevertheless distinct, populations of L5b pyramidal neurons 39
2.7 Discussion 4

CHAPTER 3: Generating tractable models for studying cell-type vulnerability and resistance in the primary motor cortex of SOD1-G93A mice 50
3.1 Breeding SOD1-G93A mice to Colgalt2 and Gprin3-TRAP mice does not disrupt disease progression 53
3.2 Both Colgalt2 and Gprin3 mice show activated glial invasion when SOD1-G93A is expressed 55
3.3 Gprin3 cells are vulnerable to degeneration in SOD1-G93A, while Colgalt2 neurons are resistant 57
3.4 Discussion 60

CHAPTER 4: Molecular responses to SOD1-G93A observed by TRAP in Colgalt2 and Gprin3 neurons 66
4.1 Isolating mRNA from Colgalt2 and Gprin3 cells expressing SOD1-G93A 68
4.2 Pre-symptomatic changes in gene expression in Colgalt2 and Gprin3 cells 71
4.3 Symptomatic changes in gene expression in Colgalt2 and Gprin3 cells reveal opposing molecular responses to SOD1-G93A expression 73
4.4 Oxidative phosphorylation genes are differentially regulated in SOD1-G93A between Colgalt2 and Gprin3 cells 77
4.5 Oxphos genes that show expression changes in SOD1-G93A are differentially expressed between healthy Colgalt2 and Gprin3 cells 82
4.6 A respiratory transcription factor is differentially expressed between Colgalt2 and Gprin3 neurons 84
4.7 Discussion 86

CHAPTER 5: Visualizing and modulating mitochondrial structure and function in the context of SOD1-G93A 92
5.1 Mitochondria of upper and lower L5b cells occupy similar volumes in the soma 94
5.2 Gprin3 cells display wider cristae than Colglat2 cells 98
5.3 LL5b cells but not UL5b cells show greater size and decreased number of mitochondria when SOD1-G93A is expressed 100

5.4 Gprin3 and surrounding cells expressing SOD1-G93A show changes in cristae morphology by EM 104
5.5 Strategies for modulating levels of respiration and ETC activity in UL5b and LL5b 106
5.5 Discussion 110

CHAPTER 6: Finding markers for L5 cell types in human motor cortex 115
6.1 Narrowing down candidate markers for L5b cells across species 116
6.2 Crym and Nefh ISH label populations of neurons in L5b of mouse primary motor cortex 120
6.3 Crym and SMI-32 staining allows for visualization of L5 cells in human primary motor cortex 122
6.4 Basic distinguishing features of marker-positive cells in medial human motor cortex and mouse M1 125
6.5 Discussion 127

CHAPTER 7: Study Conclusions 132

MATERIALS AND METHODS 140

WORKS CITED 161

INDEX OF FIGURES

CHAPTER 1

Figure 1.1: Pyramidal neuron distribution across the layers of the mammalian cortex 2

Figure 1.2: Cell types of the primary motor cortex layers may be more diverse than originally thought 5

Figure 1.3: The long-range projections of L5b cells of M1 7

Figure 1.4: The general findings of this study 14

CHAPTER 2

Figure 2.1: Expression of EGFP-L10a in mouse L5b using BAC Transgenics 20

Figure 2.2: Expression of EGFP-L10a in Colgalt2-TRAP DU9 mice is observed in L5b across the entire cortex 21

Figure 2.3: Expression of EGFP-L10a in Gprin3-TRAP ES152 is localized to anterior areas of cortex, and found in many subcortical areas of the brain 23

Figure 2.4: Colgalt2 and Gprin3 cells show distinct sublayer distribution within L5b of M1 27

Figure 2.5: Colgalt2 and Gprin3 cells are both positive for Ctip2, a marker for subcortical projection neurons of the cortex 29

Figure 2.6: Retrograde tracing from pons and cervical spinal cord labels L5b neurons in M1 31

Figure 2.7: Retrograde tracing from pons and cervical spinal cord labels Colgalt2 and Gprin3 cells 32

Figure 2.8: Colgalt2 cells project to the pons, while Gprin3 cells project to both the pons and the cervical spinal cord 33

Figure 2.9: Anterograde labeling of LL5b cells in M1 reveals projections to intermediate regions of spinal grey matter 36

Figure 2.10: PRV tracing reveals that neither Colgalt2 nor Gprin3 cells participate in forelimb control circuitry 38
Figure 2.11: Colgalt2 and Gprin3 cells have gene expression profiles that suggest that, among other neuronal populations, they are closely related 40
Figure 2.12: Colgalt2 and Gprin3 cells are related in part by their expression of known L5b genes 42
Figure 2.13: Differential expression between Colgalt2 and Gprin3 cells reveals molecular differences between UL5b and LL5b cell types 43
Figure 2.14: Summary of UL5b and LL5b anatomical divergence 45

CHAPTER 3

Figure 3.1: Expression of EGFP-L10a in Colgalt2 and Gprin3 mice does not alter the progression of disease in a SOD1-G93A context 54
Figure 3.2: GFAP-positive astrocytes invade L5b in Colgalt2 and Gprin3 mice that express SOD1-G93A 56
Figure 3.3: GFP staining reveals loss of Gprin3 cells in SOD1-G93A mice, but no loss of Colgalt2 cells 58
Figure 3.4: Gprin3 cells are lost in SOD1-G93A mice, but Colgalt2 cells remain 59
Figure 3.5: Summary of cell type-specific loss observed in L5b in SOD1-G93A mice 61

CHAPTER 4

Figure 4.1: Summary of all TRAP IP samples from Colgalt2 and Gprin3 ALS cohorts 69
Figure 4.2: Colgalt2 and Gprin3 TRAP IP samples from ALS cohorts show expression of benchmark cell type-specific genes 70
Figure 4.3: Pre-symptomatic Colgalt2 samples reveal early changes in gene expression in UL5b cells in response to SOD1-G93A 72

Figure 4.4: Pre-symptomatic Gprin3 samples reveal early changes in gene expression in LL5b cells in response to SOD1-G93A 74
Figure 4.5: Symptomatic Colgalt2 samples reveal late changes in gene expression in resistant UL5b cells in response to SOD1-G93A 76
Figure 4.6: Symptomatic Gprin3 samples reveal late changes in gene expression in vulnerable LL5b cells in response to SOD1-G93A 78
Figure 4.7: Between Colgalt2 and Gprin3 cells, mitochondrial genes show contrasting changes in gene expression in response to SOD1-G93A 80
Figure 4.8: qPCR for mitochondrial genes confirm contrasting changes in gene expression for disease Colgalt2 and Gprin3 cells 81
Figure 4.9: Mitochondrial genes, including Oxphos genes, are enriched in Gprin3 cells relative to Colgalt2 cells 83
Figure 4.10: Transcription factor motif analysis reveals motifs and factors associated with genes that change in disease 85
Figure 4.11: Summary of TRAP and RNA-Seq findings from SOD1-G93A Colgalt2-TRAP and Gprin3-TRAP animals 87

CHAPTER 5

Figure 5.1: Generating a construct for expression of a mitochondrially localized GFP reporter in a cell type-specific manner 95
Figure 5.2: UL5b and LL5b cells show similar mitochondrial volume 97
Figure 5.3: Gprin3 cells show larger mitochondrial cristae widths than Colgalt2 cells 99
Figure 5.4: Generating a Cre-independent construct for expression of TOM20-mCherry mitochondrial reporter in a cell type-specific manner across healthy and disease L5b 101
Figure 5.5: LL5b cells show changes in TOM20-mCherry distributions that are not observed in UL5b cells 103
Figure 5.6: Cells in LL5b of M1 show increased cristae width in SOD1-G93A 105

Figure 5.7: Modulating levels of Oxphos by retinoic acid injections does not alter disease progression 108
Figure 5.8: Modulating levels of Oxphos in L5b cells by Pgc1a overexpression does not alter disease progression 109
Figure 5.9: Summary of mitochondrial morphology analysis in Colgalt2 and Gprin3 cells 112

CHAPTER 6

Figure 6.1: Staining for Pcp4, Crym, and SMI-32 in mouse and human tissue allows for visualization of deep layer neurons in the motor cortex 119
Figure 6.2: FISH against Crym and Nefh labels populations of L5b cells in M1 of mouse 121
Figure 6.3: Crym and SMI-32 staining reveals distinct laminar populations of cells across human primary motor cortex 124
Figure 6.4: Crym and SMI-32 staining can anatomically dissociate putative Betz cells from other neurons in L5 of human motor cortex 126
Figure 6.5: Summary of Crym and SMI-32 L5 cell type distribution across mouse and human motor cortex 129

INDEX OF TABLES

CHAPTER 6

Table 6.1: Candidate markers for L5b cells across species 118

ABBREVIATIONS USED

CNS	Central nervous system
L1	Layer 1
L2/3	Layer 2/3
L4	Layer 4
L5a	Layer 5a
L5b	Layer 5b
L6a	Layer 6a
M1	Primary motor cortex
ALM	Anterolateral motor cortex
TRAP	Translating Ribosome Affinity Purification
ALS	Amyotrophic Lateral Sclerosis
SOD1	Superoxide dismutase 1
rAAV	Recombinant adeno-associated virus
C6	Cervical spinal cord, level 6
CC	Corpus callosum
LL5b	Lower layer 5b
UL5b	Upper layer 5b
UMN	Upper motor neuron
LMN	Lower motor neuron
PT	Pyramidal tract
GFP	Green fluorescent protein
CTB	Cholera toxin, beta subunit
PCA	Principal component analysis
DE	Differential expression
TF	Transcription factor
IT	Intratelencephalic
AP	Anterior-posterior
ML	Medial-lateral
DV	Dorsal-ventral
FC	Fold change
CPM	Counts-per-million
PRV	Pseudorabies virus
ETC	Electron transport chain
Oxphos	Oxidative phosphorylation
SL1	Retrograde AAV, Schaffer Lab
FISH	Fluorescence In situ hybridization
IF	Immunofluorescence
ROS	Reactive oxygen species
IP	Intraperitoneal or Immunoprecipitation
RA	Retinoic Acid

CHAPTER 1:

Study Introduction and Objectives

The function of the central nervous system (CNS) fundamentally relies on communication between many unique cell types. The myriad functions that are carried out by the brain via these connections reflect the diverse anatomy, morphology, and physiology of these CNS populations. Underlying this diversity are unique patterns of gene expression that provide the necessary elements for constructing each distinct cell type, both during development and in adulthood. For the mammalian neocortex, a hub for cognition and integrative processing in the brain, this means defining the laminar distribution of neuron populations that makes up its cytoarchitecture. The adult cortex is classically organized into 6 anatomically and functionally distinctive layers that each contain different subtypes of excitatory and inhibitory neurons (Brody, 1955; Jones and Wise, 1977; Krieg, 1946; Lorente de No, 1938; Wise and Jones, 1977a). The excitatory cortical populations are often referred to as pyramidal neurons because of the pyramid shape of their cell bodies (see O'Leary, 1941; Ramón y Cajal, 1911). Each layer of the cortex contains pyramidal neurons that differ in morphology, size and connectivity (Figure 1.1). The most superficial layer, Layer 1 (L1), houses the distal dendritic processes, or “apical tufts”, of deeper layer pyramidal neurons, which receive input from various modulatory subcortical areas (Lorente de No, 1938; Vaughan and Peters, 1973). Layers 2 and 3, in rodents often combined as a single Layer 2/3 (L2/3), contain small pyramidal neurons that communicate with other cortical cells in the same cortical

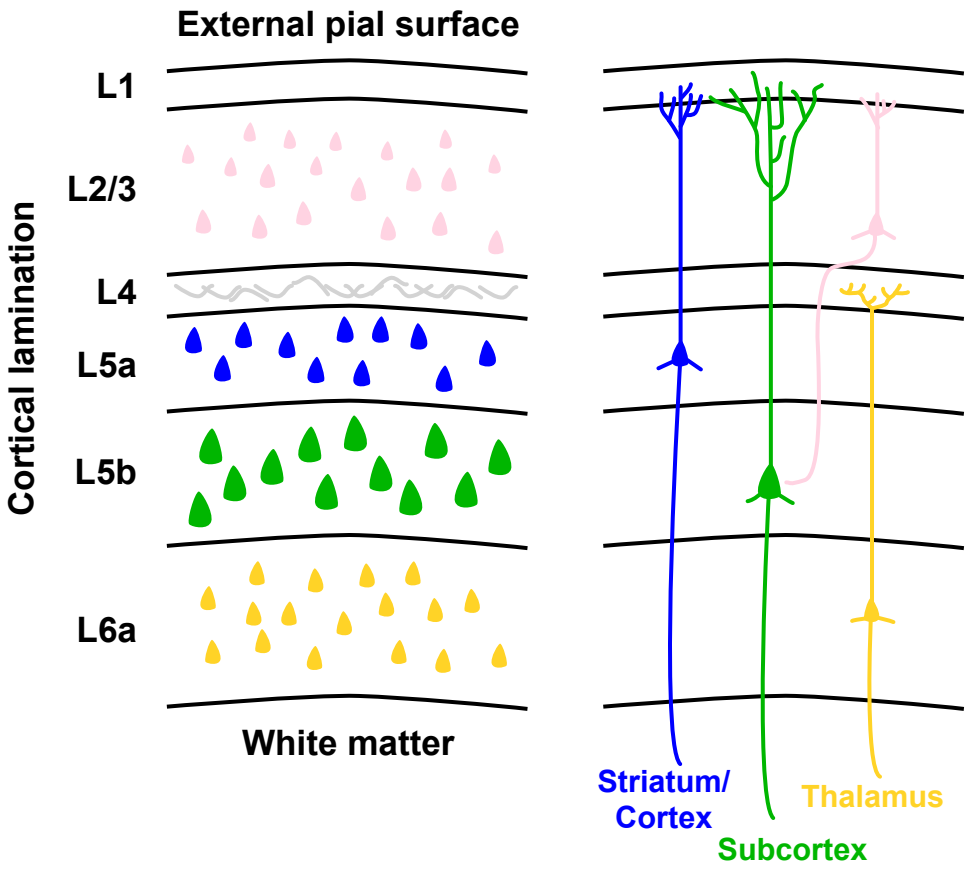

Figure 1.1: Pyramidal neuron distribution across the layers of the mammalian cortex. Model of cortical laminar cell types. L2/3 contains small neurons (pink) that project to deep layer neurons within the cortical column, and in other areas of cortex. L4 receives inputs from sensory regions of the brain. L5a cells (blue) are slightly larger, and send projections to the striatum and across other regions of cortex, include contralateral cortex. L5b is a thick layer that contains some of the largest pyramidal neurons in the cortex (green) that send projections to many different subcortical nuclei, the brainstem, and the spinal cord. L6a contains small neurons (yellow) that project to the thalamus.

column, as well as across other cortical regions (Gilbert and Kelly, 1975; Vogt and Pandya, 1978). Layer 4 (L4), where present, is an important input layer of the cortex, receiving the axon terminals of many sensory input neurons from other regions of the brain (Shatz and Stryker, 1978; Woolsey and Van der Loos, 1970). Layer 5 (L5), is composed of two major subdivisions. Layer 5a (L5a) contains large pyramidal cells that innervate neurons in the striatum and other regions of the cortex, including the opposite hemisphere, or “contralateral” cortex (Jones et al., 1975; 1977). Layer 5b (L5b) is an important effector output layer of the cortex, containing the largest pyramidal neurons that send their long-range axons to distal targets throughout the subcortical regions of the brain (Domesick, 1969; Wise and Jones, 1977b; 1977a; Wise et al., 1979). Layer 6 (L6) is primarily represented by layer 6a (L6a), which includes pyramidal neurons that are important in feedback signaling with the thalamus (Wise and Jones, 1977b).

This laminar architecture is highly conserved across different functional areas of the cortex, such as visual and auditory regions (Krieg, 1946). However, in the primary motor cortex (M1) and accessory motor regions such as anterolateral motor cortex (ALM), there are two notable differences. (1) These areas do not contain a prominent L4, and (2) they show a broader L5b thickness (Jones and Wise, 1977). Because L5b of the cortex is a key computational output layer, the greater number of pyramidal neurons that are accommodated by this widening reflect the importance of motor cortex output for signaling in motor function. The proper execution of movement requires many stages of preparatory and executive computation, and the pre-motor and motor cortices of diverse species are indispensible in this multifaceted processing. These areas help to

prepare and initiate voluntary movement (Chen et al., 2017; Churchland and Shenoy, 2007; Day et al., 1989; Economo et al., 2018; Evarts, 1968; Inagaki et al., 2018; Penfield, 1954; Roland et al., 1980; Thach, 1978), participate in the initiation and execution of dexterous movements (Evarts, 1966; Graziano et al., 2002; Gu et al., 2017a; Guo et al., 2015; Shibasaki et al., 1993), and are important in the coordination and refinement of gross movements that takes place during motor learning (Fischer, 1967; Kawai et al., 2015; Lashley, 1942). Accomplishing these varied forms of processing requires signaling to many areas of the CNS, and therefore many axonal outputs from these motor areas. And to carry these efferent messages, L5b in these regions may contain diverse populations of subcortical projection neurons, also known as corticofugal neurons, that contribute to different aspects of functional output from the motor cortex (Figure 1.2, see Yu et al., 2008).

Evidence of the heterogeneity of motor cortical neuron populations has been found in rodents, where different approaches have been employed to determine the neuronal cell type composition of the different layers. For instance, using electrophysiology, it has been revealed that in motor areas, the activity of different cells during distinct temporal and spatial phases of movement is key to the preparation and execution of the movement (Chen et al., 2017; Economo et al., 2018; Guo et al., 2015; 2014; Harrison et al., 2012). Importantly, these cells receive electrophysiological input from different sources depending on their depth in the cortex (Hooks et al., 2013; Mao et al., 2011; Petreanu et al., 2009; Ueta et al., 2014; Yu et al., 2008). Additionally, their electrophysiological properties suggest that cells in L5b can show differential degrees of

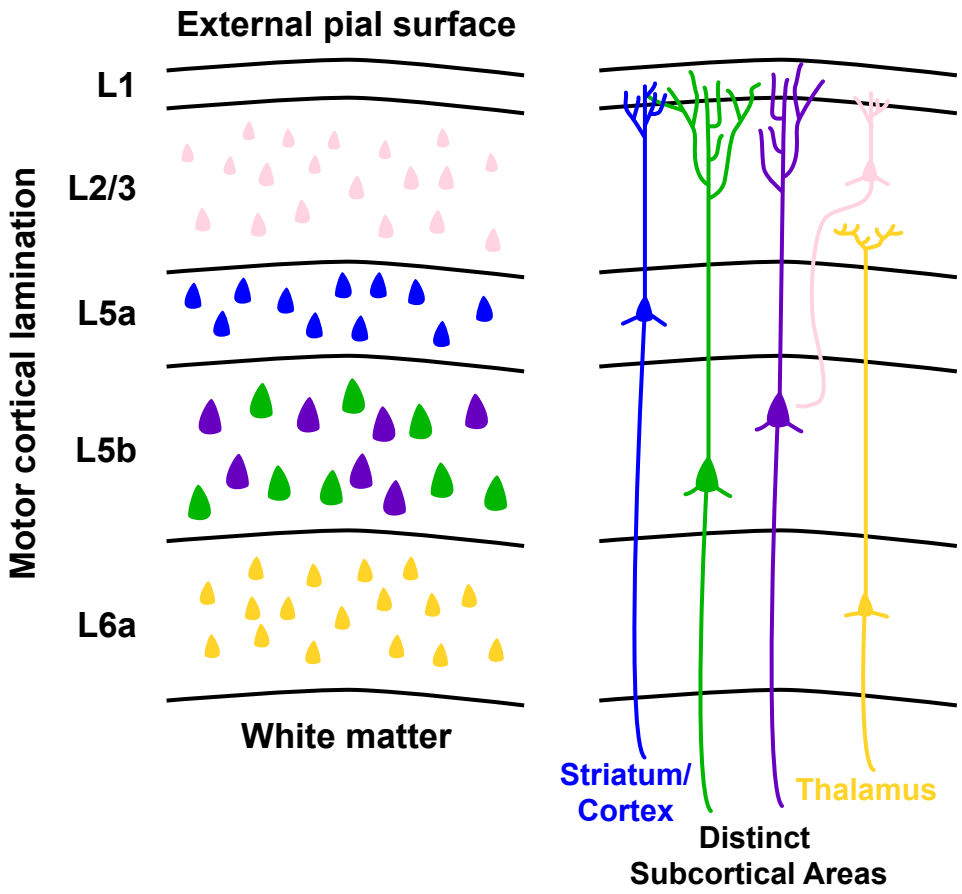

Figure 1.2: Cell types of the primary motor cortex layers may be more diverse than originally thought. The current thinking of motor cortical cytoarchitecture given published findings and the findings of this study. M1 is agranular and contains no L4. L5b is thicker in these areas and may contain distinct populations projection neurons. These cells may send projections to distinct subcortical areas throughout the brain.

the spike-frequency adaptation necessary for maintaining persistent activity (Hattox and Nelson, 2007; Oswald et al., 2013; Sheets et al., 2011; Suter et al., 2013; Tantirigama et al., 2016; 2014). Another approach used to address the heterogeneity of pyramidal neurons in the motor areas is anatomical tracing, whereby one can label neurons that project to different areas of the brain by injecting retrograde dyes and reporter-expressing viruses into these target regions. Using these labeling methods, the projections from L5b of the motor cortex haven been shown to target several different regions of the subcortex, including the thalamus, the superior colliculus, the pons, the brainstem, and the spinal cord (Figure 1.3; Arlotta et al., 2005; Economo et al., 2018; Feng et al., 2000; Gerfen et al., 2016; Oswald et al., 2013) Distinct subpopulations of L5b neurons appear to have specific combinations of collateral projections rather than each innervating all of these regions (see Economo et al., 2018). Finally, using high-throughput sequencing methods that assay whole cortical areas, it has been shown that even within individual sublayers, there may be distinct populations of cells that are differentiated by their gene expression patterns (Fame et al., 2017; Sugino et al., 2006; Tasic et al., 2016; 2018). Together these findings have all suggested that the cell type-composition of the distinct layers of motor cortical areas may be more heterogeneous than originally suspected. However, it has been difficult to consolidate the findings of these diverse studies into a comprehensive atlas of L5b cell types and their respective features. This is due to the fact that, within the same animal, it is challenging to carry out all of the various physiological, anatomical, and molecular assays used to describe cell type properties, and therefore impossible to cross-reference a particular feature with

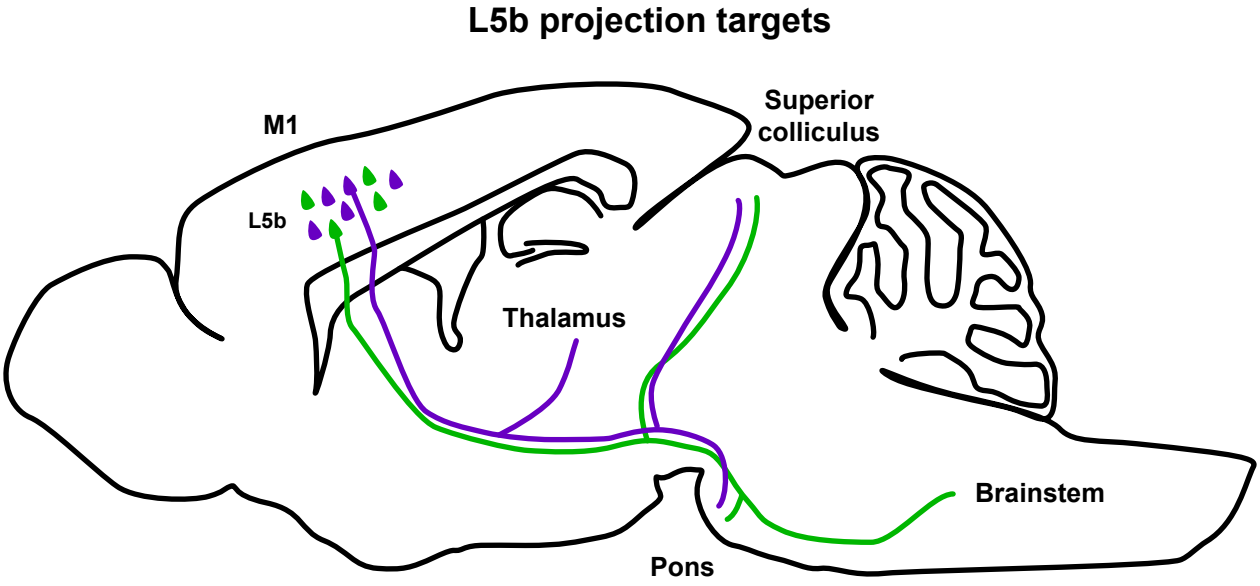

Figure 1.3: The long-range projections of L5b cells of M1. Sagittal illustration of projection patterns for the distinct L5b subpopulations of L5b cells, from recent published studies as well as findings from this study. Together, these populations send long-range projections to more proximal and distal regions of the subcortex, including the ventral posteromedial nucleus of the thalamus, the superior colliculus, the pons, and the brainstem.

a specific cell in the tissue. Without reproducible anatomical and molecular access to the individual distinct cell types of L5b, we will not be able to define the unique features of these neurons across the varied experimental paradigms used to define neuronal subpopulations.

The ability to visualize specific neuronal populations and profile their specific patterns of gene expression across experimental assays is the cornerstone of the Translating Ribosome Affinity Purification (TRAP) technique (Doyle et al., 2008; Heiman et al., 2008). The ability to introduce transgenes into the mouse genome by using Bacterial Artificial Chromosomes (BACs) was key to the development of the technique (Gong et al., 2010; 2003; Shizuya et al., 1992). TRAP relies on the expression of a subunit of the large ribosomal complex (L10a) fused to a green fluorescent protein (EGFP; EGFP-L10a). In order to express EGFP-L10a in specific cellular population of interest, a region of the genome that contains a gene selectively expressed in these cells is converted into a BAC, where EGFP-L10a is inserted by homologous recombination downstream of the promoter of the cell type-specific gene. The modified BAC is then introduced by microinjection into a fertilized mouse zygote, where it incorporates into the genome by recombination. The cell type-specific gene promoter then drives transcription of EGFP-L10a in any cells that express that gene. The fluorescent EGFP allows for the anatomical visualization of this cell type in tissue, and when isolated by immunoprecipitation (IP), also provides access to the mRNA molecules that are bound to the ribosomal complex during translation. This technique has been broadly applied in the study of the molecular underpinnings of cell type-

specific features across the CNS in both healthy and dysfunctional physiology (Nakajima et al., 2014; Schmidt et al., 2012; Virk et al., 2016). The TRAP technique is therefore ideally suited to revealing underlying molecular differences across L5b pyramidal neuron types that, starting at the level of gene expression, help establish unique neuronal properties.

While differing patterns of gene expression can impart unique functional properties and establish anatomical diversity, they can additionally create vulnerabilities to biological insult. In fact, the selective vulnerability of specific neuron populations is a hallmark of many neurodegenerative diseases. In these diseases, ubiquitously expressed mutations cause discrete populations of vulnerable cells to die because the specific molecular environment found in those cells is not able to mitigate the insult. In the case of Amyotrophic Lateral Sclerosis (ALS), loss of two different cell types is observed: upper motor neurons (UMNs) in L5 of the primary motor cortex and lower motor neurons (LMNs) in the ventral horn of the spinal cord (Charcot and Joffroy, 1869; Hammer et al., 1979). Progressive loss of these two motor neuron populations is catastrophic to motor function, and is therefore lethal to the patient. ALS patients typically become symptomatic at an average age of 55 (als.org and alsa.org), with initial symptoms often including muscle weakness and tremors. Almost 6000 patients are newly diagnosed with ALS every year in the US alone, and although disease progression rates can vary from case to case, patients typically do not survive beyond 5 years post-diagnosis. The vast majority of ALS cases (90%) occur sporadically (sALS) with no detectable heritable cause (Rowland and Shneider, 2001; Tandan and Bradley,

1985). For the remaining 10% of cases, heritable mutations to several genes- including Superoxide dismutase 1 (SOD1), C9orf72, Tar-DNA binding protein (TDP-43), and Fused in sarcoma (FUS)- account for most familial ALS (fALS) cases (DeJesus-Hernandez et al., 2011; Kwiatkowski et al., 2009; Renton et al., 2011; Rosen et al., 1993; Sreedharan et al., 2008; Vance et al., 2009)).

It is not fully understood how mutations in these ubiquitously expressed genes cause degeneration of UMNs and LMNs specifically, and no effective treatments for ALS have been developed. Nevertheless, mouse models of ALS that express mutations in the fALS-associated genes (SOD1, TDP-43, FUS, and C9orf72) have allowed us to probe disease mechanisms in a controlled context. (Gurney et al., 1994a; Liu et al., 2016; Verbeeck et al., 2012; Wegorzewska et al., 2009). These models recapitulate different features of the cellular pathologies often observed in human ALS tissues, such as cytoplasmic inclusions and cellular atrophy (Bentmann et al., 2013; Jara et al., 2012; Tsao et al., 2012; Turner and Talbot, 2008). They additionally show some of the motor deficits that are reminiscent of the symptoms developed by human ALS patients. In particular, the commonly used SOD1-G93A model (Chiu et al., 1995; Gurney et al., 1994b) shows the progressive loss of motor function and degeneration of UMNs and LMNs that is the pathological definition of ALS. As in humans, however, it is not known how ubiquitously expressed mutant SOD1 in these mice inevitably causes death of motor neurons. Yet, the field has gleaned many insights into the cellular dysfunctions that occur in response to mutant SOD1 expression (see Cleveland and Rothstein, 2001; Turner and Talbot, 2008).

In healthy cells, SOD1 acts to convert the highly reactive superoxide generated as part of various cellular functions into less reactive hydrogen peroxide (McCord and Fridovich, 1969). Mutations to 70 of the 153 SOD1 amino acids have been linked to fALS and sALS (see Turner and Talbot, 2008). Mouse models that express many of these human SOD1, including the glycine-to-alanine mutation at the 93rd amino acid (G93A), have been generated in an effort to study the effects of mutant SOD1 to cellular function. Across various SOD1 mutants appear to aggregate (Johnston et al., 2000), mislocalize to mitochondria (Higgins et al., 2002; Jaarsma et al., 2001), lose metal ion binding ability (Goto et al., 2000; Williamson et al., 2000), and cause downstream oxidative damage via nitric oxide and hydrogen peroxide substrates (Andrus et al., 1998; Beal et al., 1997; Bruijn et al., 1997a; Casoni et al., 2005; Estévez et al., 1999; Ferrante et al., 1997; Singh et al., 1998). Many of these dysfunctions have been described in studies of the SOD1-G93A model, where one of the cumulative consequences of these SOD1 phenotypes is the loss of LMNs of the spinal cord (Chiu et al., 1995; Gurney et al., 1994b). Characterizing the cellular changes occurring in LMNs during disease progression has been the primary focus of much ALS research in the SOD1-G93A mouse. This is primarily due to the fact that LMNs are readily distinguishable from other spinal cell types by their ventral localization and large size (Aitken and Bridger, 1961; Light and Metz, 1978), and are therefore relatively easy to selectively visualize in tissue. From these studies, several of the molecular responses that take place in these cells during ALS progression have been uncovered, including oxidative stress (Beal et al., 1997; Bruijn et al., 1997b; Casoni et al., 2005), axon

transport defects (Warita et al., 1999; Williamson and Cleveland, 1999; Zhang et al., 1997), dysregulation of glutamate-mediated neurotransmission and excitotoxicity (see Kuner et al., 2005; Tateno et al., 2004; Trotti et al., 1999), and misfolded protein aggregation (Bruijn et al., 1997b; Johnston et al., 2000; Watanabe and Nakamura, 2000). While determining these phenotypes is necessary for the future development of treatments and therapies, it is important to remember that ALS is clinically defined by the loss of both LMNs of the brainstem and spinal cord, and UMNs of the motor cortex. Understanding what molecular changes occur in UMNs, in complement with the responses observed in LMNs, will allow us to more effectively determine what phenotypes lead to cell type-specific loss in ALS.

Characterizing the molecular changes that occur in UMNs of the motor cortex during disease has proven challenging. Because the pyramidal neuron types in the cortex are heterogeneous, even within L5b (Krieg, 1946), visualizing these cells requires a targeted labeling approach. Using retrograde anatomical tracing methods in mouse models of ALS, including SOD1-G93A, it has been possible to study the disease-related changes that take place in corticofugal L5b cells of rodent M1 during ALS progression (Kim et al., 2017; Ozdinler et al., 2011; Yasvoina et al., 2013; Zang and Cheema, 2002), also (see Jara et al., 2014). Many of these changes are reminiscent of phenotypes observed in LMNs, such as hyperexcitability (Fogarty et al., 2015), atrophy (Ozdinler et al., 2011; Zang and Cheema, 2002), and vacuolization (Jara et al., 2012). But because the anatomical approaches used in the majority of UMN studies do not provide the ability to assess molecular cell type heterogeneity, it is still

not fully understood whether these disease phenotypes represent cell type-specific changes, or are more indicative of global L5b responses to ALS-causing mutations.

Without a method that allows for reliable visual and molecular access to individual neuronal subtypes within the potentially heterogeneous population of L5b cells, including the vulnerable UMN population, we cannot hope to fully advance our understanding of how mutant SOD1 expression can cause motor neuron-specific loss. The TRAP technique presents an ideal opportunity to anatomically characterize and molecularly profile the different L5b populations of the motor cortex in ALS to determine any subpopulation-selective responses. Additionally, and perhaps more importantly, the technique would allow us to interrogate how the cell type-specific features of the most vulnerable population of L5b neurons may be exploited by a ubiquitously expressed ALS mutation to cause selective degeneration.

In this work, we set out to uncover what unique characteristics define the vulnerable population of M1 L5b neurons relative to closely related L5b neurons in both healthy and ALS contexts (Figure 1.4). We first generated transgenic BAC transgenic mouse lines that expressed EGFP-L10a in L5b cells of M1, via the Colgalt2 and Gprin3 promoters respectively. The EGFP expression in these lines provided us with visual access to these two L5b populations, which we used to determine the laminar localization and projection patterns of these cells. We show that Colgalt2 cells are found in an upper sublayer of L5b (UL5b) and project to the pons and not the spinal cord, while the Gprin3 population is found in a discrete lower sublayer of L5b (LL5b) and projects to the pons and the spinal cord. The EGFP-L10a construct also allowed us to

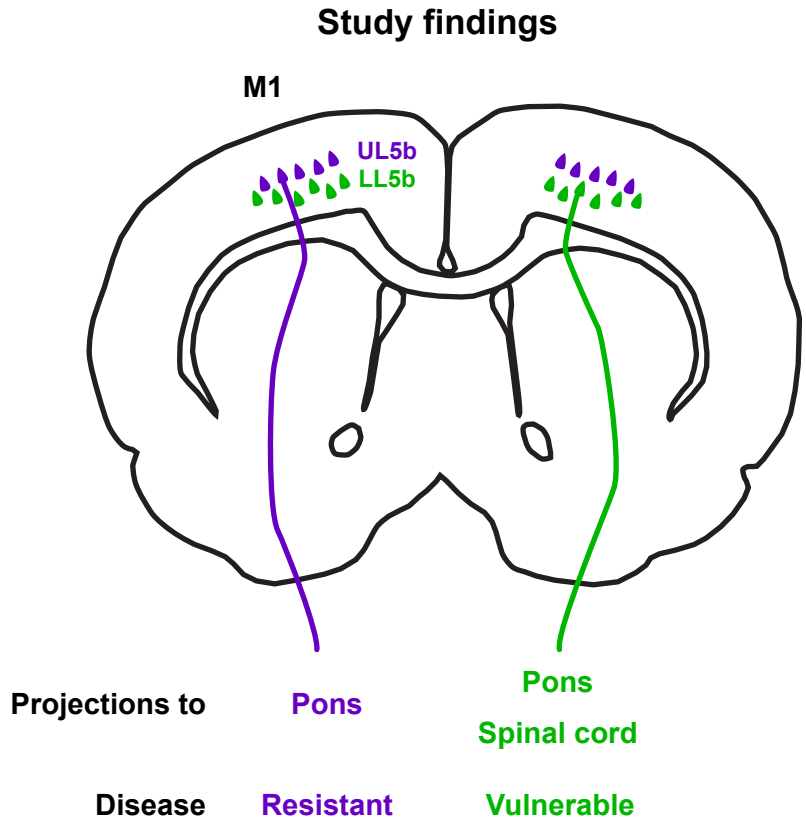

Figure 1.4: The general findings of this study. A summary of the relevant properties of L5b cells characterized in this study. Upper L5b (UL5b) Colgalt2 cells (purple) project to the pons, but not the spinal cord, and are not vulnerable in an ALS mouse model. Lower L5b (LL5b) Gprin3 cells (green) project to both the pons and spinal cord and are lost in an ALS mouse model.

perform Translating Ribosome Affinity Purification (TRAP) to molecularly profile the cells by their gene expression patterns. We determine that while these cells are very similar, they show several molecular differences that may have consequences on their neuronal function. To determine the specific vulnerability of LL5b Gprin3 cells but not UL5b Colgalt2 in ALS by crossing our lines to the SOD1-G93A ALS mouse model, we then performed TRAP in these two cell types across healthy and ALS conditions to understand what cell-type specific responses take place in a vulnerable and resistant population of neurons during disease progression. We show that these cells diverge in their molecular responses to SOD1-G93A expression across disease stages, showing a particularly contrasting response in mitochondrial gene expression modulation. We then show that these cells show changes in mitochondrial structure during disease that will need to be explored further in future studies. And lastly, we endeavor to determine whether LL5b Gprin3 cells are representative of the neurons that are thought to be ALS-vulnerable in the human motor cortex, with an eye towards to identifying markers that effectively visualize potentially disease-relevant populations.

As a whole, this study represents an assessment of the underlying anatomical and intrinsic molecular differences between M1 L5b cell types, their differential vulnerability and responses in ALS, and the translatability of their molecular identity to human motor cortex. The data collected as part of this work should serve to inform future studies of L5b anatomy and molecular biology across healthy and disease contexts, as well as across species.

CHAPTER 2:

Anatomical and molecular characterization of Colgalt2 and Gprin3 bacTRAP cell populations

The mammalian neocortex is responsible for the processing of associated inputs from diverse brain regions into relevant functional outputs. But while each cortical region receives different types of information, i.e. auditory vs. visual, the cortex classically employs the same laminar organization of neurons to process these diverse inputs. Each of five anatomically distinct layers (L2/3, L4, L5a, L5b, L6a) contains excitatory pyramidal neurons that participate in the tiered processing of afferent information (Brody, 1955; Jones and Wise, 1977; Krieg, 1946; Weiler et al., 2008). The output of this computation is ultimately transmitted out of the cortex by neurons found in its deep layers, with large L5b pyramidal neurons being important drivers of functional downstream signaling. The laminar distribution of L5b pyramidal neurons across the cortex is remarkably uniform in rodents (Krieg, 1946). In mice, it is consistently found at ~50% depth from the pial surface of the cortex, with a thickness of about 150μm (Franklin and Paxinos, 2008; Lein et al., 2007). In primary motor cortex (M1), the thickness of L5b doubles, however (Caviness, 1975; Cederquist et al., 2013). Because the proper functioning of motor cortex in motor learning (Kawai et al., 2015) and execution (Anderson et al., 2010; Chen et al., 2017; Guo et al., 2015) is highly dependent on its outputs to other brain regions, it was theorized that this thickening creates space to accommodate all of the increased number and types of subcortical

projection neurons required to carry out these motor behaviors (see Yu et al., 2008). Very recently, using a combination of viral tracing and single cell RNA-Seq, it was shown that, indeed, L5b of M1 and anterolateral motor (ALM) cortices may contain diverse pyramidal neuron types, and that together, these cells function in different stages of preparation and execution of motor output (Economo et al., 2018; Tasic et al., 2018). These cells also appear to diverge in projection pattern, with some cells showing collateral projections to proximal regions of the mid- and hindbrain, including the thalamus, the pons, and the superior colliculus, and others projecting to the superior colliculus, the pons, and distal brainstem regions (Figure 1.3; Chen et al., 2017; Economo et al., 2018). Alongside their differences in circuit participation, there is still very little known about the distinct molecular profiles of the cell types in L5b, and how their unique differences may contribute to the distinct functional properties observed for each.

Targeting L5b pyramidal neuron types for further study requires the ability to reliably visualize the cells separately across experimental paradigms. Previously generated transgenic mouse lines that target L5b, such as the commonly used Thy1-EYFP line (Bareyre et al., 2005; Feng et al., 2000; Yu et al., 2008) and Uchl1-EGFP line (Yasvoina et al., 2013), show expression of reporters and constructs across all pyramidal neurons of L5b rather than individual subtypes, and would therefore not be suitable for studies into the properties that uniquely define each subpopulation. In order to target these cells for anatomical and molecular characterization, we set out to generate BAC Transgenic mouse lines (Gong et al., 2010) that express the EGFP-

tagged ribosomal subunit L10a necessary for performing Translating Ribosome Affiinity Purification (TRAP; Doyle et al., 2008; Heiman et al., 2008) in specific subsets of L5b neurons. TRAP is a powerful gene expression profiling technique that allows for the isolation of actively translated mRNAs from specific cell types in tissues. By immunoprecipitating EGFP-tagged ribosomes that are expressed in these populations by cell type-specific promoters, one can interrogate the gene expression patterns of neuronal populations of interest. Expression of the GFP-tagged subunit in L5b cells additionally provides reliable and reproducible visualization (across generations and individuals) of each population, allowing us to carefully characterize the anatomical properties of these cell types, such as cortical localization and subcortical projection patterns. We therefore employed L5b TRAP lines to characterize the unique anatomical and molecular properties of the two subopulations of L5b projection neurons.

2.1 Anatomical distribution of EGFP-labeled cells in the Colgalt2-TRAP DU9 mouse line

In order to gain molecular and anatomical access to L5b pyramidal neurons, we set out to express the TRAP EGFP-L10a construct in L5b cells in M1 by creating a set of diverse BAC transgenic animals. The GENSAT project (Gong et al., 2003; gensat.org) produced many cell-type specific gene expression anatomical maps of the mouse brain. From these atlases, a number of genes were selected for their specific laminar expression patterns in L5 of the cortex. BACs were created to express the EGFP-L10a construct under the control of these cell-type specific gene promoters.

From the mice that resulted from this BAC transgenic approach (Figure 2.1), two of the mouse lines generated, Colgalt2-TRAP DU9 and Gprin3-TRAP ES152, showed strong expression of the TRAP construct across many cells in apparent upper and lower L5b, with expression driven by the Colgalt2 and Gprin3 BAC promoters, respectively.

Colgalt2-TRAP is expressed almost exclusively in the cortex, with very few cells observed in subcortical areas (Figure 2.2). Between +2.00-1.50 mm anterior to bregma (Figure 2.2A), Colgalt2 cells are observed at approximately half the thickness of the cortex, at a depth visually consistent with L5b across all cortical areas. In prelimbic and agranular insular cortex, some L6a cells show low levels of expression of the construct. In the dorsal transition zone, a small cluster of Colgalt2+ cells can also be seen. From +1.00-0.00 mm anterior to bregma (Figure 2.2B), cells spanned all cortical areas and appeared to be restricted entirely to L5b, with some cells again detected in L6a of insular cortex. Near bregma, the distribution of Colgalt2+ cells becomes even more restricted to L5b, but labeled cells are still observed across the entire extent of cortex. At -1.00 mm from bregma (Figure 2.2C), L5b expression of Colgalt2 is maintained, but a small number of cells are additionally observed in the medial CA2 region of hippocampus and the ventral piriform cortex/cortical-amygdalar transition region. Between -2.00-3.00 mm from bregma (Figure 2.2D), fewer cells are observed in L5b of retrosplenial cortex, with L5b in other cortical areas still showing many labeled cells. A small cluster of labeled cells was also observed in the medial hippocampus, beginning at the fasciola cinereum and spreading laterally into medial CA1 in more caudal sections. More caudally in this range, a more superficial population of labeled cells is

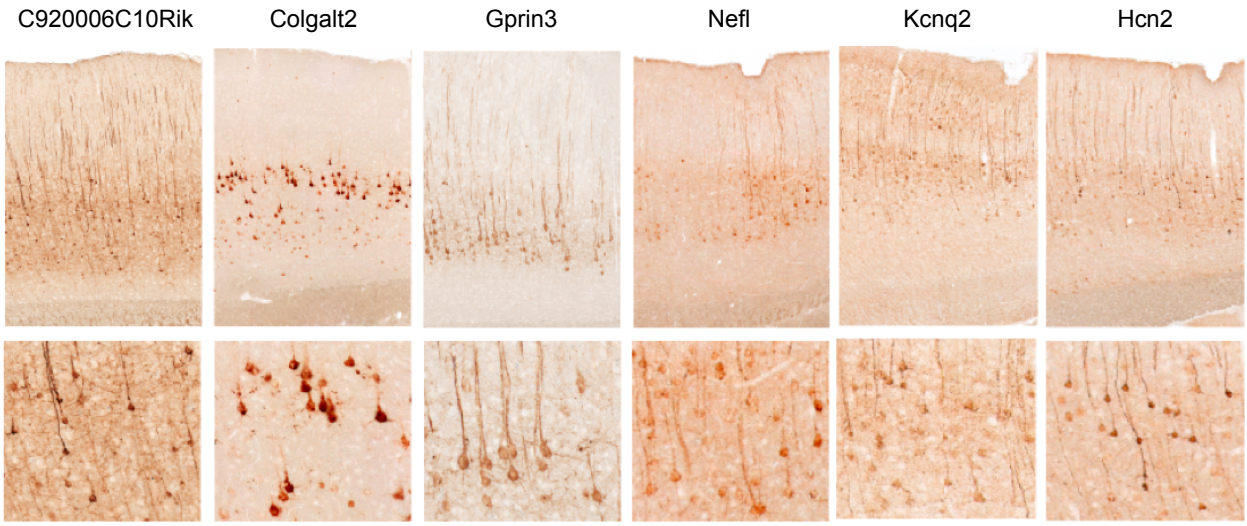

Figure 2.1: Expression of EGFP-L10a in mouse L5b using BAC Transgenics. Representative brightfield images of GFP immunostaining in mouse lines generated to express the TRAP EGFP-L10a construct specifically in L5b. Gross laminar distribution (top row) shows specific expression in L5b of M1, with more detailed distributions shown below (bottom row). Among the promoters used to drive expression of the TRAP construct, Colgalt2 and Gprin3 showed expression in the greatest numbers of cells in L5b, and thus were chosen for further assessment.

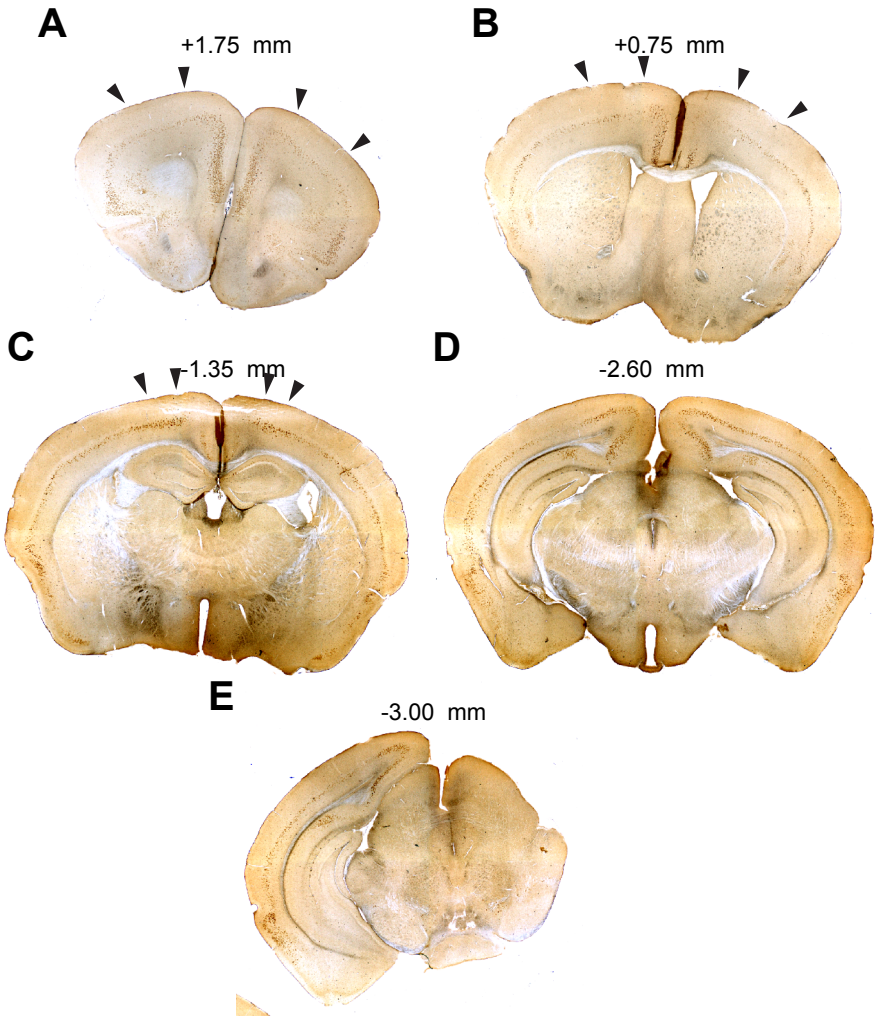

Figure 2.2: Expression of EGFP-L10a in Colgalt2-TRAP DU9 mice is observed in L5b across the entire cortex. EGFP-L10a expression visualized by GFP immunostaining and DAB deposition in brightfield-imaged coronal sections of a Colgalt2-TRAP DU9 mouse. Sections are representative of ranges of anterior-posterior locations. (A-C) The M1-containing extent of cortex shows labeled Colgalt2 cells across the whole extent of cortex. Black arrows indicate the boundaries of M1 in the medial-lateral axis. (D-E) In posterior regions of the brain, Colgalt2 is still observed across most cortical areas. Section thickness is 40μm. Listed coordinates are approximate to Paxinos atlas coordinates.

also visible in perirhinal cortex. At -3.30 mm from bregma (Figure 2.2E), the perirhinal population of Colgalt2 cells becomes more prominent, while L5b labeling in other cortical areas is maintained. A very sparse population of labeled cells is observed dorsal to the substantia nigra reticularis, possibly occupying a ventral area of the mesensephalic reticular formation. Overall, the Colgalt2-TRAP DU9 line spans L5b of almost all cortical areas, and would serve as an excellent line for visualizing this output layer across many different contexts.

2.2 Anatomical distribution of EGFP-labeled cells in the Gprin3-TRAP ES152 mouse line

Broadly, Gprin3-TRAP is expressed in many subcortical regions across the brain, as well as in L5b of certain anterior regions of the cortex (Figure 2.3). At +2.25 mm from bregma, Gprin3 cells are only observed in a wide band of pyramidal neurons at a depth consistent with L5b across secondary and primary motor cortex regions. At +2.00 mm from bregma (Figure 2.3A), Gprin3 cells in the cortex can be seen in a wide band beginning medially in secondary motor cortex and extending laterally to insular cortex. Ventrally, a cluster of cells can be seen in the shell of the nucleus accumbens, as well as a more ventral structure surrounding the ventral pallidum. At +1.00 mm from bregma, cortical Gprin3 cells can be seen in L5b, again beginning medially in secondary motor cortex, and extending laterally through secondary somatosensory cortex. Through M1, the labeled pyramidal neurons appear to “dip” to a lower sublayer of L5b, however, suggesting Gprin3 cells may have a LL5b identity in this area. Subcortically, Gprin3+

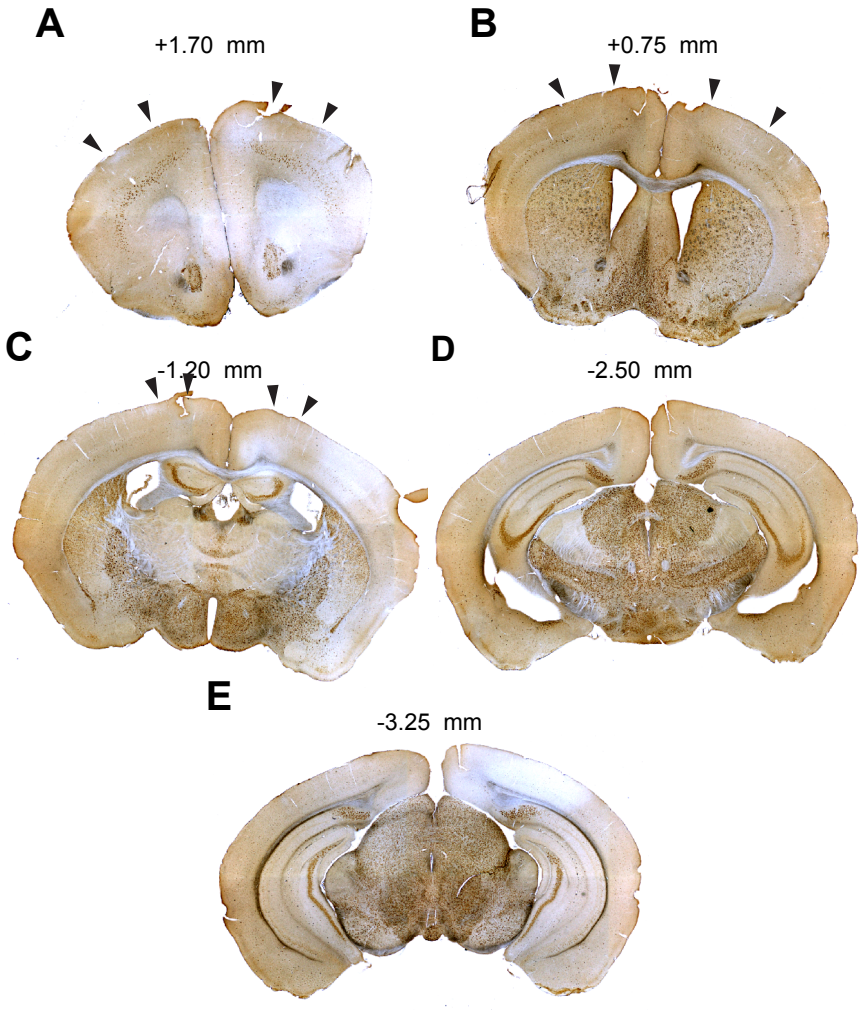

Figure 2.3: Expression of EGFP-L10a in Gprin3-TRAP ES152 is localized to anterior areas of cortex, and found in many subcortical areas of the brain. EGFP-L10a expression visualized by GFP immunostaining and DAB deposition in brightfield-imaged coronal sections of a Gprin3-TRAP ES152 mouse. Sections are representative of ranges of anterior-posterior locations. (A) In an anterior area of cortex, cortical Gprin3 cells are observed along much of the medial-lateral extent. A small number of cells is observed subcortically. Black arrows indicate the medial-lateral extent of M1. (B) Closer to Bregma, in the lateral-to-medial transition between somatosensory cortex and the lateral boundary of M1, GFP labeled cells appear to dip deeper into the cortex and remain there through to the medial boundary of M1. GFP+ cells are also seen in the striatum and other subcortical areas in this range. (C) As M1 begins to disappear in this more posterior area, GFP+ cells in the cortex become sparser. Subcortical GFP cells are found in many diverse regions here. (D-E) In posterior regions of the brain, GFP labeling is heavily concentrated to subcortical areas, and the CA3 region of hippocampus. Section thickness is 40 μm. Listed coordinates are approximate to Paxinos atlas coordinates.

cells can be seen in the striatum in a sparsely scattered pattern. Several subpopulations of labeled cells can be found in the accumbens shell, with a small number also located in the accumbens core region. A dense population of Gprin3+ cells is visible in a very ventral area of this brain region, possibly occupying the olfactory tubercle. Cells can also be seen in the lateral and medial septal nuclei and in what appears to be the island of Calleja between the accumbens shell and the spetal nuclei. At +0.50 mm from bregma (Figure 2.3B), the same distribution of labeled L5b neurons is observed in the cortex between secondary motor and secondary somatosensory cortex, with the “dip” in primary motor cortex still clearly visible. The sparse but highly expressing striatal neurons are also observed. The number of cells found in the accumbens shell is greatly reduced, with a large number of highly-expressing cells visible in the medial septal nucleus and in various ventral nuclei around the olfactory tubercle. Around bregma, the distribution of labeled cells in L5b of the cortex becomes much sparser, with fewer cells generally visible from secondary motor cortex to secondary somatosensory cortex. Many cells are still observed in the striatum, with a large number of highly-expressing cells found ventral to the anterior commissure in the various ventral nuclei found in this region. A small cluster of cells can also be seen in the anteromedial bed nucleus of the stria terminalis. An additional sparse cluster of neurons can be observed in the septofimbrial nucleus. At -0.50 mm from bregma, the number of cortical L5b cells has noticeably decreased, with some cells still remaining in the lateral regions of cortex, including the insular cortex. Subcortically, a large number of highly-expressing cells can be found in the globus pallidus and the thin band that comprises the bed nucleus of the

stria terminalis at the coordinate. A cluster of low-expressing cells can also be seen in the central medial thalamic nucleus. The ventral regions of the midbrain here, including the hypothalamus and the anterior amygdalar area, contain many labeled cells showing varying levels of expression. From -1.00-1.50 mm from bregma (Figure 2.3C), almost all labeled cortical neurons have disappeared. Gprin3+ cells are primarily localized to subcortical areas, including the dorsal striatum, the globus pallidus, the lateral habenula, the central medial, rhomboid, and reuinens nuclei of the thalamus, the zona incerta, and almost all nuclei of the hypothalamus and the medial forebrain bundle. A number of labeled cells can also be seen in the CA3 region of the hippocampus. At -2.00 mm from bregma, fewer cells are observed in the ventromedial regions of the hypothalamus, with some still remaining in the peduncular region of the lateral hypothalamus. The zona incerta still contains a dense population of labeled cells, as well as the lateral habenula, the pregeniculate nucleus, and many dorsomedial nuclei of the thalamus. Gprin3+ neurons can still be seen in the CA3 region of hippocampus, with an additional cluster of cells observed in the polymorph area of the dentate gyrus. At -2.75 mm from bregma (Figure 2.3D), Gprin3+ cells occupy almost the entire midbrain, with the exception of a lateral horn of the thalamus composed of the lateral posterior thalamic nuclei and the dorsolateral geniculate nucleus through to the retroethmoid nucleus. In the hippocampus, the CA3, polymorph dentate gyrus and the dorsal subiculum regions also contain labeled cells. The midbrain is densely populated with labeled cells through to -3.00 mm from bregma (Figure 2.3E), where the only region containing no Gprin3+ cells is the medial geniculate nucleus. At this coordinate, a

sparse population of cells in the substantia nigra reticularis and the interpeduncular nucleus can also be seen. More posterior, the superior colliculus also shows many labeled cells, along with the periaqueductal gray. The Gprin3-TRAP ES152 line is therefore useful for the study of L5b cells anterior to bregma, in anterolateral motor regions, primary motor cortex, and the accessory motor/somatosensory regions. A very large and diverse population of labeled cells is also found subcortically and in the CA3 region of hippocampus, making the Gprin3 line potentially useful in the molecular and anatomical characterization of these regions.

2.3 Colgalt2 and Gprin3 neurons represent two distinct populations of layer 5b pyramidal neurons in primary motor cortex of mouse.

Because both Colgalt2 and Gprin3 cells occupy L5b of M1, we wanted to perform a closer examination of the precise laminar distribution of the cells. We immunostained for GFP in Colglat2-TRAP and Gprin3-TRAP mice and imaged the M1 sections by confocal microscopy (Figure 2.4A-B). We then measured the depth of GFP+ cells using a custom program that measures the Euclidean distance between the pial surface and the dorsal surface of white matter. These analyses revealed that in the Colgalt2-TRAP mouse, GFP+ neurons are found at approximately 50% depth from the pial surface to the dorsal edge of the white matter of the corpus callosum (CC). This depth is consistent with a superficial sublayer of L5b (Economo et al., 2018), or upper L5b (UL5b, Figure 2.4C). The Colgalt2 cells are found between 50-60% depth in other areas of the cortex as well, suggesting they maintain this identity across all cortical regions. In

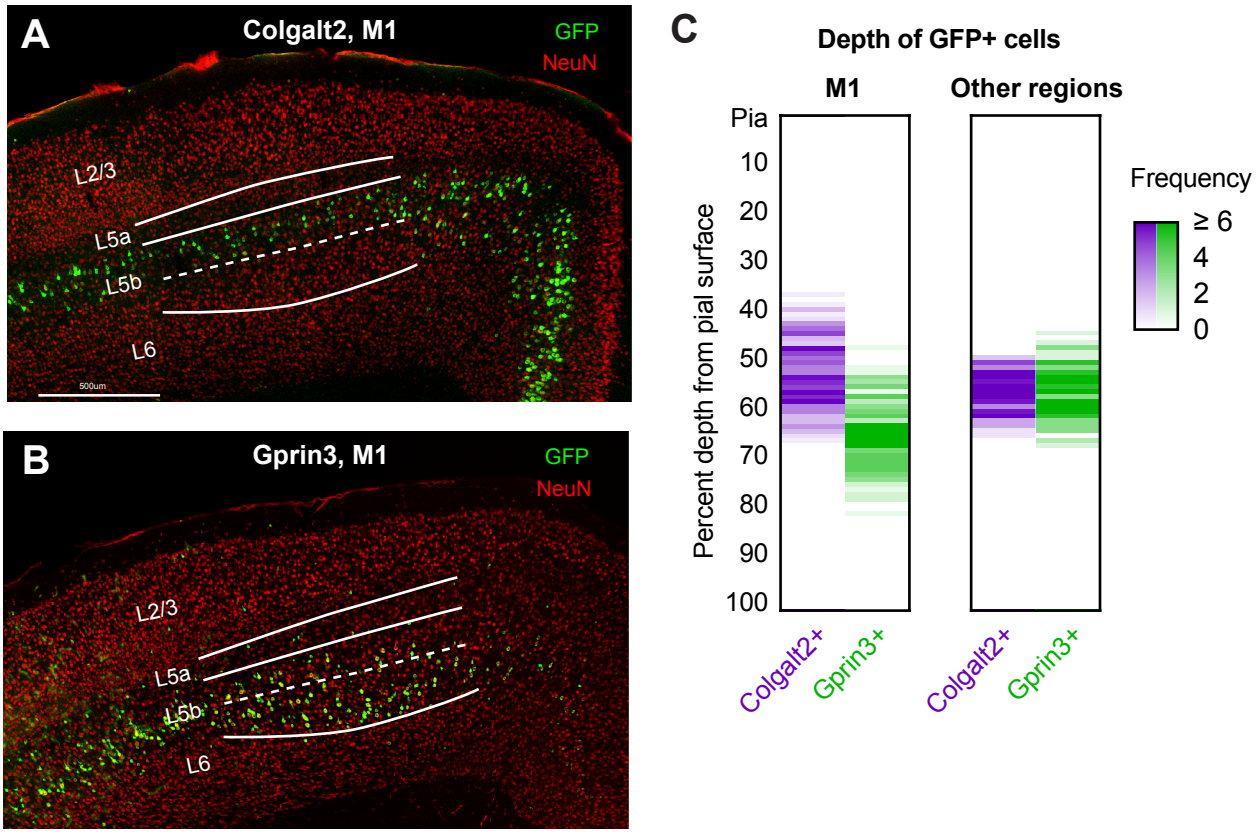

Figure 2.4: Colgalt2 and Gprin3 cells show distinct sublayer distribution within L5b of M1. (A-B) Representative images of M1 in (A) Colgalt2-TRAP and (B) Gprin3-TRAP mouse. Immunostaining for GFP (green) shows location of TRAP cells amongst all NeuN+ neurons of the cortex (red). Colgalt2 cells appear to occupy an upper sublayer of L5b (UL5b) relative to Gprin3 cells, which instead dip into a lower sublayer of L5b (LL5b) in this area. Cortical layers were delineated based on approximate depth and size of cell bodies composing each layer (scale bar = 500 μm). (C) Heatmaps indicating the frequency at which GFP labeled cells from Colgalt2 and Gprin3 M1 were found at each depth of the cortex, represented as percent depth from pial surface of the cortex. In M1, Colgalt2 cells (purple; n = 209) are found more superficially than Gprin3 cells (green; n = 163). In other cortical areas, both cell types are found at the same depth. Frequencies ≥ 6 cells are shown in the same shade of color to more readily highlight depths that contain the most labeled cells.

M1 of Gprin3 animals, GFP+ neurons were instead observed at a depth of 60-75% from the pial surface, suggesting they occupy the lower sublayer of L5b (LL5b). In other cortical areas, Gprin3 cells appeared to reside primarily at 50-60% depth, similar to Colgalt2 cell depth, suggesting that these two cell types anatomically converge in other regions of the cortex, and that the sublayer divergence is unique to M1. Together these data indicate that the Colgalt2 and Gprin3 mice represent the first transgenic lines that target expression to the two distinct sublayers of M1 L5b, allowing for the consistent and reliable visualization of these neuron populations without the use of tracers or viruses.

2.4 Colgalt2 and Gprin3 neurons share long-range projection neuron identity, but project to distinct targets.

Because L5b has been well established as an output layer of the cortex, containing large pyramidal neurons that display long-range projections targeting different areas throughout the brain, we wanted to confirm that our Colgalt2 and Gprin3 cells are indeed long-range projection neurons. We first immunostained for Ctip2, a known marker of subcortical-projection neurons, in our Colgalt2 and Gprin3 brains in order to assess co-localization with the GFP from our cells (Figure 2.5A). In Colgalt2 brains, 79% of sampled GFP+ cells were Ctip2+, and in Gprin3 mice, 94% of GFP+ cells were Ctip2+ (Figure 2.5B). Colgalt2 and Gprin3 cells additionally showed larger soma size than other pyramidal neurons in the cortex, with median Colgalt2 soma size being 233 μm2 and median Gprin3 soma size being 238 μm2, compared to 180 μm2 for a pooled population of different cortical pyramidal neurons (Figure 2.5C). Together,

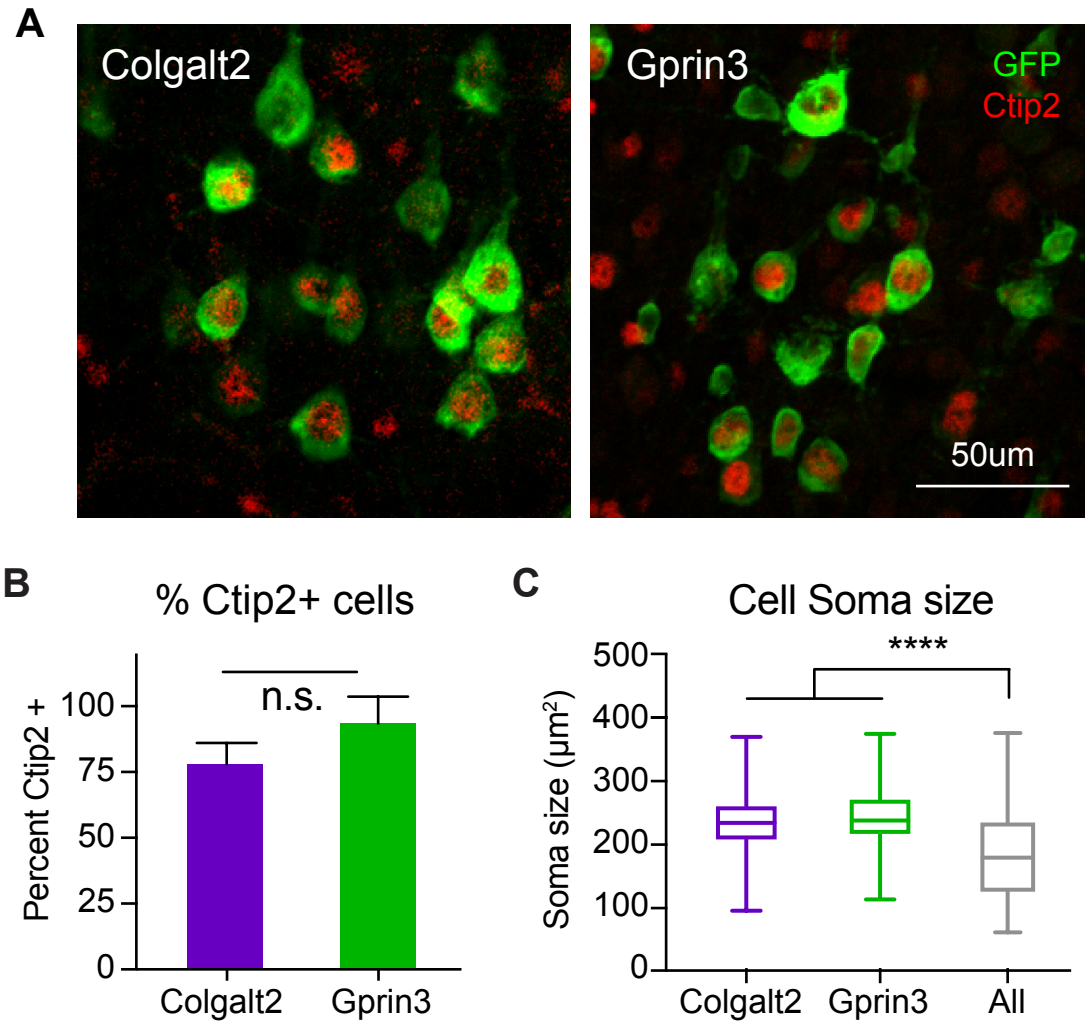

Figure 2.5: Colgalt2 and Gprin3 cells are both positive for Ctip2, a marker for subcortical projection neurons of the cortex. (A) Representative confocal images of GFP+ (green) Colgalt2 and Gprin3 cells with staining for the subcortical projection neuron marker Ctip2 (red, scale bar = 50 μm). (B) Quantification of co-localization of Ctip2 with Colgalt2 GFP (purple; n = 191 cells) and Gprin3 GFP (green; n = 135 cells) reported as percent of GFP+ cells that show Ctip2 labeling. Bars show mean±SEM (n.s. = not significant by two-tailed t-test). (C) Quantification of soma size (μm2) for GFP+ Colgalt2 cells (purple; n = 292 cells), Gprin3 cells (green; n = 285 cells), and other neurons across layers of cortex (grey; n = 1253 cells). Colgalt2 and Gprin3 cells show larger soma sizes relative to other neurons in the cortex. Box and whisker plots show median and quartile boundaries (****$p < 0.0001$ by one-way ANOVA).

these data suggest that both UL5b Colgalt2 and LL5b Gprin3 neurons share the long-range projection identity that is classically observed in L5b.

We then set out to identify the targets of the presumptive long-range axonal projections of Colgalt2 and Gprin3 cells. Across different cortical areas and species, L5b cells have been shown to project to the thalamus, superior colliculus, pons, brainstem, and spinal cord (Hattox and Nelson, 2007; Jones et al., 1977; Moya et al., 2014; Oswald et al., 2013; Wise and Jones, 1977b; Wise et al., 1979). Because UL5b and LL5b cells were recently shown to share a projection to the pons, but diverge in projections to more caudal regions (Economo et al., 2018), we chose to first assess whether our Colgalt2 and Gprin3 cells project to the pons or the cervical spinal cord. We therefore injected the retrograde tracer cholera toxin beta (CTB) into the pons and C6 cervical spinal cord (Figure 2.6A-B, left panels) in adult Colgalt2 and Gprin3 mice and visualized the retrogradely labeled cells in M1 by confocal microscopy following immunostaining for GFP and CTB (Figure 2.7A-B, left panels). The distribution of pons-CTB+ neurons varied by injection site, but cells were often observed across L5b of many different cortical areas. Neurons that were pons-CTB+ were found in both upper and lower L5b of M1, at similar depths to both Colgalt2 and Gprin3 cells, extending from 45-75% depth from the pial surface, with bimodal peaks at ~50% and ~70% depth, matching the peak depths of Colgalt2 and Gprin3 cells respectively (Figure 2.8A). When we quantified co-localization of GFP in CTB+ cells, we found that 38% of pons-CTB+ cells across both sublayers were positive for Colgalt2. When co-localization is measured only within the dorsal half of L5b that comprises UL5b, 64% of pons-CTB+ cells were positive for

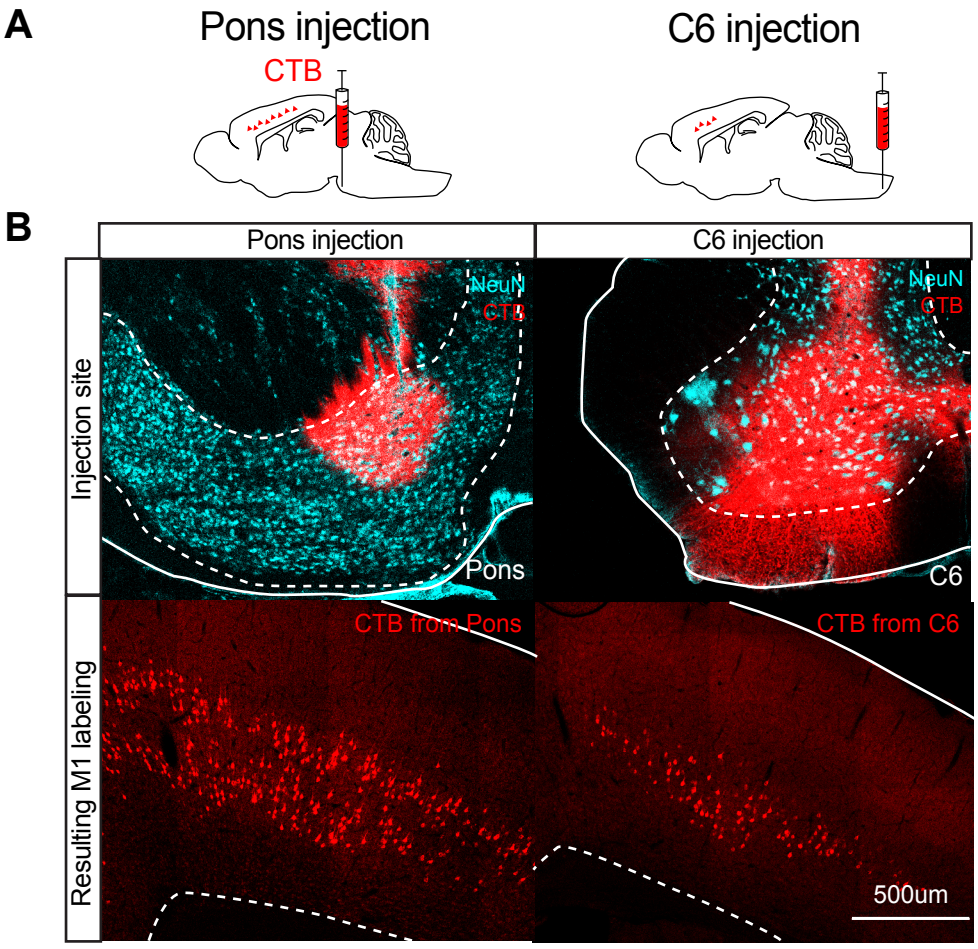

Figure 2.6: Retrograde tracing from pons and cervical spinal cord labels L5b neurons in M1. (A) Schematic representations of CTB (red) injection targets in the pons and cervical spinal cord with expected corresponding retrograde labeling in the cortex. (B, top row) Representative confocal images of CTB at the site of injection in pons (left) and C6 of the cervical spinal cord (right). Cytoarchitecture is shown with NeuN labeling (cyan). Corresponding retrograde labeling in M1 is shown with CTB staining (red). Pons injections retrogradely labeled cells across both sublayers of L5b (bottom row, left), while C6 injections only appeared to label LL5b cells (bottom row, right). Pial surface outlined with solid white line, target grey matter/white matter boundary outlined with dashed white line (scale bar = 500 μm).

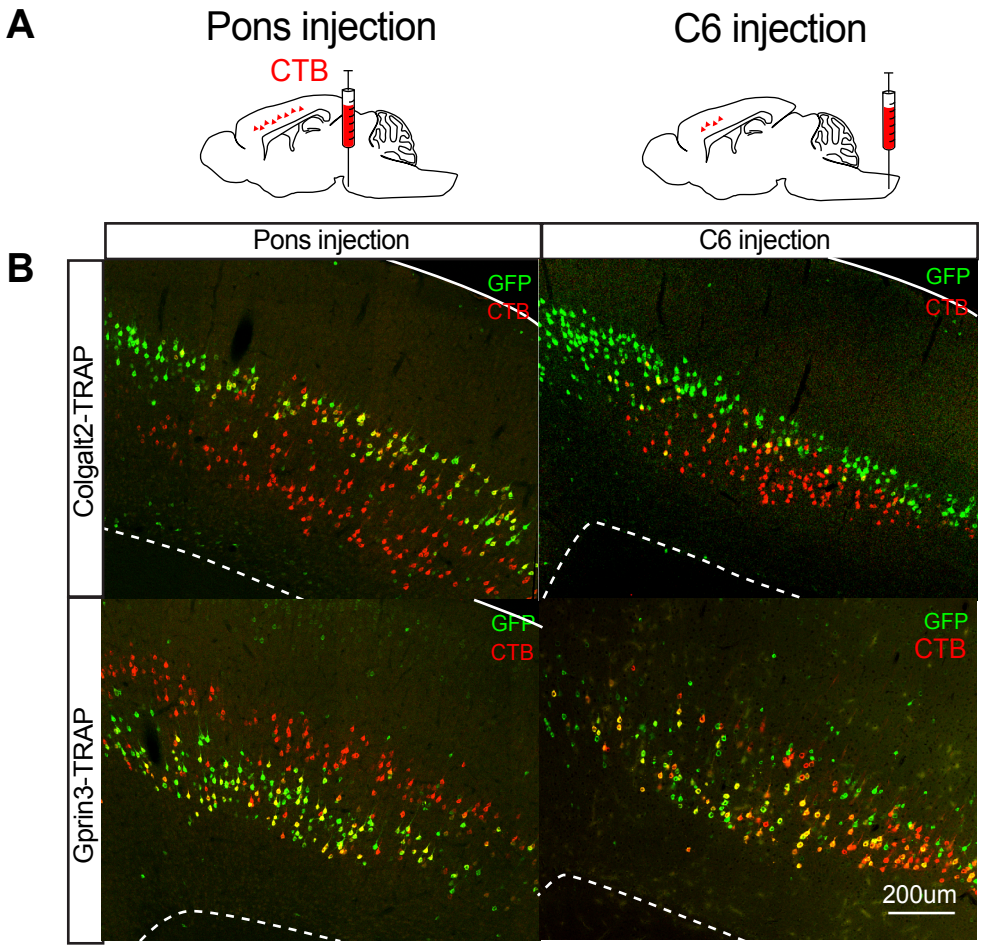

Figure 2.7: Retrograde tracing from pons and cervical spinal cord labels Colgalt2 and Gprin3 cells. (A) Schematic representations of CTB (red) injection targets in the pons and cervical spinal cord with expected corresponding retrograde labeling in the cortex. (B) Immunostaining for GFP (green) revealed CTB (red) overlap with Colgalt2 (top row) and Gprin3 (bottom row) cells. Pontine CTB cells appeared to overlap with both Colgalt2 and Gprin3 cells across both sublayers of L5b. Spinal CTB cells only appear to spatially overlap with Gprin3 cells in LL5b. Pial surface outlined with solid white line, corpus callosum outlined with dashed white line (scale bar = 200 μm).

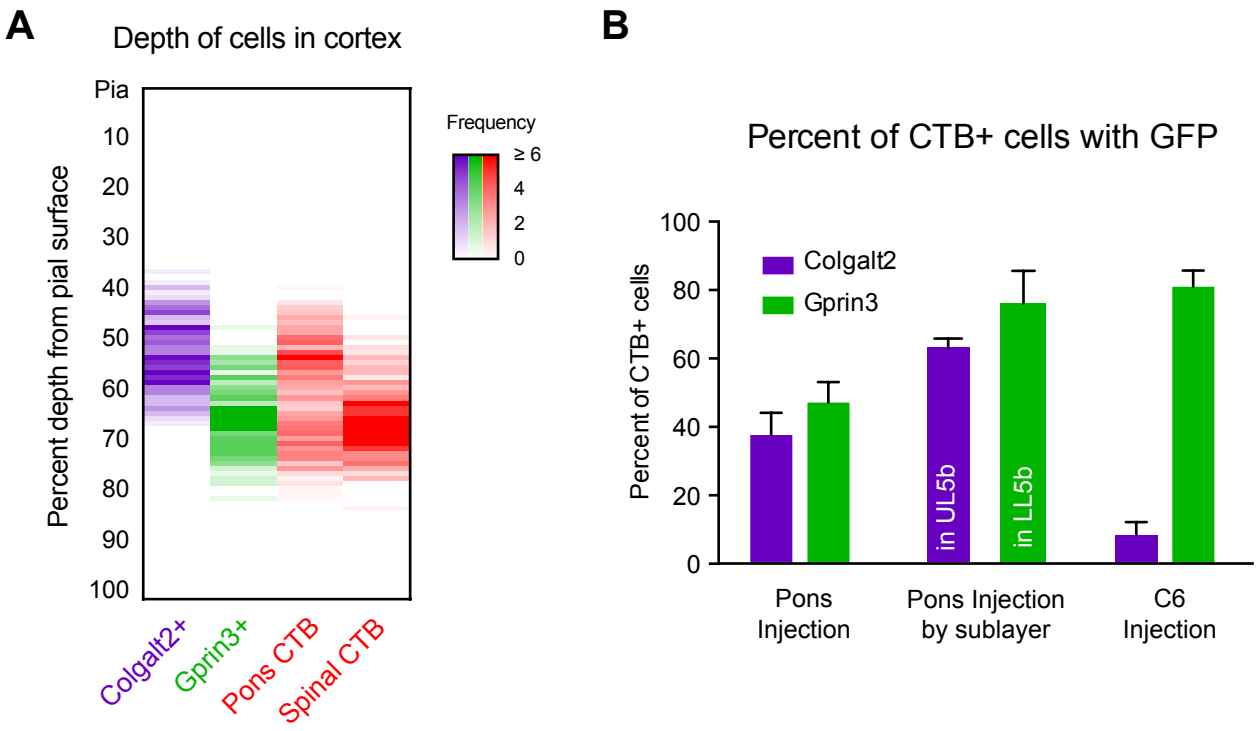

Figure 2.8 : Colgalt2 cells project to the pons, while Gprin3 cells project to both the pons and the cervical spinal cord. (A) Heatmaps showing frequency of depth localization of retrogradely labeled CTB+ cells (red), compared to depths of Colgalt2 (purple; n = 209 cells) and Gprin3 (green; n = 163 cells) cells in M1 following CTB injections into the pons and C6 of cervical spinal cord. Pontine CTB cells (n = 651 cells) distributed bimodally across both sublayers of cortex, overlapping in depth with Colgalt2 and Gprin3 cells. Spinal CTB cells (n = 192 cells) were located deeper in M1, overlapping with the Gprin3 population. Frequencies ≥ 6 cells are shown in the same shade of color to more readily highlight depths that contain the most labeled cells. (B) Quantification for co-localization of CTB with GFP from Colgalt2 (purple) and Gprin3 (green) cells following CTB injection into pons or cervical spinal cord, reported as percent of total CTB+ cell observed for each injection. 38% of pontine CTB in all of L5b cells co-localize with Colgalt2 (n = 318 cells), with 48% co-localizing with Gprin3 (n = 613 cells). More specifically, 64% of pontine CTB in UL5b co-localized with Colgalt2 cells, and 77% of pontine CTB cells in LL5b co-localized with Gprin3 GFP. Only 9% of spinal CTB co-localized with Colgalt2 (n = 190 cells), while 82% co-localized with Gprin3 cells (n = 127 cells; bars represent mean ± SEM).

Colgalt2 GFP (Figure 2.8B). In Gprin3 brains, 48% of pons-CTB+ cells across both sublayers were Gprin3 GFP positive. When only the ventral half of L5b, or LL5b, is assessed for co-localization, we found that 77% of pons-CTB+ cells co-localize with Gprin3 GFP. Additionally, ~20% of pons-CTB+ cells in UL5b co-localize with Gprin3 GFP, due to the small proportion of Gprin3 cells that occupy this sublayer. Together, these data indicate that Colgalt2 and Gprin3 neurons account for a very large majority (~85%) of pons-projecting cells of M1 L5b.

To assess spinal cord-projection identity for Colgalt2 and Gprin3 cells, we injected CTB into cervical spinal cord at the level of C6 (Figure 2.6A-B, right panels) and visualized retrogradely labeled cells in M1 by confocal microscopy (Figure 2.7A-B, right panels). C6-CTB+ cell distributions varied by injection site, but were primarily observed in M1 between 1.00 mm and -0.40 mm from Bregma. C6-CTB+ cells were primarily located at ~70% depth from pia, in what appeared to be LL5b, and at a similar depth to Gprin3 (Figure 2.8A). In Gprin3, 82% of C6-CTB+ cells were positive for Gprin3 GFP, while in Colgalt2 brains, GFP co-localization was only observed for 9% of C6-CTB+ cells (Figure 2.8B). This suggests that in addition to a projection to the pons, the majority of Gprin3 neurons have a collateral projection to the cervical spinal cord. Colgalt2 cells, in contrast, project to the pons, but not to the spinal cord. These findings confirm that UL5b and LL5b cells have divergent collateral projection patterns, and further establish the Colgalt2 and Gprin3 mouse lines as useful for the reliable visualization of divergent long-range projection L5b neuron types.

2.5 Gprin3 cells project to spinal motor neurons through an intermediate population of neurons in the central spinal cord.

Projections to the spinal cord from the cortex terminate in different functionally organized regions of the spinal grey matter (see Watson et al., 2008). We therefore wanted to determine the anatomical localization of axon terminals originating from the LL5b cells that are represented by our Gprin3 cells. To accomplish this, we injected an rAAV2 carrying a Cre-dependent EYFP construct into M1 of Gng7-Cre KH67 mice, which express Cre in all L5b cells of the cortex (Figure 2.9A). We collected the cervical spinal cord of these mice for sectioning, and visualized the EYFP-labeled terminals of the L5b cells by immunostaining and confocal microscopy. We observed labeled terminals in an intermediate region of the spinal grey matter, concentrated in lamina 5, 6, and 7 (Figure 2.9B). Only 1.64% of the ventral horn area occupied by ChAT+ alpha motor neurons showed EYFP signal (Figure 2.9C-D), suggesting that LL5b cells do not directly project onto these motor output cells. This intermediate corticospinal projection pattern that we observe additionally confirms previously reported anatomical results (Bourane et al., 2015; Hantman and Jessell, 2010; Ueno et al., 2018), where cortical L5b cells were shown to project to interneuron populations within this central region of the spinal cord.

The cervical spinal cord contains neurons that function in the control of muscles of the neck, shoulders, and forelimbs (see Bachmann et al., 2014). But given that the axons of LL5b cells do not terminate directly on alpha motor neurons, we wanted to determine whether their projection still participates in spinomuscular circuitry indirectly.

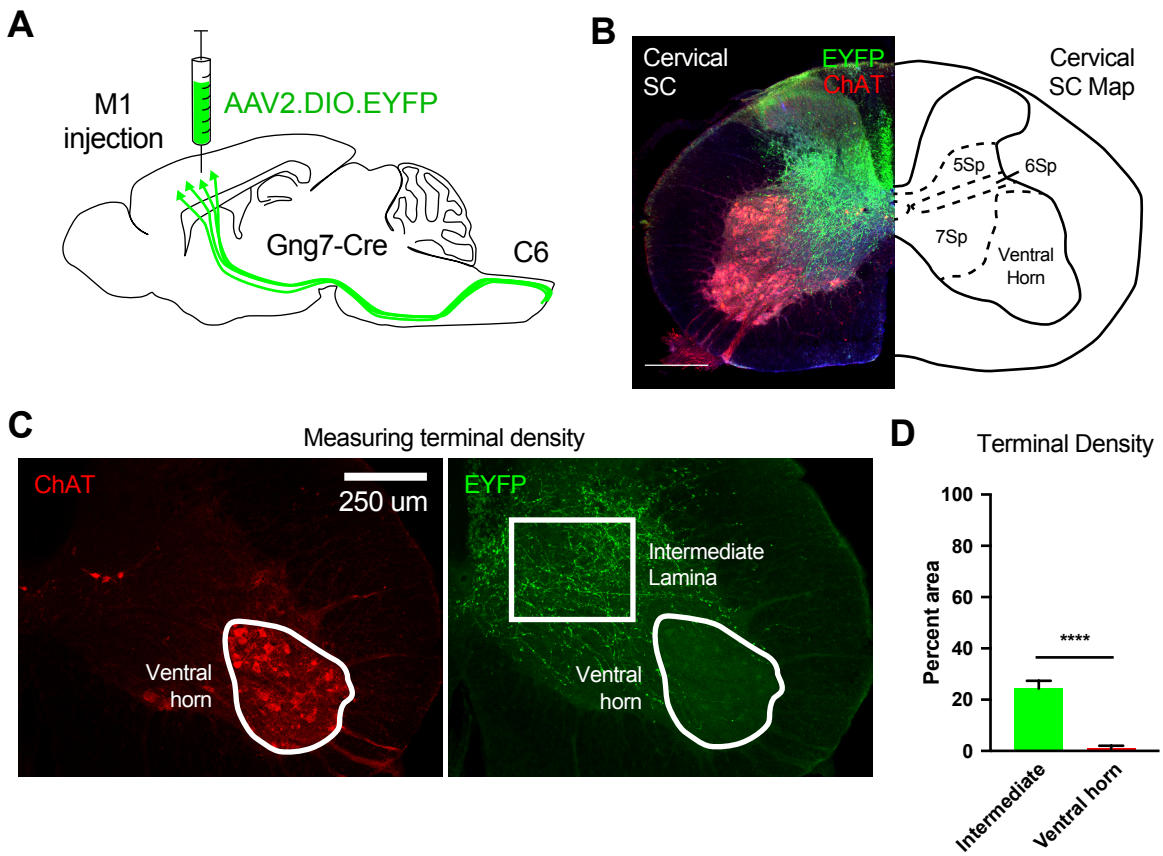

Figure 2.9: Anterograde labeling of LL5b cells in M1 reveals projections to intermediate regions of spinal grey matter. (A) Schematic illustration of Cre-dependent viral construct targeting to cortex in Gng7-Cre animal, with expected labeling of EYFP-expressing cells and their primary axons. (B) Representative confocal image of labeling observed in cervical spinal cord following Cre-dependent EYFP injection into M1. Corresponding map of spinal grey anatomy shown on the right. EYFP axons (green) show axon terminals of LL5b cells expressing the viral construct at the M1 injection site. ChAT+ cells (red) show the location of spinomuscular alpha motor neurons in the ventral horn. EYFP+ terminals are primarily apparent in the intermediate lamina 5, 6, and 7, and are not visible in the ventral horn (scale bar = 300 μm). (C) Representation of strategy for measuring density of labeled terminals in different anatomical areas of the spinal grey matter. White outlines show examples of region-of-interest boundaries used for measurement. Location of ChAT signal (red) was used to determine boundaries of ventral horn areas, while intermediate laminar areas were selected at random from regions showing EYFP signal (green; scale bar = 250 μm). (D) Quantification of percent of region-of-interest areas that showed EYFP terminal labeling after thresholding EYFP signal channel. 25% of intermediate laminar areas were occupied by EYFP+ terminals. 2% of ventral horn areas were occupied by EYFP+ terminals (****$p < 0.0001$ by two-tailed t-test; bars represent mean ± SEM).

We employed a trans-synaptic retrograde pseudorabies (PRV) viral tracing strategy to accomplish this. When injected into a target site, PRV enters the cell at the pre-synaptic terminal, and is retrogradely transported to the cell body of this primary neuron. The virus is then passed upstream across dendritic synapses, labeling any cells that project to the primary cell. This trans-synaptic transfer continues until the animal is sacrificed, labeling any cells that eventually innervate the primary neuron through indirect projections. We injected PRV293.mCherry into the upper forelimb muscles (bicep, tricep, trapezius, deltoid) of Colgalt2 and Gprin3 mice to determine if these cells indirectly participate in spinomuscular circuitry (Figure 2.10A). We then visualized mCherry reporter expression in cells after 5 days (Figure 2.10B). Consistent with our retrograde CTB injections, Colgalt2 GFP was found in 19% of forelimb-mCherry+ cells, suggesting they do not significantly contribute to forelimb spinomuscular output (Figure 2.10C). Surprisingly, while we observed many forelimb-mCherry+ cells adjacent to our Gprin3 neurons, only 30% of forelimb-mCherry+ cells co-localized with Gprin3, whereas CTB injections into C6 of the spinal cord showed an 80% overlap with Gprin3 cells. Together, these data indicate that while Gprin3 cells project to the spinal cord, they do not appear to substantially participate in forelimb control circuitry. In addition to forelimb alpha motor neuron pools, however, the cervical spinal cord contains motor neurons that control dorsomedial shoulder and neck muscles. It is therefore possible that the Gprin3 cell projections to cervical spinal cord instead participate in the control of these more anteromedial muscle groups, although more tracing experiments must be carried out to address this question.

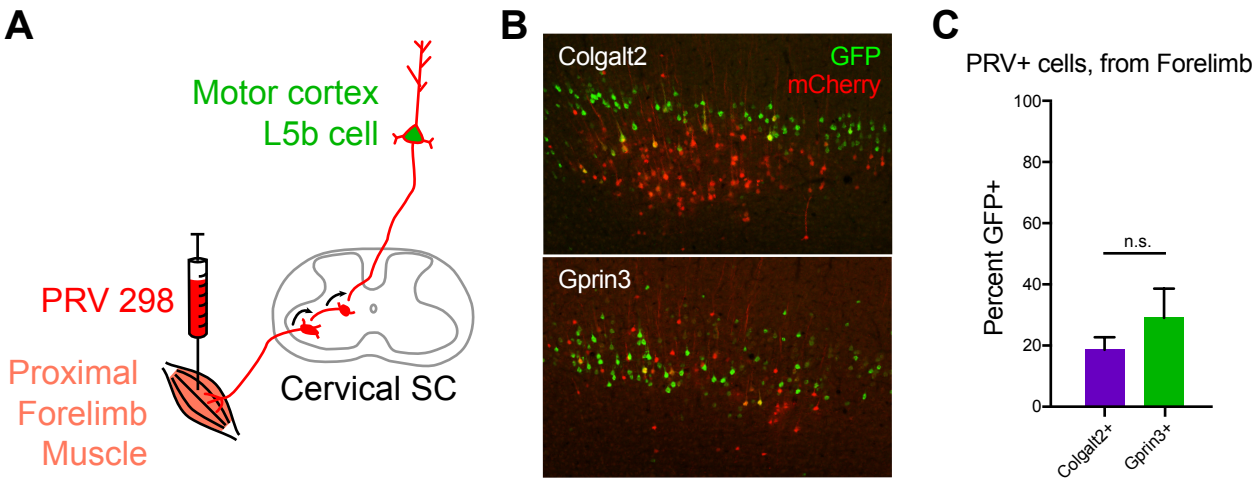

Figure 2.10: PRV tracing reveals that neither Colgalt2 nor Gprin3 cells participate in proximal forelimb muscle control circuitry. (A) Schematic illustration showing PRV expression and labeling paradigm with expected mCherry (red) expression pattern. After injection into forelimb muscles, PRV is retrogradely transported to cell bodies of innervating alpha motor neurons in the ventral horn. The virus is trans-synaptically passed retrogradely until it reaches cortical L5b cells that terminate in the spinal grey matter. (B) Representative confocal images following immunostaining for Colgalt2 (top) and Gprin3 (bottom) GFP (green), and mCherry expressed by PRV (red). mCherry+ cells appear below UL5b Colgalt2 cells and amongst LL5b Gprin3 cells. (C) Quantification for co-localization of mCherry with Colgalt2 GFP (purple) and Gprin3 GFP (green), reported as a percentage of all mCherry+ cells observed. 19% of mCherry+ cells co-localized with Colgalt2 GFP (n = 124 cells). 30% of mCherry+ cells co-localized with Gprin3 GFP (n = 206 cells). This suggests that neither cell type greatly participates in forelimb muscle control circuitry (n.s. = not significant by two-tailed t-test; bars show mean ± SEM).

2.6 Colgalt2 and Gprin3 neurons represent two molecularly related, but nevertheless distinct, populations of L5b pyramidal neurons.

Because Colgalt2 and Gprin3 cells have historically been very difficult to distinguish from each other anatomically as well as molecularly, we wanted to determine if their similarity is reflected at the level of mRNA by comparing the gene expression profiles of Colgalt2 and Gprin3 cells to other cell types in the cortex. For this, we took advantage of the controlled expression of the EGFP-L10a ribosomal subunit in our two mouse lines to perform TRAP, a technique that provides access to cell type-specific mRNAs via immunoprecipitation (IP) of the tagged ribosomal subunit (Doyle et al., 2008; Heiman et al., 2008). Ribosome bound mRNA molecules from Colgalt2 and Gprin3 cells were IP'ed from whole cortex homogenates and polysome-bound mRNAs were analyzed by high throughput RNA sequencing. We determined the success of the isolation by confirming that known pyramidal neuron marker genes were enriched and glial genes were depleted in each dataset. We then set out to determine how similar Colgalt2 and Gprin3 mRNA expression patterns are relative to other cell types in the brain. By PCA, these cells cluster closely together, along with L6a cells (Figure 2.11A). In contrast, Colgalt2 and Gprin3 cells cluster away from striatal neurons, L4 neurons in the cortex, and samples from the S100a10 mouse line that expresses in L5a neurons and endothelial cells. Next, we assessed Euclidean distance between these cell types by measuring the distances between samples in the whole transcriptome-dimensional normalized counts space. Hierarchical clustering of these distances revealed that Colgalt2 and Gprin3 cells, as well as deep L6a neurons, exist closer together in this

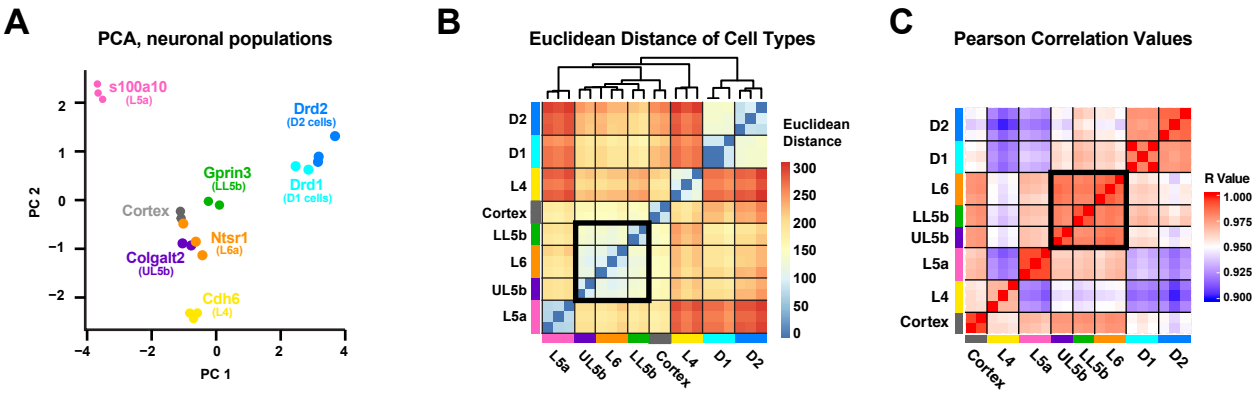

Figure 2.11: Colgalt2 and Gprin3 cells have gene expression profiles that suggest that, among other neuronal populations, they are closely related. (A) Principal component analysis (PCA) showing relative positioning of different TRAP sample replicates along the first two principal components. (B) Heatmap showing hierarchically clustered Euclidean distances between TRAP replicate samples for different cell types. Each row/column represents one replicate sample. Bold black box shows deep layer cortical cells, including UL5b Colgalt2 cells and LL5b Gprin3 cells, which cluster together and show relatively short distances between each other, suggesting they are more related to each other than to other neuronal cell types (C) Heatmap of Pearson correlation values between TRAP replicate samples for different cell types. Each row/column represents one replicate sample. Bold black box highlights the deep layer populations of UL5b Colgalt2 cells, LL5b Gprin3 cells, and L6a Ntsr1 cells, which all correlate highly, suggesting that they show similar patterns of gene expression (magenta = S100a10 L5a IP samples, purple = Colgalt2 UL5b IP samples, orange = Ntsr1 L6a IP samples, green = Gprin3 LL5b IP samples, grey = whole cortex input samples, yellow = Cdh6 L4 IP samples, cyan = Drd1 striatal IP samples, blue = Drd2 striatal IP samples).

space than they do to other cell types (Figure 2.11B). Pearson correlation of normalized gene expression counts similarly showed that deep layer neurons are highly correlated with each other (Figure 2.11C). Together, these results confirm that in the context of the whole transcriptome, UL5b Colgalt2 and LL5b Gprin3 cells are more similar to each other than to other cell types in the cortex and subcortex.

Next, we performed differential expression (DE) analysis between Colgalt2 and whole cortex input, and between Gprin3 and cortex input to determine whether known L5b marker genes are enriched in these cells relative to whole cortex (Figure 2.12A-B). We generated a list of marker genes for glutamatergic L5b neurons using the DE tool available for cortical single cell RNA-Seq data available through the Allen Brain Atlas (http://celltypes.brain-map.org/rnaseq/mouse). Both Colglat2 and Gprin3 cells expressed marker genes for L5b pyramidal tract neurons at high levels relative to whole cortical input samples (Figure 2.12C). Together, these data confirm that our Colgalt2 and Gprin3 datasets reveal a potentially fundamental molecular identity for these cells, namely that of L5b pyramidal neurons. To determine what genes instead define the molecular differences between Colgalt2 and Gprin3 cells, we performed DE analysis directly between Colgalt2 and Gprin3 cells (Figure 2.13A). Genes that showed significant (adjusted p-value < 0.05) enrichment in either cell type and with a mean Log10 counts per million (CPM) expression value greater than 3 across Colgalt2 and Gprin3 were run through gene ontology (GO) analysis to determine what pathways, classes, or groups of genes were enriched between the two cell types. GO categories returned from these analyses revealed that several genes enriched in Colgalt2 cells are

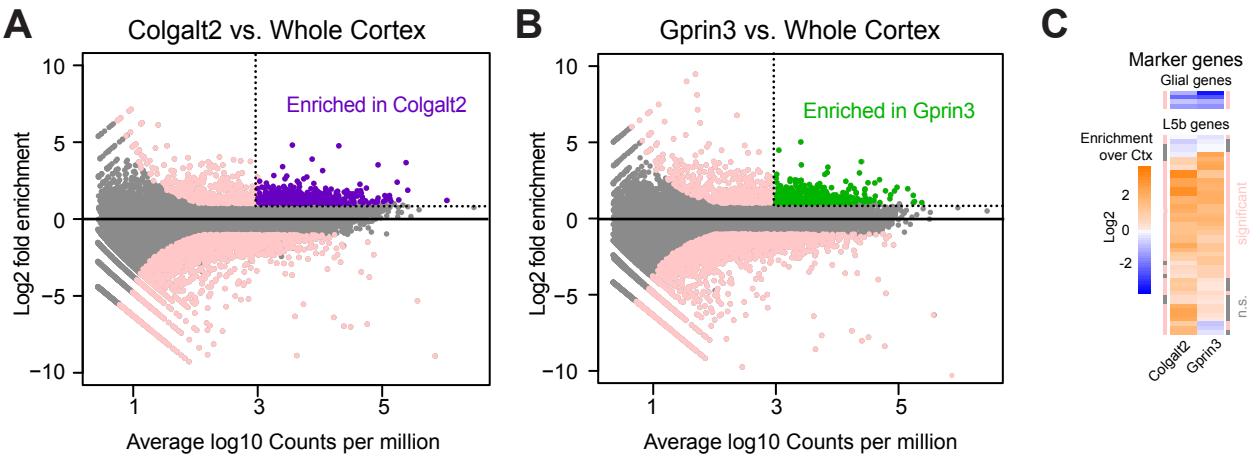

Figure 2.12: Colgalt2 and Gprin3 cells are related in part by their expression of known L5b genes. (A-B) MA Plot showing average Log10 counts per million (cpm) value and Log2 fold enrichment in IP over cortical input from differential expression (DE) analysis. Genes that showed significant enrichment (adjusted $p < 0.05$ and Log2 fold enrichment < -1 or > 1) in either IP or cortex are shown in pink. All other genes shown in grey. Genes that were highly expressed (Log10 cpm > 3) and significantly enriched in IP samples are shown in purple for Colgalt2 cells (A) and green for Gprin3 cells (B). These genes were considered to be highly expressed in their respective cell type. (C) Heatmap showing Log2 fold enrichment over cortical input for Allen Brain Atlas L5b marker genes in Colgalt2 and Gprin3 cells. Glial gene enrichment shown as a control. Sidebars show whether the gene represented in that row was significantly enriched (pink) or not significantly different (grey; n.s. = not significant). Both Colgalt2 and Gprin3 cells appear to highly express many of the known L5b marker genes, further confirming their laminar identity through their gene expression profile.

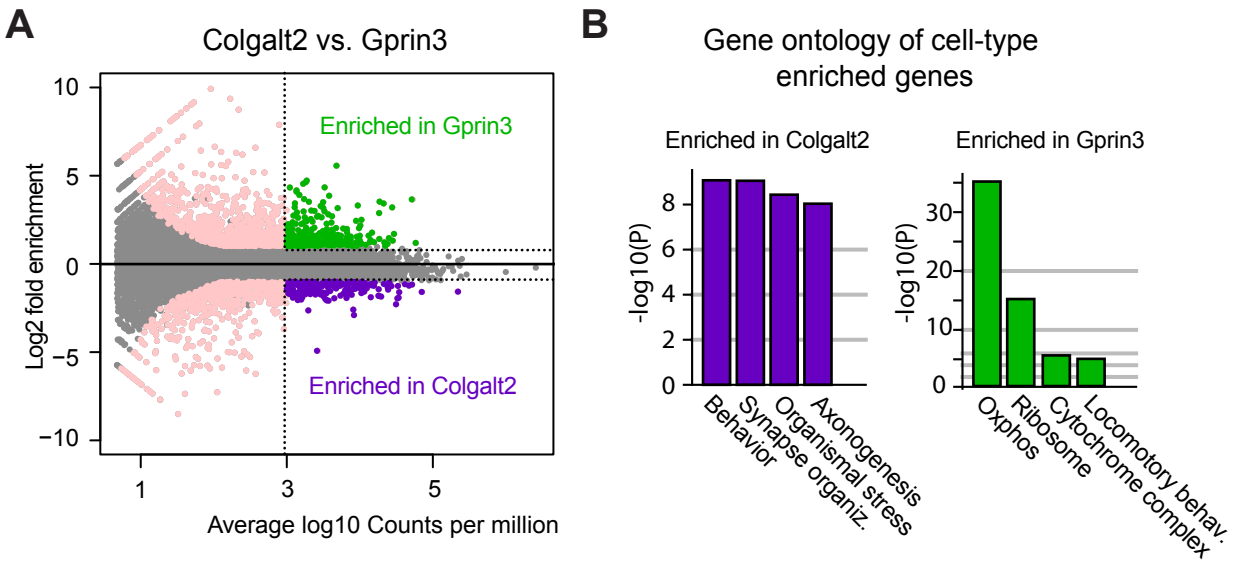

Figure 2.13: Differential expression between Colgalt2 and Gprin3 cells reveals molecular differences between UL5b and LL5b cell types. (A) MA Plot showing average Log10 counts per million (cpm) value and Log2 fold enrichment in IP over cortical input from differential expression (DE) analysis. Genes that showed significant enrichment (adjusted $p < 0.05$ and Log2 fold enrichment < -1 or > 1) in either IP or cortex are shown in pink. All other genes shown in grey. Genes that were highly expressed (Log10 cpm > 3) and significantly enriched in IP samples are shown in purple for Colgalt2 cells and green for Gprin3 cells. (B) Genes highlighted as highly enriched in Colgalt2 or Gprin3 cells were assayed for gene ontology (GO) enrichment. Classes of genes that were enriched in Colgalt2 cells (purple bars) primarily represent signaling pathways. Classes of genes enriched in Gprin3 cells (green bars) contain mitochondrial pathways (bars represent Log10 p-values for enrichment of each cateogory).

involved in maintaining neuronal structure and function (Figure 2.13B, left panel). In Gprin3 cells, many mitochondrial genes, particularly Oxphos-associated genes, showed enrichment over Colgalt2 (Figure 2.13B, right panel). While all of these data together confirm that UL5b Colgalt2 and LL5b Gprin3 cells share a basic molecular L5b identity, further highlighting the utility of transgenic lines that can distinguish between these cell types, our sequencing data also provide us with the ability to identify potentially important functional differences between the two cell types.

2.7 Discussion

Here, we present two transgenic lines that target expression of the EGFP-L10a TRAP construct to distinct populations of L5b cells in M1. We found that Colgalt2-TRAP DU9 cells are found all across the cortex, and are restricted to an upper sublayer, UL5b (Figure 2.14, left panel). Gprin3-TRAP ES152 cells are instead found primarily in rostral areas of the cortex, mostly restricted to LL5b of ALM and M1. While in M1, the distribution of Colgalt2 and Gprin3 cells is clearly divided into UL5b and LL5b, while in other areas of cortex, Colgalt2 and Gprin3 cells converge in the same layer. While the thickness of each of the 6 cortical layers often varies across the different functional regions of cortex, this subdivision of L5b appears to be unique to the motor region of cortex. The laminar distribution of L5b is likely programmed during cortical patterning in late pre-natal development. Because deep layers of the cortex are established first during cortical neuron migration in laminar development (Rakic, 1974), the differential intersections of expression gradients for cortical patterning factors such as Fgf8

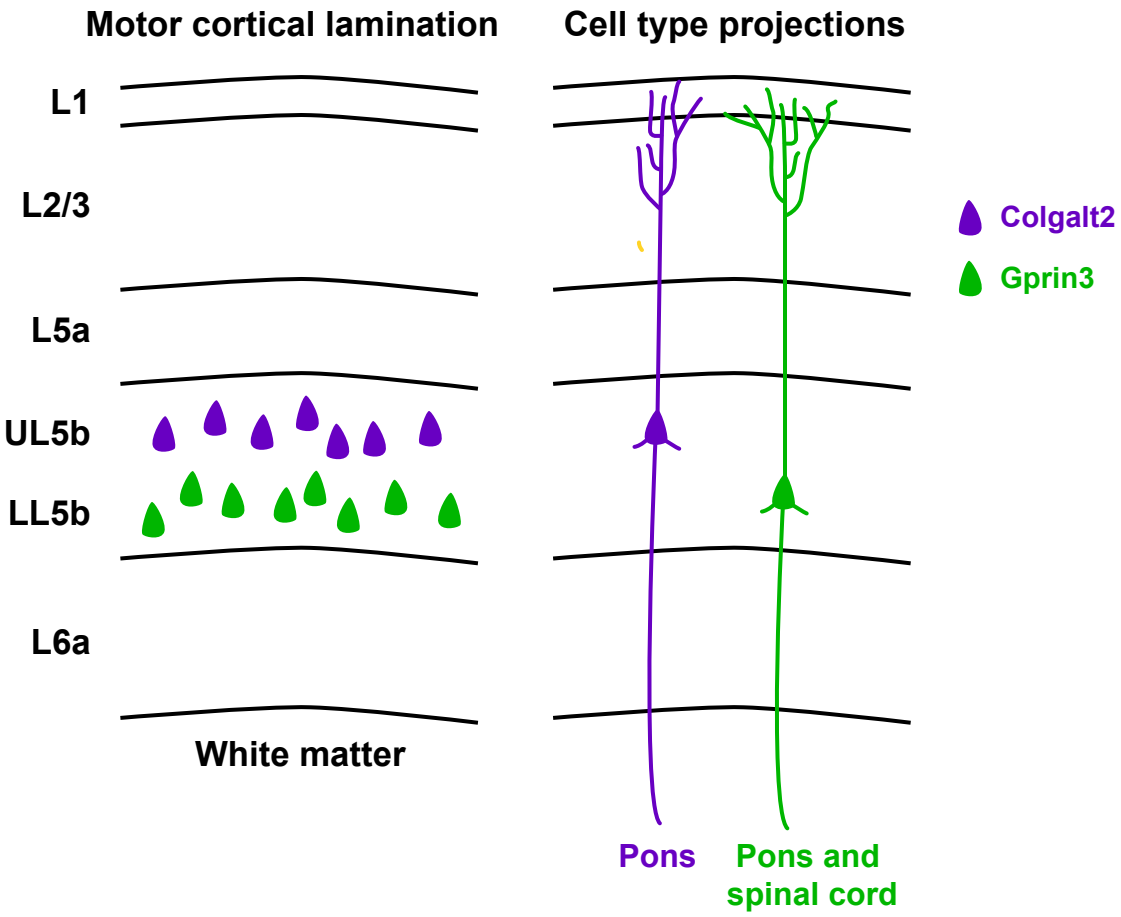

Figure 2.14: Summary of UL5b and LL5b anatomical divergence. We show that L5b in mouse M1 is subdivded into two discrete sublayers, upper L5b (UL5b) and lower L5b (LL5b) containing molecularly distinct populations of cells (left panel). We additionally show that cells found in UL5b (purple) only project to the pons, while LL5b cells (green) project to both the pons and the intermediate regions of the cervical spinal cord (right panel).

(Fukuchi-Shimogori and Grove, 2001; Garel et al., 2003) and Emx2 (Bishop et al., 2002; Hamasaki et al., 2004) may influence the timing and duration of L5b cell migration and differentiation. These timing differences could establish different thicknesses of L5b throughout the cortex, with more anteromedial regions such as M1 and ALM developing a thicker L5b than other cortical areas. Additionally, these gradients may help determine the medial-lateral and anterior-posterior extents of Colgalt2 and Gprin3 cell identity.

Once positioned in the cortex, L5b pyramidal neurons begin to send projections to various long-range target regions. Here we show that UL5b Colgalt2 cells and LL5b Gprin3 cells diverge in long-range projection patterns. While Colgalt2 cells have pyramidal tract (PT) collaterals that terminate in the pons but not the spinal cord, Gprin3 cells send PT axon collaterals to both the pons and spinal cord (Figure 2.14, right panel). For L5b cells, subcortical vs. intratelencephalic (IT, or cortico-cortical) projection is the first hierarchy of projection identity that must be determined. Expression of Fezf2 and Ctip2 (Chen et al., 2008), and absence of Satb2 (Alcamo et al., 2008) are necessary and sufficient to specify that a L5b axon should be directed subcortically. Once out of the cortex, the unique sets of transcription factors found in each cell type influence the expression of axon guidance receptors that specifically respond to attractive and repulsive cues, establishing correct collateral targeting for each neuron class (for review, see Lodato et al., 2015). The distinct subcortical projection pattern that we observe for M1 L5b cells suggests that Colgalt2 and Gprin3 cells express different genes during axon guidance that are responsible for differentiating their projection to the spinal cord and other areas. In fact, developmental evidence suggests that both UL5b

and LL5b cells develop a collateral to the spinal cord during post-natal axon outgrowth, but the collateral axon is lost for UL5b cells (Wang et al., 2017). When Lmo4 is conditionally knocked out from Emx1+ neurons during development, M1 L5b sublayer lamination is correctly established, but UL5b cells instead maintain the collateral to the spinal cord into adulthood (Cederquist et al., 2013). It would therefore be interesting to determine if in an Lmo4 conditional knock-out mouse, Colgalt2 cells would show a spinal collateral in adulthood, allowing us to probe the molecular origin of PT neuron projection divergence. Additionally, expression of the TRAP construct in this context may help to uncover the downstream receptors responsible for generating such precise axonal targeting during L5b projection patterning.

Establishing appropriate connectivity during development is critical to the proper functioning of many cortical circuits. For L5b cells, the targeting of neuronal signaling to precise areas over long distances is even more important, as they represent an important output layer of the cortex. L5b cells of M1 participate in motor planning, learning, and execution via these projections (Gu et al., 2017b; Guo et al., 2015; Kawai et al., 2015; Lashley, 1942; Suter et al., 2013). In the latter case, projections to the spinal cord communicate the information necessary for alpha motor neurons to direct the contraction of appropriate muscle groups. Our data reveal, however, that Gprin3 axons do not project directly onto alpha motor neurons of the cervical spinal cord, but instead terminate in an intermediate spinal grey area around lamina 5, 6, and 7. Together with the results from our trans-synaptic retrograde PRV tracing from forelimb muscles, these data additionally reveal that Gprin3 cells do not heavily participate in the

control of forelimb muscles through this projection. Motor neurons that control other more anterior muscle groups in the body are also found in the cervical spinal cord, and using more trans-synaptic tracing targeted to these areas, we will be able to address whether Gprin3 cells instead participate in the control of these muscle groups.

In primates, the motor cortex is important for the execution of voluntary movement (Evarts, 1968; Lee and Tatton, 1975; Thach, 1978), and the sophisticated repertoire of dexterous movements that are displayed by non-human primates, apes, and humans benefit from the direct projection of a subpopulation of L5b cells, namely corticomotoneurons, onto alpha motor neurons in the spinal cord (Iwatsubo et al., 1990). Conversely, the relative simplicity of movement patterns seen in lower mammals likely explains the lack of direct projections from M1 LL5b cells onto spinal motor neurons, although this is not fully understood (see Gu et al., 2017b). To address the functional contribution of LL5b Gprin3 cells to motor output in the mouse, we must first carefully delineate the muscle groups that receive indirect input from these cells. Additionally, specifically ablating Gprin3 cells, using either virally-delivered toxins or optogenetic silencing, can allow us to observe the behavioral consequence to these muscle groups during motor output, and begin to uncover a potential functional relationship between corticospinal neurons in the mouse and the ones found in primates.

The functional properties of distinct neuron types are influenced by the differential expression of channels, receptors, and other signaling components, both during development and in adulthood. The molecular diversity of L5b cells was recently

shown to be greater than originally known (Economo et al., 2018; Tasic et al., 2018). Here, we show that Colgalt2 and Gprin3 cell gene expression patterns suggest they are closely related, and that genes associated with establishing/maintaining L5b excitatory pyramidal neuron identity likely drive this similarity. However, Colgalt2 and Gprin3 cells show differences in gene expression that may contribute to differences in function. For instance, mitochondrial genes appear to be enriched in our Gprin3 population, perhaps because of the extra lengths of dendrites and axon that have to be energetically maintained in these cells. It would be interesting to see how the Lmo4 cKO that causes UL5b cells to develop an axonal projection to the spinal cord affects the expression level of these genes, and to determine what physiological differences in ATP-synthesis already exist between Colgalt2 and Gprin3 cells.

Overall, we show that Colgalt2 and Gprin3 cells diverge in both laminar distribution and projection identity, with both cell types displaying different distributions across whole cortex. We confirm that UL5b Colgalt2 cells in M1 project to the pons, and that M1 LL5b Gprin3 cells innervate both the pons and the spinal cord. The spinal collaterals displayed by these anterior Gprin3 cells terminate on an intermediate population of neurons rather than on alpha motor neurons directly, and these terminals do not appear to participate in upper forelimb muscle control circuits, instead potentially influencing the control of anteromedial muscles, such as neck and shoulder, indirectly. Finally, Colgalt2 and Gprin3 cells show gene expression patterns that suggest that while these cells are very similar to each other, they show key differences that may corroborate their anatomical and functional uniqueness.

CHAPTER 3:

Generating tractable models for studying cell-type vulnerability and resistance in the primary motor cortex of SOD1-G93A mice.

Amyotrophic Lateral Sclerosis (ALS) is a fatal motor neuron disease that is clinically and pathologically defined by the loss of lower motor neurons (LMNs) of the spinal cord and upper motor neurons (UMNs) of the cortex (Tandan and Bradley, 1985). The cellular features that make these populations the most vulnerable to ALS-causing mutations are not known, and the pathways that ultimately lead to death of these two populations are likewise not entirely understood. To begin to uncover these mechanisms, LMNs have been primarily targeted, as they are readily identifiable among the diverse cell types of the spinal cord by their large size, unique morphology, and ventral localization (Aitken and Bridger, 1961; Light and Metz, 1978). In fact, many of the insights into disease pathology, mechanisms, and progression have thus far originated from studies of LMNs for this reason (see Turner and Talbot, 2008). UMNs of the primary motor cortex, by virtue of being localized among cells that are morphologically very similar and share many of the same markers, have proven more difficult to study with such rigor in the disease. To understand the full spectrum of cell type-specific pathology, and if effective therapies are ever to be developed, It is essential that the molecular responses of UMNs in disease be characterized in a targeted manner.

In mouse models of ALS that express human disease mutations in TDP-43 (Wegorzewska et al., 2009), FUS (Verbeeck et al., 2012), and SOD1 (Gurney et al., 1994a), have begun to provide insights into cortical pathologies in ALS (Huang et al., 2011; Jara et al., 2015; Ozdinler et al., 2011; Tsai et al., 2010). Some of the most commonly used models leverage human mutants of Cu/Zn superoxide dismutase 1 (SOD1) to recapitulate the disease in mice (Turner and Talbot, 2008). SOD1 is an key antioxidant enzyme that converts highly reactive superoxide, generated during biological processes such as electron transport in oxidative phosphorylation (Oxphos) and in the ER (Chance et al., 1979), into less reactive hydrogen peroxide (McCord and Fridovich, 1969). The most studied mutation to SOD1 is a glycine-to-alanine missense mutation at the 93rd amino acid position, G93A. It is unclear how the SOD1-G93A mutation causes disease. At the structural level, the G93A mutation causes the Cu/Zn binding regions of the protein appear to be more disordered, potentially encouraging aggregation of the protein (Galaleldeen et al., 2009). At the enzymatic level, the activity level of human SOD1-G93A appears to increase when expressed in mice (Gurney et al., 1994a), but it is unclear whether this is true in patients with SOD1 mutations (Robberecht et al., 1994). The SOD1-G93A transgenic mouse line, Tg(SOD1*G93A)1Gur, that expresses ~25 copies of human mutant SOD1-G93A on chromosome 12 and shows disease progression and progressive motor deficits that are characteristic of human ALS (Chiu et al., 1995). More importantly, it has been shown that in addition to spinal motor neurons, neurons in L5b of M1 appear to degenerate in this model, with the spinal-projecting subpopulation of these cells appearing to be the

most vulnerable (Kassa et al., 2009; Ozdinler et al., 2011; Spalloni et al., 2011; Zang and Cheema, 2002). These cells additionally show early signs of disease in the form of ER stress, dendritic atrophy, and changes in excitability (Fogarty et al., 2015; Jara et al., 2015; 2012; Kim et al., 2017; Spalloni et al., 2011). But how mutant SOD1 disrupts cellular function and leads to death of these neurons is largely not known. Likewise, it is not understood how, even with ubiquitous expression of mutant SOD1, death is specific to motor neurons. For this reason, having molecular access to the specifically vulnerable population of UMNs would allow us to probe the causal changes that lead to downstream pathophysiology, as well as the underlying properties that may be exploited by the mutation to cause cell-type specific death.

The vulnerable population of cortical neurons has been shown to reside in L5b of M1 across species (Eisen et al., 1992; Kassa et al., 2009; Mochizuki et al., 2011; Ozdinler et al., 2011; Spalloni et al., 2011; Tandan and Bradley, 1985; Zang and Cheema, 2002), but it has not been determined whether there is a sublayer specificity to this vulnerability, i.e. whether the degenerating cells reside in UL5b, LL5b, or across all of L5b. Our Colgalt2 and Gprin3-TRAP lines are therefore ideally suited to first determine the sublayer specificity of ALS UMN vulnerability, and then to molecularly profile the vulnerable cells during disease progression. We therefore set out to generate mice that express our L5b-specific TRAP constructs in the SOD1-G93A mouse. By visualizing Colgalt2 and Gprin3 cells during disease progression, we determined whether they degenerate in this ALS model, laying the foundation for carrying out assessments of cell type-specific gene expression changes in disease.

3.1 Breeding SOD1-G93A mice to Colgalt2 and Gprin3-TRAP mice does not disrupt disease progression.

In order to generate an ALS model that would provide us with molecular access to L5b cells, we crossed the SOD1-G93A mouse to our Colgalt2-TRAP DU9 and Gprin3-TRAP ES152 mice. To confirm that crossing these mice to SOD1-G93A does not impair or alter disease progression, we evaluated the general behavior and symptom development of SOD1-G93A mice expressing either Colgalt2-TRAP or Gprin3-TRAP. Both Colgalt2 and Gprin3 mice crossed to SOD1-G93A showed no differences in survival compared to uncrossed SOD1-G93A mice (Figure 3.1A). Median survival age was approximately 160 days for all mice, consistent with published survival times for the SOD1-G93A model (Gurney et al., 1994a). Classically, the SOD1-G93A mouse begins showing signs of disease around post-natal day 60 (P60). Hindlimb tremors and rigidity appear first, followed by hindlimb weakness that progresses rostrally toward the forelimbs. These gross symptoms were observed at similar ages in our SOD1-G93A mice crossed to our TRAP lines, suggesting that disease progression in our transgenic mice was not affected. For a more quantitative assessment of disease progression, we tested the performance of our crossed mice on an accelerating rotating rod (rotarod test). Both Colgalt2 and Gprin3 mice crossed to SOD1-G93A showed progressively shorter latencies to fall off the rotarod, with disease mice falling after ~100 seconds (Figure 3.1B-C). These deficits are consistent with the disease progression observed in the SOD1-G93A model that is not crossed to TRAP lines, with rotarod performance deficits appearing around P90 (Oliván et al., 2015). Taken together, these data show

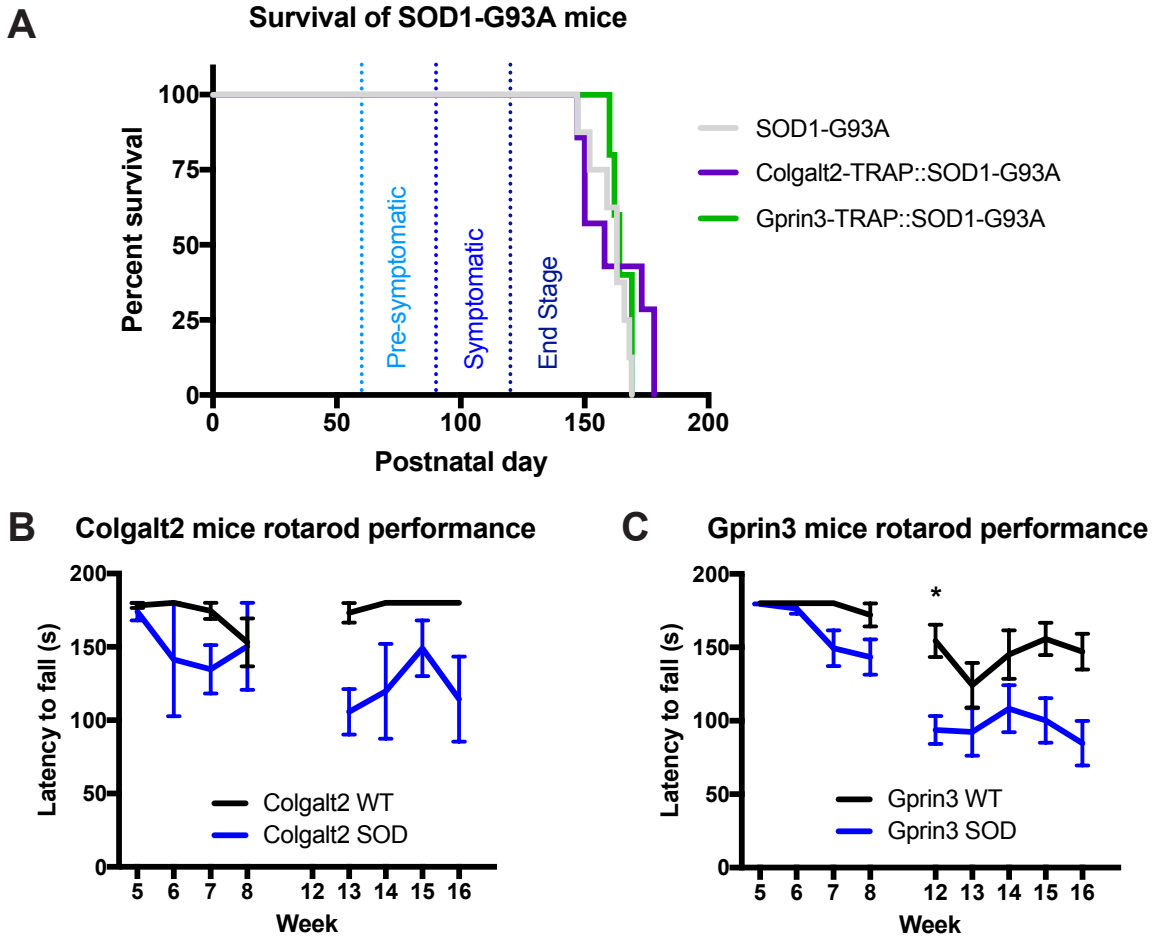

Figure 3.1: Expression of EGFP-L10a in Colgalt2 and Gprin3 mice does not alter the progression of disease in a SOD1-G93A context. (A) Survival curves showing the lifespan of SOD1-G93A mice, both uncrossed, and when crossed to either Colgalt2-TRAP DU9 or Gprin3-TRAP ES152 mice. Expression of the TRAP construct in either Colgalt2 or Gprin3 mice has no effect on survival. SOD1-G93A median survival = 163 (n = 8), Colgalt2-TRAP::SOD1-G93A median survival = 158 (n = 7) Gprin3-TRAP::SOD1-G93A median survival = 164 (n = 5). (B) Rotarod performance of Colgalt2-TRAP mice, WT vs. SOD-crossed, measured as latency to fall in seconds. Colgalt2 mice that express SOD1-G93A show a shorter latency to fall in later weeks relative to WT littermates, suggesting they develop a motor deficit over disease progression. Data presented as mean±SEM (WT group n = 4, SOD group n = 3). (C) Rotarod performance of Gprin3-TRAP mice, WT vs. SOD-crossed, measured as latency to fall in seconds. Gprin3 mice expressing SOD1-G93A also show a shorter latency to fall in later weeks when compared to WT littermates, highlighting a progressive motor deficit during disease. Data represented as mean±SEM (*$p < 0.05$, WT group n = 9, SOD group n = 12).

that the expression of the TRAP construct in the SOD1-G93A model, either under the control of the Colgalt2 or the Gprin3 promoter, does not affect disease progression, establishing these two lines as potentially useful for the characterization of cell type vulnerability and molecular responses of L5b cells when SOD1-G93A is expressed.

3.2 Both Colgalt2 and Gprin3 mice show activated glial invasion when SOD1-G93A is expressed.

In order to confirm that our TRAP-crossed SOD1-G93A mice show hallmark signs of neurodegeneration in tissue, we first looked for signs of neuro-inflammation by staining for the activated astrocyte marker GFAP. Invasion of activated glia has been observed in ALS tissues, across spinal cord and cortex (Bruijn et al., 1997b; Jaarsma et al., 2000; Kassa et al., 2009; Ozdinler et al., 2011). We therefore cervical spinal cord at a symptomatic stage of disease (> P100) to confirm broad mutant SOD1-mediated inflammation, and cortical tissue to visualize possible neuroinflammation around Colgalt2 and Gprin3 cells. Coronal sections of cervical spinal cord and cortex were made and immunostained for GFAP, as well as markers for cell types of interest: either alpha motor neuron ChAT (spinal cord) or Colgalt2/Gprin3 GFP (cortex). Images of immunostaining were collected by confocal microscopy. In the spinal cord sections at this symptomatic stage, invasion of GFAP+ activated astrocytes can be readily seen around ChAT+ alpha motor neurons of the ventral horn when SOD1-G93A is expressed (Figure 3.2A). Staining for astrocytosis in the cortex revealed the presence of activated astrocytes in M1 of both Colgalt2 and Gprin3 mice when SOD1-G93A was expressed

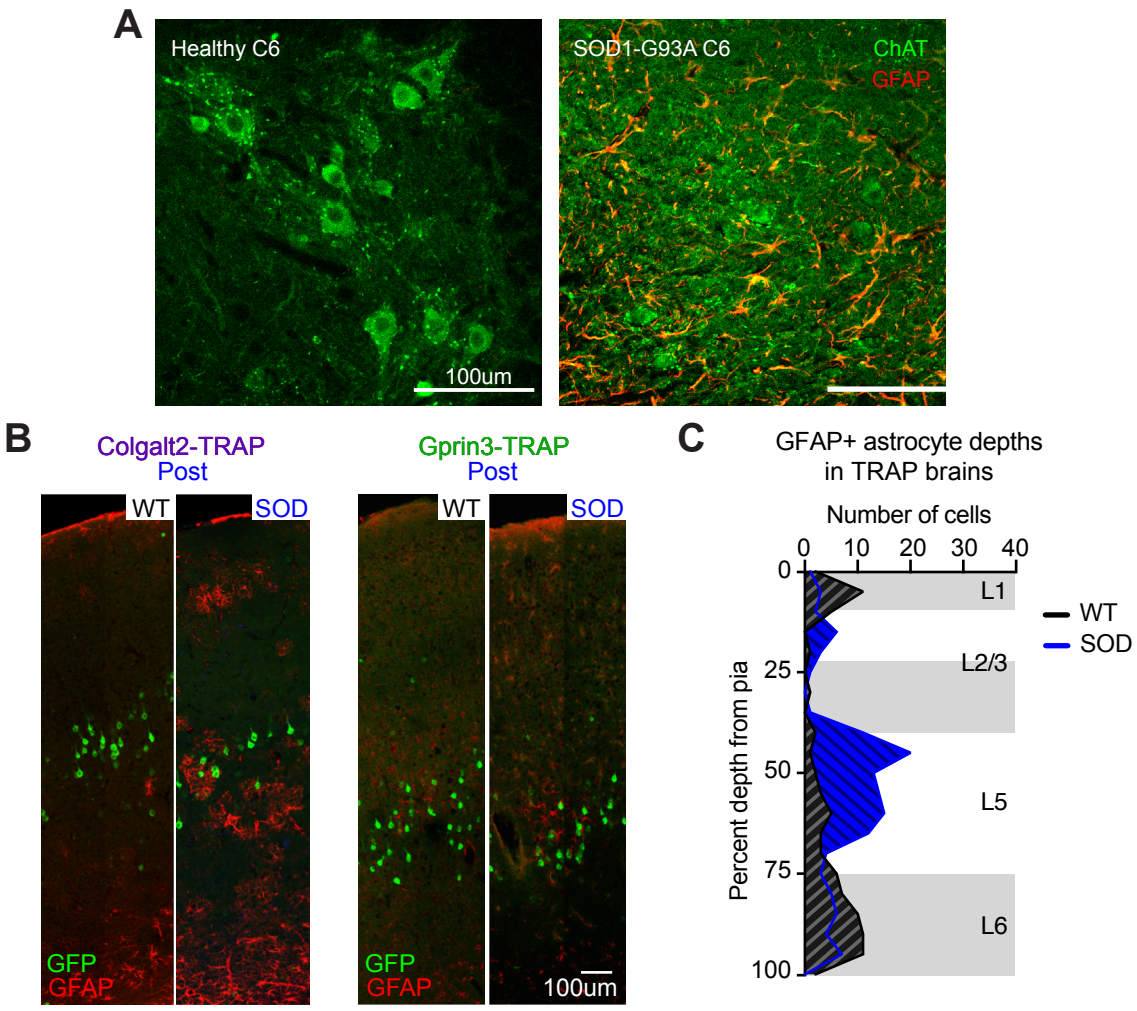

Figure 3.2: GFAP-positive astrocytes invade L5b in Colgalt2 and Gprin3 mice that express SOD1-G93A. (A) Confocal images of WT and SOD1-G93A ventral horn of cervical spinal cord at the level of C6 at symptomatic age, stained for ChAT (green) to label alpha motor neurons and GFAP (red) to visualize activated astrocytes. In SOD1-G93A, GFAP signal is observed in this area, but ChAT+ neurons disappear as they degenerate (scale bar = 100μm). (B) Representative confocal images of Colgalt2 and Gprin3 cortex, WT vs. SOD1-G93A symptomatic age, cropped to highlight depth of labeled cell populations. Colgalt2 and Gprin3 cells labeled with GFP (green), and activated astrocytes labeled with GFAP (red). Activated astrocytes can be seen in L5 around GFP+ cells in SOD1-G93A (scale bar = 100 μm). (C) Quantification of activated-astrocyte depth in WT and SOD TRAP cortex represented as a frequency distribution for percent depth from the pial surface. In SOD cortex, the presence of activated astrocytes in L5 appears to increase dramatically (WT group n = 3 animals, 86 cells. SOD group n = 3 animals, 130 cells).

(Figure 3.2B). The GFAP+ signal varied in depth, but was largely observed in L5, around the GFP+ TRAP cells (mean depth of GFAP+ cells at 54% from pia, Figure 3.2C). These data confirm that our Colgalt2 and Gprin3 transgenic mice develop one classic sign of neurodegeneration around our cells of interest, further establishing M1 as an important region to anatomically and molecularly characterize during disease progression.

3.3 Gprin3 cells are vulnerable to degeneration in SOD1-G93A, while Colgalt2 neurons are resistant.

Since L5b cells of M1 with long-range subcortical projections appear to be the most vulnerable in SOD1-G93A mice (Ozdinler et al., 2011; Zang and Cheema, 2002), and because UL5b Colgalt2 and LL5b Gprin3 cells both have long-range projections to the pons and, in the case of Gprin3 neurons, to the spinal cord, we set out to determine if either or both Colgalt2 and Gprin3 cells show vulnerability when SOD1-G93A is expressed. In order to determine direct vulnerability of Colgalt2 and Gprin3 cells to SOD1-G93A, we collected coronal brain sections from pre-symptom onset (Pre, ~P70) stage and post-symptom onset/symptomatic (Post, ~P110) stage of disease, and counted the number of GFP+ cells in 20X fields of view (FOVs, Figure 3.3). Notably, Colgalt2 cells along the extent of M1 did not show a difference in number in mice expressing SOD1-G93A (Figure 3.4A). Gprin3 neurons, in contrast, showed a significant decrease in number of around 23% at symptomatic stage (Post) across all of M1. When cell counts were instead assessed for individual anatomical positions along

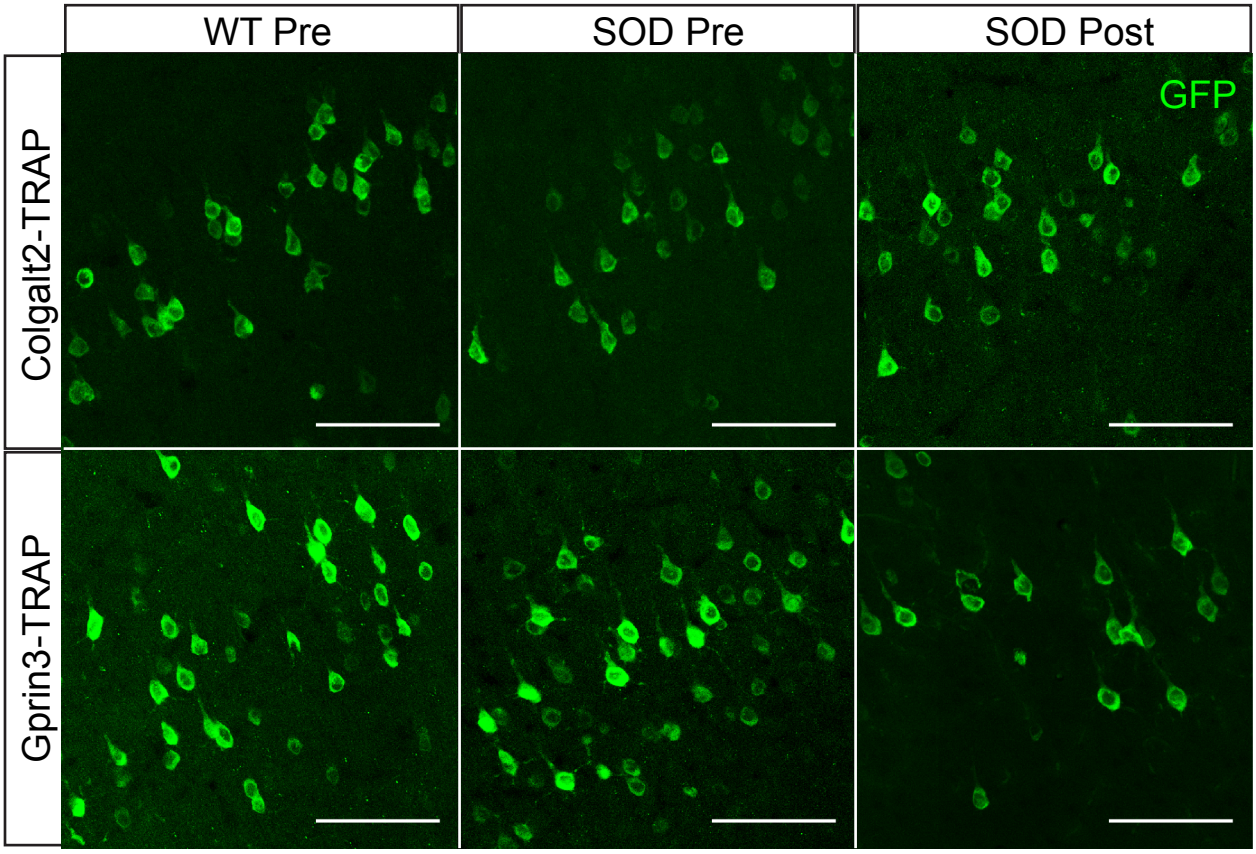

Figure 3.3: GFP staining reveals loss of Gprin3 cells in SOD1-G93A mice, but no loss of Colgalt2 cells. Representative confocal images from Colgalt2 and Gprin3 M1, in WT and SOD1-G93A showing 20X field-of-view that was used to assess density of GFP+ cells. Colgalt2 and Gprin3 cells were visualized by GFP staining (green). Images are shown for pre-symptomatic age ("Pre") WT, Pre SOD1, and post-symptom onset age ("Post") SOD1. A decreased density of GFP+ cells can be seen in symptomatic age Gprin3 M1 when SOD1-G93A is expressed (scale bars = 100 μm).

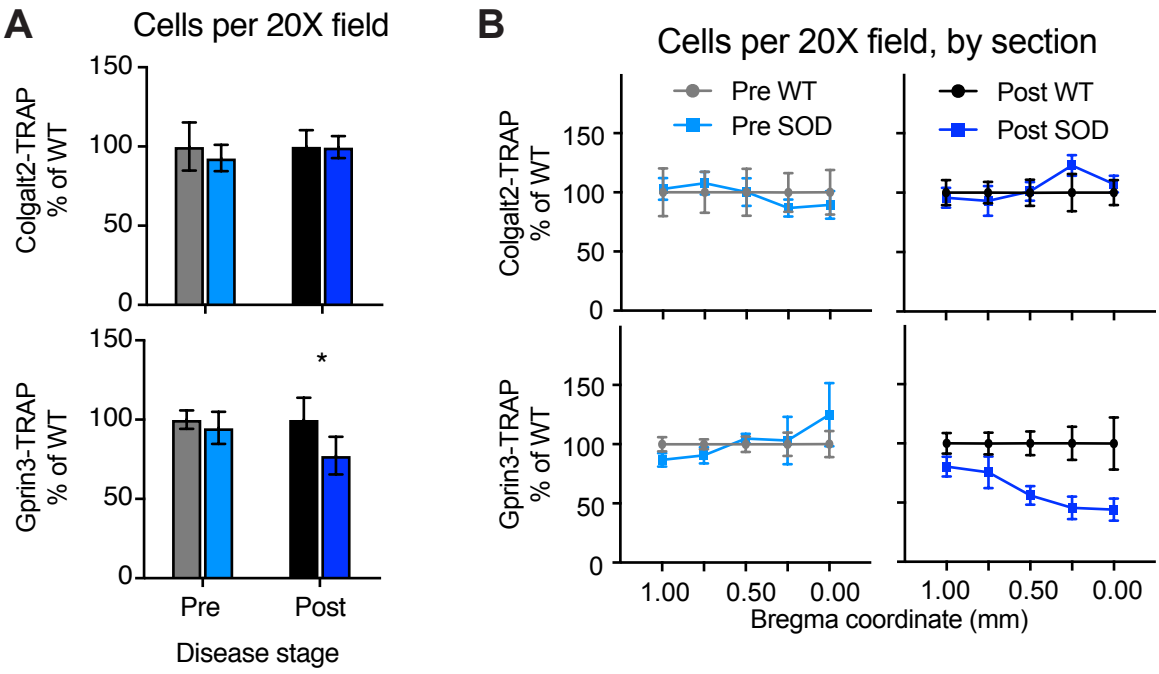

Figure 3.4: Gprin3 cells are lost in SOD1-G93A mice, but Colgalt2 cells remain. (A) GFP+ cells per 20X field in Pre and Post age Colgalt2 M1 (upper panel) and Gprin3 M1 (lower panel) between WT and SOD1-G93A, averaged across full AP extent of M1, and reported as percent of corresponding WT mean. No change in Colgalt2 cell number is observed at any stage of disease, whereas Gprin3 cells show a 23% decrease at symptomatic stage (*$p < 0.05$; bars show mean±SEM, Colgalt2 WT Pre n = 6, SOD Pre n = 7; Colgalt2 WT Post n = 4, SOD Post n = 5; Gprin3 WT Pre n = 8, SOD Pre n = 4; Gprin3 WT Post n = 7, SOD Post n = 5). (B) GFP+ cells per 20X field in Pre and Post age Colglat2 M1 (upper plots) and Gprin3 M1 (lower plots), averaged per anatomical position along the AP axis of M1, and reported as percent of corresponding WT mean. Again, Colgalt2 cells show no change in number during disease progression, but Gprin3 cells show a decrease in posterior areas of M1 of ~55% (bars show mean±SEM, Colgalt2 WT Pre n = 5, SOD Pre n = 8; Colgalt2 WT Post n = 7, SOD Post n = 5; Gprin3 WT Pre n = 8, SOD Pre n = 5; Gprin3 WT Post n = 7, SOD Post n = 5).

the anterior-posterior axis of M1, we observed a greater, although non-significant, loss of Gprin3 cells (up to 55% decrease) at more posterior M1 coordinates, revealing a potential posterior-to-anterior axis for progressive loss of cells (Figure 3.4B). We did not observe a loss of Colgalt2 cells at any coordinate along this AP extent. This loss of Gprin3 neurons but not Colgalt2 neurons in the presence of SOD1-G93A confirms that spinal-projecting neurons of M1 L5b are the most vulnerable cortical population in this model. The greatest loss of Gprin3 cells was observed in more posterior regions of M1, suggesting that even within this cell type, there may be differential vulnerability to SOD1-G93A. The data also broadly implicate an intrinsic molecular difference between Colgalt2 and Gprin3 cells as potentially underlying the distinct sensitivity to mutant SOD1 observed between the two cell types.

3.4 Discussion

Cells of L5b in rodent M1 have been shown to be vulnerable in the SOD1-G93A mouse model (Ozdinler et al., 2011; Thomsen et al., 2014; Zang and Cheema, 2002). Using molecular marker staining and retrograde tracing from subcortical regions, a temporally progressive loss of L5b neurons is observed throughout disease. Here, we show that the vulnerability of neurons observed for L5b is specific to LL5b where Gprin3 cells are found, with UL5b Colgalt2 neurons showing resistance to degeneration in SOD1-G93A mice (Figure 3.5). These findings confirm that corticospinal neurons of LL5b are likely the most vulnerable to SOD1-G93A insult. And by contrast, cells that have long-range projections to more proximal regions, such as the thalamus and pons,

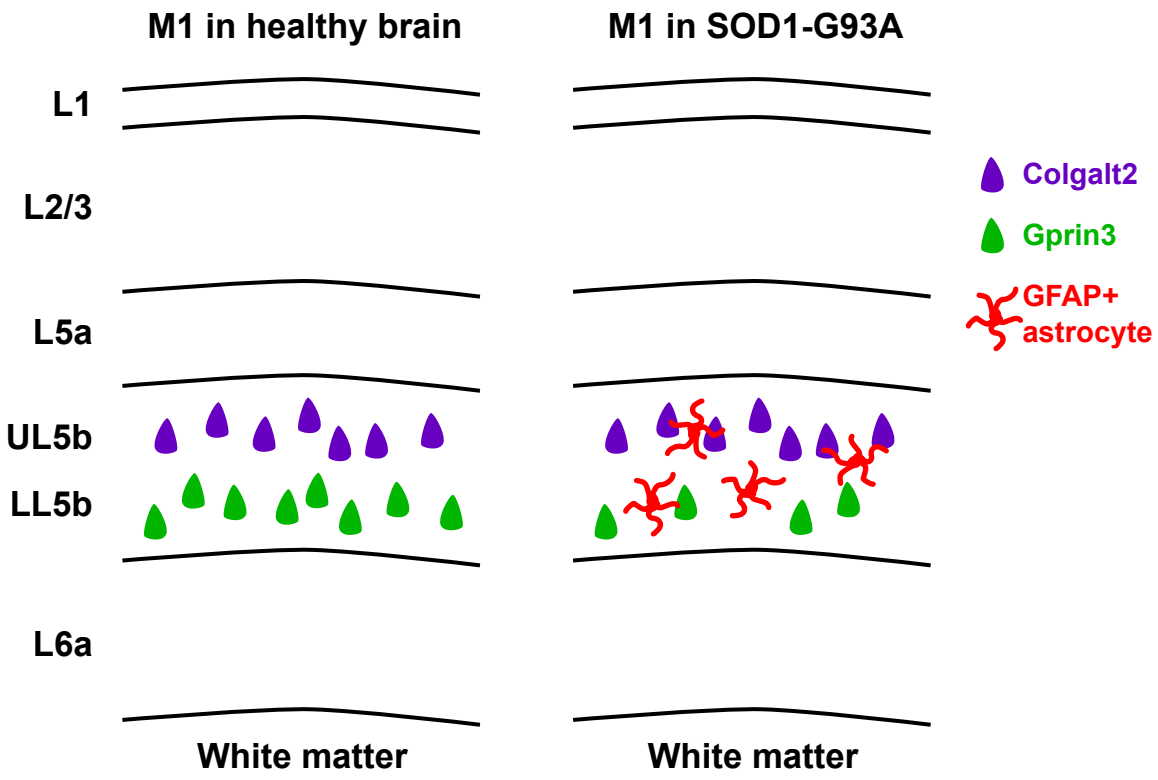

Figure 3.5: Summary of cell type-specific loss observed in L5b in SOD1-G93A mice. The We show that in SOD1-G93A mice, UL5b Colgalt2 cells (purple) do not degenerate, while LL5b Gprin3 cells (green) decrease in number. Invasion of activated astrocytes is also observed in L5b of these mice (red).

show no obvious vulnerability to degeneration. The relationship between projection identity and disease vulnerability is still a very open question, however. And given the differences in motor circuit participation for UL5b and LL5b cells, it is not understood how loss of LL5b neurons in the ALS models affects the function of motor circuitry in these animals. ALS-associated motor dysfunction in the SOD1-G93A model begins in hindlimb regions and progresses in a posterior-to-anterior manner as the animal ages, eventually affecting forelimb, shoulder and neck muscle groups (Gurney et al., 1994a). Because Gprin3 cells are found in areas that functionally map to control of anterior muscle groups (see Chapter 2), it is possible that these cells are the last to be affected during disease progression. This could explain why we observe a posterior-to-anterior gradient of Gprin3 cell loss, as cells that map to more posterior muscle groups would be lost first. In this scenario, however, it would be unlikely that loss of Gprin3 has any obvious outward consequence to gross motor output. Instead, it is possible that loss of Gprin3 cells affects the more subtle aspects of motor control, namely preparation, learning, and execution of dexterous movement (Chen et al., 2017; Guo et al., 2015; Kawai et al., 2015; Ueno et al., 2018). Unfortunately, none of the behavioral tests that we carried out in this study fully parse the cortical contribution to motor control from the spinal contribution, and therefore do not address these possibilities. It would be interesting to determine whether there is a progressive change in the ability of the mice to carry out tasks that are specifically shown to depend on M1 input. It would additionally be interesting to specifically drive loss of cortical motor neurons via toxin or Cre-dependent ablation, to more carefully assay what effect, if any, loss of the cortical

component of the motor circuit, particularly for anterior muscle groups, has on functional motor output.

It is not understood what mechanisms cause the loss of motor neurons in the spinal cord and cortex: two cell types that are distinct in regional localization, morphology, and molecular identity, but that nevertheless share a functional connection. Theories about a prion-like spread of disease between these two cell types have left many open questions (see Braak et al., 2013a; Münch et al., 2011; Polymenidou and Cleveland, 2011). Some experiments have been done to address a "dying-forward" hypothesis, where corticospinal neuron dysfunction promotes disease in the downstream alpha motor neurons of the spinal cord (Eisen et al., 1992). For instance, when mutant SOD1-G93A is knocked down in the cortex of ALS model rats, the degeneration of both upper and lower motor neurons is slowed (Thomsen et al., 2014). This suggests that the degeneration of lower motor neurons is at least tied to, and at most caused by, the degeneration of the upper motor neurons. In rodents, the innervation of UMNs onto LMNs is, as discussed previously, not direct and has an intermediate interneuron populations in between (Bourane et al., 2015; Hantman and Jessell, 2010; Ueno et al., 2018). How this interneuron population responds to disease in the context of dying-forward from the cortex is not known, but is key to understanding the mechanism by which disease is "transmitted" downstream. In humans, a direct projection between a subset of corticospinal neurons and alpha motor neurons spinal cord provides a better foundation for a direct propagation of disease between upper and lower motor neurons. For instance, hyperexcitability observed in motor cortex could

drive stress in alpha motor neurons, which may promote death of the cells (Menon et al., 2015; Vucic and Kiernan, 2006; Vucic et al., 2008). For these reasons, carefully assessing the point of origin of disease using cell-type specific ablations or more targeted expression of SOD1-G93A becomes important for understanding how this disease is able to affect two distinct cell types. Additionally, mechanisms of disease propagation would make very good targets for therapeutic intervention for halting or slowing of progression, as long as these molecular mechanisms can be said to reflect human disease pathology.

For any study that attempts to uncover innate biological properties of neurons using transgenic mouse lines, it is important to discuss the limitations in interpreting the findings. As a model for ALS, the SOD1-G93A mouse shows the loss of upper and lower motor neurons (UMNs and LMNs) that exemplifies the human disease. However there are some who question the representative capacity of the SOD1-G93A mouse for human ALS (Turner et al., 2013). This primarily derives from an inability to translate treatments that successfully slow disease progression in the mouse model into human patients (Benatar, 2007). Additionally, SOD1 models do not recapitulate all cellular pathologies observed in human patients, such as TDP-43 inclusions (Robertson et al., 2007). And while this may be explained in part by the fact that the model overexpresses mutant SOD1 at extremely high levels, it is possible that any changes that we observe in our SOD1-G93A experiments are not representative of changes that occur in human UMNs in ALS. This uncertainty cannot be resolved until a validation of mechanisms observed in this mouse model is undertaken in human tissues in the future. However, it

is important to remember, that while the pathological mechanisms that lead to cell death may not be similar in ALS across species, the selective vulnerability of motor neurons is still observed in the SOD1-G93A mouse. The model therefore still provides an important and useful platform for studying motor neuron-specific vulnerability to certain genetic perturbations, and its associated molecular changes across cell types.

CHAPTER 4:

Molecular responses to SOD1-G93A observed by TRAP in Colgalt2 and Gprin3 neurons.

Studies into molecular mechanisms of neurodegeneration focus primarily on understanding what pathways lead to cell-specific dysfunction and death. In particular, the goal is to understand how ubiquitously expressed mutations leverage unique cell type features during disease progression. In ALS, it is not known how expression of mutant SOD1 in the whole CNS causes specific death of UMNs in the cortex and LMNs in the spinal cord. A first step in understanding this phenomenon is characterizing the molecular changes that occur in these cells during disease. Neuronal dysfunction phenotypes, such as hyperexcitability and dendritic atrophy in UMNs, are now being uncovered in models of ALS (Fogarty et al., 2015; Genç et al., 2017; Jara et al., 2015; Kim et al., 2017; Ozdinler et al., 2011; Saba et al., 2015; Wegorzewska et al., 2009). Using a variety of sequencing approaches, the field has also begun to understand how gene expression changes that occur during disease progression may contribute to the phenotypes that precede cell death in the mutant SOD1 context (Bandyopadhyay et al., 2013; de Oliveira et al., 2013; 2014; Malaspina et al., 2001; Saxena et al., 2009; Sun et al., 2015). These studies have shown that underlying the gross neuronal changes are early signs of ER stress, unfolded protein response, and mitochondrial dysfunction. But because it is not trivial to isolate specific neuron populations from each other in this model (although see Saxena et al., 2009), it has been difficult to determine whether

these changes occur specifically in the vulnerable population or in the assayed tissues as a whole. Developing successful treatments or therapies for ALS will require us to determine the disease phenotypes that are specific to motor neurons over other cell types, and by contrast, the molecular coping mechanisms of cell types that are resistant to degeneration.

Despite being molecularly similar to disease-vulnerable LL5b Gprin3 (Chapter 2), our UL5b Colgalt2 cells did not appear to degenerate in the SOD1-G93A model (Chapter 3). From a disease mechanism standpoint, this presents a unique opportunity to study what specific disease-triggered gene expression changes in Gprin3 cells may lead to their selective degeneration. And more importantly, having molecular access to Colgalt2 gene expression allows us to interrogate potential coping strategies for surviving mutant SOD1 expression. Understanding these changes could then lead us to probe how the underlying intrinsic differences between these two cell types may contribute to their respective molecular responses, and inevitably cause specific vulnerability of one population over the other.

We therefore set out to determine what gene expression changes occur in Colgalt2 and Gprin3 during disease progression by performing TRAP at two different time points in SOD1-G93A animals. An early pre-symptomatic time point was assayed in order to reveal potential early regulatory mechanisms of later stage dysfunction. A symptomatic time point was collected to determine how late disease mechanisms may lead to death of LL5b Gprin3 cells, and survival of UL5b Colgalt2 cells. We then attempted to compare the findings from these disease datasets to results from our

original comparison of intrisinic cell type differences in an effort to understand how the disease-sensitive mechanisms differ between the two cell types to begin with.

4.1 Isolating mRNA from Colgalt2 and Gprin3 cells expressing SOD1-G93A.

When Colgalt2 and Gprin3 mice are crossed to SOD1-G93A, only a loss of LL5b Gprin3 neurons is observed. In order to understand what cell-type specific gene expression changes occur in these two distinct cell types in SOD1-G93A mice, we performed TRAP in our crossed mice. We isolated mRNAs from both healthy and diseased Colgalt2 and Gprin3 cells at two time points: pre-symptom onset ("Pre", ~P70), and post-symptom onset ("Post", ~P110; Figure 4.1). After sequencing immunoprecipitated (IP'ed) mRNAs, we first wanted to confirm that samples in these cohorts were enriched for genes that we knew from previous Colgalt2 and Gprin3 TRAP samples to be cell-type specific. We broadly assessed expression of these cell-type genes using aligned reads visualized in IGV viewer. Colgalt2 disease cohort samples shared expression profiles with benchmark Colgalt2 sample across cell type-specific genes such as Ctip2, Fezf2, Colgalt2, Tmem200a, Fam84b, and Kcng1 (Figure 4.2A). They additionally showed lower levels of expression for astrocyte genes highly expressed in the Aldh1l1 TRAP line. Gprin3 disease cohort samples in turn shared expression profiles for Gprin3 marker such as, Crabp1, Klhl1, Rasgrp2, and Ctip2, and were also depleted for astrocyte markers (Figure 4.2B). Additionally, replicate samples for each cell type were highly correlated with each other in whole genome expression profiles by Pearson correlation (Figure 4.2C). Together, these gene expression patterns

A

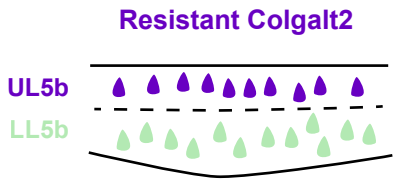

Timepoint	Control sample	Disease sample
"Pre" symptoms ~P70	Colgalt2 WT Pre	Colgalt2 SOD Pre
"Post" symptoms ~P110	Colgalt2 WT Post	Colgalt2 SOD Post

B

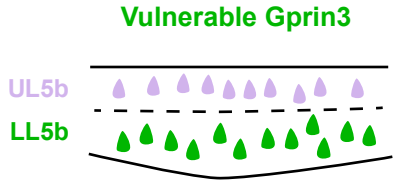

Timepoint	Control sample	Disease sample
"Pre" symptoms ~P70	Gprin3 WT Pre	Gprin3 SOD Pre
"Post" symptoms ~P110	Gprin3 WT Post	Gprin3 SOD Post

Figure 4.1: Summary of all TRAP IP samples from Colgalt2 and Gprin3 ALS cohorts. (A-B) Schematic illustrations showing approximate M1 location of cell types interest for RNA-Seq in the SOD1-G93A model. Accompanying tables indicate what samples were collected and named for each timepoint of healthy (control, WT) and disease (SOD) conditions. (A) The pre-symptomatic "Pre" timepoint (~P70) samples for Colgalt2 cells were named for "Colgalt2 WT Pre" (light grey) and "Colgalt2 SOD Pre" (light blue) for healthy and disease conditions respectively. Symptomatic "Post" timepoint (~P110) samples for Colgalt2 cells were called "Colgalt2 WT Post" (dark grey) and "Colgalt2 SOD Post" (blue) for control and disease conditions respectively. (B) The pre-symptomatic "Pre" timepoint (~P70) samples for Gprin3 cells were called for "Gprin3 WT Pre" (light grey) and "Gprin3 SOD Pre" (light blue) for healthy and disease conditions respectively. Symptomatic "Post" timepoint (~P110) samples for Gprin3 cells were named "Gprin3 WT Post" (dark grey) and "Gprin3 SOD Post" (blue) for control and disease conditions respectively.

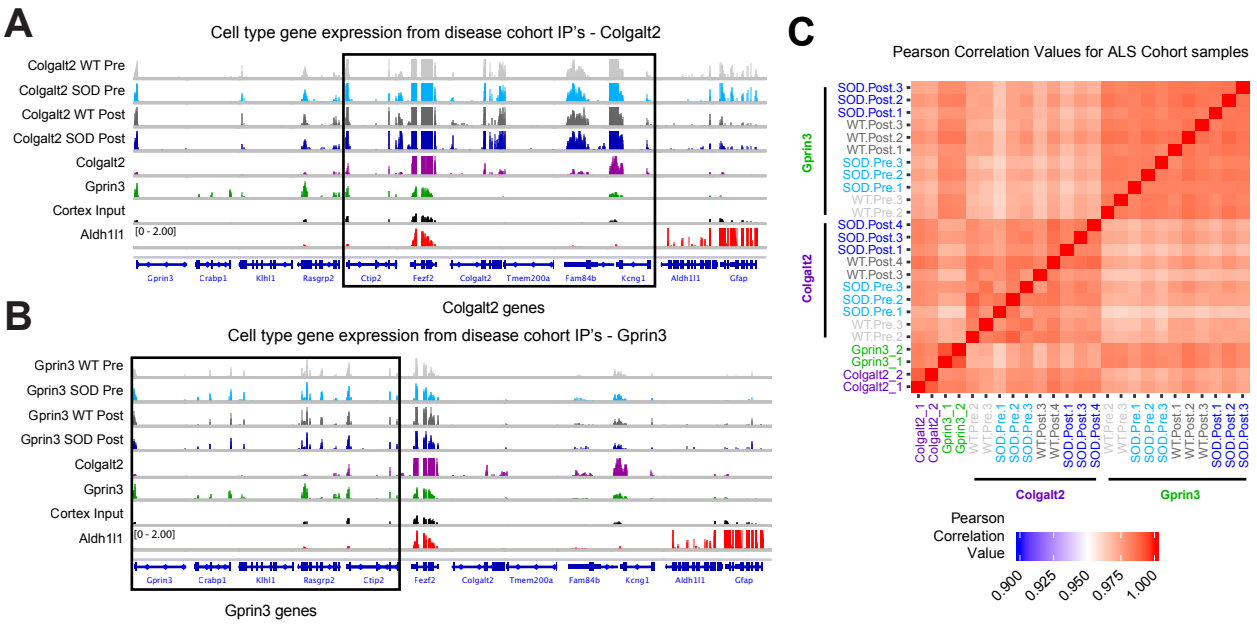

Figure 4.2: Colgalt2 and Gprin3 TRAP IP samples from ALS cohorts show expression of benchmark cell type-specific genes. (A-B) IGV Tracks showing aligned reads from RNA-Seq samples. (A) Colgalt2 WT Pre (light grey), SOD Pre (light blue), WT Post (dark grey), and SOD Post (blue) samples appear to match expression patterns for the selected genes (black box) that are enriched in the benchmark Colgalt2 replicates (purple). Additionally, the cells appear to be depleted for Aldh1l1 astrocyte marker genes relative to the astrocyte cell type (red). Gprin3 benchmark samples (green) and whole cortex input samples (black) are also shown. (B) Gprin3 WT Pre (light grey), SOD Pre (light blue), WT Post (dark grey), and SOD Post (blue) samples appear to match expression patterns for the selected genes (black box) that are enriched in the benchmark Gprin3 samples (green). Additionally, the cells appear to be depleted for astrocyte marker genes relative to the Aldh1l1 astrocyte samples (red). Colgalt2 benchmark samples (purple) and whole cortex input samples (black) are also shown. Biological replicate tracks are overlaid to better show where reads aligned most consistently across replicate samples. (C) Heatmap of Pearson correlation values for different ALS cohort samples, compared to benchmark Colgalt2 and Gprin3 samples (bottom left corner). Replicate samples and samples within cell types appear highly correlated.

indicate that RNA isolations from our populations of interest were successful and could be used for assessment of gene expression changes in disease.

4.2 Pre-symptomatic changes in gene expression in Colgalt2 and Gprin3 cells.

Changes in gene expression that precede cell loss can provide some insight into the mechanisms that lead to the initiation of cell death mechanisms. For this reason, we wanted to determine what changes occur in the degeneration-resistant Colgalt2 and vulnerable Gprin3 populations at the “Pre” disease stage in the SOD1-G93A context. We performed differential expression (DE) analysis between healthy and SOD1-G93A TRAP samples using DESeq2 with default parameters. We found that no gene fold-changes met statistical significance when the Benjamini-Hochberg-adjusted p-values were used to disprove the null hypothesis. For this reason, we opted to use the un-adjusted p-values (determined by Wald test in DESeq2; Love et al., 2014) as a more subjective measure of potential biological significance. This provided us with more genes to interrogate in later analyses and experiments, at the expense of potentially increased Type I, or false positive, error. We generated lists of genes that were up- or down-regulated in SOD1-G93A animals relative to healthy animals at this pre-symptomatic time point (by un-adjusted $p < 0.05$). In Colgalt2 cells, we observed 219 genes that were differentially expressed in SOD1-G93A. 128 genes were up-regulated, with 91 down-regulated (Figure 4.3A). Gene ontology (GO) enrichment analysis was performed using Metascape (Zhou et al., 2019) on these changed genes to determine groups and classes of genes that may be regulated in response to SOD1-G93A

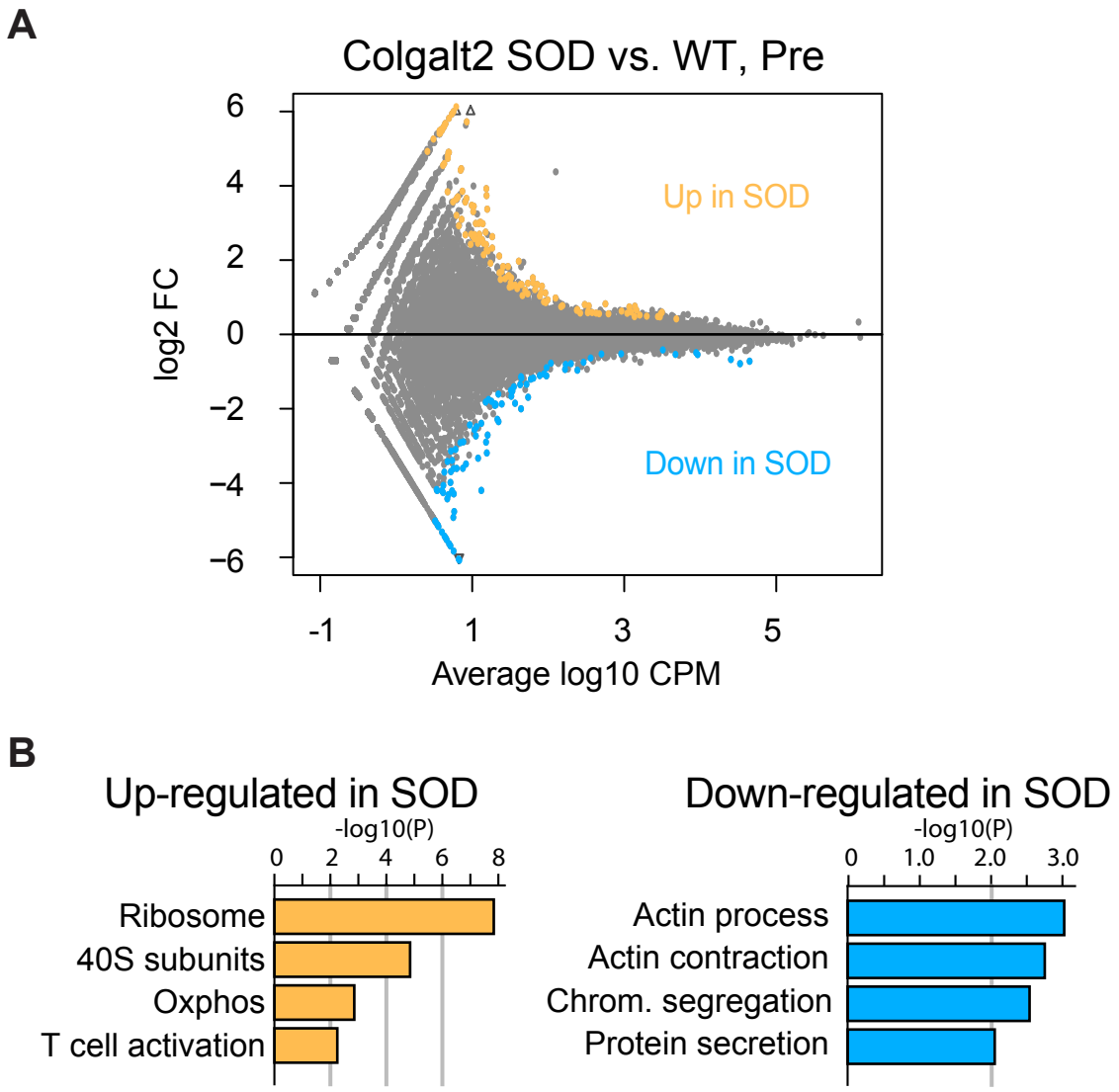

Figure 4.3: Pre-symptomatic Colgalt2 samples reveal early changes in gene expression in UL5b cells in response to SOD1-G93A. (A) MA scatter plot showing all genes plotted by average Log10 counts per million (CPM; x-axis), and Log2 fold change (FC; y-axis) in SOD (n = 2 replicates) relative to WT (n = 3 replicates) by differential expression (DE) analysis. Grey dots represent individual genes, with genes that were significantly (unadjusted p-value < 0.05) up-regulated in SOD colored light orange, and down-regulated colored in light blue. (B) Bar plots show gene ontology (GO) categories of genes that were significantly enriched among the genes that showed significant up- or down- regulation by DE analysis. Categories found in up-regualted genes (left, light orange) were primarily ribosomal. Down-regulated genes (right, light blue) included nucleotide binding genes. Bars represent Log10 p-values from GO enrichment analysis.

expression (Figure 4.3B). P-values for enriched GO categories were calculated by Metascape using the hypergeometric test and Bejamini-Hochberg correction. Ribosomal categories were enriched among up-regulated genes, suggesting that there may be increased translation in Colgalt2 cells during early stages of disease. GO categories enriched among down-regulated genes included cytoskeletal genes, implicating potential early morphological rearrangement in UL5b cells.

At this pre-symptomatic stage, Gprin3 cells showed differential regulation of 140 genes: 61 were up-regulated and 79 were down-regulated with SOD1-G93A expression (Figure 4.4A). GO analysis revealed that categories associated with ion transport were significantly enriched among the genes up-regulated in Gprin3 cells expressing SOD1-G93A (Figure 4.4B). This could indicate early changes in excitability in these cells. To further implicate this mechanism, the ion transport category was also enriched among down-regulated Gprin3 genes at this early time point. Early changes in gene expression could underlie later stage disease mechanisms, but how the changes that we observe here affect disease progression is something that needs to be further investigated.

4.3 Symptomatic changes in gene expression in Colgalt2 and Gprin3 cells reveal opposing molecular responses to SOD1-G93A expression.

To elucidate mechanisms that are differentially regulated during symptomatic stages of disease, we performed differential gene expression analysis between WT and SOD1-G93A at “Post” stage, for both Colgalt2 and Gprin3. Because Colgalt2 cells are resistant to degeneration, changes in gene expression in these cells may reveal

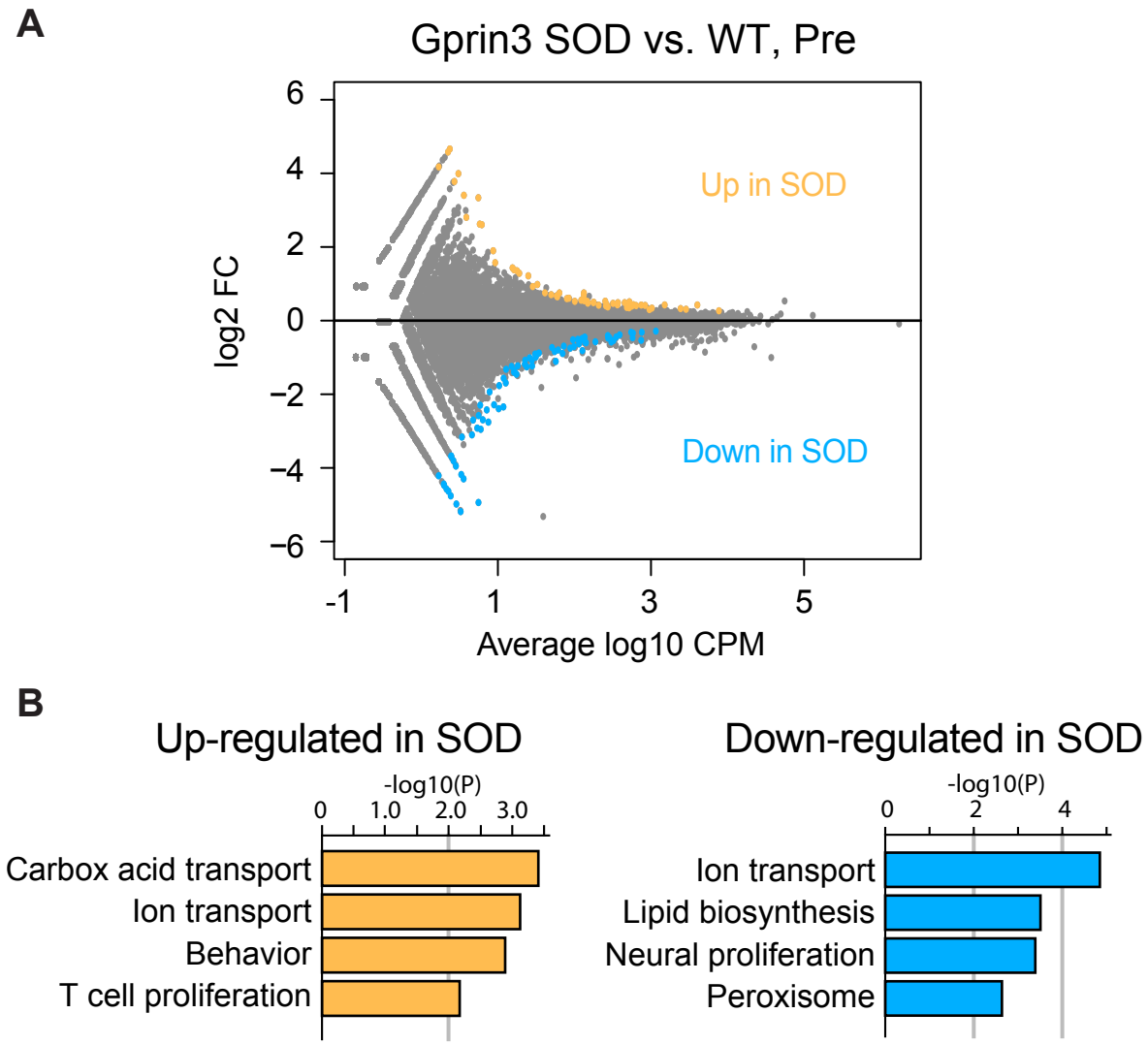

Figure 4.4: Pre-symptomatic Gprin3 samples reveal early changes in gene expression in LL5b cells in response to SOD1-G93A. (A) MA scatter plot showing all genes plotted by average Log10 counts per million (CPM; x-axis), and Log2 fold change (FC; y-axis) in SOD (n = 3 replicates) relative to WT (n = 2 replicates) by differential expression (DE) analysis. Grey dots represent individual genes, with genes that were significantly (unadjusted p-value < 0.05) up-regulated in SOD colored light orange, and down-regulated colored in light blue. (B) Bar plots show gene ontology (GO) categories of genes that were significantly enriched among the genes that showed significant up- or down- regulation by DE analysis. Categories found in up-regualted genes (left, light orange) included transcription-associated genes. Down-regulated genes (right, light blue) included zinc-finger transcription factors. Bars represent Log10 p-values from GO enrichment analysis.

molecular strategies for successfully coping with mutant SOD1 expression. In Colgalt2 cells, many more genes were significantly regulated (un-adjusted $p < 0.05$) between WT and SOD1-G93A at this stage compared to the “Pre” stage. 1076 showed significant changes in gene expression in SOD: 628 showing an up-regulation and 448 showing a down-regulation. For GO analysis, we selected genes that had a mean Log10 CPM expression value ≥ 2.5 to limit analysis to highly expressed genes whose modulation may have more functional consequence to the cells (Figure 4.5A). GO categories that were enriched in up-regulated genes were associated with oxidative phosphorylation (Oxphos) and translation (Figure 4.5B). The Oxphos gene category included Atp5l, Ndufa4, and Cox6b1, from separate components of the electron transport chain (ETC). Categories that were enriched among down-regulated genes in Colgalt2 cells at “Post” stage appeared to primarily be associated with maintaining DNA integrity. Together, these patterns suggest that Colgalt2 cells may be increasing their levels of respiration while dampening a response to DNA damage and transcription. To understand whether these changes were specific to resistant Colgalt2 cells, we assessed whether the genes that showed significant up- or down-regulation in Colgalt2 cells were similarly changed in Gprin3. We compared the directionality of WT vs. SOD LogFCs for these genes between the two cell types (Figure 4.5C). Very few of the genes that were significantly changed in Colgalt2 cells were similarly modulated in Gprin3 cells, with many genes even showing an opposing change in these cells. This finding suggests that the gene expression changes occurring in Colgalt2 cells at the symptomatic stage are specific to this resistant UL5b population.

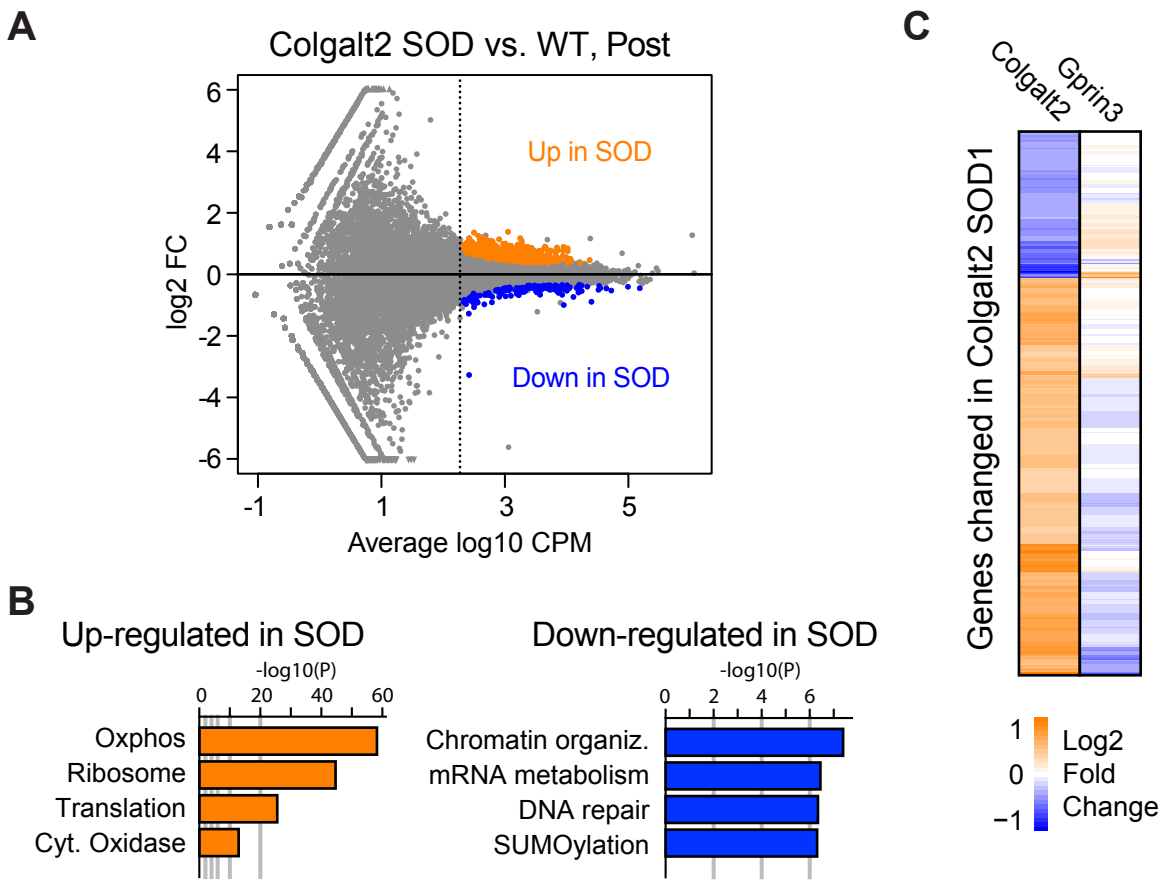

Figure 4.5: Symptomatic Colgalt2 samples reveal late changes in gene expression in resistant UL5b cells in response to SOD1-G93A. (A) MA scatter plot showing all genes plotted by average Log10 counts per million (CPM; x-axis), and Log2 fold change (FC; y-axis) in SOD (n = 3 replicates) relative to WT (n = 2 replicates) by differential expression (DE) analysis. Grey dots represent individual genes, with genes that were highly expressed (CPM > 2.5) and significantly (unadjusted p-value < 0.05) up-regulated in SOD colored dark orange, and down-regulated colored in blue. (B) Bar plots show gene ontology (GO) categories of genes that were significantly enriched among the genes that showed significant up- or down- regulation by DE analysis. Categories found in up-regualted genes (left, dark orange) included ribosomal and mitochondrial genes. Down-regulated genes (right, blue) included DNA-associated genes. Bars represent Log10 p-values from GO enrichment analysis. (C) Heatmap shows the fold-change values of genes that showed significant change in disease in Colgalt2 cells, juxtaposed with the fold-change values for the same genes from DE analysis in Gprin3 cells. Genes changed in disease in Colgalt2 cells did not generally show the same directionality or magnitude of change in Gprin3 cells in SOD, suggesting contrasting changes in response to SOD1-G93A between Colgalt2 and Gprin3 cells.

Gprin3 cells showed 620 significantly (un-adjusted $p < 0.05$) regulated genes in disease: 381 up-regulated and 239 down-regulated genes. For performing GO analysis, we once again selected genes that showed base mean Log10 CPM of ≥ 2.5, to enrich for highly expressed genes (Figure 4.6A). GO categories enriched for up-regulated genes in Gprin3 cells were primarily centered around neuronal functions and behavior (Figure 4.6B). Surprisingly, and in contrast to Colgalt2 cells, one of the categories that appeared enriched among down-regulated genes in Gprin3 cells was the Oxphos category, which included Cox5b, Ndufc1, and Atp5e. Again, to determine the cell-type specificity of these changes, we compared the LogFC directionality of significantly changed genes from Gprin3 cells to LogFCs from "Post" DE in Colgalt2 cells. We found that genes changed in "Post" Gprin3 cells rarely showed the same directionality of change in Colgalt2 cells in disease (Figure 4.6C), suggesting that the changes observed in Gprin3 cells are specific to this vulnerable LL5b cell type. A down-regulation of Oxphos genes in Gprin3 cells at this disease time point, contrasting the up-regulation of the same class of genes in Colgalt2, additionally suggests that depending on the directionality, modulating respiration during disease may have different consequences to cell survival.

4.4 Oxidative phosphorylation genes are differentially regulated in SOD1-G93A between Colgalt2 and Gprin3 cells.

Oxphos genes appeared to be up-regulated in Colgalt2 cells and down-regulated genes in Gprin3 cells by TRAP at a symptomatic time point, so we wanted to determine

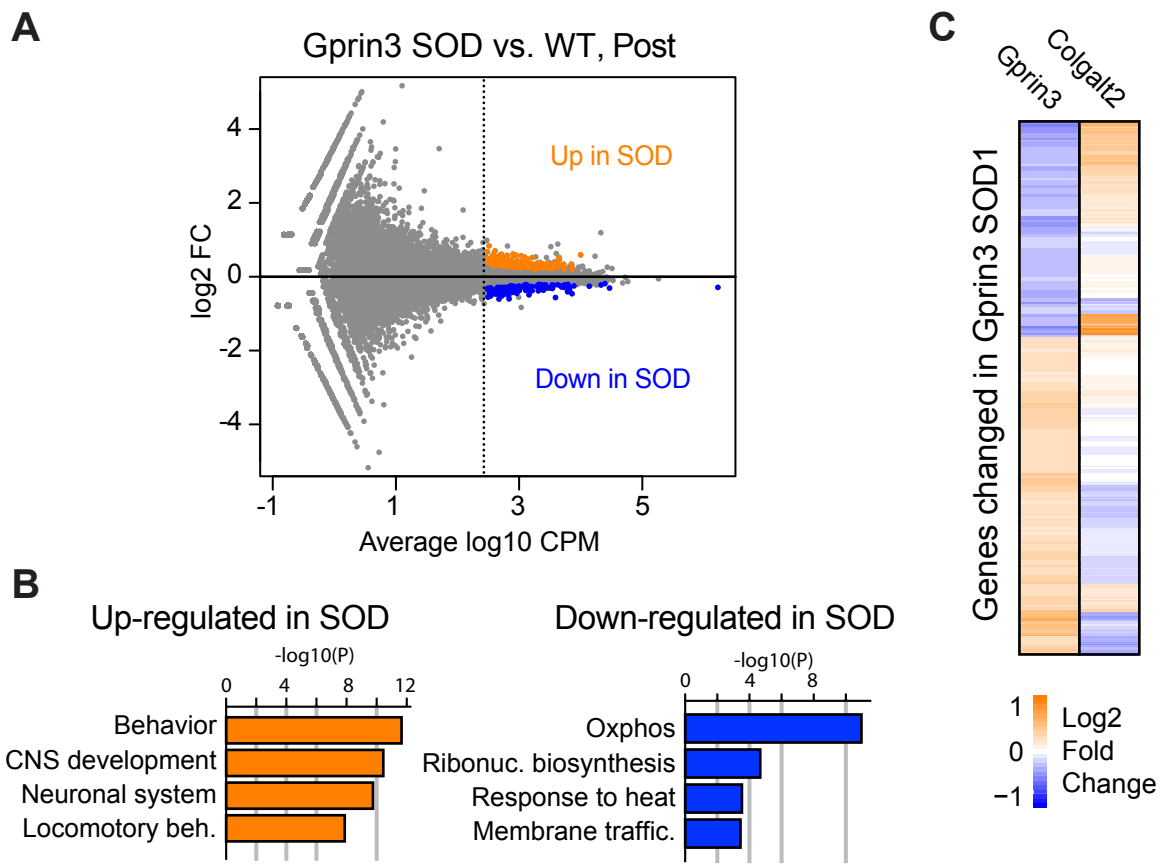

Figure 4.6: Symptomatic Gprin3 samples reveal late changes in gene expression in vulnerable LL5b cells in response to SOD1-G93A. (A) MA scatter plot showing all genes plotted by average Log10 counts per million (CPM; x-axis), and Log2 fold change (FC; y-axis) in SOD (n = 3 replicates) relative to WT (n = 3 replicates) by differential expression (DE) analysis. Grey dots represent individual genes, with genes that were highly expressed (CPM > 2.5) and significantly (unadjusted p-value < 0.05) up-regulated in SOD colored dark orange, and down-regulated colored in blue. (B) Bar plots show gene ontology (GO) categories of genes that were significantly enriched among the genes that showed significant up- or down- regulation by DE analysis. Categories found in up-regualted genes (left, dark orange) were of varying subcellular association. Down-regulated genes (right, blue) notably included mitochondrial genes. Bars represent Log10 p-values from GO enrichment analysis. (C) Heatmap shows the fold-change values of genes that showed significant change in disease in Gprin3 cells, juxtaposed with the fold-change values for the same genes from DE analysis in Colgalt2 cells. Genes changed in disease in Gprin3 cells did not generally show the same directionality or magnitude of change in Colgalt2 cells in SOD, once again suggesting contrasting changes in response to SOD1-G93A between the two cell types.

if these changes reflected a broader change in whole mitochondrial gene expression. We plotted individual LogFCs from “Pre” and “Post” disease DE in Colgalt2 and Gprin3 cells for different functional classes of mitochondrial genes, such as citric acid cycle (TCA) genes and antioxidant genes (Figure 4.7A). In Colgalt2 cells, Oxphos genes showed a particularly high proportion of significantly changed genes for “Post” stage DE, though most functional groups of mitochondrial genes appeared to skew towards up-regulated. And while fewer genes were significantly changed in Gprin3 cells at the “Post” time point, there were several significantly changed genes in the Oxphos category, with the median LogFC (black bar) for Oxphos genes indicating a general down-regulation of this category (Figure 4.7B).

We next validated these TRAP findings by performing qPCR on a subset of representative mitochondrial genes from Colgalt2 and Gprin3 ALS cohort cDNA libraries. Assayed genes were chosen from differentially expressed genes from either Colgalt2 or Gprin3 disease DE to represent either a subunit of the ETC, or a particular functional pathway. We quantified differences in the expression of these genes between conditions using the comparative cycle time (CT) method (ddCT) normalizing to Actb and Gapdh expression in each condition. P-values were calculated by two-tailed t-test on dCT replicate values between WT and SOD conditions. Colgalt2 cells showed an increased level of mitochondrial transcripts in disease relative to WT across many of the mitochondrial genes tested, especially at the “Post” disease time point (Figure 4.8A), although most of these differences were not significant. Gprin3 cells showed a slightly decreased level of Oxphos gene transcripts at “Post” between disease and WT (Figure

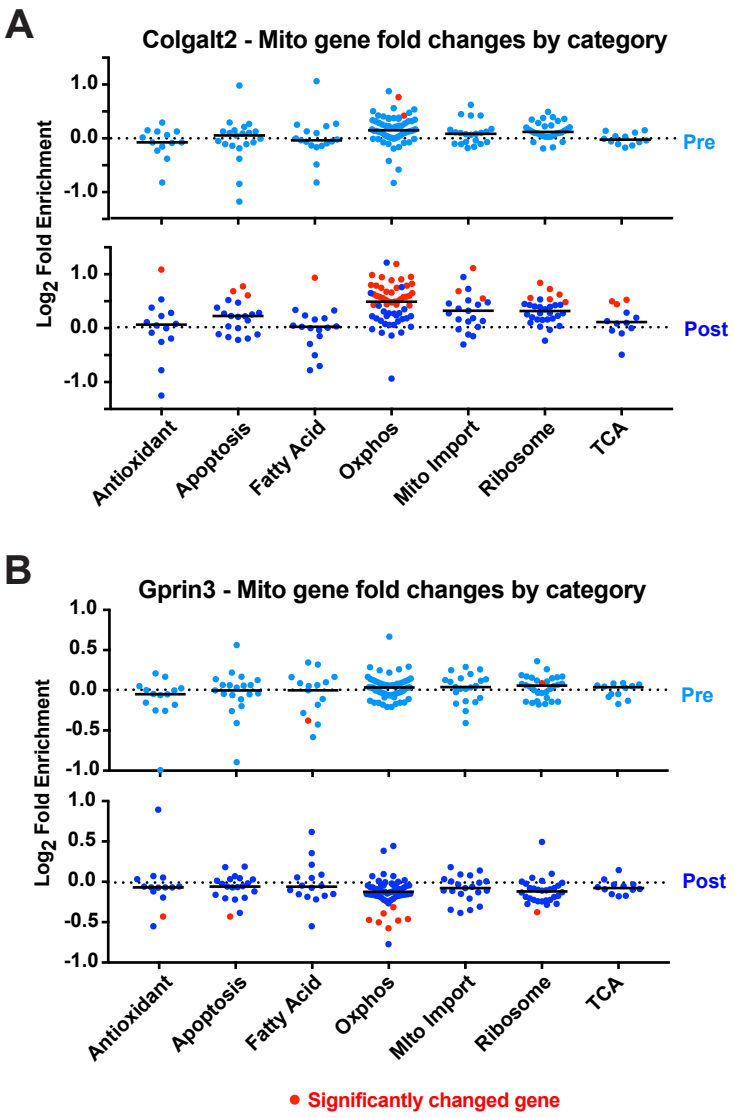

Figure 4.7: Between Colgalt2 and Gprin3 cells, mitochondrial genes show contrasting changes in gene expression in response to SOD1-G93A. (A-B) Scatterplots showing the Log2 fold-change in SOD relative to WT by RNA-Seq DE analysis for different functional categories of mitochondrial genes. Plots are shown for "Pre" DE fold-changes (light blue, upper panel) and "Post" DE fold-changes (blue, lower panel). Genes that showed a significant change (unadjusted p-value < 0.05) are colored in red. (A) Log2 fold-change scatterplots show that Oxphos genes are up-regulated in Colgalt2 cells during disease progression, along with mitochondrial genes from other functional groups. (B) Log2 fold-change scatterplots reveal that, in contrast to Colgalt2 cells, several Oxphos genes are down-regulated in symptomatic Gprin3 cells. A small subset of other mitochondrial genes also show down-regulation at this disease stage. Black bars indicate median values for each category.

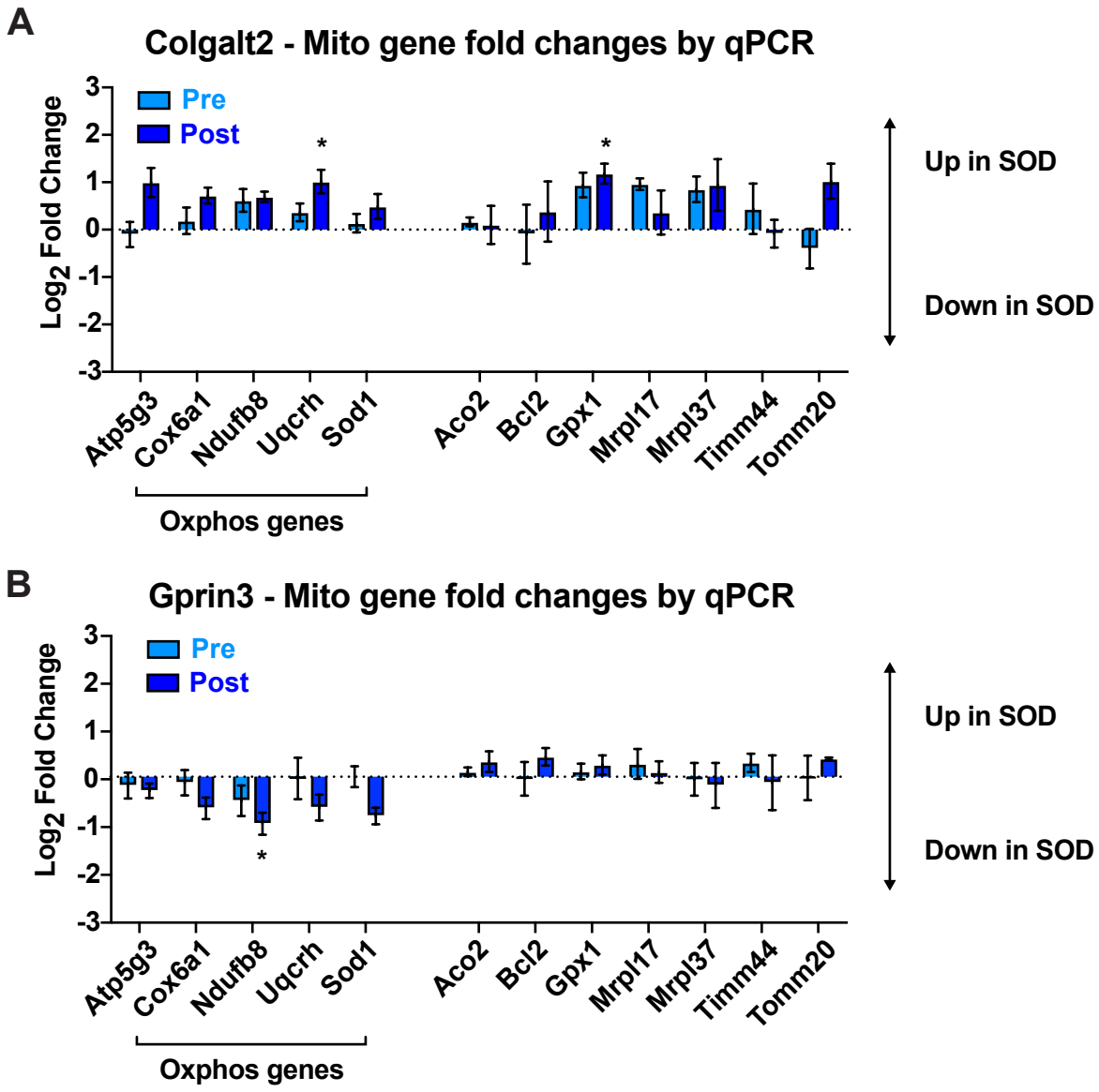

Figure 4.8: qPCR for mitochondrial genes confirm contrasting changes in gene expression for disease Colgalt2 and Gprin3 cells. (A-B) Colgalt2 and Gprin3 qPCR Log2 fold-change data for different mitochondrial genes at "Pre" (light blue bars) and "Post" (blue) stages. Values were calculated by ddCT between SOD and WT. Actb and Gapdh were used as housekeeping gene controls (bars show mean ± SEM). (A) In Colgalt2 cells, genes associated with Oxphos (left) and appear to be increased in expression in SOD relative to WT. Other mitochondrial genes (right) also appear to be up-regulated in SOD. (B) In Gprin3 cells, Oxphos genes appear to be down-regulated in SOD samples at the "Post" disease stage, while other mitochondrial genes don't appear to change (* $p < 0.05$ by two-tailed t-test of dCT values).

4.8B), but did not show similar decreases for other non-Oxphos mitochondrial genes. Again, the majority of these differences were not statistically significant. These data partly confirm the changes in Oxphos gene expression that we observed by TRAP, and indicate that among all functional groups of mitochondrial genes, Oxphos genes appear to be the most strongly targeted for gene expression modulation, particularly in the vulnerable LL5b population.

4.5 Oxphos genes that show expression changes in SOD1-G93A are differentially expressed between healthy Colgalt2 and Gprin3 cells.

Because we observed contrasting regulation of Oxphos genes in Colgalt2 and Gprin3 cells during disease, we wanted to understand how the baseline expression levels of these genes in healthy Colgalt2 and Gprin3 cells may contribute or predispose to the changes we observe during disease. We first plotted the Log2 fold-enrichment from Gprin3 vs. Colgalt2 TRAP DE for the different functional groups of mitochondrial genes (Figure 4.9A). Consistent with the GO analysis discussed previously (Chapter 2), many of the functional categories of mitochondrial genes, including Oxphos, showed genes that were enriched in Gprin3 cells. To confirm these TRAP results, we performed qPCR on Colgalt2 and Gprin3 cDNA libraries, for a representative subset of mitochondrial genes (Figure 4.9B). P-values were calculated from dCT values using two-tailed t-test. Oxphos genes appeared to be enriched in Gprin3 cells over Colgalt2 cells, anywhere between 1-fold and 3-fold (log2), although only Atp5g3 and Sod1 showed statistical significance. Other mitochondrial genes did not show similar levels of

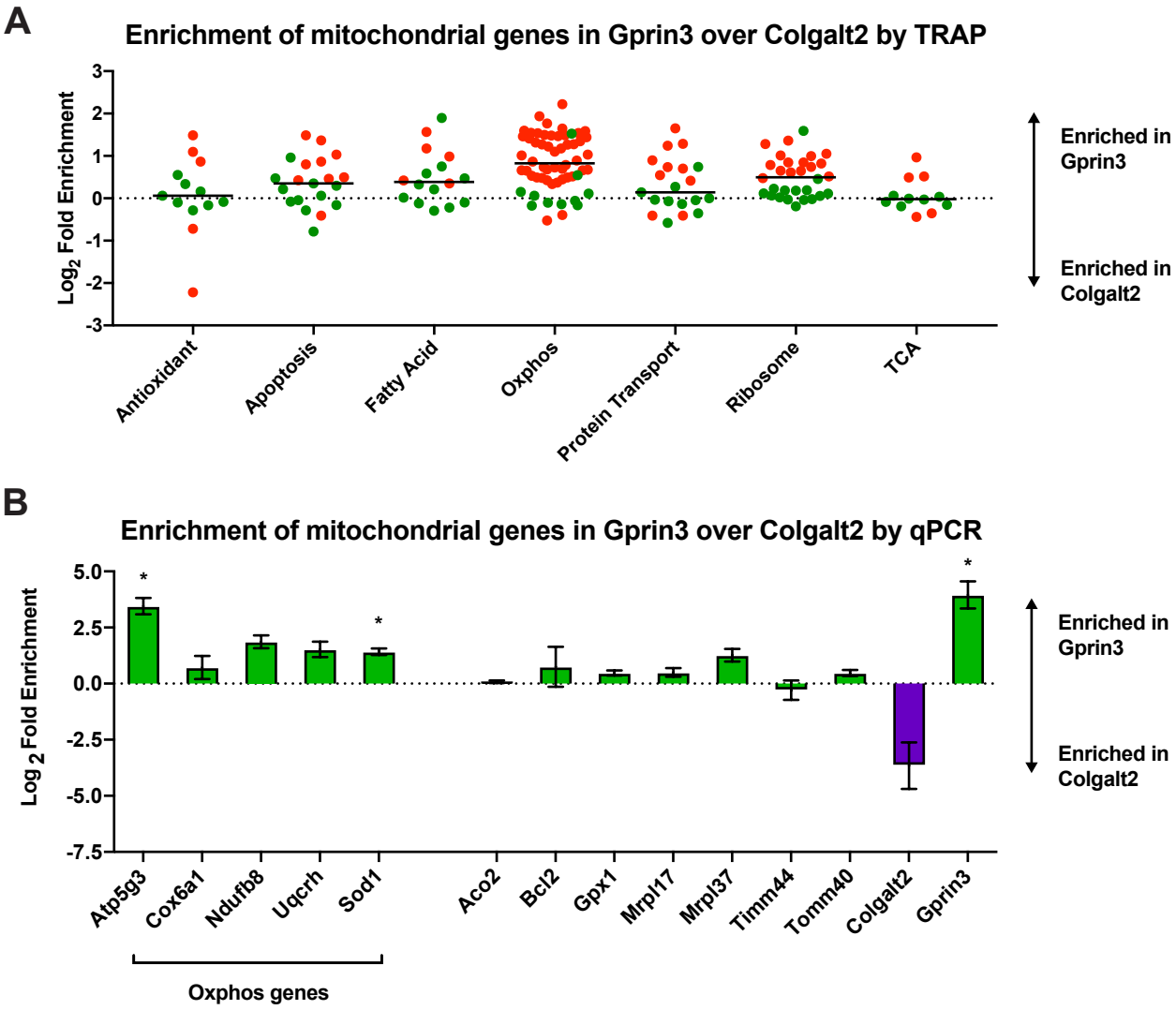

Figure 4.9: Mitochondrial genes, including Oxphos genes, are enriched in Gprin3 cells relative to Colgalt2 cells. (A) Scatterplots showing Log2 fold-enrichment from Gprin3 vs. Colgalt2 DE for different functional groups of mitochondrial genes. Individual green dots represent single genes. Red dots indicate genes that were significantly enriched. (B) Bar graph shows the Log2 fold-enrichment of different mitochondrial genes in Gprin3 cells relative to Colgalt2 cells by qPCR. Enrichment was calculated by ddCT, using Actb and Gapdh as housekeeping gene controls. Genes associated with Oxphos (shown on the left) appear to be enriched in Gprin3 cells (green bars). Other mitochondrial genes do not consistently show the same level of enrichment in Gprin3 cells, however. Purple bar shows where genes were enriched in Colgalt2 cells (bars show mean ± SEM; * $p < 0.05$ by two-tailed t-test of dCT values).

enrichment between the two cell types. These findings leave open the question of how underlying differences in mitochondrial gene expression may contribute to selective vulnerability to mutant SOD1, an enzyme closely tied to mitochondrial function. Experiments to address the functional connection between levels of mitochondrial gene expression and mitochondrial biology in these neurons, particularly in the context of SOD1-G93A, should be carried out to answer this question.

4.6 A respiratory transcription factor is differentially expressed between Colgalt2 and Gprin3 neurons.

We next wanted understand how the genes that are up- or down-regulated in disease may be modulated by upstream transcriptional regulation mechanisms. We performed HOMER TF Motif analysis, which searches the sequences found upstream of a set of genes of interest to determine if they share any TF binding motifs, and by extension, regulatory TFs. We performed this analysis on the cohort of genes that were significantly changed in “Post” disease in our two cell types. These analyses revealed several canonical TF binding motifs for these genes (Figure 4.10A). To understand how these TFs may contribute to the cell-type specific disease changes that we observe, we then set out to determine whether the TFs associated with these motifs showed differential expression between healthy Colgalt2 and Gprin3 cells. TFs for further analysis were selected if their associated motif was enriched in a statistically significant way ($p < 0.05$) in motif analysis above. We assessed relative expression values (z-scores) for these TFs between healthy Colgalt2 and Gprin3 cells, and observed that

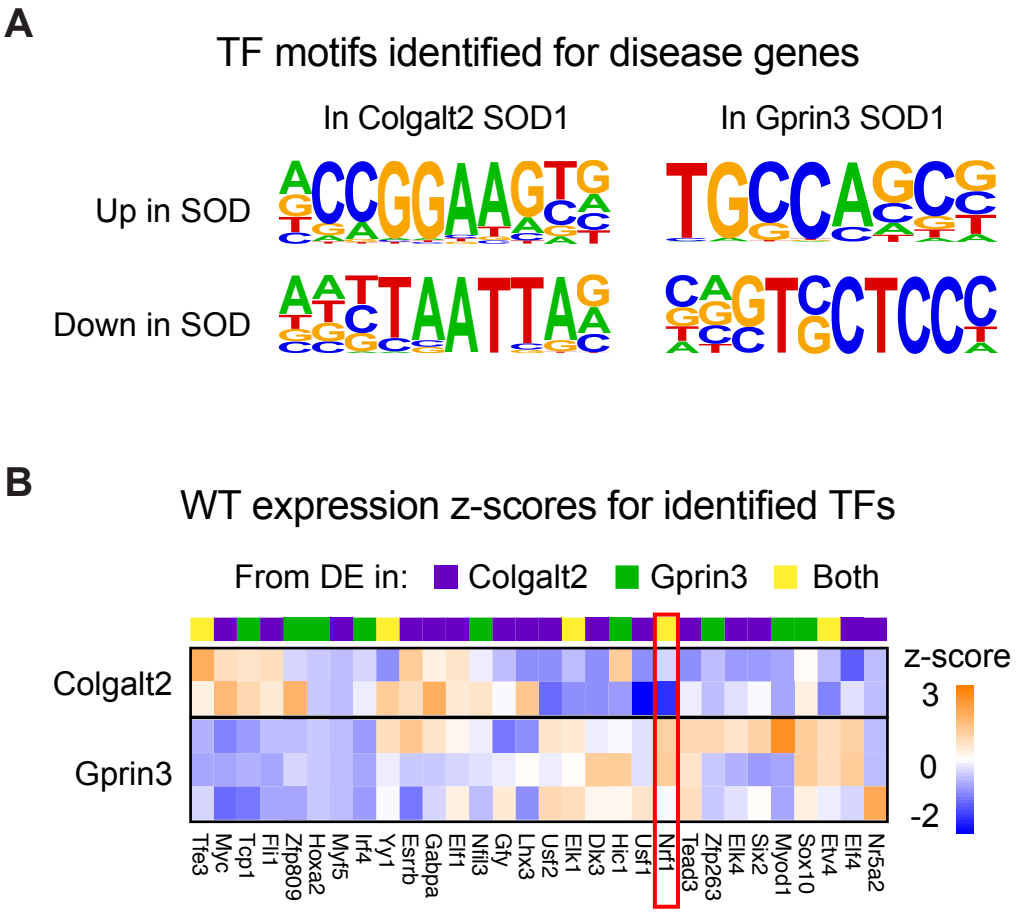

Figure 4.10: Transcription factor motif analysis reveals motifs and factors associated with genes that change in disease. (A) Examples of HOMER transcription factor (TF) motifs that were enriched among the genes that were up- (bottom row) or down-regulated (top row) during “Post” disease stage in Colgalt2 cells (left column) and Gprin3 cells (right column). (B) Heatmap showing z-scores of Colgalt2 and Gprin3 WT Pre relative gene expression values of TFs that were enriched by HOMER TF motif enrichment analysis. Several TFs appear to be differentially expressed between Colgalt2 and Gprin3 cells at this age. Of note, Nrf1, a TF that is key to mitochondrial biogenesis appears to be expressed more highly in Gprin3 cells. Annotation above the heatmap indicates whether the TF motif came from Colgalt2 disease genes (purple), Gprin3 disease genes (green), or was seen in both (yellow).

many of these TFs show differential levels of expression between these two cell types (Figure 4.10B). Notably, Nuclear Respiration Factor 1 (Nrf1), a TF important in the regulation of expression of genes associated with ETC and Oxphos, showed higher levels of expression in Gprin3 cells relative to Colgalt2 cells. These TF motif analyses suggest that distinct changes in gene expression may be influenced by differential expression of upstream factors across these two cell types, but more data are needed to understand whether there is a causal link between these two findings.

4.7 Discussion

The mutations that cause neurodegenerative disease are often found on genes that are ubiquitously expressed, but death is typically only observed for specific cell types. For many neurodegenerative diseases, it is not known how these mutations trigger the cell-type specific molecular responses that inevitably lead to death. Our Colgalt2 and Gprin3 lines present us with a unique opportunity to understand how the SOD1-G93A mutation molecularly affects two related but distinct L5b cell types, where one shows vulnerability and the other resistance to degeneration in this model. Through TRAP and RNA-Seq, we show that two distinct populations of L5b cells regulate the expression of different classes of genes in the SOD1-G93A ALS model. In particular, it appears that these two cell types differentially regulate Oxphos gene expression (Figure 4.11). The resistant UL5b Colgalt2 population shows an up-regulation of Oxphos genes, while the vulnerable LL5b Gprin3 population shows a down-regulation of these genes. Our analyses additionally reveal that in a WT condition, the vulnerable LL5b neurons

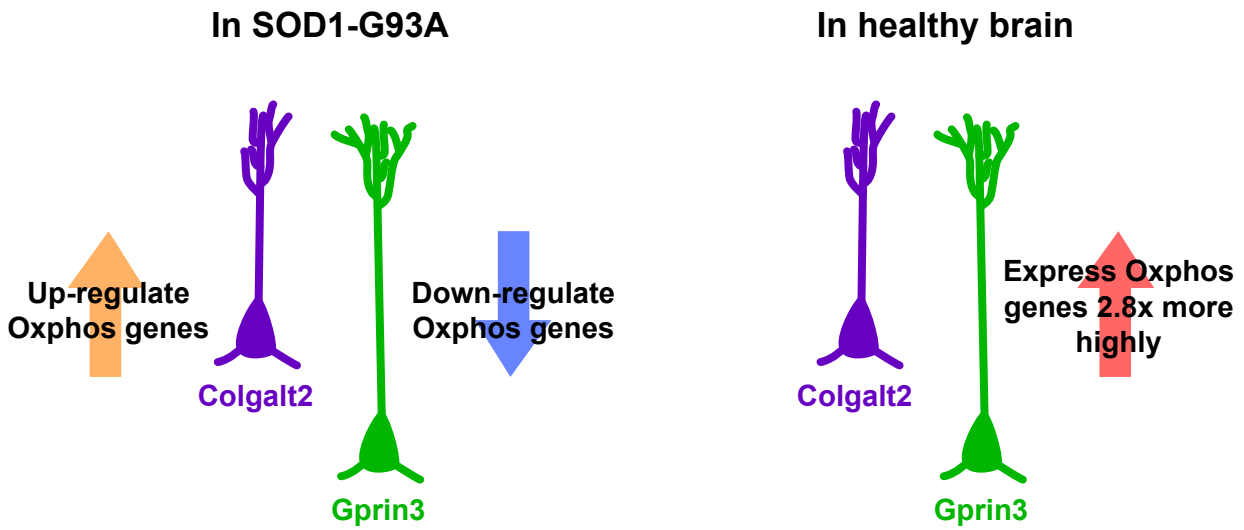

Figure 4.11: Summary of TRAP and RNA-Seq findings from SOD1-G93A Colgalt2-TRAP and Gprin3-TRAP animals. Colgalt2 cells (purple) up-regulate Oxphos gene expression at a symptomatic stage of disease (left panel), while Gprin3 cells (green) appear to instead down-regulate Oxphos genes at this stage. In healthy brains, Gprin3 cells show ~2.8x higher levels of Oxphos gene expression than Colgalt2 cells

express Oxphos genes at higher levels than the closely-related resistant UL5b cell type, suggesting that there may be underlying differences in the levels of energetic demand of these cells, and that perhaps these differences contribute to differential sensitivity to SOD1-G93A overexpression.

Mitochondrial dysfunction has been observed for many neurodegenerative diseases and their models (see Lin and Beal, 2006). In fact, changes in mitochondrial fission and fusion, as well as mitophagy are hallmarks of many neurodegenerative diseases (Bossy-Wetzel et al., 2003; Burté et al., 2015; Chen and Chan, 2009; Itoh et al., 2013; Knott et al., 2008). In models of ALS, many phenotypes associated with mitochondrial structure or function have been reported (Lopez-Gonzalez et al., 2016; Lu et al., 2012; Mattiazzi et al., 2002; Menzies et al., 2002; Vehviläinen et al., 2014). By gene expression analysis, changes in Oxphos gene expression can also be observed in disease (Bandyopadhyay et al., 2013; Olsen et al., 2002), which may manifest as changes in the protein composition of mitochondria in cells (Li et al., 2010). Additionally, a decrease in ETC enzyme activity can be observed in the spinal cord of human ALS patients (Borthwick et al., 1999; Wiedemann et al., 2002). However, many ETC and Oxphos genes are expressed throughout the body, leaving open the question of how a ubiquitously expressed disease mutation can cause cell type-specific mitochondrial dysfunction, and how cell-type specific features may affect the levels of gene expression for key cell biological pathways.

Regulation of mitochondrial gene expression is influenced by many different functional signaling pathways in the cell. A principal effector of these signals is Pgc1a,

and the nuclear respiratory factors Nrf1 and Nrf2, which directly bind the promoters of metabolic genes to increase their expression (Scarpulla, 2011; Virbasius et al., 1993a; 1993b; Wu et al., 1999). Homeostatic sensing mechanisms regulate the activation of these factors in an effort to maintain the levels of ATP production necessary for proper cellular functions. For neurons, this energetic tuning, as well as mitochondrial Ca2+ buffering, is essential for carrying out neuronal functions such as pre- and post-synaptic signaling, axon transport, and action potential propagation (Kann and Kovács, 2007; Zenisek and Matthews, 2000). SOD1-G93A overexpression is thought to cause many disruptions in neuronal function (see Geevasinga et al., 2016; Ilieva et al., 2009), but it is not known whether mitochondrial dysfunction is a direct result of mutant insult or indirectly caused by other disease pathologies. It is similarly not understood how the changes in mitochondrial gene expression commonly observed in neurodegenerative diseases lead to death or survival of cells. In our case, the resistant Colglat2 cells showed a striking up-regulation of Oxphos genes in disease. It is not clear whether this change represents a successful coping strategy for SOD1-G93A overexpression, or if it reflects a response to other cellular dysfunctions not measured here. It is likewise not clear whether a down-regulation of Oxphos genes in vulnerable Gprin3 cells is causal to death or merely a hallmark of general dysfunction caused by SOD1-G93A. Testing the causal relationship between mitochondrial gene expression changes and cellular pathologies would not be trivial, as regulating the abundance, localization, or function of an entire organelle requires very careful control over the many cellular mechanisms and factors, such as Pgc1a and Nrf1, that modulate its features. It is nevertheless essential

that this relationship be studied carefully to understand what role mitochondria play in cell-type specific vulnerability in disease.

Our data additionally reveal that in the healthy brain, there appear to be underlying differences in mitochondrial gene expression between L5b cells. It is not known how different cellular properties and features influence the relative levels of mitochondrial gene expression that may differ from neuron type to neuron type. More specifically, why does a LL5b neuron express Oxphos genes at higher levels than an UL5b neuron? One possible explanation for this takes into consideration a difference in cell size due to differing lengths of axonal projections. Additional collaterals to long-range targets, such as the spinal cord, could require more ATP for active transport across their lengths. Another possible explanation considers that different neuron types within a region of cortex display different levels and patterns of activity as they process afferent input. This is dependent on the amount and type of signals they receive, as well the levels of downstream activity- ie. action potentials- they have to produce. In order to maintain active signaling in the neuron, levels of ATP and Ca2+ must be tightly regulated, in part by mitochondria (Kann and Kovács, 2007). But in order to understand the causal link between cellular function and dysfunction in the cell and changes in mitochondrial gene expression, the general neuronal properties listed above would need to be perturbed in a tightly regulated manner. For instance, if levels of Oxphos gene expression could be up- or down-regulated in our two cell types, we could begin to understand the effects of changes in mitochondrial gene expression on the regulation of cellular energetics.

One caveat to note from the TRAP findings of this study is that while we do observe many changes in gene expression due expression of mutant SOD1, we were surprised to find no changes in previously reported ER stress, unfolded protein response, or cell death gene expression in our datasets, across any time point we assayed. It is possible that these cellular mechanisms are activated in an extremely transient manner, and would require us to perform RNA-Seq with greater temporal resolution during disease progression. For the Gprin3 population, however, we additionally observe fewer changes in gene expression between SOD1 and WT overall. This may also be in part due to the heterogeneous timing of disease progression that we observe anatomically, where more posterior Gprin3 cells appear to be lost first in the disease. In a scenario where posterior Gprin3 cells are mixed with anterior Gprin3 cells when isolating RNA, the more advanced disease mechanisms would be diluted by the earlier responses, minimizing the appearance of both in the dataset. These molecular experiments should perhaps be repeated with a more careful anterior-posterior anatomical dissection for cellular isolation to assay the distinct “stages” of disease that may be occurring across the global Gprin3 population. Nevertheless, the Oxphos gene expression changes that we observe in the global populations of Colgalt2 and Gprin3 cells are robust, and present an avenue for further biological assessment in ALS.

CHAPTER 5:

Visualizing and modulating mitochondrial structure and function in the context of SOD1-G93A

Mitochondrial structure and function are regulated by many different cellular mechanisms (Boldogh and Pon, 2006; Jeyaraju et al., 2009; Scarpulla, 2011; Vander Heiden et al., 1997). Mitochondrial fission, fusion (Cagalinec et al., 2013), trafficking (Mironov, 2006), and energetic homeostasis (Kann and Kovács, 2007) are additionally influenced by many of the properties and functions of a neuron. Processes such as synaptic signaling, axon potential propagation, and membrane potential maintenance (Attwell and Laughlin, 2001; MacAskill and Kittler, 2010; Miller and Sheetz, 2004; Mironov, 2009) require a substantial amount of energy to carry out. Mitochondrial dysfunctions can in turn be found downstream of many cellular pathologies (Budd and Nicholls, 1996; Rainbolt et al., 2014), and in fact are often observed in neurodegenerative diseases (see Bossy-Wetzel et al., 2003; Chen and Chan, 2009; Cozzolino et al., 2013; Knott et al., 2008; Lin and Beal, 2006; Moreira et al., 2010). In ALS and its models, changes decreases in ETC complex activity (Borthwick et al., 1999; Wiedemann et al., 2002), mitochondrial vacuolization (Dal Canto and Gurney, 1995; Kong and Xu, 1998; Wong et al., 1995), and dysregulated structural dynamics (Magrané et al., 2009; Song et al., 2013) are often observed (see also Lopez-Gonzalez et al., 2016; Lu et al., 2012; Mattiazzi et al., 2002; Menzies et al., 2002; Vehviläinen et al., 2014). But the cell-type specificity of dysfunctional regulation of mitochondrial structure

and function in this disease has not been thoroughly assessed. For the SOD1-G93A ALS model, elucidating cell-type specific changes to mitochondria is of particular interest because of SOD1's antioxidant role in clearing reactive oxygen species generated during ETC (McCord and Fridovich, 1969; Okado-Matsumoto and Fridovich, 2001), and because many of the dysfunctions observed for mutant SOD1, such as oxidative stress (Beal et al., 1997; Casoni et al., 2005; Estévez et al., 1999) and protein aggregation (Bruijn et al., 1997b; 1998; Watanabe et al., 2001) can have consequences to mitochondrial function (Cole et al., 2010; Salehi et al., 2015). In our studies, despite SOD1 ubiquitous expression, we observed contrasting changes in mitochondrial gene expression across disease-vulnerable LL5b Gprin3 and disease-resistant UL5b Colgalt2 cells when SOD1-G93A is expressed in the animal (Chapter 4). In Colgalt2 cells, at a symptomatic stage of disease, Oxphos gene expression increased relative to a healthy age-matched control. In vulnerable Gprin3 cells, we detected a decrease in the level of Oxphos gene expression that contrasted the change in Colgalt2 cells. When we assessed the levels of mitochondrial gene expression between Colgalt2 and Gprin3 cells in healthy animals, we determined that Gprin3 cells are enriched for Oxphos genes relative to Colgalt2 cells, indicating that these cell types enter into a disease context with differing levels of expression of respiration genes to begin with.

In order to more precisely understand how levels of mitochondrial gene expression and expression of SOD1-G93A affect the structure and function of mitochondria, we set out to characterize mitochondrial morphology in a cell-type specific manner in L5b cells across both healthy and ALS animals. Additionally, we attempted to modulate levels of

Oxphos to determine the causal relationship between levels of Oxphos gene expression and disease progression in our cell types.

5.1 Mitochondria of upper and lower L5b cells occupy similar volumes in the soma.

In order to understand how UL5b and LL5b cell types differ in their mitochondrial composition, we set out to visualize the mitochondria in these cells in a cell-type specific manner. We chose to virally target expression of a mitochondrial reporter to L5b cells that express Cre-recombinase in the Gng7-Cre KH67 mouse line. To accomplish this, we cloned the coding region for an EGFP construct with an N-terminal mitochondrial localization signal (MitoGFP, Addgene plasmid #50057; Sancak et al., 2013) into a pAAV plasmid that contained DIO Lox sites (Figure 5.1B). We packaged the construct into rAAV2/9 for neuronal transduction. When the virus is injected into the pons of Gng7-Cre mouse, which expresses Cre in L5b cells across the cortex (Figure 5.1B), expression of MitoGFP can be observed in L5b cells across the entire cortex (Figure 5.1C). Because expression is observed in both the upper and lower sublayers of M1, the cells can be specifically classified as UL5b or LL5b cells depending on their visual depth in L5b, thereby giving us visual access to mitochondria within both L5b cell types in an internally controlled system.

Given that Gprin3 cells show a higher level of expression of Oxphos genes when compared to Colgalt2 cells (see Chapter 2 and 4), we wanted to determine if this had any overt effect on gross mitochondrial morphology in these neurons. We injected the

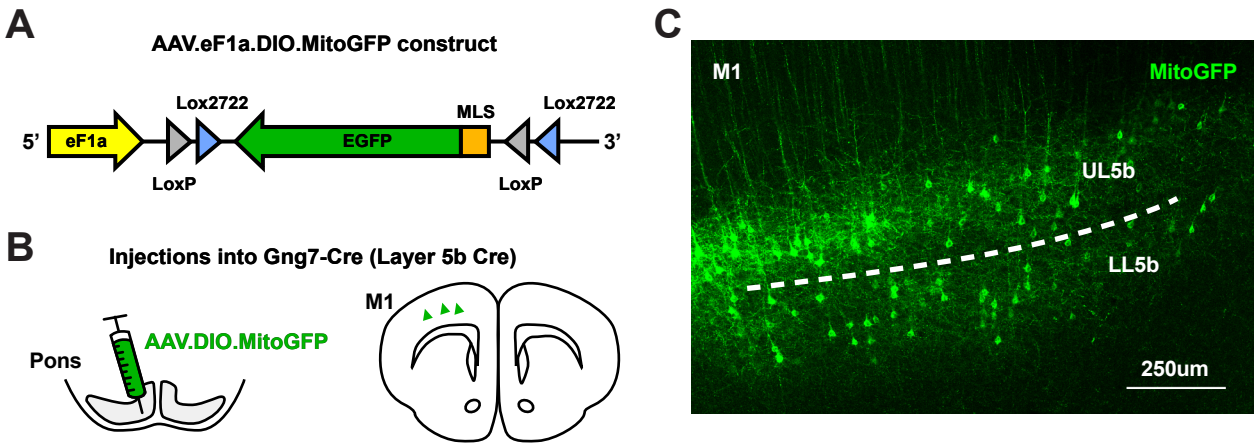

Figure 5.1: Generating a construct for expressing a mitochondrially localized GFP reporter in a cell type-specific manner. (A) Schematic illustration of the mitoGFP expression construct cloned into a viral expression plasmid and packaged into an AAV capsid. The EGFP coding sequence with an N-terminal mitochondrial localization signal (MLS) was DIO floxed for Cre-dependent constitutive expression by an eF1a promoter. (B) Schematic illustration of the experimental design showing the pontine viral injection paradigm and expected expression patterns in M1 of the Gng7-Cre mice. MitoGFP will be expressed in Cre-expressing L5b cells by transduction of the virus because of their projections to the pons. (C) Representative confocal image of mitoGFP expression (green) in M1 of a Gng7-Cre mouse following an injection of AAV.DIO.mitoGFP into the pons. Dashed line delineates the estimated boundary between UL5b and LL5b used to classify the cells during subsequent analysis. Both sublayers of L5b show expression of mitoGFP due to their shared projection to the pons (scale bar = 250 μm).

Cre-dependent mitoGFP virus into the pons of Gng7-Cre mice. In this way, we were able to label the mitochondria of UL5b and LL5b cells with mitoGFP that could be visualized by confocal microscopy (Figure 5.2A). Additionally, to visualize Oxphos machinery in our cells, we performed immunostaining for Cox6c, a component of complex IV of the ETC, in these tissues. UL5b and LL5b cells were sampled from laminar subdivisions that were visually established at low magnification, and high-magnification (63X) confocal images of individual labeled cells were collected. To account for differences in levels of expression of the reporter and in antibody detection caused by differential depth within the section, each image was thresholded such that the same percentages of total pixels were included above the threshold limit across all images. We first assessed what percentage of the cytoplasm was occupied by MitoGFP+ mitochondria in L5b cells by calculating the area of GFP signal relative to the total area of cytoplasm (Figure 5.2A outlines). Mitochondria appear to occupy approximately 24% of the cytoplasmic space in both UL5b and LL5b cells (Figure 5.2B). The total number of Cox6c + puncta, in these cells also appeared to be the same (Figure 5.2C). We next determined the size of the Cox6c particles in UL5b and LL5b cells, and found that LL5b cells showed slightly larger Cox6c+ particles than UL5b cells (difference of 0.0196 μm2), although this difference was not statistically significant. When we normalized the Cox6c+ area to the MitoGFP+ area, we also found that LL5b cells show a slightly greater level of Cox6c signal per area of MitoGFP+ mitochondria (difference of 0.1333), although again, this difference was not significant. Together these data suggest that while total mitochondrial volume may not be different between

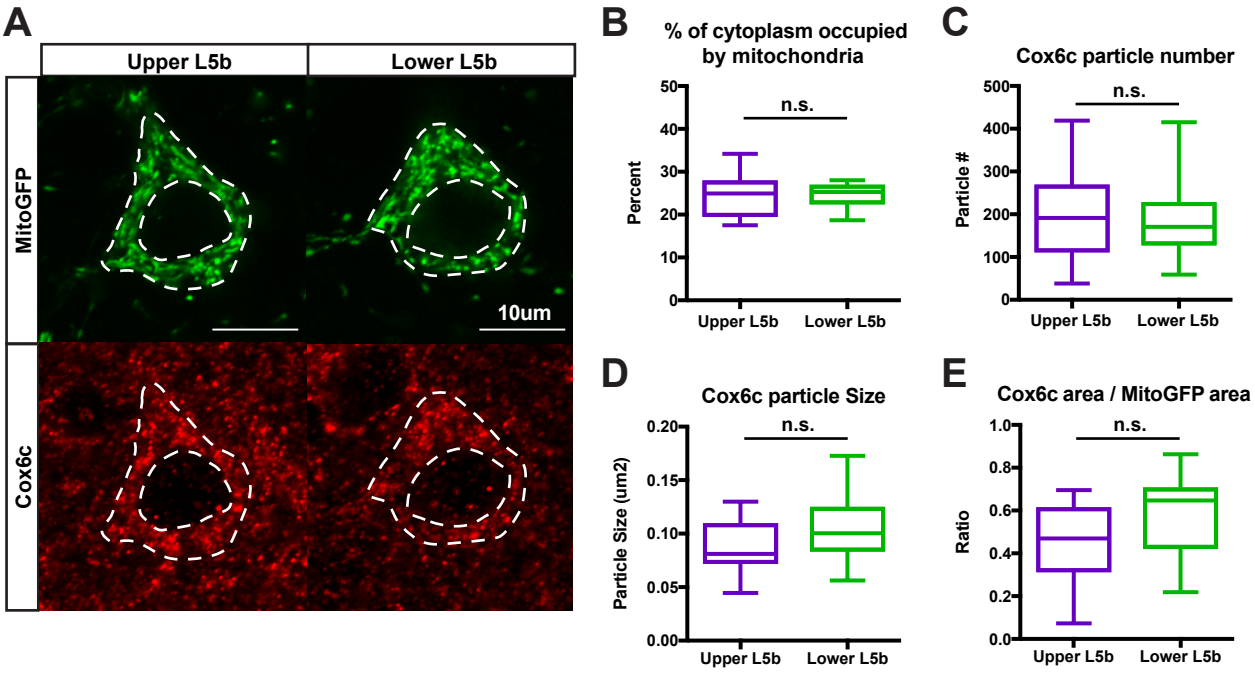

Figure 5.2: UL5b and LL5b cells show similar mitochondrial volume. (A) Representative 100X confocal images of UL5b (left) and LL5b (right) cells expressing mitoGFP (green). Dashed white lines outline the areas of cytoplasmic space in the cells that were delineated for analyses of mitochondrial size, number, etc. (scale bar = 10 μm). (B) Distributions of cytoplasmic area occupied by mitoGFP signal shown as box and whisker to highlight median and quartile boundaries and expressed as percent of total cytoplasmic area. UL5b (purple; n = 13 cells) and LL5b (green; n = 14 cells) cells do not appear to differ in mitochondrial density. (C) Number of Cox6c immunostaining "particles" after thresholding. There was no difference in the number of Cox6c "particles" found between UL5b (n = 14 cells) and LL5b (n = 14 cells) cells. (D) Box and whisker plots showing the quantification of the size of Cox6c immunostaining "particles". There appeared to be no difference between UL5b and LL5b Cox6c particle size. (E) Cox6c density per mitochondrial area, expressed as a ratio of Cox6c immunostaining area to mitoGFP area. LL5b cells show a slightly greater density of Cox6c staining per mitochondrial area, although this difference was not statistically significant (p = 0.1071; n.s. = not significant by two-tailed t-test).

UL5b and LL5b cells, the number of ETC components per mitochondrion may be subtly different, with LL5b cells showing a slightly greater density of Cox6c signal than UL5b cells.

5.2 Gprin3 cells display wider cristae than Colgalt2 cells.

Inner mitochondrial membrane complexity, or cristae morphology, is often used as a proxy for levels of ETC machinery in mitochondria, as structural determinants, such as Opa1, interact with some components of the ETC to physically produce the bend in the inner mitochondrial membrane that creates cristae structure (Lee and Yoon, 2018; Quintana-Cabrera et al., 2018). In order to determine how different levels of Oxphos gene expression observed between healthy Colgalt2 and Gprin3 cells affect mitochondrial morphology in these cells with greater detail, we visualized mitochondria by EM in healthy Colgalt2 and Gprin3 TRAP animals. To identify our cell types of interest under the microscope, we immunostained for GFP using a standard immunogold amplification protocol for EM imaging. In images of Colgalt2 and Gprin3 soma, we measured the widths of individual cristae when they could be visualized readily (Figure 5.3A). These analyses revealed that Colgalt2 cells had significantly narrower cristae than Gprin3 cells, with average cristae appearing 59% as wide (21.58 nm Colgalt2, 36.31 nm Gprin3) as Gprin3 cristae (Figure 5.3B). This suggests that Colgalt2 cells have more complex inner mitochondrial membrane structure that may contain greater levels of ETC machinery. These findings are inconsistent with the difference in the level of Oxphos gene expression we observed by TRAP, where we

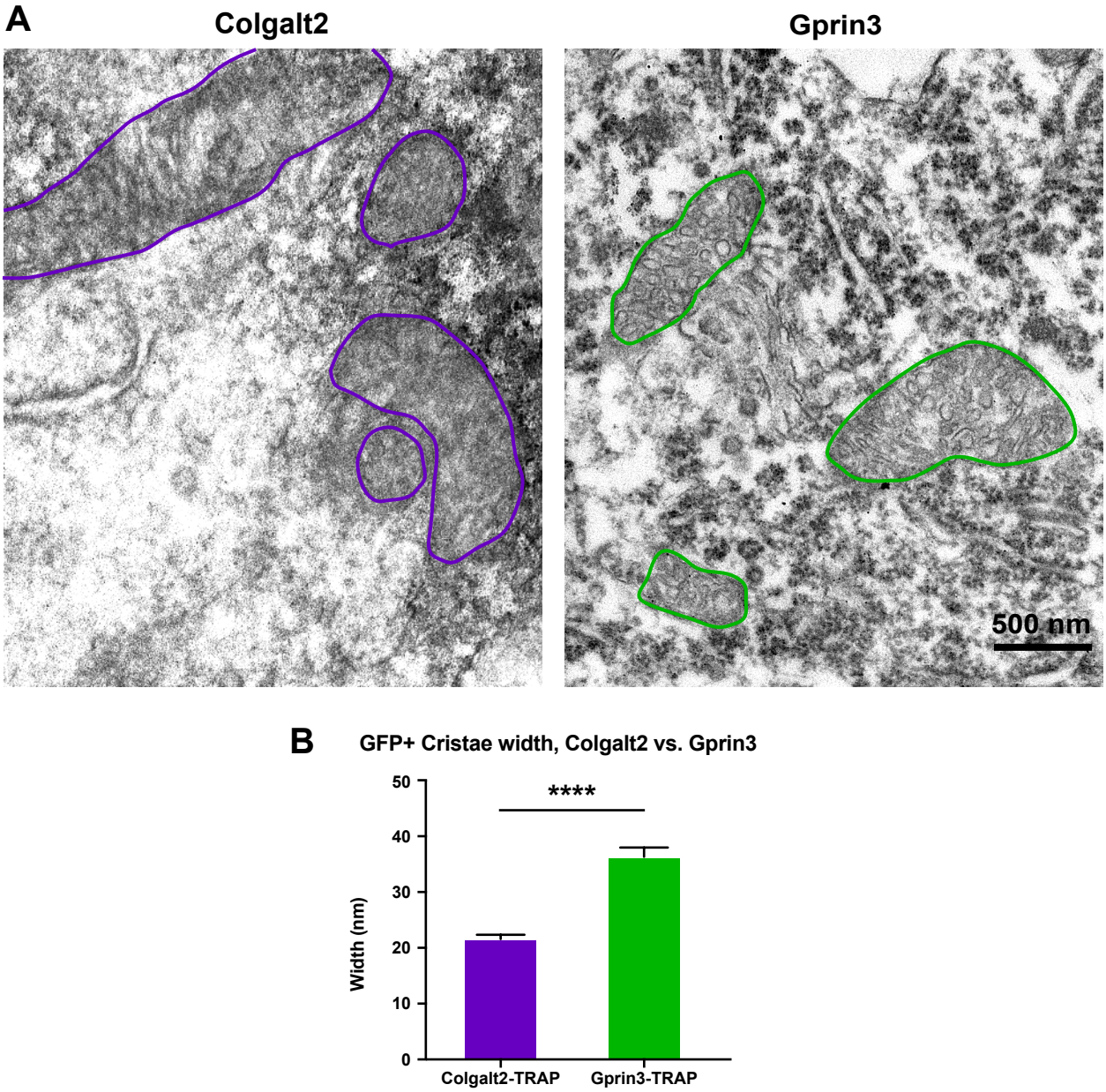

Figure 5.3: Gprin3 cells show larger mitochondrial cristae widths than Colgalt2 cells. (A) Representative electron micrographs of Colgalt2 and Gprin3 cytoplasm containing mitochondria, outlined in purple for Colgalt2 and green for Gprin3. Immunogold particles in the image indicate the presence of EGFP-L10a used to determine cell type identity (scale bar = 500 nm). (B) Quantification of cristae widths (in μm) observed across cell types. Colgalt2 cristae (purple) had a mean width of 21 nm (n = 101 cristae), with Gprin3 cells (green) showing a larger mean cristae width of 36 nm (n = 103 cristae; **** $p < 0.0001$ by two-tailed t-test).

observe that Gprin3 cells express Oxphos genes at a higher level than Colgalt2 cells. These findings are preliminary, and should therefore be repeated to confirm the difference observed. Additionally, further investigation into Oxphos output in Colgalt2 and Gprin3 cells is required in order to understand how Oxphos gene expression leads to differences in the energetic biology of these cells.

5.3 LL5b cells but not UL5b cells show greater size and decreased number of mitochondria when SOD1-G93A is expressed.

It is often difficult to maintain Cre transgenic expression when studying the effects of an additional disease transgene, such as SOD1-G93A, on organismal biology. For this reason, we sought to develop a viral expression system that would allow for cell type-specific visualization of mitochondria without the expression of Cre. For this, we chose to employ a new retrograde AAV variant, rAAV2-retro (Tervo et al., 2016), here referred to as “SL1”. Because different cell types often show distinct projection patterns to various regions of the brain, targeting injections of this Cre-independent retrograde expression vector to the unique projections of these cells can label them in a type-specific manner. We cloned a C-terminal mCherry-tagged human TOMM20, an outer mitochondrial membrane transporter, into a Cre-independent pAAV plasmid (Addgene plasmid # 55146, Michael Davidson, Figure 5.4A). In collaboration with the Janelia Farm Virus Core, the vector was packaged into the SL1 virus, which enters neurons at the pre-synaptic terminal and is transported retrogradely to the nucleus where it can be expressed. When this virus is injected into the pons of the mouse (Figure 5.4B),

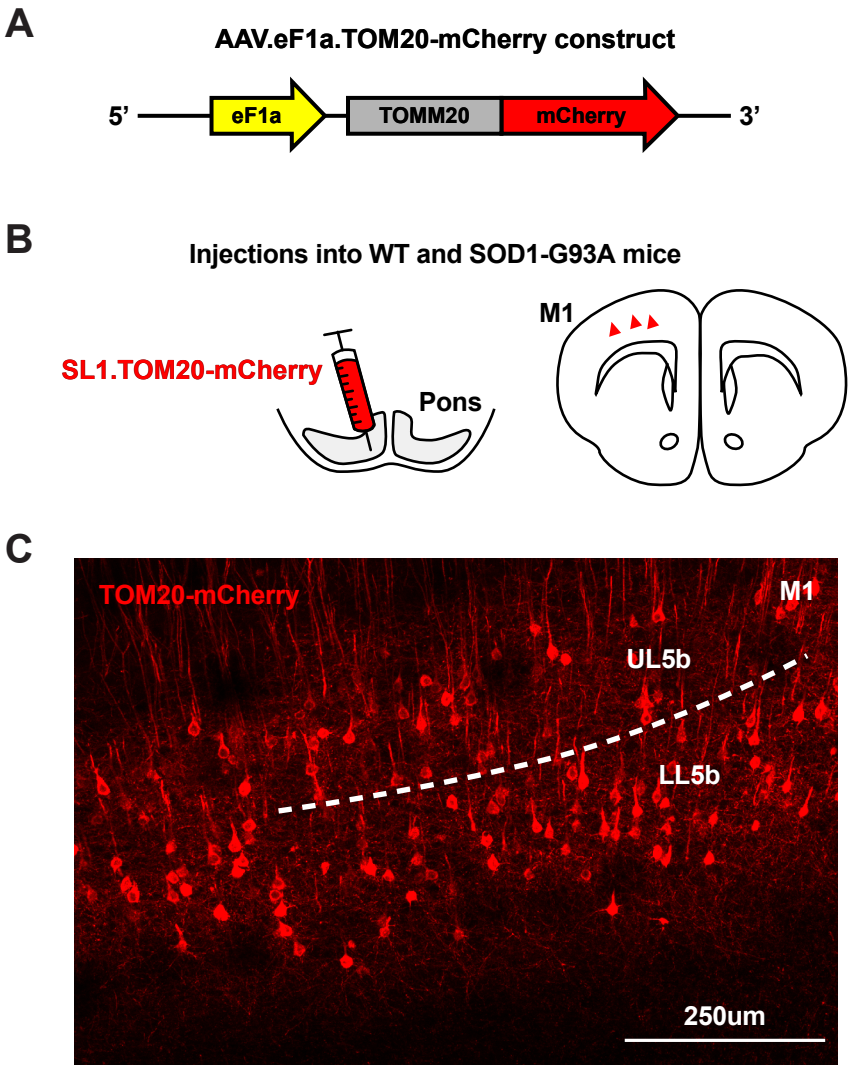

Figure 5.4: Generating a Cre-independent construct for expression of TOM20-mCherry mitochondrial reporter in a cell type-specific manner across healthy and disease L5b. (A) Schematic diagram of construct for eF1a-driven constitutive expression of TOM20-mCherry. Construct was packaged into a retrograde AAV capsid (SL1) for retrograde transduction of neurons. (B) Illustration of the experimental design paradigm for pontine injection of SL1.TOM20-mCherry (red), and resulting expression in M1 following retrograde transport from pontine terminals. (C) Representative confocal image of TOM20-mCherry expression in M1 of a WT mouse. Dashed line indicates the approximate boundary between UL5b and LL5b that was used to classify the cell types for analysis. Both sublayers show expression of the construct following injection into the pons due to their shared projection to this region (scale bar = 250 μm).

expression of the TOM20-mCherry construct is observed across L5b the cortex(Figure 5.4C), allowing for visualization of UL5b and LL5b mitochondria in a once again internally controlled system.

Because we observed contrasting changes in Oxphos gene expression between Colgalt2 and Gprin3 mice during disease, we wanted to assess gross morphological differences between WT and SOD1-G93A mitochondria in UL5b and LL5b cells at a symptomatic stage. Because we already required the SOD1-G93A transgenic mouse line for these experiments, to avoid introducing a second transgenic Cre mouse, we used the Cre-independent SL1.TOM20-mCherry retrograde viral system to visualize L5b mitochondria in disease. By injecting this virus into the pons, we were able to label both UL5b and LL5b cells in M1 of WT and SOD1-G93A mice (Figure 5.4C). After visually assessing upper or lower L5b identity at low magnification, we acquired high-magnification (100X) images of individual cells containing mCherry+ mitochondria (Figure 5.5A) in order to quantify gross morphological features. Once again, images were thresholded so that the upper 25% of all pixels in the pixel value distribution were included above the threshold limit. In UL5b cells, the size of mCherry+ particles was the same between WT and SOD. Similarly, there was no difference in the total area of the cytoplasm occupied by mCherry+ mitochondria or in the number of mitochondrial particles per cell (Figure 5.5B). This suggests that while Colgalt2 cells up-regulate levels of Oxphos gene expression in disease, there may not be an overt change in mitochondrial size or shape to reflect this change. We next analyzed morphology of LL5b cell mitochondria. In SOD, LL5b cells show slightly larger mCherry+ particle sizes

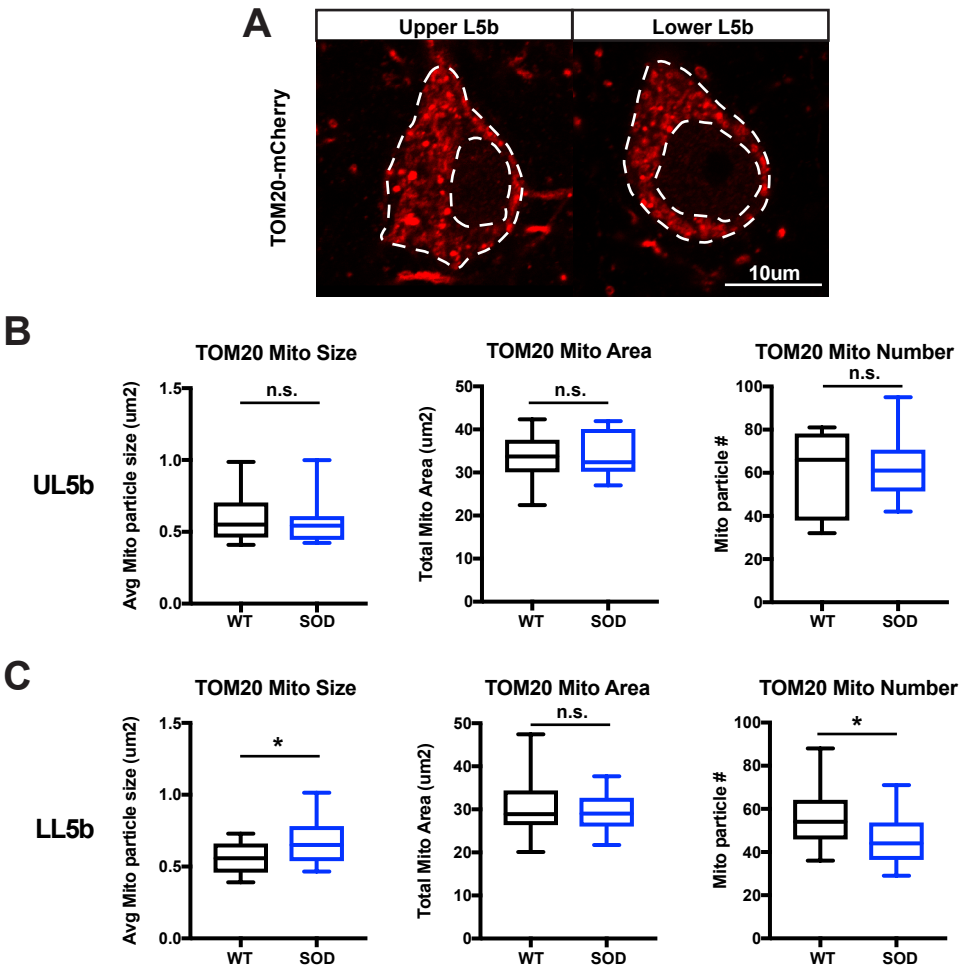

Figure 5.5: LL5b cells show changes in TOM20-mCherry distributions that are not observed in UL5b cells. (A) Representative confocal images of TOM20-mCherry labeling (red) in UL5b (left) and LL5b (right) cells. Dashed lines indicate the boundaries of cytoplasmic space that were analyzed for various properties of TOM20-mCherry labeling, such as size, area, etc. (scale bar = 10 μm). (B) Distributions of quantified properties of thresholded TOM20-mCherry labeling "particles" in UL5b cells across WT (black) and SOD1-G93A (SOD; blue). No significant difference was observed between WT (n = 11 cells) and SOD (n = 9 cells) for particle size (μm2; left), total labeled area (μm2; middle), or total number (right; n.s. = not significant by two-tailed t-test). (C) Distributions of quantified properties of thresholded TOM20-mCherry labeling "particles" in LL5b cells across WT and SOD. No significant difference was observed between WT (n = 15 cells) and SOD (n = 21 cells) for total area of TOM20-mCherry labeling (μm2; middle). However, a significant difference was noted for TOM20-mCherry particle size and total number, showing an increase and a decrease in SOD, respectively (*$p < 0.05$, n.s. = not significant by two-tailed t-test).

relative to WT cells (Figure 5.5C). There was no difference in the total area occupied by these particles in the cytoplasm, however. This necessitated that the number of mitochondria be lower in SOD, which is indeed what was observed. These data indicate that LL5b cells may decrease the number of discrete mitochondria in response to SOD1-G93A, while maintaining total mitochondrial volume. It is difficult to reconcile these findings with the Oxphos gene expression decrease that we observe by TRAP, as it does not address morphology due to Oxphos changes, but rather broad morphological rearrangements of mitochondria. But, together, these data highlight that UL5b and LL5b cells may show contrasting mitochondrial changes at the level of gross morphology and distribution in SOD1-G93A, where LL5b cells show a decrease in the number of mitochondria that is not observed in UL5b cells.

5.4 Gprin3 and surrounding cells expressing SOD1-G93A show changes in cristae morphology by EM.

To better visualize mitochondrial ultrastructure and its changes in LL5b Gprin3 cells, we visualized WT and SOD1-G93A Gprin3 cells by EM. We immunostained for GFP with immunogold amplification in order to easily identify our cells of interest under the microscope. In images of Gprin3 soma (Figure 5.6A), we measured individual cristae widths in the mitochondria of Gprin3 cells, as well as in cells that were immediately adjacent to the GFP+ Gprin3 cells. The widths of cristae in both Gprin3 and neighboring cells appeared to increase in SOD1-G93A (Figure 5.6B), suggesting that these cells may be decreasing levels of ETC components in the inner mitochondrial

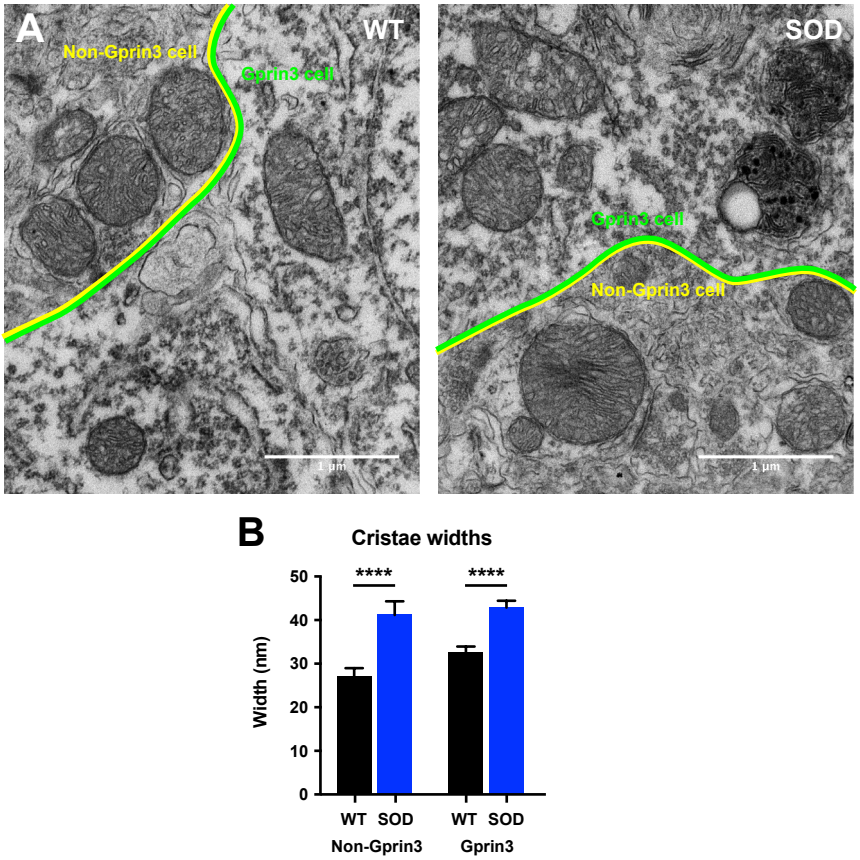

Figure 5.6: Cells in LL5b of M1 show increased cristae width in SOD1-G93A. (A) Representative electron micrographs of WT (left) and SOD1-G93A (SOD; right) LL5b, containing GFP+ Gprin3 cells (outlined in green) and adjacent GFP- cells of indeterminate identity (outlined in yellow; scale bar = 1 μm). (B) Quantification of cristae widths (nm) between WT (black) and SOD (blue) for GFP+ Gprin3 cells (WT n = 316, SOD n = 302 cristae) and adjacent GFP- cells (WT n = 76, SOD n = 72 cristae). Both cell types show an increase in cristae width in SOD (****$p < 0.0001$ by two-tailed t-test). (C) Quantification of density of matter within each mitochondrion, reported as the mean pixel value measured within each mitochondrion normalized to the mean pixel value of "empty" cytoplasm, and represented as a frequency distribution of normalized pixel values. In both GFP- and GFP+ cells, SOD mitochondria (blue distribution) showed a decrease in normalized pixel value relative to WT mitochondria (black line), suggesting that the mean pixel value in SOD mitochondria became darker. This in turn suggests that more "material" is found inside each mitochondrion in disease. Yellow and green bars highlight the distance between the WT and SOD distribution means for GFP- (WT n = 80, SOD n = 166 mitochondria) and GFP+ (WT n = 240, SOD n = 166 mitochondria) cells respectively.

membrane in disease. These results require a more exhaustive study of cell-type specific mitochondrial changes in SOD1-G93A to understand, including staining for components of the Oxphos pathway, and functional analyses of mitochondrial function across different cell types in disease.

5.5 Strategies for modulating levels of respiration and ETC activity in UL5b and LL5b cells.

Our characterization of mitochondrial morphology, alongside our TRAP gene expression findings, suggests that there are some changes in structural mitochondrial, and possibly respiration, during disease progression. In order to determine how these changes may affect the survival or vulnerability of L5b cells to SOD1-G93A, particularly because we observed an increase in Oxphos gene expression in ALS-resistant UL5b cells, we attempted to increase the levels of respiration in these cells. We first opted to leverage an endogenous signaling mechanism to increase the levels of Oxphos in the mouse by injecting mice with all-trans retinoic acid (RA). RA treatment in cell culture has been shown to increase the levels of respiration in cells (Tourniaire et al., 2015), and retinoid signaling additionally appears to be disrupted in ALS (Kolarcik and Bowser, 2012; Malaspina et al., 2001). We wanted to determine if increased Oxphos by RA signaling would change the survival time or disease progression of SOD1-G93A mice. We performed intraperitoneal (IP) injections of RA (1 mg/kg animal weight) or corn oil vehicle (4 ul/g animal weight) every two days into SOD1-G93A mice beginning at a symptomatic stage to determine if increased RA levels would have any effect on

disease survival time or progression. Survival time did not appear to be affected in RA-injected animals (Figure 5.7A). To determine any changes to symptom onset or progression, we also subjectively assessed symptom severity during treatment by noting the presence of tremors, limb weakness, limb dragging, and overall mobility impairment. However, we found no significant difference in symptom progression between RA- and vehicle-injected animals (Figure 5.7B).

The lack of cell-type specificity in this RA strategy set us to next attempt a more targeted modulation of Oxphos gene expression using a cell-type specific approach. Pgc1a has been shown to induce mitochondrial biogenesis and respiration through increased expression and activation of nuclear respiratory factors (NRFs; Uldry et al., 2006; Wu et al., 1999). Additionally, exogenous expression of Pgc1a in cultured SOD1-G93A cells was shown to normalize mitochondrial structural changes and prevent cell death (Song et al., 2013). We therefore packaged a pAAV plasmid containing a human copy of the Pgc1a coding sequence under the control of a constitutive CMV promoter (Figure 5.8A, Xiong et al., 2015) into the retrograde SL1 virus for overexpression. By injecting this virus into the left pons of pre-symptomatic Gprin3 animals, we could retrogradely target the GFP+ LL5b cells and in the ipsilateral left hemisphere of M1 for Pgc1a overexpression, while leaving the contralateral right hemisphere unaffected as an internal control (Figure 5.8B). Tissues were collected when mice reached end stage of disease and required euthanasia. We immunostained for GFP and counted the number of GFP+ Gprin3 cells in the left and right hemispheres in both WT and SOD1-G93A to determine if increased Oxphos by Pgc1a overexpression had any effect on cell

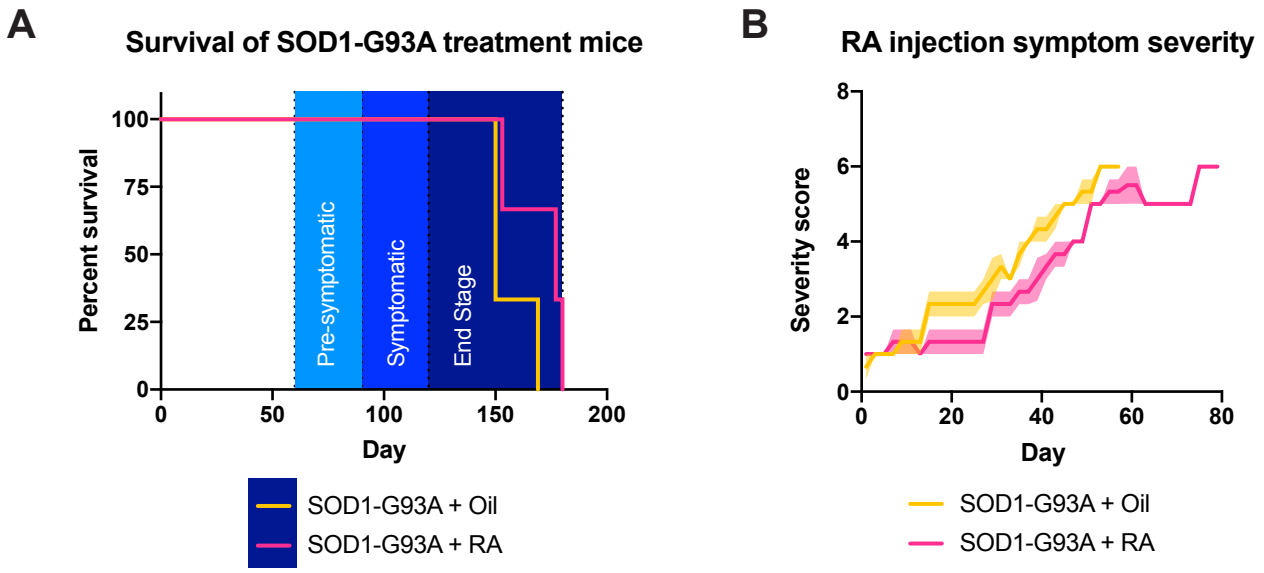

Figure 5.7: Modulating levels of Oxphos by retinoic acid injections does not alter disease progression. (A) Survival curves showing survival of SOD1-G93A mice that received IP injections of either oil vehicle (yellow curve; median survival = 150 days; n = 3 mice) or retinoic acid (RA; magenta curve; median survival = 177 days; n = 3 mice). (B) Subjective symptom severity score plotted as a function of time for SOD1-G93A mice that received IP injections of either oil vehicle (yellow curve; n = 3 mice) or RA (magenta curve; n = 3 mice). Increased symptom severity score indicates increased overt symptom severity in the animal (lines show mean values for each time point, with shading indicating SEM).

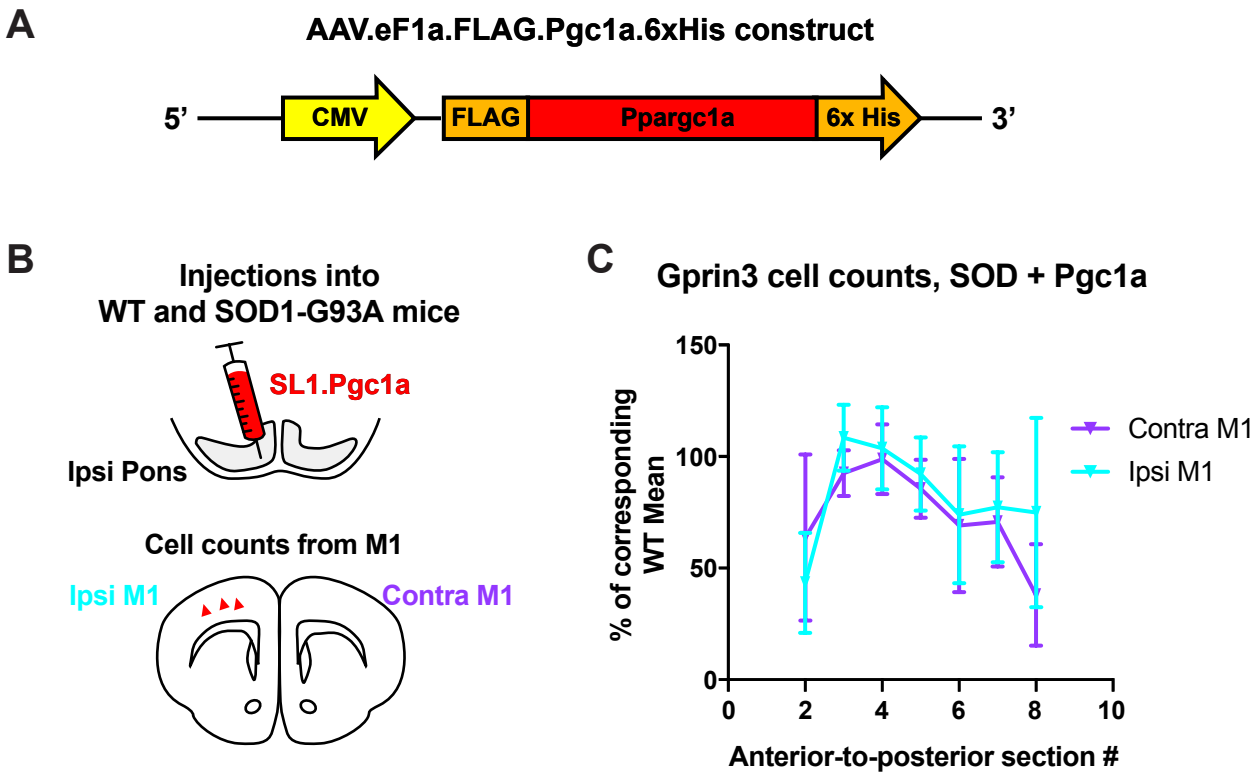

Figure 5.8: Modulating levels of Oxphos in L5b cells by Pgc1a overexpression does not alter disease progression. (A) Schematic of viral construct for constitutive CMV-driven overexpression of exogenous Pgc1a. (B) Schematic illustration of the experimental design showing the pontine viral injection paradigm and expected ipislateral (cyan) expression patterns relative to contralateral cortex (purple) in M1 of WT or SOD1-G93A mice. (C) Cell counts along the AP extent of M1 for M1 ipsilateral to the injection site ("Ipsi M1"; cyan) and M1 controlateral to the injection site ("Contra M1"; purple). No significant difference in cell number was noted between Ipsi M1 (n = 6 animals) and Contra M1 (n = 6 animals). Values are reported as a percent of the Pgc1a-injected WT mean at the matching anatomical coordinate (points indicate mean values for each coordinate, with bars showing SEM).

survival. We found no significant difference between the number of Gprin3 cells across the ipsilateral left and contralateral right hemispheres (Figure 5.8C), suggesting that Pgc1a overexpression in these cells may does not affect cell survival. One notable caveat to this experimental design was that we relied on the HA and His tags to visualize exogenous Pgc1a overexpression. Immunodetection of these tags proved difficult in our tissues, so we were not able to determine to what extent Pgc1a overexpression overlapped with our Gprin3 population. This confound could be corrected if the experiment were repeated with a Pgc1a construct that additionally expresses a reporter that can be easily visualized in tissue. Additionally, Pgc1a activation is post-translationally regulated by many upstream molecular signaling pathways (see Austin and St-Pierre, 2012), potentially limiting an overexpression strategy. Overall, our two Oxphos modulation strategies were technically limited in various ways, making it difficult to interpret the results from each experiment in the biological context of mutant SOD1. However, they serve to highlight the need for careful targeting and assessment of gene expression modulation when studying neuronal ATP-synthesis, and reveal how even heavy-handed approaches to modulate levels of Oxphos may not always present the most effective strategies for studying the effect of changes in respiration on cellular biology.

5.6 Discussion

Mitochondrial morphology can reflect many functional and dysfunctional states of a cell. In particular, many neurodegenerative diseases display changes in mitochondrial

structure and function (Bossy-Wetzel et al., 2003; Burté et al., 2015; Chen and Chan, 2009; Itoh et al., 2013; Knott et al., 2008). In the ALS SOD1-G93A model, we observed contrasting changes in Oxphos gene expression between degeneration-vulnerable Gprin3 and resistant Colgalt2, as well as baseline differential enrichment of these genes in healthy Gprin3 cells over Colgalt2 cells (Chapter 4). We therefore set out to determine if changes in gene expression reflect alterations in mitochondrial structure that could be visualized at the subcellular level. We observed that in healthy Colgalt2 and Gprin3 cells, there is a slightly greater amount of Cox6c signal per mitochondrial area in Gprin3 cells, but Colgalt2 cells show narrower cristae by EM (Figure 5.9). These findings lie in opposition to each other, indicating that Gprin3 neurons display greater levels of the Oxphos component Cox6c, but wider cristae that are associated with lower levels of ATP synthesis. Because cristae width can be regulated at the level of energetic demand based on activity patterns (Cserép et al., 2018), one possible explanation for this finding is Colgalt2 neurons are more active than Gprin3 cells, and per-mitochondrion levels of Oxphos proteins that are higher than in Gprin3 neurons. It is also possible that cristae width does not provide the best proxy for overall levels of ETC proteins in these cells, or that the Oxphos enrichment that we observe in Gprin3 gene expression reflects a cell-type specific assembly of ETC components. Indeed, it has been shown that for Complex IV (COX) in particular, there are tissue-specific isoforms that differ across cell types (Hüttemann et al., 2001; Stiburek et al., 2005). It is therefore possible that different expression levels of Cox6c and other subunits observed between Colgalt2 and Gprin3 cells do not reflect different levels of Oxphos, but rather cell-type

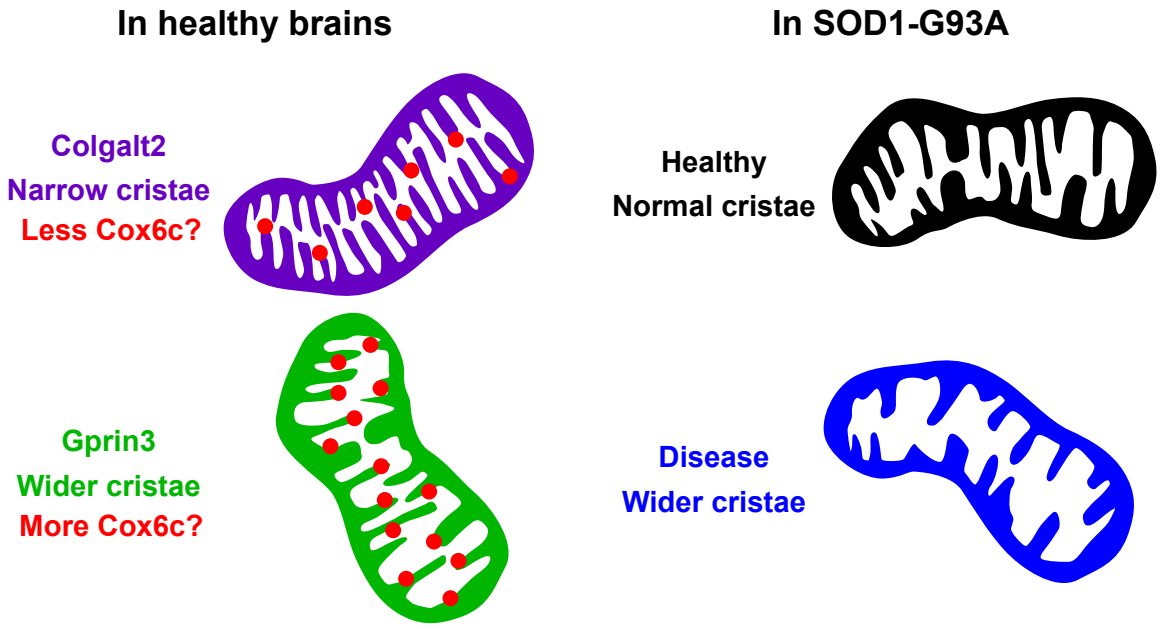

Figure 5.9: Summary of mitochondrial morphology analysis in Colgalt2 and Gprin3 cells. Mitochondria of Colgalt2 cells (purple) appear to have narrower cristae by EM, but fewer Cox6c puncta (red) per mitochondrial area than Gprin3 mitchondria (green). Gprin3 mitochondria appear to have wider cristae (left panel). In SOD1-G93A mitochondria (blue), cristae of L5 cells appear to increase in size relative to healthy L5 mitochondria (black; right panel)

specific differences in complex make-up. These differences would still present a very interesting avenue for the establishment of potential cell-type specific differences in how ATP is synthesized, even if rates of synthesis are not affected by different subunit composition of the ETC complexes.

Because metabolism appears to be affected with mutant SOD1 expression (Allen et al., 2014), and because we observed contrasting changes in Oxphos gene expression changes between resistant Colgalt2 and vulnerable Gprin3 cells (Chapter 4), we next determined how these changes manifest themselves in mitochondrial structure during disease. We found no significant changes in overt mitochondrial morphology in Colgalt2 cells when SOD1-G93A was expressed, but observed that Gprin3 neurons show a decrease in mitochondrial number coupled with an increase in individual mitochondrion size. By EM, cristae widths appeared to increase in SOD1-G93A in both Gprin3 mitochondria and GFP- neighboring mitochondria. These data indicate that in Gprin3 cells, the overt size and number of mitochondria are regulated simultaneously with inner mitochondrial membrane structure. In mutant SOD1 animals, dilated cristae and overt vacuolization of mitochondria have been reported during disease progression (Dal Canto and Gurney, 1995; Kong and Xu, 1998; Wong et al., 1995). The increased width of Gprin3 cell cristae is consistent with these findings, and suggests that these cells produce less ATP in the disease state. It is not clear to what extent this is causal to cell death, however, as these changes appear to precede apoptosis in LMNs (Bendotti et al., 2001). Additionally, the cristae widening we observed does not appear to be cell type specific, as neighboring cells show a similar phenotype, suggesting it may be a

generic response to SOD1-G93A expression. While we were not able to identify the types of cells that composed these neighboring populations, whether glial or neuronal, it is possible that dysfunction in these surrounding cells influences Gprin3 cells in a likewise adverse way (Tripathi et al., 2017; Vargas et al., 2005). In order to understand this further, we must perform the same assessment of mitochondrial structure in Colgalt2 cells during disease, and compare the changes to changes in neighboring cells. It will also be important to identify the cell types that represent these neighboring populations, particularly because neighboring astrocytes may be experiencing mitochondrial dysfunction as well (Cassina et al., 2008).

We next wanted to understand how modulation of Oxphos gene expression may affect disease progression by employing both global and cell-type specific inducers of respiration and Oxphos gene expression. Neither strategy provided conclusive results with regards to disease progression or survival, as there were various technical limitations with each strategy. This does not except dysfunction of mitochondria from affecting disease progression, however, because our sequencing data and morphological analyses suggest that there may be disease-related changes in mitochondrial function in L5b cells. Given the link between mitochondrial dysfunction and neurodegenerative diseases, including ALS (Chen and Chan, 2009; Cozzolino et al., 2013; Lin and Beal, 2006; Moreira et al., 2010), it is very much worth exploring how cell type-specific changes in mitochondrial structure and function affect the health of the vulnerable LL5b cells in ALS, particularly in the context of underlying cell-specific differences in respiration in the healthy brain.

CHAPTER 6:

Finding markers for L5 cell types in human motor cortex

The diversity of L5b projection neuron types in the motor cortex of rodents is only now being elucidated. Using BAC transgenic animals expressing TRAP, we have shown that in mice, M1 L5b contains two distinct populations of corticofugal neurons that each occupies its own discrete sublayer. Colgalt2 cells of the upper L5b sublayer (UL5b) project to the pons but not spinal cord, while Gprin3 neurons found in the lower sublayer (LL5b) project to both the pons and the spinal cord (see Chapter 2). This newly described heterogeneity in L5b cell type identity in mouse M1 now raises the question of whether a similar diversity exists across L5 of the motor cortex in other species. This is particularly important to understand in the context of ALS, where we show that corticospinal LL5b Gprin3 cells are vulnerable to degeneration. Because corticospinal neurons of the human primary motor cortex are thought to be the most vulnerable cortical population in ALS (Eisen and Weber, 2001; Eisen et al., 1992; Tandan and Bradley, 1985), it is important to understand whether our mouse findings represent a cell type-specific vulnerability that recapitulates the human condition. Uncovering the cell-type specificity of L5 neuron degeneration in human ALS would ultimately allow us to explore the translatability of our findings in ALS mouse models to relevance in human disease.

The cell type diversity of human cortex has been challenging to define. While many have shown the laminar distributions of single markers through

immunohistochemical staining (see Jacobs et al., 2018), they have rarely been able to determine the cell type-specificity of these markers across neurons in the same layer. This is primarily due to the technical limitations present in performing combinatorial immunofluorescence staining in tissues that, through the various stages of post-mortem handling, develop high levels of auto-fluorescence. However, combinatorial marker staining through multi-channel immunofluorescence is required to understand the molecular overlap of different cortical populations in the absence of anatomical tracing and transgenic reporters. For this reason, we set out to first establish a reliable immunofluorescence protocol for human neuronal staining and visualization in the primary motor cortex. Using the molecular profiles for the distinct mouse L5b cell types available through our Gprin3 TRAP profiling, we also sought out a combination of markers that can allow us to distinguish populations of L5 cells across mouse and human motor cortex. With the EGFP expressed in these TRAP cells, we are additionally able validate the specificity of candidate markers to L5b cells. With these markers, we aim to not only characterize the heterogeneity of L5 pyramidal neuron types in this region of cortex, but also to provide a system for reliably visualizing the populations of cells that are relevant to cortical degeneration in ALS.

6.1 Narrowing down candidate markers for L5b cells across species.

In order to identify combinations of markers that are able to distinguish L5b subpopulations in mouse and human tissue, we first generated a list of possible candidate genes thought to be specifically expressed in L5 cells. Using a combination of

TRAP data, available ISH data from the Allen Brain Atlas, as well as previously reported markers for L5b cells, a set of candidate genes was generated (Table 6.1). We tested antibodies against these markers, or in situ hybridization (ISH) probes when efficacious antibodies could not be obtained, and assessed the specific localization of staining within L5b of mouse M1. Results from this screen are summarized in Table 6.1. We found that in some cases, markers were distributed across more layers than just L5b in mouse (labeled "~Yes" in Table 6.1), but were still included for human L5 marker screening as long as strong staining in mouse L5b cells was evident. Many of the markers that showed L5b staining in mouse did not work in human primary motor cortex staining (labeled "No" in Table 6.1), however we did see L5 staining for three of the markers that we tested across mouse and human tissue: Pcp4, SMI-32 (a non-phosphorylated variant of Nefh) and Crym (Figure 6.1). Pcp4 was more broadly distributed across all cells in the deep layers of mouse M1 from L5a to L6a (Figure 6.1A, top panel). Crym was visible in what appeared to be LL5b cells, but was also observed in some L6a cells (Figure 6.1A, middle panel). SMI-32 appeared to more selectively label neurons across upper and lower L5b, with very few cells observed in other layers (Figure 6.1A, bottom panels). In human motor cortex, Pcp4 staining appeared to be principally localized to a visually estimated L5, with a small subset of cells visible in L3 (Figure 6.1B, top panel). Crym staining appeared to label L5 cells exclusively (Figure 6.1B, middle panel), while SMI-32 appeared to label a diverse set of neurons across L5 and L3 (Figure 6.1B, lower panel). Because they appeared to more selectively label specific subpopulations of L5b cells in the mouse, we selected Crym and Nefh/SMI-32

Table 6.1: Candidate markers for L5b cells across species. If marker appeared to specifically stain L5b in M1 of either mouse or human, it appears labeled as "Yes". If a marker stained L5b cells as well as other cells in the cortex, it is labeled as "~Yes". If a marker failed to stain L5b cells, it appears labeled as "No". Markers were selected based on apparent specificity in published studies, Allen Brain Atlas data, and RNA-Seq data from motor cortex.

Markers for L5b cells across species

Marker	Stains L5b in Mouse	Stains L5b in Human
Bcat1	Yes	No
Crim1	No	No
Crym	~Yes	Yes
Cygb	No	No
Gng7	Yes	No
Lypd1	~Yes	No
Nefh, aka SMI-32	Yes	~Yes
Nurr1	No	No
Pcp4	~Yes	Yes
Penk	No	No
Scn4b	Yes	No
Sh3bgrl2	No	No

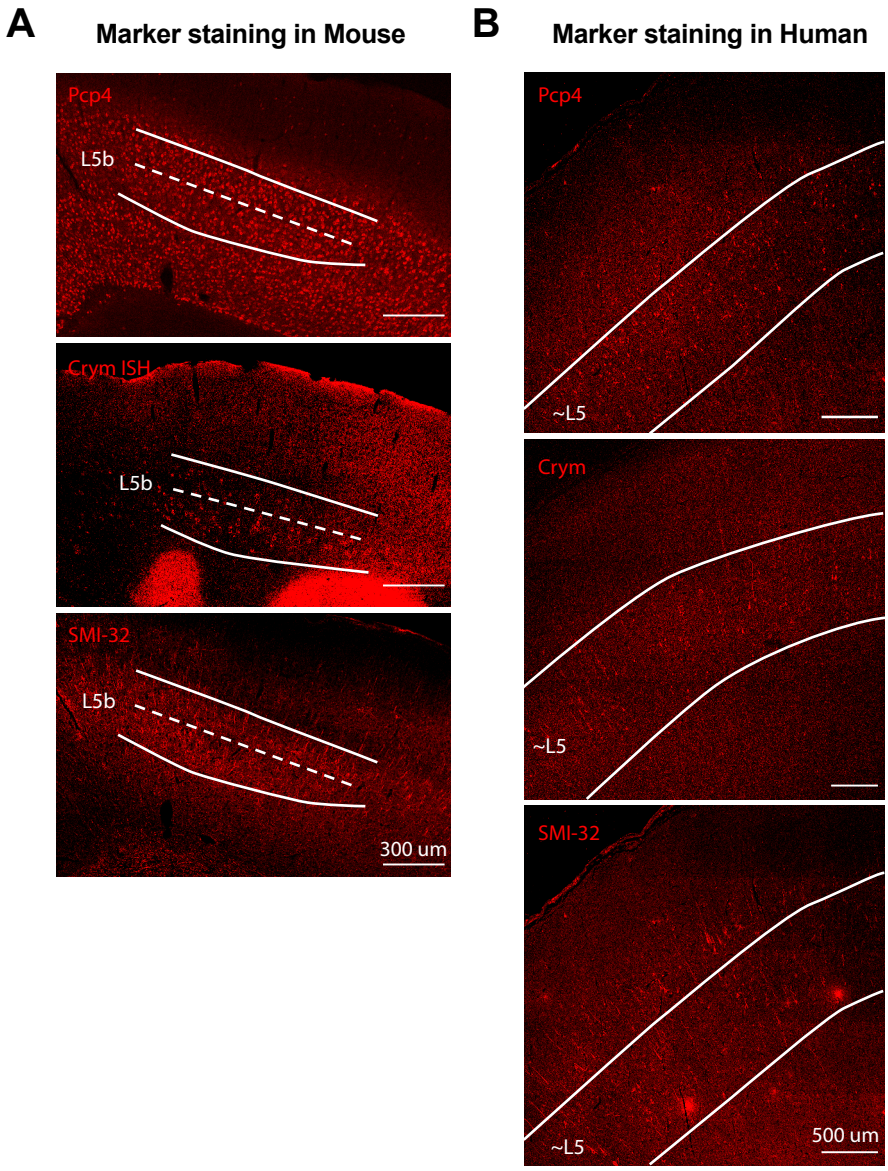

Figure 6.1 Staining for Pcp4, Crym, and SMI-32 in mouse and human tissue allows for visualization of deep layer neurons in the motor cortex. (A) Representative confocal images of Pcp4 and SMI-32 immunofluorescence, and Crym FISH, showing the laminar distribution of signal across mouse motor cortex. Solid white lines indicate the visually estimated dorsal and ventral boundaries of L5b, with the dashed line showing the approximate location of the subdivision between UL5b and LL5b (scale bar = 300 μm). (B) Representative confocal images of Pcp4, Crym, and SMI-32 immunostaining in human motor cortex. Solid white lines indicate visually estimated dorsal and ventral boundaries of L5 in each section (scale bar = 500 μm).

as our markers of interest for determining subpopulation distributions across L5 in mouse and human primary motor cortex. Additionally, Crym and SMI-32 have been individually used to label L5 neurons across species in other studies, with SMI-32 the most commonly used to visualize large neurons in the motor cortex of many animals (Arlotta et al., 2005; Campbell and Morrison, 1989; Fink et al., 2015; Molnár and Cheung, 2006; Rouaux and Arlotta, 2013). We therefore additionally took this as an opportunity to clarify the subpopulation specificity of these markers within L5 of mouse and human.

6.2 Crym and Nefh ISH label populations of neurons in L5b of mouse primary motor cortex.

Crym and SMI-32 have previously been used as markers for L5b cells (Arlotta et al., 2005; Campbell and Morrison, 1989; Fink et al., 2015; Molnár and Cheung, 2006; Rouaux and Arlotta, 2013). However, until recently, the heterogeneity of cell types in L5b was poorly understood, so it was not clear what subpopulations may be targeted in staining for these markers. Unfortunately, we were not able to visualize immunofluorescence staining for Crym tissue sections, so we opted to instead perform fluorescence in situ hybridization (FISH) on sections from Gprin3-TRAP brains using probes against Crym and Nefh to determine marker co-localization with our LL5b cell types. Immunofluorescence staining for GFP was performed following ISH for these markers, and the sections were imaged by confocal microscopy (Figure 6.2A). Crym+ cells were distributed across the deepest layers of the cortex, including L5a and L6a

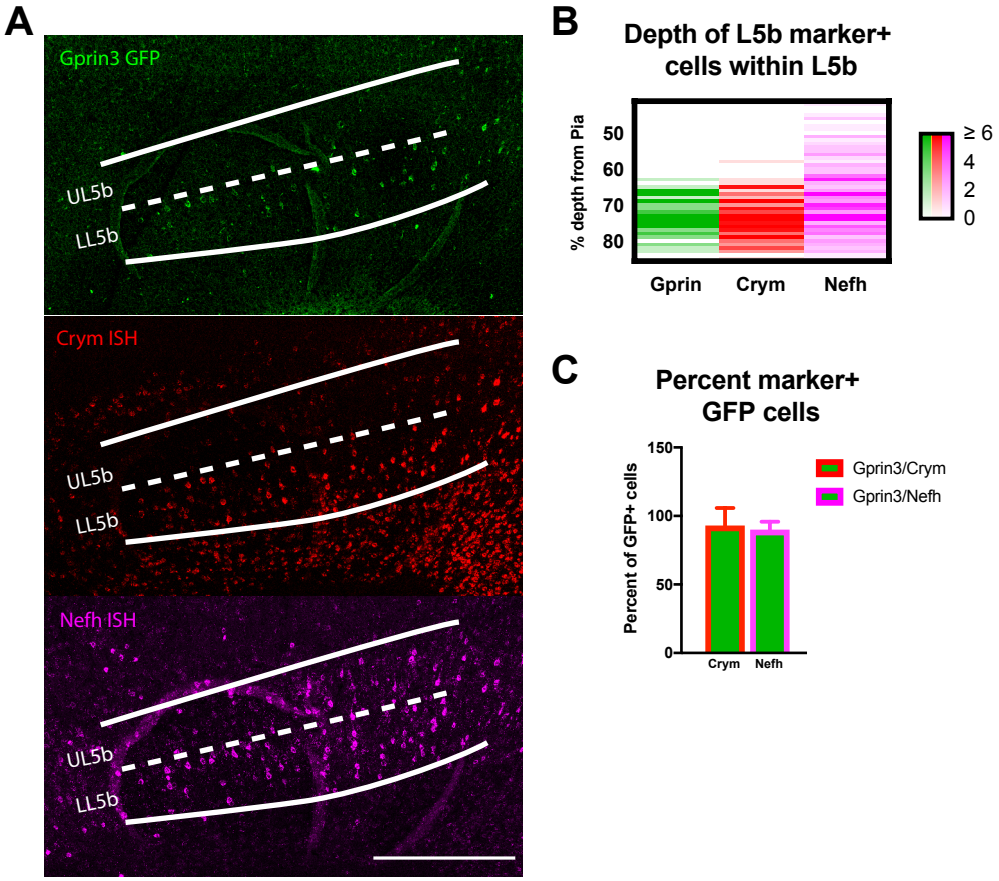

Figure 6.2: FISH against Crym and Nefh labels populations of L5b cells in M1 of mouse. (A) Representative confocal images of Gprin3 M1 showing GFP immunostaining (green; top row), Crym ISH (red; middle row), and Nefh ISH (magenta; bottom row). In L5b, Crym is primarily observed in LL5b, while Nefh signal appears to span both UL5b and LL5b. Solid white lines delineate the estimated upper and lower boundaries of L5b, and dashed white line indicates the approximate division between UL5b and LL5b (scale bar = 300 μm). (B) Heatmaps indicating the depths of L5b marker+ cells within L5b, shown as percent of depth from the pial surface and represented as frequency of appearance at that depth. Gprin3 cells (green; n = 62 cells) were found deep in the cortex at ~75% depth, and represent a LL5b population. Crym+ cells (red; n = 106 cells) were also seen at this depth, suggesting they also label LL5b cells. Nefh+ cells (magenta; n = 183 cells) were found in this LL5b region as well as superficially, in what is likely UL5b. Frequencies ≥ 6 are shown in the same shade to more readily highlight the depths at which cells were the most concentrated. (C) Quantification for co-localization of Gprin3 GFP (n = 73 cells) with Crym and Nefh ISH labeling. 92% of GFP+ cells were Crym+ (red outline) and 89% of GFP+ cells were Nefh+ (magenta outline; bars show mean ± SEM).

(Figure 6.2A, middle panel), but within L5b, were only observed in the lower sublayer (Figure 6.2B). Nefh+ cells in L5b were instead distributed across both sublayers of M1 L5b (Figure 6.2A, bottom panel), although their distribution appeared to be slightly more concentrated to LL5b (Figure 6.2B). Crym co-localized with 92% of Gprin3 cells, and Nefh co-localized with 89% of Gprin3 cells (Figure 6.2C). These data suggest that while Nefh may label cells across both sublayers of L5b based on its broader distribution across this layer, Crym appears to more exclusively label the corticospinal Gprin3 population over other L5b cells. We will need to carry out the same marker staining approach in Colgalt2 tissues to determine the specificity of these markers in UL5b, but with these results, we have established a combinatorial set of markers that may allow for the visualization of this LL5b population in non-transgenic animals.

6.3 Crym and SMI-32 staining allows for visualization of L5 cells in human primary motor cortex.

To determine if Crym and Nefh additionally allow for visualization of L5 cell types in human motor cortex, we performed dual staining for Crym and SMI-32 (the non-phosphorylated variant of Nefh), in human primary motor cortex sections (Figure 6.3). Paraffin-embedded blocks of different regions of motor cortex were sectioned to between 10 and 14 μm (depending on brain bank source). Slides with mounted sections were deparaffinized before performing acid and heat-based antigen retrieval and immunofluorescence staining. Images of Crym and SMI-32 immunostained sections were then collected by confocal microscopy. Boundaries of cortical lamination were

estimated visually based on neuron size and approximate depth, and with the help of published data on cortical lamination in primates. In a lateral area of motor cortex associated with the control of facial and neck muscles (Figure 6.3A, see Penfield and Boldrey, 1937), the distribution of SMI-32+ cells appeared broad. Large SMI-32+ cells were observed in deep L3, with a subset of SMI-32+ cells in L5 showing lower levels of signal (Figure 6.3B, right panel). The distribution of SMI-32 staining that we observed here is consistent with previously reported localization of SMI-32+ cells across different areas of primate cortex (Campbell and Morrison, 1989). Additionally, this distribution is distinct from what we observed for Nefh staining in mouse, where Nefh+ cells were found almost entirely in L5b. Crym+ cells in the lateral region of human motor cortex were observed in deeper L5, with a small subset of cells positive for both Crym and SMI-32 found at this depth. In a medial area of motor cortex that maps to limb control (Figure 6.3A), a subset of SMI-32+ cells was also observed in deep L3, with the majority of SMI-32+ cells localizing to L5 (Figure 6.3B, right panel). Many of the SMI-32+ cells in L5 appeared to also be positive for Crym in this medial region, with the exception of the occasional very large pyramidal neuron that appeared to be selectively positive for SMI-32 (white arrow in Figure 6.3B, right panel). These anatomical data suggest that, even across different subregions of human motor cortex, the laminar distribution of Crym and SMI-32+ cells can vary, and that this may represent a diversity of L5 cell types in these areas.

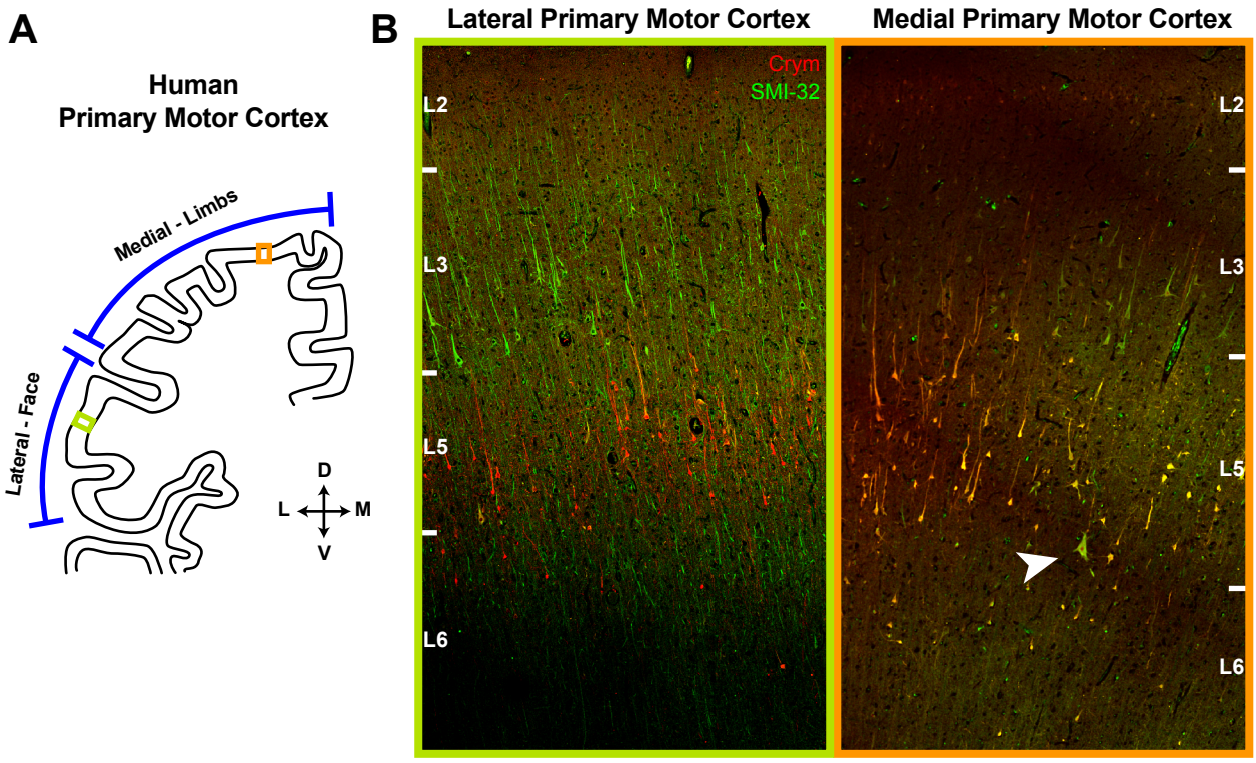

Figure 6.3: Crym and SMI-32 staining reveals distinct laminar populations of cells across human primary motor cortex. (A) Schematic representation of the regions of primary motor cortex that were targeted for staining. The medial region of motor cortex functionally maps to limb regions, and is thought to be the primary area containing Betz cells. The lateral area maps to facial regions and is thought to not contain many corticomotoneurons. Axial legend is shown in the bottom right (D = dorsal, V = ventral, M = medial, L = lateral). (B) Representative confocal images showing the laminar distribution of Crym and SMI-32 marker immunostaining in lateral motor cortex (left) and medial motor cortex (right). In lateral motor cortex, Crym (red) appeared to specifically label a population of L5 cells. SMI-32 (green) strongly labeled a population of large L3 cells and weakly labeled a subset of L5 cells. In medial motor cortex, Crym again appeared to specifically label a population of L5 cells. SMI-32 in this medial region also strongly labeled the same subset of L5 cells, and weakly labeled a small subset of L3 cells. Occasionally, a very large SMI-32+ cell that was negative for Crym was also seen in L5 of this medial region (white arrow). Approximate layer boundaries according to cell sizes and published marker distributions.

6.4 Basic distinguishing features of marker-positive cells in medial human motor cortex and mouse M1.

In order to determine if human and mouse L5 share similar Crym and SMI-32 cell type composition and features, we broadly assessed the population make-up of the marker stained cells, as well the relative size for each type across species. In LL5b of mouse M1, 64% of labeled cells were positive for both Crym and Nefh ISH, 31% were positive for Nefh only, and 5% were positive for Crym only (Figure 6.4C). Using Gprin3 GFP as a marker for corticospinal identity, we then assessed the population make-up of corticospinal LL5b cells (Figure 6.4A). 90% of Gprin3 cells were positive for both Crym and Nefh, 7% were positive for Nefh only, and 3% were positive for Crym only (Figure 6.4C). The Gprin3 population that was positive for only Nefh did not show any difference in soma size to Gprin3 cells that were positive for both Crym and Nefh (Figure 6.4D). Together, these data suggest that, while marker stained cells do not differ in size, even within LL5b, there may be further subpopulations of neurons that have yet to be defined.

In human medial motor cortex, Crym and SMI-32 double positive cells made up 96% of labeled cells in L5 (Figure 6.4B-C). Additionally, we observed a very small proportion of L5 cells (3%) that showed strong SMI-32 signal, but weakly stained or did not stain for Crym. These SMI-32-positive/Crym-negative cells display significantly larger soma than the rest of the Crym+ population of L5 cells (Figure 6.4E), and were primarily found in deep L5. The very large neurons that reside in the medial regions of motor cortex in L5 of human motor cortex are thought to represent the corticomotoneuron Betz cell population important for dexterous movement of proximal

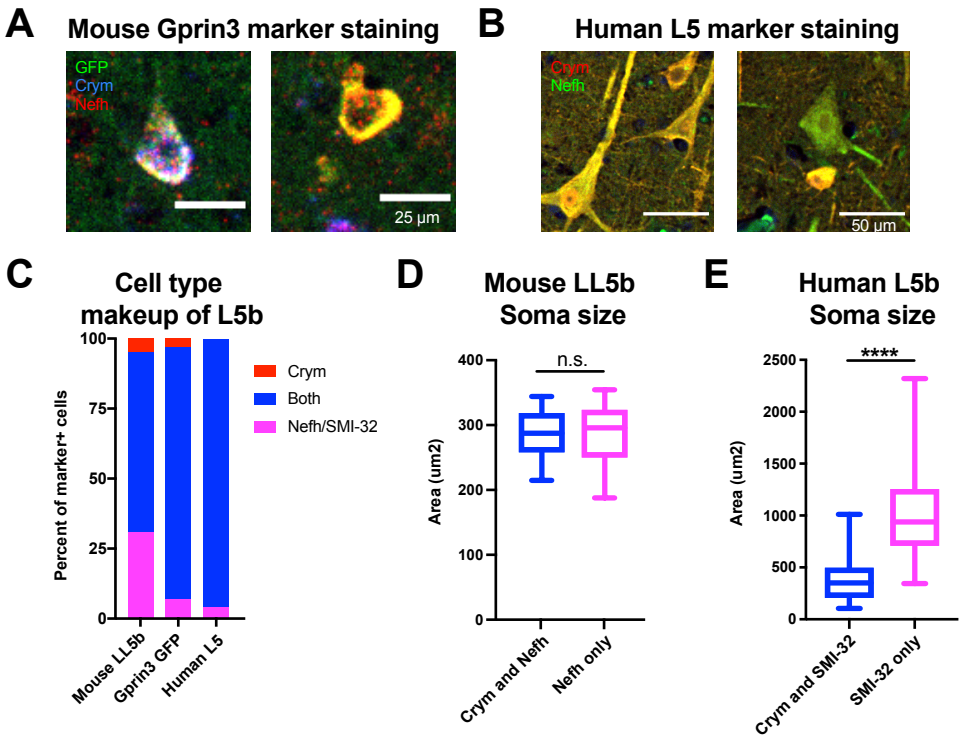

Figure 6.4: Crym and SMI-32 staining can anatomically dissociate putative Betz cells from other neurons in L5 of human motor cortex. (A) Representative images of LL5b Gprin3 cells in mouse M1, stained for GFP (green), Crym ISH (blue), and Nefh ISH (red). Most GFP+ cells stain positive for both Crym and Nefh ISH (left), with a small subset only staining positive for Nefh ISH (right; scale bar = 25 μm). (B) Representative images of human L5 cells that were double-positive for Crym (red) and SMI-32 (green; left), and a putative Betz cell that was only positive for SMI-32 (scale bar = 50 μm). (C) Stacked bar graphs show composition of marker+ cells for all cells in LL5b, Gprin3 GFP+ cells in LL5b, and human L5. Across all of mouse LL5b (including GFP+ and GFP- cells), 64% of cells are double positive for Crym and Nefh ISH (blue bar), 31% were positive for only Nefh ISH (magenta bar), and 5% were positive for Crym ISH (red bar; n = 229 cells). 90% of LL5b Gprin3 cells are positive for both Crym and Nefh ISH, 7% were only Nefh ISH+, and 3% were only Crym ISH+ (n = 60 cells). In human, 96% of L5 cells are positive for both Crym and SMI-32, with remaining 4% showing only SMI-32 labeling (n = 158 cells). (D-E) Quantifications of soma size for different marker+ cell types in mouse LL5b and human L5. In mouse (D), all cell types appeared to be of similar size (Both n = 19 cells; Nefh only n = 24 cells; n.s. = not significant by two-tailed t-test).In human (E), cells that were positive for only SMI-32 tended to be larger than cells that were double-positive for Crym and SMI-32 (Both n = 54 cells; SMI-32 only n = 11; ****$p < 0.0001$ in two-tailed t-test).

and distal limbs (Kaiserman-Abramof and Peters, 1972; Rivara et al., 2003; Walshe, 1942). Our marker staining suggests that the very large L5 cells that we observed as being SMI-32-positive and Crym-negative in medial motor cortex may also represent this Betz cell population. If so, these results present the first combinatorial molecular marker staining that has dissociated Betz cells from the broader L5 population of human primary motor cortex.

Together, these anatomical data suggest that using Crym and SMI-32 marker staining in tandem can reveal diverse populations of L5 cell types across both mouse and human motor cortex, and that even within the mouse corticospinal population (represented by Gprin3), there may be more cell type heterogeneity than originally thought. More experiments must be carried out to understand the anatomical and molecular relationship between these L5 cells across species, particularly if the Gprin3 cells are to be treated as representative of ALS-vulnerable populations in humans.

6.5 Discussion

Parsing the cell types that compose the human cortex has proven very difficult. Without the ability to perform anatomical tracing, differentiating the cell types by projection pattern in tissue has not been possible. Cell types in the motor cortex have until now primarily been classified by their electrophysiological responses during functional motor tasks in vivo (Phillips, 1956), and by their relative cell body sizes in tissue sections (Kaiserman-Abramof and Peters, 1972; Rivara et al., 2003). Discovering markers that allow us to visually distinguish motor cortical cell types from each other

would greatly advance our ability to anatomically characterize subpopulations of L5 cells in both healthy and disease tissues.

In rodents, it is possible to easily screen markers for specific neuronal subpopulations alongside anatomical tracing or transgenic cell type reporters. However, the extent to which these populations represent human neuron types is a subject of much controversy, particularly in the motor cortex, where the divergence in axonal projection anatomy and functional contributions of this area to movement across species are readily evident (see Lemon and Griffiths, 2005; Yoshida and Isa, 2018). But in order to begin establishing cell type relationships across L5 of rodents and primates, we must first determine the cellular make-up of the population important for motor cortex output.

We set out to screen various putative L5 markers and their antibodies for the ability to stain specific subpopulation of L5b cell types in mouse and human motor cortex. We show that staining for Crym and SMI-32 (a variant of Nefh), markers previously used separately to visualize populations of L5b cells across species, can successfully be carried out in tandem in post-mortem, fixed human cortex sections. In combination, these markers reveal distinct subpopulations of L5 cells in human: a Crym+/SMI-32+ population that appears to account for the vast majority of L5 cells in the medial motor region and likely includes corticospinal neurons, and a subset that is only positive for SMI-32 (Figure 6.5). This cells of the latter population are not only larger than their Crym+ counterparts, but it is only found in medial and not lateral regions of the motor cortex of the human. These characteristics suggest that these

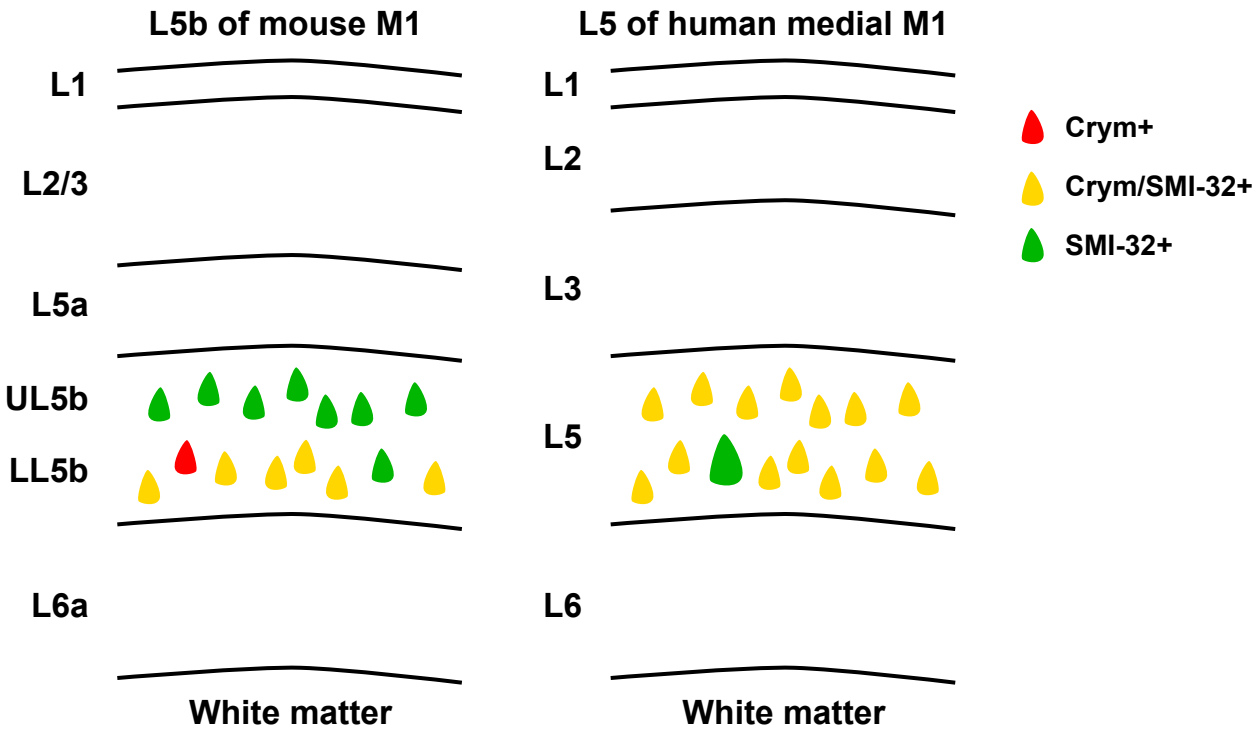

Figure 6.5: Summary of Crym and SMI-32 L5 cell type distribution across mouse and human motor cortex. Within L5b of the mouse, Crym staining (red) appears to be primarily restricted to LL5b, where cells are primarily double positive for Crym and SMI-32 (yellow). Rare subsets of LL5b cells only stain positive for either SMI-32 (green) or Crym. In human medial motor cortex, L5 shows a majority of pyramidal neurons that are positive for both Crym and SMI-32. Rarely, a very large SMI-32+ neuron is seen among these cells. These may be Betz cells

neurons may be Betz cells, which are thought to be corticomotoneurons that synapse directly onto alpha motor neurons of the spinal cord (Kaiserman-Abramof and Peters, 1972; Walshe, 1942). It is thought that these neurons participate in the control of proximal and distal limb movements and produce dexterous movement by so doing (Heffner and Masterton, 1983; Yoshida and Isa, 2018). Until now, Betz cells have been typically identified solely by their large size relative to other L5 cells (Braak et al., 2017; Genç et al., 2017; Hammer et al., 1979). However, in conditions where Betz cells atrophy and therefore change in size (Genç et al., 2017), this strategy would not allow for the identification of Betz cells that fall below a size threshold due to pathological changes. For this reason, having markers that can be used to visualize these cells reliably is key for further study of changes in Betz cell morphology and number in diseases such as ALS.

Even with marker staining, we cannot know whether the Crym+/SMI-32+ human L5 cells that we observe share the same anatomical identity as Gprin3 cells by projection pattern. In other words, if a subset of Crym-/Nefh+ Gprin3 cells molecularly represents a Betz-like population that projects directly onto alpha motor neurons, why does this Gprin3 subpopulation not directly innervate spinal motor neurons in the mouse? Interestingly, during post-natal rodent development, a subset of corticospinal projection cells extend a collateral axon into the ventral horn that is then retracted (Gu et al., 2017b; Kuang and Kalil, 1994; Maeda et al., 2016). If these collaterals are instead allowed to endure by conditionally knocking-out PlexA1, a semaphorin receptor that is important in axon guidance and pruning (Bagri et al., 2003; Winberg et al., 1998), these

animals outperform WT mice in dexterous movement tasks (Gu et al., 2017a). This suggests that while LL5b cells of M1 may not directly innervate alpha motor neurons in mice, they may have the capacity to do so. Does this mean that the molecular identity of the corticospinal population is similar to Betz cells even transiently? This may be reflected in their molecular identity, so it would be very interesting to determine to what extent a corticomotoneuron Gprin3 population in PlexA1 cKO mice overlaps with corticospinal and cortiomotorneuron populations in human motor cortex.

While it is currently not feasible to confirm the corticospinal identity of our marker+ cells in human tissue, however, it may be possible to do so in non-human primates, which also contain Betz cells in primary motor cortex (Jacobs et al., 2018). Staining for Crym and Nefh in non-human primate non-human primate (NHP) motor cortex, coupled with retrograde tracing from the spinal cord, could give us a better understanding of how translatable this marker identity for corticospinal neurons is across rodents and primates. Extrapolating the projection patterns and marker staining of NHP Betz cells to human Betz cells is likely the only way to know how well our combinatorial marker staining distinguishes cells based on projection identity. Corroborating marker staining with NHP anatomical tracing would also allow us to determine with greater certainty, what neuron types in human L5 are likely the most vulnerable in ALS, and to understand to what extent projection identity contributes to this vulnerability. Using our markers, we should therefore attempt to determine whether Crym+ and Nefh+ cell types show greater vulnerability in disease, and whether loss of these cells reflects corticospinal neuron vulnerability in ALS.

CHAPTER 7:

Study Conclusions

This study represents an endeavor to determine how cortical L5b neurons of primary motor cortex are uniquely defined in both healthy and disease contexts. Using a combination of anatomical, molecular, and sequencing techniques, we have begun to outline the features that distinguish these cells, and how these features may be relevant in the study of cell type-specific vulnerability in ALS.

We show that L5b is laminarly composed of two distinct sublayers: upper L5b (UL5b) and lower L5b (LL5b; Chapter 2, Figure 2.14). UL5b contains cells that project to the pons but not the spinal cord (Figure 1.4). LL5b instead contains neurons that send axon collaterals to both the pons and cervical spinal cord. Using BAC transgenic animals, we show that two cell types that occupy these sublayers, Colgalt2 cells of UL5b and Gprin3 cells of LL5b, appear to be molecularly similar by TRAP RNA-Seq relative to other cell types in the cortex, but are nevertheless distinct in ways that may be functionally important. In an animal model of ALS carrying the SOD1-G93A mutation, the Colgalt2 population does not degenerate, while the Gprin3 population is lost as the disease progresses (Chapter 3, Figure 3.5). Colgalt2 cells appear to increase their levels of Oxphos gene expression during disease, while Gpri3 cells decrease it (Chapter 4, Figure 4.11), potentially revealing a coping strategy in the case of Colgalt2 cells, and a dysfunctional mechanism in the case of Gprin3 cells. Underlying these disease-related changes are intrinsic differences in mitochondria between the two cell types that

may predispose the cells to differentially respond to mutant SOD1 expression. Finally, we show that gene expression profiles of these L5b cells in mouse primary motor cortex can be used to screen for markers of L5 cells in human primary motor cortex (Chapter 6, Figure 6.5), and that these markers allow for distinguishing a putative ALS-vulnerable Betz cell population from other pyramidal neurons in L5.

The projection patterns of L5 of the cortex have been broadly characterized (Arlotta et al., 2005; Economo et al., 2018; Feng et al., 2000; Gerfen et al., 2016; Oswald et al., 2013). While it was known that deep layer 5b cortiospinal neurons in the motor cortex have collateral projections to the pons in rodents (Heffner et al., 1990; Ugolini and Kuypers, 1986), we and others are providing novel evidence that reveals that within M1 L5b, there exists an upper sublayer just above the corticospinal L5b cells that contains a second corticofugal population that projects no further than the pons (Chapter 2; Economo et al., 2018). Independently, the corticopontine population has been described for many regions of the cortex across many species (Leergaard and Lakke, 1995; Moya et al., 2014; Wiesendanger and Wiesendanger, 1979; 1982). During early post-natal development in the visual cortex, these corticopontine are initially corticospinal and have a collateral to the pons. By ~P10, the spinal collateral is retracted (Stanfield and O'Leary, 1985). A similar pattern of development was incidentally described for corticopontine cells of the primary motor cortex (Wang et al., 2017). Indeed it appears that the field has been circling around the discovery of two distinct corticofugal populations in M1 L5b for a long time but, due to limitations in the ability to simultaneously visualize multiple cell types, has not managed to distinguish them from

each other. The ability to independently visualize the two populations studied here using BAC transgenics, with the help of retrograde labeling, was invaluable in being able to distinguish these populations.

Layer 5b pyramidal neurons in primary motor cortex of rodents were already known to be vulnerable in human ALS and its models (Hammer et al., 1979; Ozdinler et al., 2011; Tandan and Bradley, 1985; Zang and Cheema, 2002). Because the heterogeneity of L5b corticofugal populations in M1 L5b had not yet been established, the cellular specificity of this loss has not been addressed. Our corticopontine Colgalt2 and corticospinal Gprin3 TRAP lines allowed us to confirm that neuronal loss appears to be specific to corticospinal L5b neurons in M1, rather than affecting all L5b projection neurons. Additionally, the expression of the TRAP construct in these cells presented us with the opportunity to molecularly profile a vulnerable and a closely related, but resistant, population for innately distinct features, as well as unique responses to expression of mutant SOD1. These experiments revealed that UL5b cells respond by up-regulating Oxphos gene expression, while LL5b cells down-regulate the expression of these metabolic genes (Chapter 4, Figure 4.11). We also observe that the baseline levels of Oxphos gene expression between these two cell types are different, with LL5b Gprin3 cells displaying 2.8x greater levels of expression than Colgalt2 cells.

Very few studies in ALS have attempted to determine the cell type-specificity of molecular changes in disease. This is of course extremely valuable, as slowing disease progression is valuable in the management of ALS in humans. However, from a basic research standpoint, the truly fundamental question in ALS remains: Why do

corticospinal motor neurons and spinal motor neurons selectively degenerate in this disease? And how is it that many different mutations can lead to the specific degeneration of these populations? Because ALS is not a monogenic disease, we must consider how the cells may instead be broadly incapable of coping with the stress of different types of mutant insult. And so the discussion of cell type specific vulnerability leads us think about how the unique features of these cells may be exploited by all of the mutations associated with ALS.

We have two examples of cell-type specific degeneration in discrete CNS structures that allow us to explore possible theories: corticospinal neuron loss in L5b of the motor cortex, and alpha motor neuron loss in the ventral horn of the spinal cord. The intrinsic features uniquely shared by these two neurons may help us understand what establishes them as the most vulnerable in the disease. For instance, within their respective regions, these cells are among the largest, as they have very large soma relative to other cell types in the same structure. They also have the longest axons in the CNS, with terminals extending to very distal regions. These two structural features likely require a great deal of energy to maintain, and in fact, our data suggest that corticospinal LL5b cells express Oxphos genes at higher levels than their more proximally-projecting UL5b counterparts (Chapters 2, Figure 2.14 and 4, Figure 4.11). If one additionally considers that motor neurons display high levels of electrophysiological activation during motor behaviors (Burke et al., 1973; Evarts, 1966; 1968; Thach, 1978) that also demand a great deal of energy to produce, we begin to paint a picture of two cell types that must tightly control energetic homeostasis to maintain proper functioning.

Disruptions to this metabolic balance via dysfunction of antioxidant mechanisms in the case of mutant SOD1, or by introducing additional sources of energetic demand in the form of irreversible stress granule formation in the case of mutant TDP-43, FUS, and C9orf72 (Mori et al., 2013; Tan et al., 2007; Vance et al., 2009), could have catastrophic effects in these neurons. Diverting metabolic resources to coping with these dysfunctions could eventually lead the cells to degenerate. In support of this idea, we observe an increase in Oxphos gene expression during disease in UL5b Colgalt2 cells that are resistant to degeneration in the SOD1-G93A model (Chapter 4, Figure 4.11). Perhaps coping with mutant SOD1 expression requires that respiration be increased to provide sufficient energy to fuel mechanisms that mitigate mutant SOD1 damage. In the case of LL5b Gprin3 cells that do degenerate, they may not be able to sufficiently increase Oxphos gene expression because they already express these genes at such high levels in their baseline state. Thus the inability to energetically cope with cellular dysfunction may be what ultimately leads to their loss. But these theories require us to more carefully understand the causal link between respiration and cell death in the context of ALS mutations, and to carefully confirm the changes in mitochondrial ATP-synthesis occurring in cells during disease progression.

Another important consideration in the cell type-specificity of vulnerability that we observe is the contribution of the anatomical projection itself. The fact that corticomotoneurons in the human motor cortex directly innervate LMNs (Kaiserman-Abramof and Peters, 1972; Walshe, 1942) has led many in the field to consider that the disease and its associated dysfunctions may be propagated from one cell type to

another via some mechanism of transfer. The “dying-forward” hypothesis for disease spread, in particular, has a basis in many studies of dysfunction and symptom origin during pathology. For instance, it has been shown that UMNs develop a hyperexcitability phenotype pre-symptomatically in disease (Eisen et al., 1993; Mills, 2003; Mills and Nithi, 1997). It is thought that this increased activity drives the downstream LMNs to stress in forcing an electrophysiological response. The “dying-back” hypothesis also has some basis in ALS symptomology, where some patients display the muscle weakness and fatigability associated with LMN loss before showing signs of tremor and fasiculation that are more associated with UMN loss (Ravits et al., 2007). In this scenario, antidromic stimulation initiated at the UMN-LMN synapse could propagate a hyperexcitability phenotype originating in LMNs. For both “dying-back” and “dying-forward”, the transfer of misfolded and aggregated protein from one motor neuron to another via a prion-like mechanism has also been posited as a possible mechanism of disease propagation along this circuit (see Braak et al., 2013b; Münch et al., 2011; Polymenidou and Cleveland, 2011). But while the direct projection of human corticomotoneurons onto LMNs allows us to consider the possibility of direct transfer of disease between these cells, it is important to remember that in mice, there is no direct projection between vulnerable corticospinal neurons and alpha motor neurons (see Chapter 2, Figure 2.14), and yet degeneration of these cells is still observed. The intermediate spinal neuron population that exists to disynaptically transmit information from the cortex to the spinomuscular system has not been thoroughly characterized. Markers for these cells are now being established (Ueno et al., 2018), which will be

important tools in the study of potential disease propagation across spinal synapses in the ALS mouse. Until we can understand how all the cells of this corticospinomuscular circuit are affected during disease progression, we will not be able to determine how the corticospinal projection of LL5b cells contributes to establishing their vulnerability in this disease.

The divergence in corticospinal projection anatomy between rodents and primates has been a subject of much evolutionary debate. Functionally, corticospinal neuron populations across rodents and primates function in the control of voluntary movement and in motor learning (Deecke et al., 1969; Evarts, 1966; 1968; Fischer, 1967; Guo et al., 2015; Kawai et al., 2015; Lashley, 1924; Thach, 1978; Wang et al., 2017). The direct projections observed for primate corticomotoneurons are thought to additionally be important for the execution of more dexterous movements by prehensile appendages in primate species (Heffner and Masterton, 1983; Yoshida and Isa, 2018). Rodents display a relatively simple repertoire of movements, even for trained dexterous behaviors (Guo et al., 2015; Wang et al., 2017), all of which can be carried out without a direct projection onto spinal motor neurons. The innate species divergence in corticospinal projection anatomy between dexterous and non-dexterous mammals therefore leaves open the question of whether L5b cell types across these species are molecularly related.

We show here that corticospinal LL5b Gprin3 cells, despite not having a direct projection onto alpha motor neurons, show the vulnerability in ALS that has been shown for corticomotoneurons of the human motor cortex (see Chapter 3, Figure 3.5; Braak et

al., 2017; Genç et al., 2017; Hammer et al., 1979; Tandan and Bradley, 1985). We therefore ask how L5 cell types may be related to each other across these species. Understanding whether molecularly defined L5 cell types of human motor cortex exist in mouse motor cortex may allow us to translate the molecular findings from studies of disease rodent models to relevance in human ALS. In this work, we show that markers identified from molecular and anatomical studies of LL5b Gprin3 cells can be used to visualize populations of L5 cells in the human motor cortex (Chapter 6, Figure 6.5). Additionally, we were able to use a combinatorial staining approach for Crym and SMI-32 to distinguish a potential Betz corticomotoneuronal cell type from the broader population of L5 cells. These markers will be useful in further understanding the relationship between corticospinal and corticomotoneuronal populations across species, and will allow for the characterization of cell type specificity of L5 neuronal loss in human ALS.

Together, the findings of this study carry forward our understanding of cell type-specific features that define L5b corticofugal cell types in health and disease. We hope that these findings help to inform studies of motor cortical anatomy across species and ALS disease mechanisms in the motor cortex.

MATERIALS AND METHODS

Animals

All animal procedures and experiments were done with approval from The Rockefeller University Institutional Animal Care and Use Committee (IACUC) and in accordance with National Institutes of Health (NIH) policies and guidelines.

Colgalt2-TRAP DU9 and Gprin3-TRAP ES152 mice, as well as TRAP lines for other cortical cell types, were generated using BAC methods and transgenics (Gong et al., 2010; 2002) at The Rockefeller University. Sequence homology to the region upstream of the ATG start codon of the Colgalt2 and Gprin3 genes was cloned into the pS296 targeting vector (Heiman et al., 2008) containing EGFP-L10a. Recombination was performed in competent DH10β bacteria containing a pSV1.RecA plasmid by electroporating the BAC into the cells. The modified BAC was isolated and microinjected into the pronuclei of fertilized FVB/N mouse oocytes at 0.5 ng/μl. Transgenic founder mice were generated and crossed to C57BL/6J mice. F1 progeny were screened for proper transgene expression by EGFP genotyping and immunohistochemistry. Expression in L5b was used a benchmark for transgenic line expansion. C57Bl/6J (Jackson Laboratory, #000664) were used for breeding in this study. The Tg(SOD1*G93A)1Gur mice (Jackson Laboratory, #002726) were used for ALS work.

Plasmids and vectors

The pAAV-CMV-Flag-PGC1a-6His was a gift from Connie Cepko (Addgene plasmid #67637; http://n2t.net/addgene:67637; RRID:Addgene_67637). The plasmid was unedited before packaging into the retroAAV2 (or "SL1; Tervo et al., 2016) virus in collaboration with the Janelia Farm Viral core. The MitoGFP construct was acquired from the pLYS1-FLAG-MitoGFP-HA plasmid, as a gift from Vamsi Mootha (Addgene plasmid #50057; http://n2t.net/addgene:50057; RRID:Addgene_50057). The coding region was cloned into a Cre-dependent DIO pAAV plasmid (Nectow et al., 2017) by adding plasmid sequence homology to the MitoGFP insert at its 5' and 3' ends. The virus was then packaged into AAV2/9 by UPenn Viral Vector core. The TOMM20-mCherry construct was also acquired from the mCherry-TOMM20-N-10 plasmid, as a gift from Michael Davidson (Addgene plasmid #55146; http://n2t.net/addgene:55146; RRID:Addgene_55146), and was cloned by homologous recombination into a non-Cre-dependent version of the above pAAV plasmid for constitutive expression. The construct was packaged into the "SL1" virus in collaboration with the Janelia Farm Viral core. PCR to add sequence homology was performed using CloneAmp HIFI PCR reagents (Takara). All cloning reactions were carried out using the In-Fusion HD cloning system (Takara) for homologous recombination insertion.

The following primer sequences were used to add sequence homology for homologous recombination cloning reactions:

Cloning reaction	FWD/REV	Sequence (5' to 3')
MitoGFP into DIO pAAV	FWD	TCGTGAGGTACCGGATCCATGGCGGCCG
	REV	GCTTGATATCGAATTCTTATGCGTAGTCAGGC
TOMM20-mCherry into pAAV	FWD	TGAGGTACCGGATCCATGGTGGGTCGGAAC
	REV	CTTGATATCGAATTCTTACTTGTACAGCTCGTCCATGCC

qPCR:

Reactions for qPCR were carried out using LightCycler 480 SYBR Green I Master (Roche). All samples were run in triplicate. A LightCycler 480 (Roche) was used to carry out reactions with default SYBR Green I protocol. Primers were targeted to 3' ends of spliced transcript sequences. The maximum second derivative of each amplification curve was taken as the cycle time (CT) value for analysis. CT values that were > ±1 CT from the rest of the replicate samples were excluded from analysis as long as 2 replicates still remained. The average of the Actb and Gapdh CTs were used for housekeeping gene controls. ddCT calculations for mitochondrial gene qPCR in disease cohorts were carried out on average replicate CT values as follows:

$$-\left(\mathrm{CT}_{\text{Mito gene}} - \mathrm{CT}_{\text{housekeeping}}\right)_{\mathrm{SOD}} - \left(\mathrm{CT}_{\text{Mito gene}} - \mathrm{CT}_{\text{housekeeping}}\right)_{\mathrm{WT}}$$

ddCT calculations for mitochondrial gene qPCR in healthy cell type samples were carried out on averaged replicate CT values as follows:

$$-\left(\mathrm{CT}_{\text{Mito gene}} - \mathrm{CT}_{\text{housekeeping}}\right)_{\mathrm{Gprin3}} - \left(\mathrm{CT}_{\text{Mito gene}} - \mathrm{CT}_{\text{housekeeping}}\right)_{\mathrm{Colgalt2}}$$

The following primer sequences were used for mitochondrial qPCR reactions:

Gene name	FWD/REV	Sequence (5’ to 3’)
Aco2	FWD	CCCCTCCGACTATAACAAGATTC
	REV	TCTCGTTGAAGGTGTGGTTC
Actb	FWD	GGCTGAGGACTTTGTACATT
	REV	GGACTTCCTGTAACCACTTATT
Atp5g3	FWD	GATCTTGTTTGCCATGTAACAG
	REV	GGAGTCACAGCAAGATACAC
Bcl2	FWD	GATGACTGAGTACCTGAACCG
	REV	CAGAGACAGCCAGGAGAAATC
Colgalt2	FWD	CCTTGGGTGTTCGGTATTT
	REV	ACTCAGTCTCCCTTCACTT
Cox6a1	FWD	GACCCTTACTCTGTGTGGA
	REV	AGCAGAAGGGATGGAAGA
Gapdh	FWD	GAGCATCTCCCTCACAATTT
	REV	GGGTGCAGCGAACTTTAT
Gprin3	FWD	TCTGAGAGACCTAGGAGTAAAC
	REV	GCTTTGCTTCACTCTTGTATTC
Gpx1	FWD	GTTTCCCGTGCAATCAGTTC
	REV	AGCCTTCTCACCATTCACTTC
Mrpl17	FWD	TCGATTATGGAAAGCTGGGC
	REV	TTGTGTAGTTCCCATTCTGACC
Mrpl37	FWD	GACTCAGACCAGCTCCTTTAC
	REV	ACACCATGCAAGTACAGAGC
Ndufb8	FWD	CGAAGCAGTACCCTTACAATAA
	REV	CCATCAAGCCTCCTCAGATA
Sod1	FWD	GGGCAAAGGTGGAAATGA
	REV	ACCACACAGGGAATGTTTAC
Sod2	FWD	TGCTCTAATCAGGACCCATTG
	REV	CATTCTCCCAGTTGATTACATTCC

Timm13	FWD	TGAGGGTGGGTTAAGTGT
	REV	GCTCCTTTGGTGCTTATGT
Timm44	FWD	TCAAGAACTCCAAAGGCGAG
	REV	GAGGCTGAGATGTCCAGAAG
Tomm20	FWD	TGACAAATGCCATTGCTGTG
	REV	ATCTTCAGCCAAGCTCTGAG
Tomm40	FWD	GTGGGTGTGGAGTTTGAGG
	REV	CCCACGATCCAGTTACTGTTC
Tomm70a	FWD	CTGAAGCCAGGACATACTTG
	REV	TATTGGACAGCTCTGGAAATAC
Uqcrh	FWD	CACTGGGAATCAGGAACAG
	REV	GCTAGTCACACAGAAGAGAAG

Rotarod:

WT and SOD1-G93A mice were trained on the apparatus for three days beginning at ~P35 (5 weeks of age) and then tested once weekly for 6 weeks. During the test, acceleration was increased from 5-18 rpm over the course of 180 seconds and the latency to fall was measured for two trials. Falls were detected automatically by a sensor at the base of the apparatus.

Surgeries

CTB injections:

Animals were anesthetized via IP injection of 1% Ketamine/0.1% Xylazine (doses 1 mL/kg and 0.1 mL/kg respectively) in 0.9% saline. Following anesthesia, animals were positioned on the stereotaxic apparatus and skin was incised above the skull.

Coordinates (from bregma) for thalamus injections were AP -1.85 mm, ML +/- 1.5 mm, DV -3.2 mm. Pons injections were made at AP -4.1 mm, ML +/-0.6 mm, DV -5.2 mm. Holes were drilled in the skull at the target coordinates using a dental drill. Cholera toxin beta (Alexa 555-conjugated CTB, Thermo Fisher) was injected using a Hamilton syringe with a pulled glass capillary pipette at a rate of 0.1 μL/min to a total volume of 0.25 μL. Incisions were closed using Vetbond (3M) For spinal cord injections, an incision was made from the base of the neck down between the shoulder blades to target the cervical vertebrae. Back and shoulder muscles were separated by cutting connective ligaments with a scalpel. Once the spinal column was exposed, connective tissue was pushed aside slowly using the scalpel blade. Using forceps and surgical scissors, the C6 vertebrae was cut away to reveal the dura and spinal tissue. After carefully cutting a hole in the dura using forceps and scalpel, CTB was injected at a rate of 0.1 μL/min to a total of 0.15-0.20 μL at the following coordinates: AP C6, ML +/-0.4 mm, DV ~ -1.1 mm. Sutures were used to reposition back and shoulder muscles before suturing the incision. Animals were allowed to recover in clean cages over a warming plate, and were given low dose ibuprofen in drinking water during recovery. Animals were perfused after at least 48 hrs following surgery to allow tracer to fully travel the length of the axons.

AAV Injections:

Animals were anesthetized via IP injection of 1% Ketamine/0.1% Xylazine (doses 1 mL/kg and 0.1mL/kg respectively) in 0.9% saline. Mice were then head-fixed into stereotaxic apparatus, and the scalp was resected before drilling small bores over target

injection sites. For labeling LL5b terminals in the spinal cord, AAV.DIO.EYFP was injected at a rate of 0.1 μL/min to a total of 0.15-0.25 μL into the motor cortex of Gng7-Cre mice at AP +0.5 mm, ML +/-1.3 mm, DV -0.75 mm from bregma. Mice were allowed to recover post-operatively before being placed back into the colony room. The virus was allowed to express for 4-5 weeks before collecting tissues, with weekly checks of mouse health being performed throughout. For mitochondrial labeling and Pgc1a overexpression experiments, AAV9.Ef1a.DIO.mitoGFP.WPRE.hGH, SL1.Ef1a.TOM20.mCherry, or SL1.CMV.FLAG.Pgc1a.6XHis was injected into the pons of mice via angled injection to AP -4.15, ML +/-2.01, DV -5.05, 15° from vertical. After suturing was completed, mice were allowed to recover in clean cages over a warming plate, and were given low dose ibuprofen in drinking water for up to one week following the surgery. Viral expression was allowed to continue for 4-5 weeks before collecting tissues, with periodic health checks performed during this time.

PRV injections:

HA-mCherry-expressing Pseudorabies virus (PRV) 298 was generously provided by Lisa Pomeranz in the lab of Jeffery Friedman at The Rockefeller University. Mice were anesthetized as described above. The dorsal face of left upper forelimb muscles were exposed by a cutaneous incision extending from the lateral shoulder to just medial to the elbow. 1μl injections of PRV were made at a rate of 0.25 μL/min into bicep, tricep, trapezius, and deltoideus using a Hamilton syringe with a pulled glass capillary pipette for a total of ~5 μl total. Incision was sutured and mice were allowed to recover post-op

in BSL-2 quarantine. Mice were given low dose ibuprofen in drinking water during recovery. Mice were closely monitored twice daily for 5 days, at which point they were perfused and spinal and brain tissues were collected.

RA Injections

A 40 ml stock solution of 2.5 mg/ml all-trans retinoic acid (RA) in corn oil (100 mg in 40 ml) was made and stored at -20°C. 0.25 mg/ml working solutions in corn oil were made fresh before injections, and animals were injected to a total of 1 mg/kg animal weight, twice the dose described in (Kwok et al., 2012). Control mice were injected with corn oil vehicle at a dose of 4 μl/g animal weight. IP injections of either RA or vehicle were performed three times per week starting from ~P85 until end stage euthanasia. Overt symptoms were recorded and a subjective score was assigned post-hoc, blind to condition.

Tissue collection

Mouse tissue collection:

Mice received an IP injection of 1% Ketamine/0.1% Xylazine (lethal doses 2 mL/kg and 0.2 mL/kg respectively). The animals were then perfused transcardially first with approximately 40 mL of sterile phosphate buffered saline (PBS) pH 7.4, followed by approximately 30 mL of 4% paraformaldehyde (PFA) in PBS. Brain and spinal cord were removed and placed in 4% PFA overnight at 4°C with shaking. Tissues were then transferred to 30% w/v sucrose in PBS and stored at 4°C. Brain and spinal cord tissues

were sectioned on freezing microtome at a thickness of 40 μm. To section spinal cord tissue on the microtome, tissue was first embedded in Richard Allen Scientific Neg-50 (Thermo Fisher) over a slurry of 100% EtOH and dry ice. Sections were stored in non-freezing storage media (25% w/v ethylene glycol, 25% glycerol, 50% PBS) at -20°C until further processing. Before staining or mounting, sections were washed 3 x 5 min with PBS.

Human brain tissue:

Human cortex tissue samples were received from the Miami Brain Bank, as well at the University of Maryland Brain Bank (operating under NIH Neurobio Bank licensing). Lateral motor cortex brain tissues were acquired from the University of Maryland Brain Bank as formalin-fixed tissue blocks. Blocks were embedded in paraffin and sectioned to ~15 μm by the Weill Cornell Medicine Imaging Core. Slides of medial motor cortex sections were sent to our lab from the Miami Brain Bank.

Primate brain tissues:

Primate brain sections were collected in collaboration with colleagues in the Friewald lab at the Rockefeller University. The left hemisphere of a rhesus macaque brain was immediately immersed into a solution of 3.75% acrolein/2% PFA in phosphate buffer (PB). Tissue was then washed in PB before shipping to Neuroscience Associates (Knoxville, TN), where it was embedded in a gelatin-based matrix for serial sectioning.

40 μm sections were collected and immersed in a preservation solution before being returned to our lab.

Staining and Histology

Immunostaining:

The following antibodies were used in study:

Antigen	Species	Vendor	Catalog #	Application	Dilution
GFP	Chicken	Abcam	ab13970	IF, IHC	1:2000
RFP	Rabbit	Abcam	ab62341	IF	1:1000
NeuN	Mouse	Millipore	MAB377	IF	1:1000
GFAP	Rabbit	Thermo F.	Ab-4	IF	1:500
ChAT	Goat	Millipore	AB144P	IF	1:100
CTB	Rabbit	Abcam	ab34992	IF	1:1000
SMI-32	Mouse	Millipore	NE-1023	IF	1:250
SMI-32	Rabbit	Abcam	ab8135	IF	1:1000
Crym	Rabbit	Santa Cruz	sc-366780	IF	1:100
Crym	Mouse	Abcam	ab54669	IF	1:500
Pcp4	Rabbit	Santa Cruz	sc-74816	IF	1:100
Secondaries	Donkey	Jackson Immuno.		IF	1:500

All fluorescent antibody staining experiments were performed on free-floating tissue as follows: sections were washed in PBS pH 7.4, 3 x 5 min to remove anti-freezing storage solution. Sections were incubated with 2.5% Normal Donkey serum (NDS, Jackson Immuno) and 2.5% TritonX-100 for approximately 30 mins. Sections were then incubated in 1% NDS and 1% TritonX-100 with primary antibodies overnight at room temperature with shaking. Sections were washed with PBS 3 x 5 min before incubating

in 1% NDS with fluorescent secondary antibodies for approximately 1 hour. Sections were washed with PBS 3 x 5 min before being mounted on slides and coverslipped with Prolong Gold with DAPI (Thermo). Sections were then visualized using a confocal microscope. On-slide staining was performed in largely the same way, with antibody incubations being carried out in a humidified chamber.

For non-fluorescent immunohistochemistry, a 10 min incubation in 0.3% hydrogen peroxide in PBS and 3 x 5 min PBS washes preceded the blocking/permeabilization step. A biotinylated secondary antibody was used, followed by a 1 hr incubation in ABC solution (Vector Labs). DAB (Vector Labs) was then used to deposit the stain at the site of antigen. Sections were then visualized using a brightfield microscope.

Primate tissue staining:

Because primate sections that were used in this study were made from acrolein-fixed tissue, Schiff bases needed to be reduced prior to staining to quench auto-fluorescence caused by fixation. For this, we adapted the protocol from (Luquin et al., 2010). Briefly, prior to staining, free-floating primate sections were washed 3 x 5 min 0.1M phosphate buffer (PB), pH 7.4. They were then incubated in a freshly-made solution of 1% sodium borohydride ($NaBH_4$) in 0.1M PB for 30 min at RT with agitation. Sections were then washed 3 x 5 min in 0.1M PB, followed by 3 x 5 min PBS pH 7.4. Sections were incubated for 30 min in a solution of 50% EtOH/0.3% H_2O_2 in PBS at RT with agitation. Sections were washed 3 x 5 min in PBS and mounted onto charged slides. Sections

were dried on a 60°C heat block, re-submerged briefly in PBS and dried again. On-slide staining was performed as described above for free-floating sections.

Human tissue staining:

All human sections were stained on slides, as tissue was collected from FFPE blocks. Immediately before staining, slides were deparaffinized by first submerging the sections in Xylenes for 6 min, and subsequently washing in descending concentrations of EtOH in water (100%, 100%, 95%, 70%, 50%) for 3 min each. Slides were then rinsed twice in water before being submerged in PBS. Antigen unmasking was performed before immunostaining. A solution of 0.1M sodium citrate, pH 6.0 with 0.5% TritonX-100 was brought to 90°C using a microwave, and sections were immersed in this solution for 10 min. Solution was maintained at 90°C as needed during incubation with low power microwave heating. The solution with submerged slides was allowed to come to room temperature before the slides were removed and washed with PBS. Concentrations for serums, Triton, and antibodies, as well as incubation times, were identical to free-floating protocol.

Fluorescence In-situ hybridization (FISH):

Cryostat sections (14 μm) for FISH experiments were made from PFA perfusion-fixed and 30% sucrose cryopreserved brains that we were embedded in OTC freezing media. On-slide labeling was performed using RNAscope ISH technology and its associated kits. Probes against Crym (ACD Biotech, #466131) and Nefh (ACD Biotech, #443671)

were used to label L5b cells in Colgalt2 and Gprin3 sections using the RNAscope Multiplex Fluorescent Reagent Kit v2 (ACD Biotech, #323100). All steps were carried out according to manufacturer recommendations in protocol #323100-USM, available on the manufacturer website. Immunostaining after ISH was performed on-slide as described above.

Confocal fluorescence and brightfield microscopy

A Zeiss Axio Observer.Z1 with LSM 700 confocal microscope equipped with 50 mW, 400-640 nm lasers was used for all fluorescent visualizations. Zen software (Zeiss) was used for acquisition of images. For brightness and contrast adjustments, as well as image analysis, FIJI was used (ImageJ, SciJava; Rueden et al., 2017; Schindelin et al., 2012; Schneider et al., 2012). For acquisition of brightfield images of DAB-stained sections, a Zeiss Axio Imager.M2 was used. Neurolucida was used to acquire tiled images of whole sections.

Electron Microscopy (EM)

Immunostaining:

EM experiments were performed in collaboration with the Electron Microscopy Resource Center at The Rockefeller University, and the following procedure was adapted from the protocol written by K. Uryu. “Base buffer” below refers to either 75 mM Na-cacodylate buffer pH 7.4, used for immunostaining in WT Colgalt2 sample preparations, or 100 mM Tris buffer, pH 7.4 at 4°C used in immunostaining of WT vs

SOD Gprin3 samples. Animal tissues were perfuse-fixed in 4% PFA (Electron Microscopy Sciences) in 75 mM Na-cacodylate buffer. 50 μm sections were collected in cold base buffer using a vibratome (Leica). Sections were washed in 0.5% H_2O_2 in base buffer to quench endogenous peroxidase activity. After washing in base buffer 4 x 15 min, sections were washed in a blocking solution of 3% Bovine Serum Albumin (BSA), and 0.1% saponin in base buffer. Anti-GFP primary antibody incubations were done in a solution of 3% BSA with 0.1% saponin in base buffer for 48 hrs at 4°C. Sections were washed 4 x 15 min in base buffer, and were then incubated with biotinylated secondary antibody in base buffer containing 3% BSA and 0.1% saponin for 2 hrs at 4°C. Sections were washed in base buffer 4 x 15 min, then incubated in ABC complex solution (1 μL solution A + 1 μL solution B per 1 mL of base buffer; Vector Science Labs) with 3% BSA and 0.1% saponin for 1 hr. Sections were washed 3 x 15 min before being incubated in a solution of DAB (Vector Science Labs) + Urea H_2O_2 in base buffer for several minutes until proper tissue contrast was achieved. Sections were rinsed in base buffer and fixed in 2.5% gluteraldehyde in 75 mM Na-Cacodylate buffer overnight at 4°C.

Silver enhancement:

Fixed sections were washed with 75 mM Na-cacodylate buffer before being rinsed with 2% sodium acetate in H_2O for 10 min. Sections were then incubated in a developer solution of 3% Methenamine, 5% silver nitrate, and 1% sodium tetraborate for 15 min at 60°C. Sections were then washed once again in 2% sodium acetate, followed by an incubation in 3% sodium thiosulfate. Gold toning was performed by incubating sections

in 0.1% gold chloride for 5 min. Sections were then washed in 2% sodium acetate for 10 min, 3% sodium tetraborate for 5 min, and 2% sodium acetate again for 10 min. After rinsing in 75 mM Na-cacodylate buffer, sections were fixed with 2.5% gluteraldehyde in 75 mM Na-cacodylate overnight at 4°C.

Osmication and Eponate infiltration:

Sections were washed in 75 mM Na-cacodylate before Osmication for ultra-structure preservation. Sections were then incubated in a solution of 1% osmium tetra-oxide with 1% potassium ferrocyanide in cacodylate buffer for 30 min on ice. Sections were then washed 3 x 5 min in Na-cacodylate buffer. They were then treated with a 2% solution of uranium acetate in H_2O for 30 min. Sections were then progressively dehydrated in increasing concentrations of ethanol (50%, 70%, 95%, 100% x 2) 5 min each using a microwave oven. Resin was then infiltrated into the sections by first immersing in a 1:1 solution of acetone and resin mixture (25 mL EPON812, 18 mL NMA, 7 mL DDSA, and 0.60 mL DMP-30) in a microwave under vacuum. Sections were immersed in 100% resin mixture for further infiltration 2 x, then left in fresh resin in a 70°C incubator to polymerize overnight. Sections were immersed one last time in 100% resin under vacuum for 4 hrs. Resin-embedded sections were placed between two sheets of aclar plastic to embed at 60°C for 48 hrs. Ultra-thin sections were made by staff at the EMRC.

Image analyses

Multi-channel signal co-localization:

For co-localization analyses, position markers were placed in FIJI over any cells that appeared subjectively positive for a marker. The position markers were saved as ROIs in the ROI manager and placed over the next channel image of interest. The number of points that were positive in this second channel was counted as being double-positive. This analysis framework was used for CTB/GFP and PRV-mCherry/GFP co-localization in retrograde tracing, and for L5b marker co-localization in mouse and human tissues.

Cell counts:

For determining loss of GFP+ cells in SOD1-G93A mice, a 3 x 2 x 3 (w x h x z) z-stack tile scan of 20X fields was acquired on the confocal microscope. Every 6th section between +1.00 mm and +0.00 mm to Bregma was imaged (one section every ~240 μm), with each hemisphere being imaged separately. The z-stacks were collapsed in FIJI using the maximum intensity projection. Cells were then counted only if apical dendrite was clearly visible. All counting was performed blind to disease condition.

Cell depth analyses:

Cell depths were determined using a custom script (github.com/mvmoya) written for FIJI/ImageJ that calculates the percentage depth from pia and white matter. The pial and white matter surfaces are manually delineated, and the points are placed on the image to mark the locations of the cells. The algorithm then draws a reference line that

is perpendicular to the pial line and intersects the cell's point and terminates at the intersection with the white matter line. The cell's percent distance from the pial line along the reference line is then calculated reported and as a percentage depth from pia.

Terminal densities in spinal cord:

Terminal densities for Gng7-Cre EYFP+ axon terminals were measured by thresholding the EYFP channel image until terminals were exclusively visible in the image. The ventral horn ROI was generated by outlining the area that contained ChAT+ alpha motor neurons in the ChAT channel, and overlaying the resulting ROI onto the EYFP channel. The density of thresholded terminals was returned by the built-in "Area Fraction" tool found in FIJI/ImageJ. The density of terminals in the intermediate lamina was measured by drawing a representative rectangular ROI over these regions and returning the same measurement as described above.

Mitochondrial signal quantification:

Images of fluorescently-labeled mitochondria following mitoGFP or TOM20-mCherry viral expression and immunostaining were collected at 63X-100X magnification and analyzed in FIJI/ImageJ. Cytoplasmic space (excluding the nucleus) was outlined for each neuronal cell body for which an apical dendrite could be observed. The area within this cytoplasmic region was thresholded so as to only include the upper 25% of values in the pixel depth distribution. This proportional thresholding strategy was chosen over setting a fixed value for upper thresholding in order to normalize across cells located at

different depths in the section that presumably were exposed to different levels of antibody penetration. The thresholded image was then run through the “Particle Analyzer” built into FIJI/ImageJ, to assess size, total area, number, and density of discrete “particles” containing mitochondrial signal.

Cristae width measurements:

Electron micrographs were analyzed in FIJI/ImageJ. After importing the image, the spatial resolution of the image was set in FIJI according to the magnification settings and resolution used for acquiring the image. The width was measured in the narrowest dimension for all cristae where both apposing membranes could be readily seen. All mitochondria found in each micrograph were scanned for detectable cristae, regardless of size, shape or subcellular location.

TRAP and RNA-Seq analyses

TRAP:

TRAP experiments from cortical cell types were performed as previously described (Heiman et al., 2008). For cell type characterizations, ~P40 animals were sacrificed, and whole cortex dissected in ice-chilled HBSS containing 2.5 mM HEPES-KOH (pH 7.4), 35 mM glucose, 4 mM $NaHCO_3$, and 100 µg/ml cycloheximide. Cortices from 3 animals were pooled per biological replicate, with 3 replicates per cell type being prepared in total (9 animals). Samples were homogenized in extraction buffer containing 10 mM HEPES-KOH (pH 7.4), 150 mM KCl, 5 mM $MgCl_2$, 0.5 mM DTT, 100 µg/ml

cycloheximide, RNasin (Promega) and SUPERas-In (Life Technologies) RNase inhibitors, and Complete-EDTA-free protease inhibitors (Roche), and then centrifuged at 2000 x g to clear lysate debris. IGEPAL CA- 630 (NP-40, Sigma) and DHPC (Avanti Polar Lipids, Alabaster, AL) were added to the resulting supernatant to a concentration of 1% each, followed by 20,000 x g centrifugation. Polysomes were immunoprecipitated (IP'ed) using 100 μg custom monoclonal anti-GFP antibodies (50 μg of clone 19C8 with 50 μg of clone 19F7) bound to biotinylated Protein L (Pierce, Thermo Fisher) coated streptavidin-coated magnetic beads (Thermo Fisher), and washed with high salt buffer containing 10 mM HEPES-KOH (pH 7.4), 350 mM KCl, 5 mM $MgCl_2$, 1% IGEPAL CA-630, 0.5 mM DTT, 100 µg/ml cycloheximide, and RNasin RNase inhibitors (Promega). Overnight IP's were eluted and purified using Absolutely RNA Nanoprep kit (Agilent). RNA quality was assessed using Nanodrop spectrophotometer and Agilent 2100 Bioanalyzer. Samples with RNA integrity values > 7 were used to prepare libraries for sequencing.

RNAs from TRAP IPs (15 ng per sample) were converted to cDNA using the Nugen Ovation RNA-Seq System V2 kit. cDNAs were then fractionated by sonication and libraries were made using the Illumina TrueSeq RNA Sample Preparation kit v2, following manufacturer's instructions. Sequencing was run on a machine at The Rockefeller University Genomics core using the Illumina HiSeq 2500 platform (Illumina). For disease TRAP cohorts, whole cortices from ~P70 (pre-symptomatic) and ~P110 (symptomatic) timepoints were collected from healthy and SOD1-G93A-crossed Colgalt2 and Gprin3 animals and homogenized, and polysomes were IP'ed also as

described above. At this point, Gprin3 RNA was sent to Dr. Hemali Phatnani at the New York Genome Center (NYGC) for cDNA conversion, library sample preparation, and sequencing. Colgalt2 cDNA libraries were instead prepared in our lab as described above. Prepared libraries were multiplexed to 6 samples and sent to the NYGC for sequencing.

Sequencing analyses:

Returned sequences in FASTQ files were first aligned to mm10 annotated mouse genome using STAR aligner (Dobin et al., 2013) version 2.0.0e_r291. Whole gene counts from exon-mapping aligned reads were quantified using HTSeq (Anders et al., 2015) version 0.6.0, and the htseq-count module. Differential expression analysis on whole gene counts was performed in DESeq2 version 1.22.2 in RStudio version 1.1.463 (Love et al., 2014), RStudio Team (2015). RStudio: Integrated Development for R. RStudio, Inc., Boston, MA, URL http://www.rstudio.com/) using all default parameters. Additional analysis packages can be found in the analysis source code, available on github.com/mvmoya. For determining significantly enriched genes in Colgalt2, Gprin3, and whole cortex cell type characterizations, adjusted p-values were used to determine statistically significant relevant genes ($p < 0.05$). Because very few genes showed adjusted p-values below 0.05 when comparing the same cell type across healthy and disease conditions, un-adjusted p-values were used in disease analyses so as to increase the number of genes available for gene ontology enrichment. Gene ontology enrichment analyses were performed using Metascape (metascape,org; Zhou et al.,

2019) with default parameters. Transcription factor motif enrichment analysis were performed using HOMER (Heinz et al., 2010), searching -1500 upstream of the transcription start site to 500 bases downstream of the transcription start site.

WORKS CITED

Aitken, J.T., and Bridger, J.E. (1961). Neuron size and neuron population density in the lumbosacral region of the cat's spinal cord. Journal of Anatomy *95*, 38–53.

Alcamo, E.A., Chirivella, L., Dautzenberg, M., Dobreva, G., Fariñas, I., Grosschedl, R., and McConnell, S.K. (2008). Satb2 regulates callosal projection neuron identity in the developing cerebral cortex. Neuron *57*, 364–377.

Allen, S.P., Rajan, S., Duffy, L., Mortiboys, H., Higginbottom, A., Grierson, A.J., and Shaw, P.J. (2014). Superoxide dismutase 1 mutation in a cellular model of amyotrophic lateral sclerosis shifts energy generation from oxidative phosphorylation to glycolysis. Neurobiol. Aging *35*, 1499–1509.

Anders, S., Pyl, P.T., and Huber, W. (2015). HTSeq--a Python framework to work with high-throughput sequencing data. Bioinformatics *31*, 166–169.

Anderson, C.T., Sheets, P.L., Kiritani, T., and Shepherd, G.M.G. (2010). Sublayer-specific microcircuits of corticospinal and corticostriatal neurons in motor cortex. Nature Publishing Group *13*, 739–744.

Andrus, P.K., Fleck, T.J., Gurney, M.E., and Hall, E.D. (1998). Protein oxidative damage in a transgenic mouse model of familial amyotrophic lateral sclerosis. Journal of Neurochemistry *71*, 2041–2048.

Arlotta, P., Molyneaux, B.J., Chen, J., Inoue, J., Kominami, R., and Macklis, J.D. (2005). Neuronal subtype-specific genes that control corticospinal motor neuron development in vivo. Neuron *45*, 207–221.

Attwell, D., and Laughlin, S.B. (2001). An energy budget for signaling in the grey matter of the brain. J. Cereb. Blood Flow Metab. *21*, 1133–1145.

Austin, S., and St-Pierre, J. (2012). PGC1α and mitochondrial metabolism--emerging concepts and relevance in ageing and neurodegenerative disorders. J. Cell. Sci. *125*, 4963–4971.

Bachmann, L.C., Lindau, N.T., Felder, P., and Schwab, M.E. (2014). Sprouting of Brainstem–Spinal Tracts in Response to Unilateral Motor Cortex Stroke in Mice. Journal of Neuroscience *34*, 3378–3389.

Bagri, A., Cheng, H.-J., Yaron, A., Pleasure, S.J., and Tessier-Lavigne, M. (2003). Stereotyped pruning of long hippocampal axon branches triggered by retraction inducers of the semaphorin family. Cell *113*, 285–299.

Bandyopadhyay, U., Cotney, J., Nagy, M., Oh, S., Leng, J., Mahajan, M., Mane, S., Fenton, W.A., Noonan, J.P., and Horwich, A.L. (2013). RNA-Seq Profiling of Spinal Cord Motor Neurons from a Presymptomatic SOD1 ALS Mouse. PLoS ONE *8*, e53575.

Bareyre, F.M., Kerschensteiner, M., Misgeld, T., and Sanes, J.R. (2005). Transgenic labeling of the corticospinal tract for monitoring axonal responses to spinal cord injury. Nat Med *11*, 1355–1360.

Beal, M.F., Ferrante, R.J., Browne, S.E., Matthews, R.T., Kowall, N.W., and Brown, R.H. (1997). Increased 3-nitrotyrosine in both sporadic and familial amyotrophic lateral sclerosis. Ann Neurol. *42*, 644–654.

Benatar, M. (2007). Lost in translation: treatment trials in the SOD1 mouse and in human ALS. Neurobiol. Dis. *26*, 1–13.

Bendotti, C., Calvaresi, N., Chiveri, L., Prelle, A., Moggio, M., Braga, M., Silani, V., and De Biasi, S. (2001). Early vacuolization and mitochondrial damage in motor neurons of FALS mice are not associated with apoptosis or with changes in cytochrome oxidase histochemical reactivity. Journal of the Neurological Sciences *191*, 25–33.

Bentmann, E., Haass, C., and Dormann, D. (2013). Stress granules in neurodegeneration--lessons learnt from TAR DNA binding protein of 43 kDa and fused in sarcoma. Febs J. *280*, 4348–4370.

Bishop, K.M., Rubenstein, J.L.R., and O'Leary, D.D.M. (2002). Distinct actions of Emx1, Emx2, and Pax6 in regulating the specification of areas in the developing neocortex. Journal of Neuroscience *22*, 7627–7638.

Boldogh, I.R., and Pon, L.A. (2006). Interactions of mitochondria with the actin cytoskeleton. Biochim. Biophys. Acta *1763*, 450–462.

Borthwick, G.M., Johnson, M.A., Ince, P.G., Shaw, P.J., and Turnbull, D.M. (1999). Mitochondrial enzyme activity in amyotrophic lateral sclerosis: implications for the role of mitochondria in neuronal cell death. Ann Neurol. *46*, 787–790.

Bossy-Wetzel, E., Barsoum, M.J., Godzik, A., Schwarzenbacher, R., and Lipton, S.A. (2003). Mitochondrial fission in apoptosis, neurodegeneration and aging. Current Opinion in Cell Biology *15*, 706–716.

Bourane, S., Grossmann, K.S., Britz, O., Dalet, A., Del Barrio, M.G., Stam, F.J., Garcia-Campmany, L., Koch, S., and Goulding, M. (2015). Identification of a spinal circuit for light touch and fine motor control. Cell *160*, 503–515.

Braak, H., Brettschneider, J., Ludolph, A.C., Lee, V.M., Trojanowski, J.Q., and Del Tredici, K. (2013a). Amyotrophic lateral sclerosis--a model of corticofugal axonal spread. Nat Rev Neurol *9*, 708–714.

Braak, H., Brettschneider, J., Ludolph, A.C., Lee, V.M., Trojanowski, J.Q., and Del Tredici, K. (2013b). Amyotrophic lateral sclerosis—a model of corticofugal axonal spread. Nat Rev Neurol *9*, 708.

Braak, H., Ludolph, A.C., Neumann, M., Ravits, J., and Del Tredici, K. (2017). Pathological TDP-43 changes in Betz cells differ from those in bulbar and spinal α-motoneurons in sporadic amyotrophic lateral sclerosis. Acta Neuropathol. *133*, 79–90.

Brody, H. (1955). Organization of the cerebral cortex. III. A study of aging in the human cerebral cortex. J. Comp. Neurol. *102*, 511–516.

Bruijn, L.I., Beal, M.F., Becher, M.W., Schulz, J.B., Wong, P.C., Price, D.L., and Cleveland, D.W. (1997a). Elevated free nitrotyrosine levels, but not protein-bound nitrotyrosine or hydroxyl radicals, throughout amyotrophic lateral sclerosis (ALS)-like disease implicate tyrosine nitration as an aberrant in vivo property of one familial ALS-linked superoxide dismutase 1 mutant. Proc. Natl. Acad. Sci. U.S.a. *94*, 7606–7611.

Bruijn, L.I., Becher, M.W., Lee, M.K., Anderson, K.L., Jenkins, N.A., Copeland, N.G., Sisodia, S.S., Rothstein, J.D., Borchelt, D.R., Price, D.L., et al. (1997b). ALS-linked SOD1 mutant G85R mediates damage to astrocytes and promotes rapidly progressive disease with SOD1-containing inclusions. Neuron *18*, 327–338.

Bruijn, L.I., Houseweart, M.K., Kato, S., Anderson, K.L., Anderson, S.D., Ohama, E., Reaume, A.G., Scott, R.W., and Cleveland, D.W. (1998). Aggregation and motor neuron toxicity of an ALS-linked SOD1 mutant independent from wild-type SOD1. Science *281*, 1851–1854.

Budd, S.L., and Nicholls, D.G. (1996). Mitochondria, calcium regulation, and acute glutamate excitotoxicity in cultured cerebellar granule cells. Journal of Neurochemistry *67*, 2282–2291.

Burke, R.E., Levine, D.N., Tsairis, P., and Zajac, F.E. (1973). Physiological types and histochemical profiles in motor units of the cat gastrocnemius. J. Physiol. (Lond.) *234*, 723–748.

Burté, F., Carelli, V., Chinnery, P.F., and Yu-Wai-Man, P. (2015). Disturbed mitochondrial dynamics and neurodegenerative disorders. Nat Rev Neurol *11*, 11–24.

Cagalinec, M., Safiulina, D., Liiv, M., Liiv, J., Choubey, V., Wareski, P., Veksler, V., and Kaasik, A. (2013). Principles of the mitochondrial fusion and fission cycle in neurons. J. Cell. Sci. *126*, 2187–2197.

Campbell, M.J., and Morrison, J.H. (1989). Monoclonal antibody to neurofilament protein (SMI-32) labels a subpopulation of pyramidal neurons in the human and monkey neocortex. J. Comp. Neurol. *282*, 191–205.

Casoni, F., Basso, M., Massignan, T., Gianazza, E., Cheroni, C., Salmona, M., Bendotti, C., and Bonetto, V. (2005). Protein nitration in a mouse model of familial amyotrophic lateral sclerosis: possible multifunctional role in the pathogenesis. J. Biol. Chem. *280*, 16295–16304.

Cassina, P., Cassina, A., Pehar, M., Castellanos, R., Gandelman, M., de León, A., Robinson, K.M., Mason, R.P., Beckman, J.S., Barbeito, L., et al. (2008). Mitochondrial dysfunction in SOD1G93A-bearing astrocytes promotes motor neuron degeneration: prevention by mitochondrial-targeted antioxidants. Journal of Neuroscience *28*, 4115–4122.

Caviness, V.S. (1975). Architectonic map of neocortex of the normal mouse. J. Comp. Neurol. *164*, 247–263.

Cederquist, G.Y., Azim, E., Shnider, S.J., Padmanabhan, H., and Macklis, J.D. (2013). Lmo4 establishes rostral motor cortex projection neuron subtype diversity. Journal of Neuroscience *33*, 6321–6332.

Chance, B., Sies, H., and Boveris, A. (1979). Hydroperoxide metabolism in mammalian organs. Physiol. Rev. *59*, 527–605.

Charcot, J.M., and Joffroy, A. (1869). Deux cas d'atrophie musculaire progressive: avec lésions de la substance grise et des faisceaux antéro-latéraux de la moelle épinière. V. Masson.

Chen, B., Wang, S., and Hattox, A. (2008). The Fezf2–Ctip2 genetic pathway regulates the fate choice of subcortical projection neurons in the developing cerebral cortex.

Chen, H., and Chan, D.C. (2009). Mitochondrial dynamics--fusion, fission, movement, and mitophagy--in neurodegenerative diseases. Hum. Mol. Genet. *18*, R169–R176.

Chen, T.-W., Li, N., Daie, K., and Svoboda, K. (2017). A Map of Anticipatory Activity in Mouse Motor Cortex. Neuron *94*, 866–879.e4.

Chiu, A.Y., Zhai, P., Dal Canto, M.C., Peters, T.M., Kwon, Y.W., Prattis, S.M., and Gurney, M.E. (1995). Age-dependent penetrance of disease in a transgenic mouse model of familial amyotrophic lateral sclerosis. Mol. Cell. Neurosci. *6*, 349–362.

Churchland, M.M., and Shenoy, K.V. (2007). Delay of movement caused by disruption of cortical preparatory activity. J. Neurophysiol. *97*, 348–359.

Cleveland, D.W., and Rothstein, J.D. (2001). From Charcot to Lou Gehrig: deciphering selective motor neuron death in ALS. Nat Rev Neurosci *2*, 806–819.

Cole, N.B., Daniels, M.P., Levine, R.L., and Kim, G. (2010). Oxidative stress causes reversible changes in mitochondrial permeability and structure. Exp. Gerontol. *45*, 596–602.

Cozzolino, M., Ferri, A., Valle, C., and Carrì, M.T. (2013). Mitochondria and ALS: implications from novel genes and pathways. Mol. Cell. Neurosci. *55*, 44–49.

Cserép, C., Pósfai, B., Schwarcz, A.D., and Dénes, Á. (2018). Mitochondrial Ultrastructure Is Coupled to Synaptic Performance at Axonal Release Sites. Eneuro *5*, ENEURO.0390–17.2018.

Dal Canto, M.C., and Gurney, M.E. (1995). Neuropathological changes in two lines of mice carrying a transgene for mutant human Cu,Zn SOD, and in mice overexpressing wild type human SOD: a model of familial amyotrophic lateral sclerosis (FALS). Brain Research *676*, 25–40.

Day, B.L., Rothwell, J.C., Thompson, P.D., Maertens de Noordhout, A., Nakashima, K., Shannon, K., and Marsden, C.D. (1989). Delay in the execution of voluntary movement by electrical or magnetic brain stimulation in intact man. Evidence for the storage of motor programs in the brain. Brain *112 (Pt 3)*, 649–663.

de Oliveira, G.P., Alves, C.J., and Chadi, G. (2013). Early gene expression changes in spinal cord from SOD1(G93A) Amyotrophic Lateral Sclerosis animal model. Front. Cell. Neurosci. *7*, 216.

de Oliveira, G.P., Maximino, J.R., Maschietto, M., Zanoteli, E., Puga, R.D., Lima, L., Carraro, D.M., and Chadi, G. (2014). Early gene expression changes in skeletal muscle from SOD1(G93A) amyotrophic lateral sclerosis animal model. Cell. Mol. Neurobiol. *34*, 451–462.

Deecke, L., Scheid, P., and Kornhuber, H.H. (1969). Distribution of readiness potential, pre-motion positivity, and motor potential of the human cerebral cortex preceding voluntary finger movements. Exp Brain Res *7*, 158–168.

DeJesus-Hernandez, M., Mackenzie, I.R., Boeve, B.F., Boxer, A.L., Baker, M., Rutherford, N.J., Nicholson, A.M., Finch, N.A., Flynn, H., Adamson, J., et al. (2011). Expanded GGGGCC Hexanucleotide Repeat in Noncoding Region of C9ORF72 Causes Chromosome 9p-Linked FTD and ALS. Neuron *72*, 245–256.

Dobin, A., Davis, C.A., Schlesinger, F., Drenkow, J., Zaleski, C., Jha, S., Batut, P., Chaisson, M., and Gingeras, T.R. (2013). STAR: ultrafast universal RNA-seq aligner. Bioinformatics *29*, 15–21.

Domesick, V.B. (1969). Projections from the cingulate cortex in the rat. Brain Research *12*, 296–320.

Doyle, J.P., Dougherty, J.D., Heiman, M., Schmidt, E.F., Stevens, T.R., Ma, G., Bupp, S., Shrestha, P., Shah, R.D., Doughty, M.L., et al. (2008). Application of a translational profiling approach for the comparative analysis of CNS cell types. Cell *135*, 749–762.

Economo, M.N., Viswanathan, S., Tasic, B., Bas, E., Winnubst, J., Menon, V., Graybuck, L.T., Nguyen, T.N., Smith, K.A., Yao, Z., et al. (2018). Distinct descending motor cortex pathways and their roles in movement. Nature *563*, 79–84.

Eisen, A., and Weber, M. (2001). The motor cortex and amyotrophic lateral sclerosis. Muscle Nerve *24*, 564–573.

Eisen, A., Kim, S., and Pant, B. (1992). Amyotrophic lateral sclerosis (ALS): a phylogenetic disease of the corticomotoneuron? Muscle Nerve *15*, 219–224.

Eisen, A., Pant, B., and Stewart, H. (1993). Cortical excitability in amyotrophic lateral sclerosis: a clue to pathogenesis. Can J Neurol Sci *20*, 11–16.

Estévez, A.G., Crow, J.P., Sampson, J.B., Reiter, C., Zhuang, Y., Richardson, G.J., Tarpey, M.M., Barbeito, L., and Beckman, J.S. (1999). Induction of nitric oxide-dependent apoptosis in motor neurons by zinc-deficient superoxide dismutase. Science *286*, 2498–2500.

Evarts, E.V. (1966). Pyramidal tract activity associated with a conditioned hand movement in the monkey. J. Neurophysiol. *29*, 1011–1027.

Evarts, E.V. (1968). Relation of pyramidal tract activity to force exerted during voluntary movement. J. Neurophysiol. *31*, 14–27.

Fame, R.M., Dehay, C., Kennedy, H., and Macklis, J.D. (2017). Subtype-Specific Genes that Characterize Subpopulations of Callosal Projection Neurons in Mouse Identify Molecularly Homologous Populations in Macaque Cortex. Cereb. Cortex *27*, 1817–1830.

Feng, G., Mellor, R.H., Bernstein, M., Keller-Peck, C., Nguyen, Q.T., Wallace, M., Nerbonne, J.M., Lichtman, J.W., and Sanes, J.R. (2000). Imaging neuronal subsets in transgenic mice expressing multiple spectral variants of GFP. Neuron *28*, 41–51.

Ferrante, R.J., Shinobu, L.A., Schulz, J.B., Matthews, R.T., Thomas, C.E., Kowall, N.W., Gurney, M.E., and Beal, M.F. (1997). Increased 3-nitrotyrosine and oxidative damage in mice with a human copper/zinc superoxide dismutase mutation. Ann Neurol. *42*, 326–334.

Fink, K.L., Strittmatter, S.M., and Cafferty, W.B.J. (2015). Comprehensive Corticospinal Labeling with mu-crystallin Transgene Reveals Axon Regeneration after Spinal Cord Trauma in ngr1–/– Mice. J Comp Physiol A.

Fischer, E. (1967). Factors affecting motor learning. American Journal of Physical Medicine & Rehabilitation *46*, 511.

Fogarty, M.J., Noakes, P.G., and Bellingham, M.C. (2015). Motor cortex layer V pyramidal neurons exhibit dendritic regression, spine loss, and increased synaptic excitation in the presymptomatic hSOD1(G93A) mouse model of amyotrophic lateral sclerosis. Journal of Neuroscience *35*, 643–647.

Franklin, K., and Paxinos, G. (2008). The Mouse Brain in Stereotaxic Coordinates (Academic Press).

Fukuchi-Shimogori, T., and Grove, E.A. (2001). Neocortex patterning by the secreted signaling molecule FGF8. Science *294*, 1071–1074.

Galaleldeen, A., Strange, R.W., Whitson, L.J., Antonyuk, S.V., Narayana, N., Taylor, A.B., Schuermann, J.P., Holloway, S.P., Hasnain, S.S., and Hart, P.J. (2009). Structural and biophysical properties of metal-free pathogenic SOD1 mutants A4V and G93A. Arch. Biochem. Biophys. *492*, 40–47.

Garel, S., Huffman, K.J., and Rubenstein, J.L.R. (2003). Molecular regionalization of the neocortex is disrupted in Fgf8 hypomorphic mutants. Development *130*, 1903–1914.

Geevasinga, N., Menon, P., Ozdinler, P.H., Kiernan, M.C., and Vucic, S. (2016). Pathophysiological and diagnostic implications of cortical dysfunction in ALS. Nat Rev Neurol *12*, 651–661.

Genç, B., Jara, J.H., Lagrimas, A.K.B., Pytel, P., Roos, R.P., Mesulam, M.M., Geula, C., Bigio, E.H., and Ozdinler, P.H. (2017). Apical dendrite degeneration, a novel cellular pathology for Betz cells in ALS. Sci. Rep. *7*, 41765.

Gerfen, C.R., Economo, M.N., and Chandrashekar, J. (2016). Long distance projections of cortical pyramidal neurons. J. Neurosci. Res.

Gilbert, C.D., and Kelly, J.P. (1975). The projections of cells in different layers of the cat's visual cortex. J. Comp. Neurol. *163*, 81–105.

Gong, S., Kus, L., and Heintz, N. (2010). Rapid bacterial artificial chromosome modification for large-scale mouse transgenesis. Nat Protoc *5*, 1678–1696.

Gong, S., Yang, X.W., Li, C., and Heintz, N. (2002). Highly efficient modification of bacterial artificial chromosomes (BACs) using novel shuttle vectors containing the R6Kgamma origin of replication. Genome Res. *12*, 1992–1998.

Gong, S., Zheng, C., Doughty, M.L., Losos, K., Didkovsky, N., Schambra, U.B., Nowak, N.J., Joyner, A., Leblanc, G., Hatten, M.E., et al. (2003). A gene expression atlas of the central nervous system based on bacterial artificial chromosomes. Nature *425*, 917–925.

Goto, J.J., Zhu, H., Sanchez, R.J., Nersissian, A., Gralla, E.B., Valentine, J.S., and Cabelli, D.E. (2000). Loss of in vitro metal ion binding specificity in mutant copper-zinc superoxide dismutases associated with familial amyotrophic lateral sclerosis. J. Biol. Chem. *275*, 1007–1014.

Graziano, M.S.A., Taylor, C.S.R., and Moore, T. (2002). Complex movements evoked by microstimulation of precentral cortex. Neuron *34*, 841–851.

Gu, Z., Kalambogias, J., Yoshioka, S., Han, W., Li, Z., Kawasawa, Y.I., Pochareddy, S., Li, Z., Liu, F., Xu, X., et al. (2017a). Control of species-dependent cortico-motoneuronal connections underlying manual dexterity. Science *357*, 400–404.

Gu, Z., Serradj, N., Ueno, M., Liang, M., Li, J., Baccei, M.L., Martin, J.H., and Yoshida, Y. (2017b). Skilled Movements Require Non-apoptotic Bax/Bak Pathway-Mediated Corticospinal Circuit Reorganization. Neuron *94*, 626–641.e4.

Guo, J.-Z., Graves, A.R., Guo, W.W., Zheng, J., Lee, A., Rodríguez-González, J., Li, N., Macklin, J.J., Phillips, J.W., Mensh, B.D., et al. (2015). Cortex commands the performance of skilled movement. Elife *4*, e10774.

Guo, Z.V., Li, N., Huber, D., Ophir, E., Gutnisky, D., Ting, J.T., Feng, G., and Svoboda, K. (2014). Flow of cortical activity underlying a tactile decision in mice. Neuron *81*, 179–194.

Gurney, M.E., Pu, H., Chiu, A.Y., Dal Canto, M.C., Polchow, C.Y., Alexander, D.D., Caliendo, J., Hentati, A., Kwon, Y.W., and Deng, H.X. (1994a). Motor neuron degeneration in mice that express a human Cu,Zn superoxide dismutase mutation. Science *264*, 1772–1775.

Gurney, M.E., Pu, H., Chiu, A.Y., Dal Canto, M.C., Polchow, C.Y., Alexander, D.D., Caliendo, J., Hentati, A., Kwon, Y.W., and Deng, H.X. (1994b). Motor neuron degeneration in mice that express a human Cu,Zn superoxide dismutase mutation. Science *264*, 1772–1775.

Hamasaki, T., Leingärtner, A., Ringstedt, T., and O'Leary, D.D.M. (2004). EMX2 regulates sizes and positioning of the primary sensory and motor areas in neocortex by direct specification of cortical progenitors. Neuron *43*, 359–372.

Hammer, R.P., Tomiyasu, U., and Scheibel, A.B. (1979). Degeneration of the human Betz cell due to amyotrophic lateral sclerosis. Experimental Neurology *63*, 336–346.

Hantman, A.W., and Jessell, T.M. (2010). Clarke's column neurons as the focus of a corticospinal corollary circuit. Nature Neuroscience *13*, 1233–1239.

Harrison, T.C., Ayling, O.G.S., and Murphy, T.H. (2012). Distinct cortical circuit mechanisms for complex forelimb movement and motor map topography. Neuron *74*, 397–409.

Hattox, A.M., and Nelson, S.B. (2007). Layer V neurons in mouse cortex projecting to different targets have distinct physiological properties. J. Neurophysiol. *98*, 3330–3340.

Heffner, C.D., Lumsden, A.G., and O'Leary, D.D. (1990). Target control of collateral extension and directional axon growth in the mammalian brain. Science *247*, 217–220.

Heffner, R.S., and Masterton, R.B. (1983). The role of the corticospinal tract in the evolution of human digital dexterity. Brain Behav. Evol. *23*, 165–183.

Heiman, M., Schaefer, A., Gong, S., Peterson, J.D., Day, M., Ramsey, K.E., Suárez-Fariñas, M., Schwarz, C., Stephan, D.A., Surmeier, D.J., et al. (2008). A Translational Profiling Approach for the Molecular Characterization of CNS Cell Types. Cell *135*, 738–748.

Heinz, S., Benner, C., Spann, N., Bertolino, E., Lin, Y.C., Laslo, P., Cheng, J.X., Murre, C., Singh, H., and Glass, C.K. (2010). Simple combinations of lineage-determining transcription factors prime cis-regulatory elements required for macrophage and B cell identities. Molecular Cell *38*, 576–589.

Higgins, C.M.J., Jung, C., Ding, H., and Xu, Z. (2002). Mutant Cu, Zn superoxide dismutase that causes motoneuron degeneration is present in mitochondria in the CNS. Journal of Neuroscience *22*, RC215.

Hooks, B.M., Mao, T., Gutnisky, D.A., Yamawaki, N., Svoboda, K., and Shepherd, G.M.G. (2013). Organization of cortical and thalamic input to pyramidal neurons in mouse motor cortex. Journal of Neuroscience *33*, 748–760.

Huang, C., Zhou, H., Tong, J., Chen, H., Liu, Y.-J., Wang, D., Wei, X., and Xia, X.G. (2011). FUS transgenic rats develop the phenotypes of amyotrophic lateral sclerosis and frontotemporal lobar degeneration. PLoS Genet. *7*, e1002011.

Hüttemann, M., Kadenbach, B., and Grossman, L.I. (2001). Mammalian subunit IV isoforms of cytochrome c oxidase. Gene *267*, 111–123.

Ilieva, H., Polymenidou, M., and Cleveland, D.W. (2009). Non-cell autonomous toxicity in neurodegenerative disorders: ALS and beyond. The Journal of Cell Biology *187*, 761–772.

Inagaki, H.K., Inagaki, M., Romani, S., and Svoboda, K. (2018). Low-Dimensional and Monotonic Preparatory Activity in Mouse Anterior Lateral Motor Cortex. Journal of Neuroscience *38*, 4163–4185.

Itoh, K., Nakamura, K., Iijima, M., and Sesaki, H. (2013). Mitochondrial dynamics in neurodegeneration. Trends in Cell Biology *23*, 64–71.

Iwatsubo, T., Kuzuhara, S., Kanemitsu, A., Shimada, H., and Toyokura, Y. (1990). Corticofugal projections to the motor nuclei of the brainstem and spinal cord in humans. Neurology *40*, 309–309.

Jaarsma, D., Haasdijk, E.D., Grashorn, J.A., Hawkins, R., van Duijn, W., Verspaget, H.W., London, J., and Holstege, J.C. (2000). Human Cu/Zn superoxide dismutase (SOD1) overexpression in mice causes mitochondrial vacuolization, axonal degeneration, and premature motoneuron death and accelerates motoneuron disease in mice expressing a familial amyotrophic lateral sclerosis mutant SOD1. Neurobiol. Dis. *7*, 623–643.

Jaarsma, D., Rognoni, F., van Duijn, W., Verspaget, H.W., Haasdijk, E.D., and Holstege, J.C. (2001). CuZn superoxide dismutase (SOD1) accumulates in vacuolated mitochondria in transgenic mice expressing amyotrophic lateral sclerosis-linked SOD1 mutations. Acta Neuropathol. *102*, 293–305.

Jacobs, B., Garcia, M.E., Shea-Shumsky, N.B., Tennison, M.E., Schall, M., Saviano, M.S., Tummino, T.A., Bull, A.J., Driscoll, L.L., Raghanti, M.A., et al. (2018). Comparative morphology of gigantopyramidal neurons in primary motor cortex across mammals. J. Comp. Neurol. *526*, 496–536.

Jara, J.H., Genc, B., Cox, G.A., Bohn, M.C., Roos, R.P., Macklis, J.D., Ulup nar, E., and Hande Ozdinler, P. (2015). Corticospinal Motor Neurons Are Susceptible to Increased ER Stress and Display Profound Degeneration in the Absence of UCHL1 Function. Cerebral Cortex 1–14.

Jara, J.H., Genç, B., Klessner, J.L., and Ozdinler, P.H. (2014). Retrograde labeling, transduction, and genetic targeting allow cellular analysis of corticospinal motor neurons: implications in health and disease. Front Neuroanat *8*, 16.

Jara, J.H., Villa, S.R., Khan, N.A., Bohn, M.C., and Ozdinler, P.H. (2012). AAV2 mediated retrograde transduction of corticospinal motor neurons reveals initial and selective apical dendrite degeneration in ALS. Neurobiol. Dis. *47*, 174–183.

Jeyaraju, D.V., Cisbani, G., and Pellegrini, L. (2009). Calcium regulation of mitochondria motility and morphology. Biochim. Biophys. Acta *1787*, 1363–1373.

Johnston, J.A., Dalton, M.J., Gurney, M.E., and Kopito, R.R. (2000). Formation of high molecular weight complexes of mutant Cu, Zn-superoxide dismutase in a mouse model for familial amyotrophic lateral sclerosis. Proc. Natl. Acad. Sci. U.S.a. *97*, 12571–12576.

Jones, E.G., and Wise, S.P. (1977). Size, laminar and columnar distribution of efferent cells in the sensory-motor cortex of monkeys. J. Comp. Neurol. *175*, 391–438.

Jones, E.G., Burton, H., and Porter, R. (1975). Commissural and cortico-cortical “columns” in the somatic sensory cortex of primates. Science *190*, 572–574.

Jones, E.G., Coulter, J.D., Burton, H., and Porter, R. (1977). Cells of origin and terminal distribution of corticostriatal fibers arising in the sensory-motor cortex of monkeys. J. Comp. Neurol. *173*, 53–80.

Kaiserman-Abramof, I.R., and Peters, A. (1972). Some aspects of the morphology of Betz cells in the cerebral cortex of the cat. Brain Research *43*, 527–546.

Kann, O., and Kovács, R. (2007). Mitochondria and neuronal activity. Am. J. Physiol., Cell Physiol. *292*, C641–C657.

Kassa, R.M., Mariotti, R., Bonaconsa, M., Bertini, G., and Bentivoglio, M. (2009). Gene, cell, and axon changes in the familial amyotrophic lateral sclerosis mouse sensorimotor cortex. J. Neuropathol. Exp. Neurol. *68*, 59–72.

Kawai, R., Markman, T., Poddar, R., Ko, R., Fantana, A.L., Dhawale, A.K., Kampff, A.R., and Ölveczky, B.P. (2015). Motor cortex is required for learning but not for executing a motor skill. Neuron *86*, 800–812.

Kim, J., Hughes, E.G., Shetty, A.S., Arlotta, P., Goff, L.A., Bergles, D.E., and Brown, S.P. (2017). Changes in the Excitability of Neocortical Neurons in a Mouse Model of Amyotrophic Lateral Sclerosis Are Not Specific to Corticospinal Neurons and Are Modulated by Advancing Disease. Journal of Neuroscience *37*, 9037–9053.

Knott, A.B., Perkins, G., Schwarzenbacher, R., and Bossy-Wetzel, E. (2008). Mitochondrial fragmentation in neurodegeneration. Nat Rev Neurosci *9*, 505–518.

Kolarcik, C.L., and Bowser, R. (2012). Retinoid signaling alterations in amyotrophic lateral sclerosis. Am J Neurodegener Dis *1*, 130–145.

Kong, J., and Xu, Z. (1998). Massive mitochondrial degeneration in motor neurons triggers the onset of amyotrophic lateral sclerosis in mice expressing a mutant SOD1. J. Neurosci. *18*, 3241–3250.

Krieg, W.J.S. (1946). Connections of the cerebral cortex; the albino rat; structure of the cortical areas. J. Comp. Neurol. *84*, 277–323.

Kuang, R.Z., and Kalil, K. (1994). Development of specificity in corticospinal connections by axon collaterals branching selectively into appropriate spinal targets. J. Comp. Neurol. *344*, 270–282.

Kuner, R., Groom, A.J., Müller, G., Kornau, H.-C., Stefovska, V., Bresink, I., Hartmann, B., Tschauner, K., Waibel, S., Ludolph, A.C., et al. (2005). Mechanisms of disease: motoneuron disease aggravated by transgenic expression of a functionally modified AMPA receptor subunit. Ann. N. Y. Acad. Sci. *1053*, 269–286.

Kwiatkowski, T.J., Bosco, D.A., LeClerc, A.L., Tamrazian, E., Vanderburg, C.R., Russ, C., DAVIS, A., Gilchrist, J., Kasarskis, E.J., Munsat, T., et al. (2009). Mutations in the FUS/TLS Gene on Chromosome 16 Cause Familial Amyotrophic Lateral Sclerosis. Science *323*, 1205–1208.

Kwok, S.-K., Park, M.-K., Cho, M.-L., Oh, H.-J., Park, E.-M., Lee, D.-G., Lee, J., Kim, H.-Y., and Park, S.-H. (2012). Retinoic acid attenuates rheumatoid inflammation in mice. J. Immunol. *189*, 1062–1071.

Lashley, K.S. (1924). Studies of cerebral function in learning. Arch NeurPsych *12*, 249.

Lashley, K.S. (1942). Studies of Cerebral Function in Learning. Arch NeurPsych *12*, 249–276.

Lee, H., and Yoon, Y. (2018). Mitochondrial Membrane Dynamics-Functional Positioning of OPA1. Antioxidants (Basel) *7*.

Lee, R.G., and Tatton, W.G. (1975). Motor responses to sudden limb displacements in primates with specific CNS lesions and in human patients with motor system disorders. Can J Neurol Sci *2*, 285–293.

Leergaard, T., and Lakke, E. (1995). Topographical organization in the early postnatal projection: A carbocyanine dye and 3-D computer reconstruction study in the rat - Leergaard - 2004 - The Journal of Comparative Neurology - Wiley Online Library. J Comp Physiol A.

Lein, E.S., Hawrylycz, M.J., Ao, N., Ayres, M., Bensinger, A., Bernard, A., Boe, A.F., Boguski, M.S., Brockway, K.S., Byrnes, E.J., et al. (2007). Genome-wide atlas of gene expression in the adult mouse brain. Nature *445*, 168–176.

Lemon, R.N., and Griffiths, J. (2005). Comparing the function of the corticospinal system in different species: organizational differences for motor specialization? Muscle Nerve *32*, 261–279.

Li, Q., Vande Velde, C., Israelson, A., Xie, J., Bailey, A.O., Dong, M.-Q., Chun, S.J., Roy, T., Winer, L., Yates, J.R., et al. (2010). ALS-linked mutant superoxide dismutase 1 (SOD1) alters mitochondrial protein composition and decreases protein import. Proceedings of the National Academy of Sciences *107*, 21146–21151.

Light, A.R., and Metz, C.B. (1978). The morphology of the spinal cord efferent and afferent neurons contributing to the ventral roots of the cat. J. Comp. Neurol. *179*, 501–515.

Lin, M.T., and Beal, M.F. (2006). Mitochondrial dysfunction and oxidative stress in neurodegenerative diseases. Nature *443*, 787–795.

Liu, Y., Pattamatta, A., Zu, T., Reid, T., Bardhi, O., Borchelt, D.R., Yachnis, A.T., and Ranum, L.P.W. (2016). C9orf72 BAC Mouse Model with Motor Deficits and Neurodegenerative Features of ALS/FTD. Neuron *90*, 521–534.

Lodato, S., Shetty, A.S., and Arlotta, P. (2015). Cerebral cortex assembly: generating and reprogramming projection neuron diversity. Trends Neurosci. *38*, 117–125.

Lopez-Gonzalez, R., Lu, Y., Gendron, T.F., Karydas, A., Tran, H., Yang, D., Petrucelli, L., Miller, B.L., Almeida, S., and Gao, F.-B. (2016). Poly(GR) in C9ORF72-Related ALS/FTD Compromises Mitochondrial Function and Increases Oxidative Stress and DNA Damage in iPSC-Derived Motor Neurons. Neuron *92*, 383–391.

Lorente de No, R. (1938). Cerebral cortex: architecture, intracortical connections, motor projections. Physiology of the Nervous System 288–313.

Love, M.I., Huber, W., and Anders, S. (2014). Moderated estimation of fold change and dispersion for RNA-seq data with DESeq2. Genome Biol. *15*, 550.

Lu, J., Duan, W., Guo, Y., Jiang, H., Li, Z., Huang, J., Hong, K., and Li, C. (2012). Mitochondrial dysfunction in human TDP-43 transfected NSC34 cell lines and the protective effect of dimethoxy curcumin. Brain Research Bulletin *89*, 185–190.

Luquin, E., Pérez-Lorenzo, E., Aymerich, M.S., and Mengual, E. (2010). Two-color fluorescence labeling in acrolein-fixed brain tissue. J. Histochem. Cytochem. *58*, 359–368.

MacAskill, A.F., and Kittler, J.T. (2010). Control of mitochondrial transport and localization in neurons. Trends in Cell Biology *20*, 102–112.

Maeda, H., Fukuda, S., Kameda, H., Murabe, N., Isoo, N., Mizukami, H., Ozawa, K., and Sakurai, M. (2016). Corticospinal axons make direct synaptic connections with spinal motoneurons innervating forearm muscles early during postnatal development in the rat. J. Physiol. (Lond.) *594*, 189–205.

Magrané, J., Hervias, I., Henning, M.S., Damiano, M., Kawamata, H., and Manfredi, G. (2009). Mutant SOD1 in neuronal mitochondria causes toxicity and mitochondrial dynamics abnormalities. Hum. Mol. Genet. *18*, 4552–4564.

Malaspina, A., Kaushik, N., and de Belleroche, J. (2001). Differential expression of 14 genes in amyotrophic lateral sclerosis spinal cord detected using gridded cDNA arrays. Journal of Neurochemistry *77*, 132–145.

Mao, T., Kusefoglu, D., Hooks, B.M., Huber, D., Petreanu, L., and Svoboda, K. (2011). Long-Range Neuronal Circuits Underlying the Interaction between Sensory and Motor Cortex. Neuron *72*, 111–123.

Mattiazzi, M., D'Aurelio, M., Gajewski, C.D., Martushova, K., Kiaei, M., Beal, M.F., and Manfredi, G. (2002). Mutated Human SOD1 Causes Dysfunction of Oxidative Phosphorylation in Mitochondria of Transgenic Mice. Journal of Biological Chemistry *277*, 29626–29633.

McCord, J.M., and Fridovich, I. (1969). Superoxide dismutase. An enzymic function for erythrocuprein (hemocuprein). J. Biol. Chem. *244*, 6049–6055.

Menon, P., Kiernan, M.C., and Vucic, S. (2015). Cortical hyperexcitability precedes lower motor neuron dysfunction in ALS. Clin Neurophysiol *126*, 803–809.

Menzies, F.M., Cookson, M.R., Taylor, R.W., Turnbull, D.M., Chrzanowska-Lightowlers, Z.M.A., Dong, L., Figlewicz, D.A., and Shaw, P.J. (2002). Mitochondrial dysfunction in a cell culture model of familial amyotrophic lateral sclerosis. Brain *125*, 1522–1533.

Miller, K.E., and Sheetz, M.P. (2004). Axonal mitochondrial transport and potential are correlated. J. Cell. Sci. *117*, 2791–2804.

Mills, K.R. (2003). The natural history of central motor abnormalities in amyotrophic lateral sclerosis. Brain *126*, 2558–2566.

Mills, K.R., and Nithi, K.A. (1997). Corticomotor threshold is reduced in early sporadic amyotrophic lateral sclerosis. Muscle Nerve *20*, 1137–1141.

Mironov, S.L. (2006). Spontaneous and evoked neuronal activities regulate movements of single neuronal mitochondria. Synapse *59*, 403–411.

Mironov, S.L. (2009). Complexity of mitochondrial dynamics in neurons and its control by ADP produced during synaptic activity. Int. J. Biochem. Cell Biol. *41*, 2005–2014.

Mochizuki, Y., Mizutani, T., Shimizu, T., and Kawata, A. (2011). Proportional neuronal loss between the primary motor and sensory cortex in amyotrophic lateral sclerosis. Neurosci. Lett. *503*, 73–75.

Molnár, Z., and Cheung, A.F.P. (2006). Towards the classification of subpopulations of layer V pyramidal projection neurons - ScienceDirect. Neuroscience Research *55*, 105–115.

Moreira, P.I., Zhu, X., Wang, X., Lee, H.-G., Nunomura, A., Petersen, R.B., Perry, G., and Smith, M.A. (2010). Mitochondria: a therapeutic target in neurodegeneration. Biochim. Biophys. Acta *1802*, 212–220.

Mori, K., Weng, S.-M., Arzberger, T., May, S., Rentzsch, K., Kremmer, E., Schmid, B., Kretzschmar, H.A., Cruts, M., Van Broeckhoven, C., et al. (2013). The C9orf72 GGGGCC repeat is translated into aggregating dipeptide-repeat proteins in FTLD/ALS. Science *339*, 1335–1338.

Moya, M.V., Siegel, J.J., McCord, E.D., Kalmbach, B.E., Dembrow, N., Johnston, D., and Chitwood, R.A. (2014). Species-specific differences in the medial prefrontal projections to the pons between rat and rabbit. J. Comp. Neurol. *522*, 3052–3074.

Münch, C., O'Brien, J., and Bertolotti, A. (2011). Prion-like propagation of mutant superoxide dismutase-1 misfolding in neuronal cells. Proceedings of the National Academy of Sciences *108*, 3548–3553.

Nakajima, M., Görlich, A., and Heintz, N. (2014). Oxytocin Modulates Female Sociosexual Behavior through a Specific Class of Prefrontal Cortical Interneurons. Cell *159*, 295–305.

Nectow, A.R., Moya, M.V., Ekstrand, M.I., Mousa, A., McGuire, K.L., Sferrazza, C.E., Field, B.C., Rabinowitz, G.S., Sawicka, K., Liang, Y., et al. (2017). Rapid Molecular Profiling of Defined Cell Types Using Viral TRAP. Cell Rep *19*, 655–667.

O'Leary, J.L. (1941). Structure of the area striata of the cat. J. Comp. Neurol. *75*, 131–164.

Okado-Matsumoto, A., and Fridovich, I. (2001). Subcellular distribution of superoxide dismutases (SOD) in rat liver: Cu,Zn-SOD in mitochondria. J. Biol. Chem. *276*, 38388–38393.

Oliván, S., Calvo, A.C., Rando, A., Muñoz, M.J., Zaragoza, P., and Osta, R. (2015). Comparative study of behavioural tests in the SOD1G93A mouse model of amyotrophic lateral sclerosis. Exp. Anim. *64*, 147–153.

Olsen, M.K., Roberds, S.L., Ellerbrock, B.R., Fleck, T.J., McKinley, D.K., and Gurney, M.E. (2002). Disease mechanisms revealed by transcription profiling in SOD1-G93A transgenic mouse spinal cord. Ann Neurol. *50*, 730–740.

Oswald, M.J., Tantirigama, M.L.S., Sonntag, I., Hughes, S.M., and Empson, R.M. (2013). Diversity of layer 5 projection neurons in the mouse motor cortex. Front. Cell. Neurosci. *7*, 174.

Ozdinler, P.H., Benn, S., Yamamoto, T.H., Güzel, M., Brown, R.H., and Macklis, J.D. (2011). Corticospinal motor neurons and related subcerebral projection neurons undergo early and specific neurodegeneration in hSOD1G^{93}A transgenic ALS mice. Journal of Neuroscience *31*, 4166–4177.

Penfield, W. (1954). Mechanisms of voluntary movement. Brain *77*, 1–17.

Penfield, W., and Boldrey, E. (1937). Somatic motor and sensory representation in the cerebral cortex of man as studied by electrical stimulation. Brain *60*, 389–443.

Petreanu, L., Mao, T., Sternson, S.M., and Svoboda, K. (2009). The subcellular organization of neocortical excitatory connections. Nature *457*, 1142–1145.

Phillips, C.G. (1956). Cortical motor threshold and the thresholds and distribution of excited Betz cells in the cat. Q J Exp Physiol Cogn Med Sci *41*, 70–84.

Polymenidou, M., and Cleveland, D.W. (2011). The seeds of neurodegeneration: prion-like spreading in ALS. Cell *147*, 498–508.

Quintana-Cabrera, R., Quirin, C., Glytsou, C., Corrado, M., Urbani, A., Pellattiero, A., Calvo, E., Vázquez, J., Enríquez, J.A., Gerle, C., et al. (2018). The cristae modulator Optic atrophy 1 requires mitochondrial ATP synthase oligomers to safeguard mitochondrial function. Nat Commun *9*, 3399.

Rainbolt, T.K., Saunders, J.M., and Wiseman, R.L. (2014). Stress-responsive regulation of mitochondria through the ER unfolded protein response. Trends Endocrinol. Metab. *25*, 528–537.

Rakic, P. (1974). Neurons in rhesus monkey visual cortex: systematic relation between time of origin and eventual disposition. Science *183*, 425–427.

Ramón y Cajal, S. (1911). Histologie du système nerveux de l'homme et des vertébrés. Maloine, Paris *2*, 153–173.

Ravits, J., Paul, P., and Jorg, C. (2007). Focality of upper and lower motor neuron degeneration at the clinical onset of ALS. Neurology *68*, 1571–1575.

Renton, A.E., Majounie, E., Waite, A., Simón-Sánchez, J., Rollinson, S., Gibbs, J.R., Schymick, J.C., Laaksovirta, H., van Swieten, J.C., Myllykangas, L., et al. (2011). A hexanucleotide repeat expansion in C9ORF72 is the cause of chromosome 9p21-linked ALS-FTD. Neuron *72*, 257–268.

Rivara, C.-B., Sherwood, C.C., Bouras, C., and Hof, P.R. (2003). Stereologic characterization and spatial distribution patterns of Betz cells in the human primary motor cortex. Anat Rec a Discov Mol Cell Evol Biol *270*, 137–151.

Robberecht, W., Sapp, P., Viaene, M.K., Rosen, D., McKenna-Yasek, D., Haines, J., Horvitz, R., Theys, P., and Brown, R. (1994). Cu/Zn superoxide dismutase activity in familial and sporadic amyotrophic lateral sclerosis. Journal of Neurochemistry *62*, 384–387.

Robertson, J., Sanelli, T., Xiao, S., Yang, W., Horne, P., Hammond, R., Pioro, E.P., and Strong, M.J. (2007). Lack of TDP-43 abnormalities in mutant SOD1 transgenic mice shows disparity with ALS. Neurosci. Lett. *420*, 128–132.

Roland, P.E., Larsen, B., Lassen, N.A., and Skinhoj, E. (1980). Supplementary motor area and other cortical areas in organization of voluntary movements in man. J. Neurophysiol. *43*, 118–136.

Rosen, D.R., Siddique, T., Patterson, D., Figlewicz, D.A., Sapp, P., Hentati, A., Donaldson, D., Goto, J., O'Regan, J.P., Deng, H.-X., et al. (1993). Mutations in Cu/Zn superoxide dismutase gene are associated with familial amyotrophic lateral sclerosis. Nature *362*, 59–62.

Rouaux, C., and Arlotta, P. (2013). Direct lineage reprogramming of post-mitotic callosal neurons into corticofugal neurons in vivo. Nat Cell Biol *15*, 214–221.

Rowland, L.P., and Shneider, N.A. (2001). Amyotrophic Lateral Sclerosis. N Engl J Med *344*, 1688–1700.

Rueden, C.T., Schindelin, J., Hiner, M.C., DeZonia, B.E., Walter, A.E., Arena, E.T., and Eliceiri, K.W. (2017). ImageJ2: ImageJ for the next generation of scientific image data. BMC Bioinformatics *18*, 529.

Saba, L., Viscomi, M.T., Caioli, S., Pignataro, A., Bisicchia, E., Pieri, M., Molinari, M., Ammassari-Teule, M., and Zona, C. (2015). Altered Functionality, Morphology, and Vesicular Glutamate Transporter Expression of Cortical Motor Neurons from a Presymptomatic Mouse Model of Amyotrophic Lateral Sclerosis. Cerebral Cortex *25*.

Salehi, M., Nikkhah, M., Ghasemi, A., and Arab, S.S. (2015). Mitochondrial membrane disruption by aggregation products of ALS-causing superoxide dismutase-1 mutants. Int. J. Biol. Macromol. *75*, 290–297.

Sancak, Y., Markhard, A.L., Kitami, T., Kovács-Bogdán, E., Kamer, K.J., Udeshi, N.D., Carr, S.A., Chaudhuri, D., Clapham, D.E., Li, A.A., et al. (2013). EMRE is an essential component of the mitochondrial calcium uniporter complex. Science *342*, 1379–1382.

Saxena, S., Cabuy, E., and Caroni, P. (2009). A role for motoneuron subtype-selective ER stress in disease manifestations of FALS mice. Nature Publishing Group *12*, 627–636.

Scarpulla, R.C. (2011). Metabolic control of mitochondrial biogenesis through the PGC-1 family regulatory network. Biochim. Biophys. Acta *1813*, 1269–1278.

Schindelin, J., Arganda-Carreras, I., Frise, E., Kaynig, V., Longair, M., Pietzsch, T., Preibisch, S., Rueden, C., Saalfeld, S., Schmid, B., et al. (2012). Fiji: an open-source platform for biological-image analysis. Nat. Methods *9*, 676–682.

Schmidt, E.F., Warner-Schmidt, J.L., Otopalik, B.G., Pickett, S.B., Greengard, P., and Heintz, N. (2012). Identification of the cortical neurons that mediate antidepressant responses. Cell *149*, 1152–1163.

Schneider, C.A., Rasband, W.S., and Eliceiri, K.W. (2012). NIH Image to ImageJ: 25 years of image analysis. Nat. Methods *9*, 671–675.

Shatz, C.J., and Stryker, M.P. (1978). Ocular dominance in layer IV of the cat's visual cortex and the effects of monocular deprivation. J. Physiol. (Lond.) *281*, 267–283.

Sheets, P.L., Suter, B.A., Kiritani, T., Chan, C.S., Surmeier, D.J., and Shepherd, G.M.G. (2011). Corticospinal-specific HCN expression in mouse motor cortex: Ih-dependent synaptic integration as a candidate microcircuit mechanism involved in motor control. J. Neurophysiol.

Shibasaki, H., Sadato, N., Lyshkow, H., Yonekura, Y., Honda, M., Nagamine, T., Suwazono, S., Magata, Y., Ikeda, A., and Miyazaki, M. (1993). Both primary motor cortex and supplementary motor area play an important role in complex finger movement. Brain *116 (Pt 6)*, 1387–1398.

Shizuya, H., Birren, B., Kim, U.J., Mancino, V., Slepak, T., Tachiiri, Y., and Simon, M. (1992). Cloning and stable maintenance of 300-kilobase-pair fragments of human DNA in Escherichia coli using an F-factor-based vector. Proc. Natl. Acad. Sci. U.S.a. *89*, 8794–8797.

Singh, R.J., Karoui, H., Gunther, M.R., Beckman, J.S., Mason, R.P., and Kalyanaraman, B. (1998). Reexamination of the mechanism of hydroxyl radical adducts formed from the reaction between familial amyotrophic lateral sclerosis-associated Cu,Zn superoxide dismutase mutants and H2O2. Proc. Natl. Acad. Sci. U.S.a. *95*, 6675–6680.

Song, W., Song, Y., Kincaid, B., Bossy, B., and Bossy-Wetzel, E. (2013). Mutant SOD1G93A triggers mitochondrial fragmentation in spinal cord motor neurons: neuroprotection by SIRT3 and PGC-1α. Neurobiol. Dis. *51*, 72–81.

Spalloni, A., Origlia, N., Sgobio, C., Trabalza, A., Nutini, M., Berretta, N., Bernardi, G., Domenici, L., Ammassari-Teule, M., and Longone, P. (2011). Postsynaptic alteration of NR2A subunit and defective autophosphorylation of alphaCaMKII at threonine-286 contribute to abnormal plasticity and morphology of upper motor neurons in presymptomatic SOD1G93A mice, a murine model for amyotrophic lateral sclerosis. Cereb. Cortex *21*, 796–805.

Sreedharan, J., Blair, I.P., Tripathi, V.B., Hu, X., Vance, C., Rogelj, B., Ackerley, S., Durnall, J.C., Williams, K.L., Buratti, E., et al. (2008). TDP-43 Mutations in Familial and Sporadic Amyotrophic Lateral Sclerosis. Science *319*, 1668–1672.

Stanfield, B.B., and O'Leary, D.D. (1985). The transient corticospinal projection from the occipital cortex during the postnatal development of the rat. J. Comp. Neurol. *238*, 236–248.

Stiburek, L., Vesela, K., Hansikova, H., Pecina, P., Tesarova, M., Cerna, L., Houstek, J., and Zeman, J. (2005). Tissue-specific cytochrome c oxidase assembly defects due to mutations in SCO2 and SURF1. Biochem. J. *392*, 625–632.

Sugino, K., Hempel, C.M., Miller, M.N., Hattox, A.M., Shapiro, P., Wu, C., Huang, Z.J., and Nelson, S.B. (2006). Molecular taxonomy of major neuronal classes in the adult mouse forebrain. Nature Neuroscience *9*, 99–107.

Sun, S., Sun, Y., Ling, S.-C., Ferraiuolo, L., McAlonis-Downes, M., Zou, Y., Drenner, K., Wang, Y., Ditsworth, D., Tokunaga, S., et al. (2015). Translational profiling identifies a cascade of damage initiated in motor neurons and spreading to glia in mutant SOD1-mediated ALS. Proceedings of the National Academy of Sciences *112*, E6993–E7002.

Suter, B.A., Migliore, M., and Shepherd, G.M.G. (2013). Intrinsic electrophysiology of mouse corticospinal neurons: a class-specific triad of spike-related properties. Cerebral Cortex *23*, 1965–1977.

Tan, C.-F., Eguchi, H., Tagawa, A., Onodera, O., Iwasaki, T., Tsujino, A., Nishizawa, M., Kakita, A., and Takahashi, H. (2007). TDP-43 immunoreactivity in neuronal inclusions in familial amyotrophic lateral sclerosis with or without SOD1 gene mutation. Acta Neuropathol. *113*, 535–542.

Tandan, R., and Bradley, W.G. (1985). Amyotrophic lateral sclerosis: Part 1. Clinical features, pathology, and ethical issues in management. Ann Neurol. *18*, 271–280.

Tantirigama, M.L.S., Oswald, M.J., Clare, A.J., Wicky, H.E., Day, R.C., Hughes, S.M., and Empson, R.M. (2016). Fezf2 expression in layer 5 projection neurons of mature mouse motor cortex. J. Comp. Neurol. *524*, 829–845.

Tantirigama, M.L.S., Oswald, M.J., Duynstee, C., Hughes, S.M., and Empson, R.M. (2014). Expression of the developmental transcription factor Fezf2 identifies a distinct subpopulation of layer 5 intratelencephalic-projection neurons in mature mouse motor cortex. Journal of Neuroscience *34*, 4303–4308.

Tasic, B., Menon, V., Nguyen, T.N., Kim, T.K., Jarsky, T., Yao, Z., Levi, B., Gray, L.T., Sorensen, S.A., Dolbeare, T., et al. (2016). Adult mouse cortical cell taxonomy revealed by single cell transcriptomics. Nature Neuroscience *19*, 335–346.

Tasic, B., Yao, Z., Graybuck, L.T., Smith, K.A., Nguyen, T.N., Bertagnolli, D., Goldy, J., Garren, E., Economo, M.N., Viswanathan, S., et al. (2018). Shared and distinct transcriptomic cell types across neocortical areas. Nature *563*, 72–78.

Tateno, M., Sadakata, H., Tanaka, M., Itohara, S., Shin, R.-M., Miura, M., Masuda, M., Aosaki, T., Urushitani, M., Misawa, H., et al. (2004). Calcium-permeable AMPA receptors promote misfolding of mutant SOD1 protein and development of amyotrophic lateral sclerosis in a transgenic mouse model. Hum. Mol. Genet. *13*, 2183–2196.

Tervo, D.G.R., Hwang, B.-Y., Viswanathan, S., Gaj, T., Lavzin, M., Ritola, K.D., Lindo, S., Michael, S., Kuleshova, E., Ojala, D., et al. (2016). A Designer AAV Variant Permits Efficient Retrograde Access to Projection Neurons. Neuron *92*, 372–382.

Thach, W.T. (1978). Correlation of neural discharge with pattern and force of muscular activity, joint position, and direction of intended next movement in motor cortex and cerebellum. J. Neurophysiol. *41*, 654–676.

Thomsen, G.M., Gowing, G., Latter, J., Chen, M., Vit, J.P., Staggenborg, K., Avalos, P., Alkaslasi, M., Ferraiuolo, L., Likhite, S., et al. (2014). Delayed Disease Onset and Extended Survival in the SOD1G93A Rat Model of Amyotrophic Lateral Sclerosis after Suppression of Mutant SOD1 in the Motor Cortex. Journal of Neuroscience *34*, 15587–15600.

Tourniaire, F., Musinovic, H., Gouranton, E., Astier, J., Marcotorchino, J., Arreguin, A., Bernot, D., Palou, A., Bonet, M.L., Ribot, J., et al. (2015). All-trans retinoic acid induces oxidative phosphorylation and mitochondria biogenesis in adipocytes. J. Lipid Res. *56*, 1100–1109.

Tripathi, P., Rodriguez-Muela, N., Klim, J.R., de Boer, A.S., Agrawal, S., Sandoe, J., Lopes, C.S., Ogliari, K.S., Williams, L.A., Shear, M., et al. (2017). Reactive Astrocytes Promote ALS-like Degeneration and Intracellular Protein Aggregation in Human Motor Neurons by Disrupting Autophagy through TGF-β1. Stem Cell Reports *9*, 667–680.

Trotti, D., Rolfs, A., Danbolt, N.C., Brown, R.H., and Hediger, M.A. (1999). SOD1 mutants linked to amyotrophic lateral sclerosis selectively inactivate a glial glutamate transporter. Nature Neuroscience *2*, 427–433.

Tsai, K.-J., Yang, C.-H., Fang, Y.-H., Cho, K.-H., Chien, W.-L., Wang, W.-T., Wu, T.-W., Lin, C.-P., Fu, W.-M., and Shen, C.-K.J. (2010). Elevated expression of TDP-43 in the forebrain of mice is sufficient to cause neurological and pathological phenotypes mimicking FTLD-U. J. Exp. Med. *207*, 1661–1673.

Tsao, W., Jeong, Y.H., Lin, S., Ling, J., Price, D.L., Chiang, P.-M., and Wong, P.C. (2012). Rodent models of TDP-43: recent advances. Brain Research *1462*, 26–39.

Turner, B.J., and Talbot, K. (2008). Transgenics, toxicity and therapeutics in rodent models of mutant SOD1-mediated familial ALS. Prog. Neurobiol. *85*, 94–134.

Turner, M.R., Hardiman, O., Benatar, M., Brooks, B.R., Chiò, A., de Carvalho, M., Ince, P.G., Lin, C., Miller, R.G., Mitsumoto, H., et al. (2013). Controversies and priorities in amyotrophic lateral sclerosis. Lancet Neurol *12*, 310–322.

Ueno, M., Nakamura, Y., Li, J., Gu, Z., Niehaus, J., Maezawa, M., Crone, S.A., Goulding, M., Baccei, M.L., and Yoshida, Y. (2018). Corticospinal Circuits from the Sensory and Motor Cortices Differentially Regulate Skilled Movements through Distinct Spinal Interneurons. Cell Rep *23*, 1286–1300.e1287.

Ueta, Y., Otsuka, T., Morishima, M., Ushimaru, M., and Kawaguchi, Y. (2014). Multiple layer 5 pyramidal cell subtypes relay cortical feedback from secondary to primary motor areas in rats. Cerebral Cortex *24*, 2362–2376.

Ugolini, G., and Kuypers, H.G. (1986). Collaterals of corticospinal and pyramidal fibres to the pontine grey demonstrated by a new application of the fluorescent fibre labelling technique. Brain Research *365*, 211–227.

Uldry, M., Yang, W., St-Pierre, J., Lin, J., Seale, P., and Spiegelman, B.M. (2006). Complementary action of the PGC-1 coactivators in mitochondrial biogenesis and brown fat differentiation. Cell Metabolism *3*, 333–341.

Vance, C., Rogelj, B., Hortobágyi, T., De Vos, K.J., Nishimura, A.L., Sreedharan, J., Hu, X., Smith, B., Ruddy, D., Wright, P., et al. (2009). Mutations in FUS, an RNA processing protein, cause familial amyotrophic lateral sclerosis type 6. Science *323*, 1208–1211.

Vander Heiden, M.G., Chandel, N.S., Williamson, E.K., Schumacker, P.T., and Thompson, C.B. (1997). Bcl-xL regulates the membrane potential and volume homeostasis of mitochondria. Cell *91*, 627–637.

Vargas, M.R., Pehar, M., Cassina, P., Martínez-Palma, L., Thompson, J.A., Beckman, J.S., and Barbeito, L. (2005). Fibroblast growth factor-1 induces heme oxygenase-1 via nuclear factor erythroid 2-related factor 2 (Nrf2) in spinal cord astrocytes: consequences for motor neuron survival. J. Biol. Chem. *280*, 25571–25579.

Vaughan, D.W., and Peters, A. (1973). A three dimensional study of layer I of the rat parietal cortex. J. Comp. Neurol. *149*, 355–370.

Vehviläinen, P., Koistinaho, J., and Gundars, G. (2014). Mechanisms of mutant SOD1 induced mitochondrial toxicity in amyotrophic lateral sclerosis. Front. Cell. Neurosci. *8*, 126.

Verbeeck, C., Deng, Q., DeJesus-Hernandez, M., Taylor, G., Ceballos-Diaz, C., Kocerha, J., Golde, T., Das, P., Rademakers, R., Dickson, D.W., et al. (2012). Expression of Fused in sarcoma mutations in mice recapitulates the neuropathology of FUS proteinopathies and provides insight into disease pathogenesis. Mol Neurodegener *7*, 53.

Virbasius, C.A., Virbasius, J.V., and Scarpulla, R.C. (1993a). NRF-1, an activator involved in nuclear-mitochondrial interactions, utilizes a new DNA-binding domain conserved in a family of developmental regulators. Genes & Development *7*, 2431–2445.

Virbasius, J.V., Virbasius, C.A., and Scarpulla, R.C. (1993b). Identity of GABP with NRF-2, a multisubunit activator of cytochrome oxidase expression, reveals a cellular role for an ETS domain activator of viral promoters. Genes & Development *7*, 380–392.

Virk, M.S., Sagi, Y., Medrihan, L., Leung, J., Kaplitt, M.G., and Greengard, P. (2016). Opposing roles for serotonin in cholinergic neurons of the ventral and dorsal striatum. Proceedings of the National Academy of Sciences *113*, 734–739.

Vogt, B.A., and Pandya, D.N. (1978). Cortico-cortical connections of somatic sensory cortex (areas 3, 1 and 2) in the rhesus monkey. J. Comp. Neurol. *177*, 179–191.

Vucic, S., and Kiernan, M.C. (2006). Novel threshold tracking techniques suggest that cortical hyperexcitability is an early feature of motor neuron disease. Brain *129*, 2436–2446.

Vucic, S., Nicholson, G.A., and Kiernan, M.C. (2008). Cortical hyperexcitability may precede the onset of familial amyotrophic lateral sclerosis. Brain *131*, 1540–1550.

Walshe, F. (1942). The giant cells of Betz, the motor cortex, and the pyramidal tract: a critical review. Brain *65*, 409–461.

Wang, X., Liu, Y., Li, X., Zhang, Z., Yang, H., Zhang, Y., Williams, P.R., Alwahab, N.S.A., Kapur, K., Yu, B., et al. (2017). Deconstruction of Corticospinal Circuits for Goal-Directed Motor Skills. Cell.

Warita, H., Itoyama, Y., and Abe, K. (1999). Selective impairment of fast anterograde axonal transport in the peripheral nerves of asymptomatic transgenic mice with a G93A mutant SOD1 gene. Brain Research *819*, 120–131.

Watanabe, M., Dykes-Hoberg, M., Culotta, V.C., Price, D.L., Wong, P.C., and Rothstein, J.D. (2001). Histological evidence of protein aggregation in mutant SOD1 transgenic mice and in amyotrophic lateral sclerosis neural tissues. Neurobiol. Dis. *8*, 933–941.

Watanabe, Y., and Nakamura, H. (2000). Control of chick tectum territory along dorsoventral axis by Sonic hedgehog. Development *127*, 1131–1140.

Watson, C., Paxinos, G., and Kayalioglu, G. (2008). The Spinal Cord (Elsevier).

Wegorzewska, I., Bell, S., Cairns, N.J., Miller, T.M., and Baloh, R.H. (2009). TDP-43 mutant transgenic mice develop features of ALS and frontotemporal lobar degeneration. Proceedings of the National Academy of Sciences *106*, 18809–18814.

Weiler, N., Wood, L., Yu, J., Solla, S.A., and Shepherd, G.M.G. (2008). Top-down laminar organization of the excitatory network in motor cortex. Nature Neuroscience *11*, 360–366.

Wiedemann, F.R., Manfredi, G., Mawrin, C., Beal, M.F., and Schon, E.A. (2002). Mitochondrial DNA and respiratory chain function in spinal cords of ALS patients. Journal of Neurochemistry *80*, 616–625.

Wiesendanger, R., and Wiesendanger, M. (1979). An anatomical investigation of the corticopontine projection in the primate (Macaca fascicularis and Saimiri sciureus)--II. The projection from frontal and parietal association areas. Neuroscience *4*, 747–765.

Wiesendanger, R., and Wiesendanger, M. (1982). The corticopontine system in the rat. I. Mapping of corticopontine neurons. J. Comp. Neurol. *208*, 215–226.

Williamson, T.L., and Cleveland, D.W. (1999). Slowing of axonal transport is a very early event in the toxicity of ALS-linked SOD1 mutants to motor neurons. Nature Neuroscience *2*, 50–56.

Williamson, T.L., Corson, L.B., Huang, L., Burlingame, A., LIU, J., Bruijn, L.I., and Cleveland, D.W. (2000). Toxicity of ALS-linked SOD1 mutants. Science *288*, 399.

Winberg, M.L., Noordermeer, J.N., Tamagnone, L., Comoglio, P.M., Spriggs, M.K., Tessier-Lavigne, M., and Goodman, C.S. (1998). Plexin A is a neuronal semaphorin receptor that controls axon guidance. Cell *95*, 903–916.

Wise, S.P., and Jones, E.G. (1977a). Cells of origin and terminal distribution of descending projections of the rat somatic sensory cortex. J. Comp. Neurol. *175*, 129–157.

Wise, S.P., and Jones, E.G. (1977b). Somatotopic and columnar organization in the corticotectal projection of the rat somatic sensory cortex. Brain Research *133*, 223–235.

Wise, S.P., Murray, E.A., and Coulter, J.D. (1979). Somatotopic organization of corticospinal and corticotrigeminal neurons in the rat. Neuroscience *4*, 65–78.

Wong, P.C., Pardo, C.A., Borchelt, D.R., Lee, M.K., Copeland, N.G., Jenkins, N.A., Sisodia, S.S., Cleveland, D.W., and Price, D.L. (1995). An adverse property of a familial ALS-linked SOD1 mutation causes motor neuron disease characterized by vacuolar degeneration of mitochondria. Neuron *14*, 1105–1116.

Woolsey, T.A., and Van der Loos, H. (1970). The structural organization of layer IV in the somatosensory region (SI) of mouse cerebral cortex. The description of a cortical field composed of discrete cytoarchitectonic units. Brain Research *17*, 205–242.

Wu, Z., Puigserver, P., Andersson, U., Zhang, C., Adelmant, G., Mootha, V., Troy, A., Cinti, S., Lowell, B., Scarpulla, R.C., et al. (1999). Mechanisms controlling mitochondrial biogenesis and respiration through the thermogenic coactivator PGC-1. Cell *98*, 115–124.

Xiong, W., MacColl Garfinkel, A.E., Li, Y., Benowitz, L.I., and Cepko, C.L. (2015). NRF2 promotes neuronal survival in neurodegeneration and acute nerve damage. J. Clin. Invest. *125*, 1433–1445.

Yasvoina, M.V., Genç, B., Jara, J.H., Sheets, P.L., Quinlan, K.A., Milosevic, A., Shepherd, G.M.G., Heckman, C.J., and Ozdinler, P.H. (2013). eGFP expression under UCHL1 promoter genetically labels corticospinal motor neurons and a subpopulation of degeneration-resistant spinal motor neurons in an ALS mouse model. Journal of Neuroscience *33*, 7890–7904.

Yoshida, Y., and Isa, T. (2018). Neural and genetic basis of dexterous hand movements. Current Opinion in Neurobiology *52*, 25–32.

Yu, J., Anderson, C.T., Kiritani, T., Sheets, P.L., Wokosin, D.L., Wood, L., and Shepherd, G.M.G. (2008). Local-Circuit Phenotypes of Layer 5 Neurons in Motor-Frontal Cortex of YFP-H Mice. Front Neural Circuits *2*, 6.

Zang, D.W., and Cheema, S.S. (2002). Degeneration of corticospinal and bulbospinal systems in the superoxide dismutase 1(G93A G1H) transgenic mouse model of familial amyotrophic lateral sclerosis. Neurosci. Lett. *332*, 99–102.

Zenisek, D., and Matthews, G. (2000). The role of mitochondria in presynaptic calcium handling at a ribbon synapse. Neuron *25*, 229–237.

Zhang, B., Tu, P., Abtahian, F., Trojanowski, J.Q., and Lee, V.M. (1997). Neurofilaments and orthograde transport are reduced in ventral root axons of transgenic mice that express human SOD1 with a G93A mutation. The Journal of Cell Biology *139*, 1307–1315.

Zhou, Y., Zhou, B., Pache, L., Chang, M., Khodabakhshi, A.H., Tanaseichuk, O., Benner, C., and Chanda, S.K. (2019). Metascape provides a biologist-oriented resource for the analysis of systems-level datasets. Nat Commun *10*, 1523.